DOCTORAT MATIERE BRETAGNE MOLECULES LOIRE ET MATERIAUX

UNIVERSITÉ DE NANTES

THESE DE DOCTORAT DE

L'UNIVERSITE DE NANTES

COMUE UNIVERSITE BRETAGNE LOIRE

ECOLE DOCTORALE N° 596
Matière Molécules et Matériaux
Spécialité : *Chimie Physique, Chimie Théorique*

Par

Pauline VÉRITÉ

Modelling of excited state proton transfer in fluorescent dyes

Thèse présentée et soutenue à Nantes, le 30 Juin 2020
Unité de recherche : CEISAM – UMR CNRS 6230, Faculté des Sciences et Techniques,
2 rue de la Houssinière, 44322 Nantes Cedex3

Rapporteurs avant soutenance :

Ilaria Ciofini	Directrice de recherche Chimie ParisTech
Tangui Le Bahers	Maître de conférences ENS Lyon

Composition du Jury :

Ilaria Ciofini	Directrice de recherche Chimie ParisTech
Tangui Le Bahers	Maître de conférences ENS Lyon
Morgane Vacher	Chargée de recherche Université de Nantes
Président du Jury Gilles Ulrich	Directeur de recherche Université de Strasbourg
Directeur de thèse Denis Jacquemin	Professeur d'université Université de Nantes

Résumé

L'exploration de colorants subissant un transfert de proton intramoléculaire à l'état excité (ESIPT, Figure 1) avec des calculs *ab initio* est au cœur de cette thèse. Le processus ESIPT est un mécanisme fascinant et souvent complexe,[1–6] ouvrant la voie à un large éventail d'applications tels que les OLEDs, les colorants laser, les portes logiques, les photostabilisateurs, ou encore les sondes pour différents analytes. Dans ce manuscrit sont présentés mes travaux de thèse visant à modéliser les propriétés électroniques (stabilité, absorption, émission) de cette classe spécifique de colorants fluorescents.

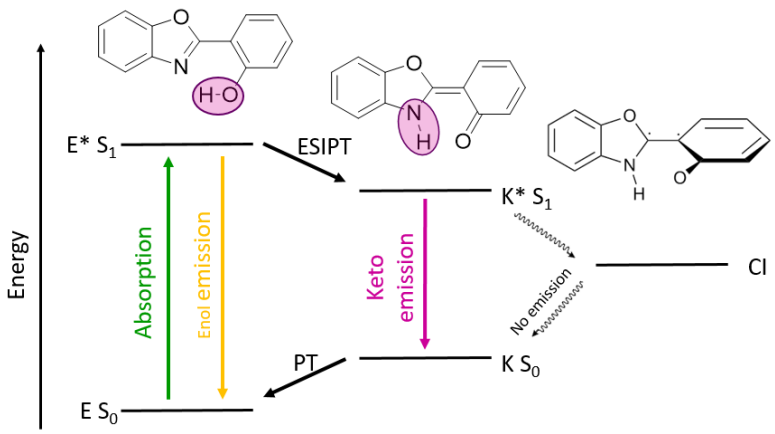

Figure 1: Processus ESIPT typique: l'absorption de la forme énol, stable à l'état fondamental, est suivie par un transfert de proton à l'état excité (ESIPT) pour obtenir l'état excité céto qui peut émettre de la lumière. Une torsion de cette dernière peut également se produire conduisant à une intersection conique (CI) et à une relaxation non radiative vers l'état fondamental.

Le processus ESIPT apparaît principalement dans les molécules contenant un cycle à cinq ou à six membres comprenant une liaison hydrogène intramoléculaire. Dans ce manuscrit, toutes les molécules étudiées présentent un cycle à 6 chaînons ainsi qu'une interaction N$\cdots$HO. Sous photo-excitation, l'atome d'hydrogène peut être transféré entre les deux sites pour former un tautomère, généralement appelé structure céto (K*, pour *keto*), contrairement à la forme originale énol (E) qui prédomine généralement à l'état électronique fondamental. Le but de ce processus est de stabiliser l'état excité. Comme l'illustre la Figure 1, une autre diminution d'énergie peut se produire via la torsion autour la liaison centrale (formellement double) de la forme K*, ce qui conduit à une intersection conique

(CI) puis à l'état fondamental. Lorsque ce processus de torsion est limité, la forme K* est un tautomère stable qui peut émettre efficacement de la lumière à une grande longueur d'onde avec un très grand déplacement de Stokes par rapport à l'absorption énol (E). Les réarrangements importants de la densité électronique et donc de la géométrie entre les isomères absorbants et émetteurs (énol et céto, respectivement) sont responsables de ce grand déplacement de Stokes, caractéristique des colorants ESIPT.

Une partie importante de mon travail de thèse a été réalisée en étroite collaboration avec l'équipe du Dr. Gilles Ulrich à l'Université de Strasbourg. En effet, mon doctorat a été financé par l'ANR (*Agence nationale de la recherche*) dans le cadre du projet GeDEMi, piloté par le Dr. Gilles Ulrich et le Pr. Denis Jacquemin. Ce projet visait à rationaliser et optimiser des molécules présentant une émission double (deux bandes de fluorescence non dues à un couplage vibronique) à l'aide du mécanisme ESIPT. La rationalisation des propriétés électroniques de systèmes ESIPT a été pilotée par le Pr. Denis Jacquemin à l'Université de Nantes, ce qui a conduit à mon recrutement en tant que doctorante. Le deuxième objectif, la synthèse et caractérisation optique, a été réalisé par l'équipe du Dr. Gilles Ulrich à l'Université de Strasbourg, dont le Dr. Julien Massue et la Dr. Antoinette De Nicola sont membres. Cette équipe a également recruté un doctorant pour réaliser ce projet: Thibault Pariat. Au cours de cette collaboration, plus de quarante colorants ESIPT ont été synthétisés, caractérisés, et modélisés grâce à la collaboration des deux équipes. Trente-quatre de ces composés sont présentés dans ce manuscrit et, comme attendu, une partie de ces résultats a également été présentée dans plusieurs publications associées.[7–10] Ces colorants ont été conçus pour être hautement émissifs en solution mais également à l'état solide et sont basés sur un cœur de la famille "HBX" [2-(2'-hydroxyphenyl)benzoxazole (HBO), 2-(2'-hydroxyphenyl)benzimidazole (HBI) et 2-(2'-hydroxy-phenyl)benzothiazole (HBT)].[11–13] L'objectif initial de ce projet consistait à obtenir de nouvelles sondes fluorescentes ratiométriques. Sur les trente-quatre colorants rapportés ici, et étudiés dans le benzène et le toluène, 9% présentent des émissions des deux tautomères à l'état excité, 6 % de la forme énol, et la majorité d'entre eux, 85%, présentent une fluorescence ESIPT provenant de la forme céto. Si l'optimisation de systèmes doublement émissif pour obtenir des sondes fluorescentes ratiométriques reste encore à perfectionner, nos connaissances pour contrôler l'émission et pour atteindre des fluorophores à forte luminescence ont été fortement améliorées. Ainsi, il est notable que certains des fluorophores obtenus pendant ce projet sont parmi les plus brillants disponibles à ce jour.

La luminescence ainsi que la stabilité des tautomères sont des propriétés pouvant être déterminées grâce à des méthodes de calculs *ab-initio*. Dans le cadre de mes travaux de thèse, la théorie de la fonctionnelle de la densité (DFT) ainsi que sa version dépendante du temps (TD-DFT) ont été employées pour étudier différents composés ESIPT. Pour affiner la qualité des énergies totales et de transition calculées, des corrections d'énergies ont été ajoutées à l'aide de calculs post Hartree-Fock, et plus précisément, de calculs ADC(2) et CC2. Une attention particulière a été portée à la modélisation de

l'environnement. Pour ce faire le modèle de continuum (PCM: *Polarizable Continuum Model*) a été systématiquement associé aux calculs (TD-)DFT. En sus, différentes formulations ont été employées: non seulement celle de la réponse linéaire (LR) mais aussi celle de la réponse linéaire corrigée (cLR). Chacune de ces formulations est adaptée à une situation spécifique: LR dans le cas d'un état excité fortement localisé et cLR pour la description de systèmes à transfert de charge. Dans le cas des colorants ESIPT, les transitions électroniques sont typiquement plus fortement autorisées pour la forme énol que céto, les moments dipolaires des deux tautomères sont également fortement différents. Grâce à une approche originale, utilisée pour la première fois pour un large jeu de colorants, les corrections apportées par les formulations LR et cLR ont été prises en compte simultanément au cours de ma thèse.

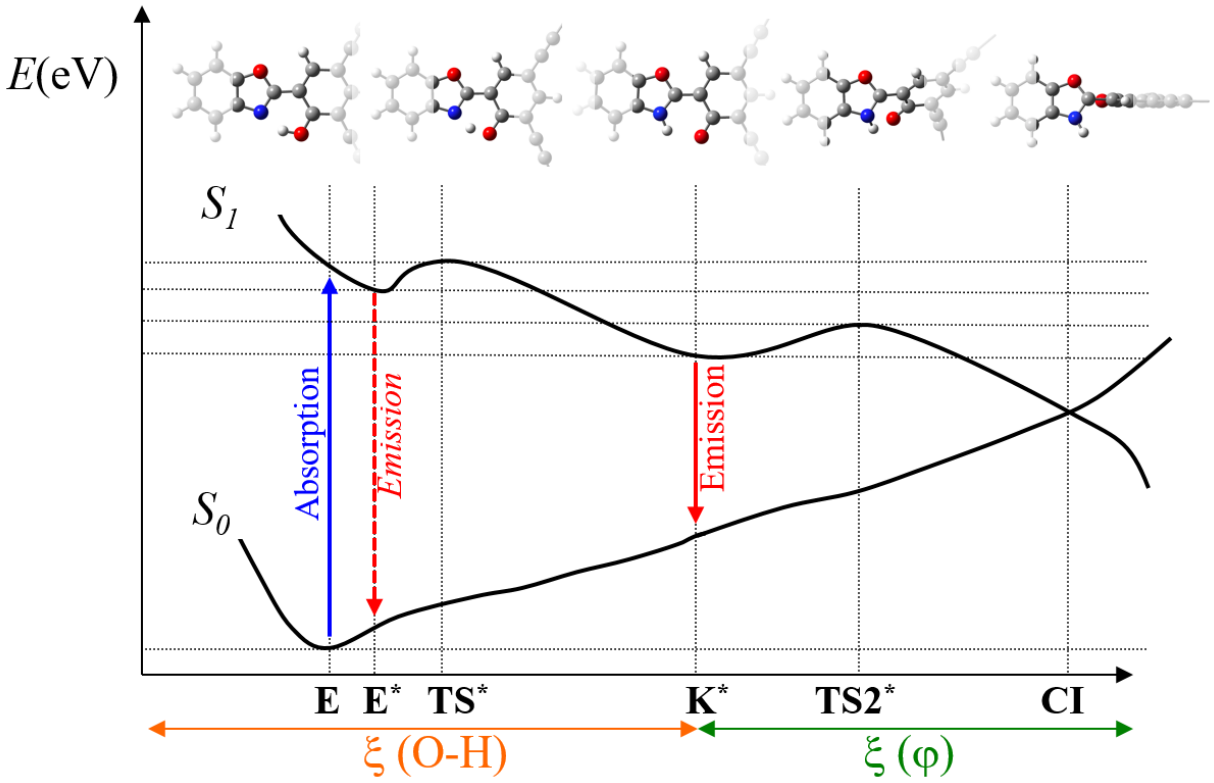

Figure 2: Représentation de la surface d'énergie potentielle (PES) au cours du processus ESIPT. Les coordonnées en X correspondent au processus ESIPT (en orange) et à la torsion entre les deux fragments après transfert de protons (en vert). Pour ces deux processus, les états de transition sont notés TS* et TS2*, respectivement. L'intersection conique (CI) est également représentée mais n'a pas été explorée de manière explicite dans le cadre de mes travaux.

Pour caractériser le mécanisme ESIPT de chaque système étudié durant cette thèse une approche de calcul systématique a été mise en place, voir la Figure 2. Tout d'abord, la structure énol à l'état fondamental est optimisée. A partir de cette structure, une estimation de l'absorption verticale est obtenue ainsi que de la différence de densité électronique (EDD) entre l'état fondamental et l'état excité pour visualiser le changement dans la répartition de la densité induite par l'absorption de lumière. En-

suite, les tautomères énol et céto ont été optimisés à l'état excité et leurs énergies d'émission verticales calculées. La stabilité relative de ces formes a été évaluée pour définir laquelle est la plus stable et produira probablement la fluorescence. Le transfert de protons peut être modulé par la barrière entre les deux tautomères. Cette barrière est estimée par optimisation de l'état de transition "réel" entre E* et K*, appelé TS*. La vibration correspondant à la fréquence imaginaire associée à ce TS* doit bien évidemment représenter le transfert du proton entre les atomes d'oxygène et d'azote. Enfin, l'état de transition entre K* et l'intersection conique, appelé TS2*, a été optimisée. Avec cette barrière, la probabilité de décroissance non radiative via cette intersection peut être grossièrement évaluée et peut être reliée au rendement quantique de fluorescence mesuré expérimentallement.

Les systèmes issus de la collaboration avec l'équipe strasbourgeoise sont tous basés sur des cœurs HBX (HBO, HBT et HBI) et comprennent un seul site ESIPT, voir Figure 3. La double luminescence ne peut donc résulter que de la coexistence de deux formes, les tautomères énol et céto, ou, alternativement, la formation de l'anion à l'état excité. Pour atteindre la double émission, le noyau HBT (X = S) a montré des résultats très prometteurs, mais son rendement quantique de fluorescence (Φ_f) est malheureusement très faible (∼1 %). Pour améliorer le Φ_f, diverses substitutions ont été explorées. Cette stratégie a également été appliquée aux noyaux HBO (X = O) et HBI (X = NH) pour moduler les intensités relatives des émissions E* et K*. En effet, le cœur HBI peut être considéré comme un point de départ judicieux en raison de son très grand Φ_f (∼ 36 %).

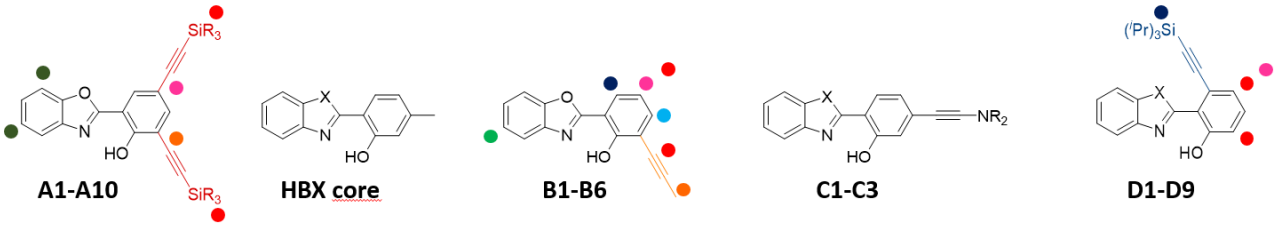

Figure 3: Aperçu des différentes séries de structures issues de notre collaboration avec l'équipe de Strasbourg. X = O, S et NH. Les points de couleur représentent les positions des substitutions étudiées dans chaque série.

L'introduction d'un groupement ethynylaniline en position *meta'* (conduisant à une structure linéaire) du groupe hydroxyl permet d'obtenir les trois différents profils d'émission (énol, céto, et double) dans un milieu apolaire et aprotique (benzène), tous avec un Φ_f assez élevé (> 15 %). Selon la nature du substituant, des émissions cétonique ou doubles ont été observées avec les architectures HBT et HBI (céto avec aniline, double avec diméthylamine). La substitution en *meta* du cœur HBO par un ethynylaniline stabilise fortement la forme énol qui devient la forme émissive. Cette stabilisation par la substitution *meta'* n'a pas été obtenue avec d'autres substituants, tels que l'ethynyl-tolyl (étudié dans le toluène). La seule différence entre ces deux fragments est la présence ou l'absence d'un donneur d'électrons, un effet mis en évidence par les représentations de la différence de densité électronique.

L'ajout de substituants (trialkylsilyl-acétylène et tolyl-acétylène) sur les autres postions (*meta*,

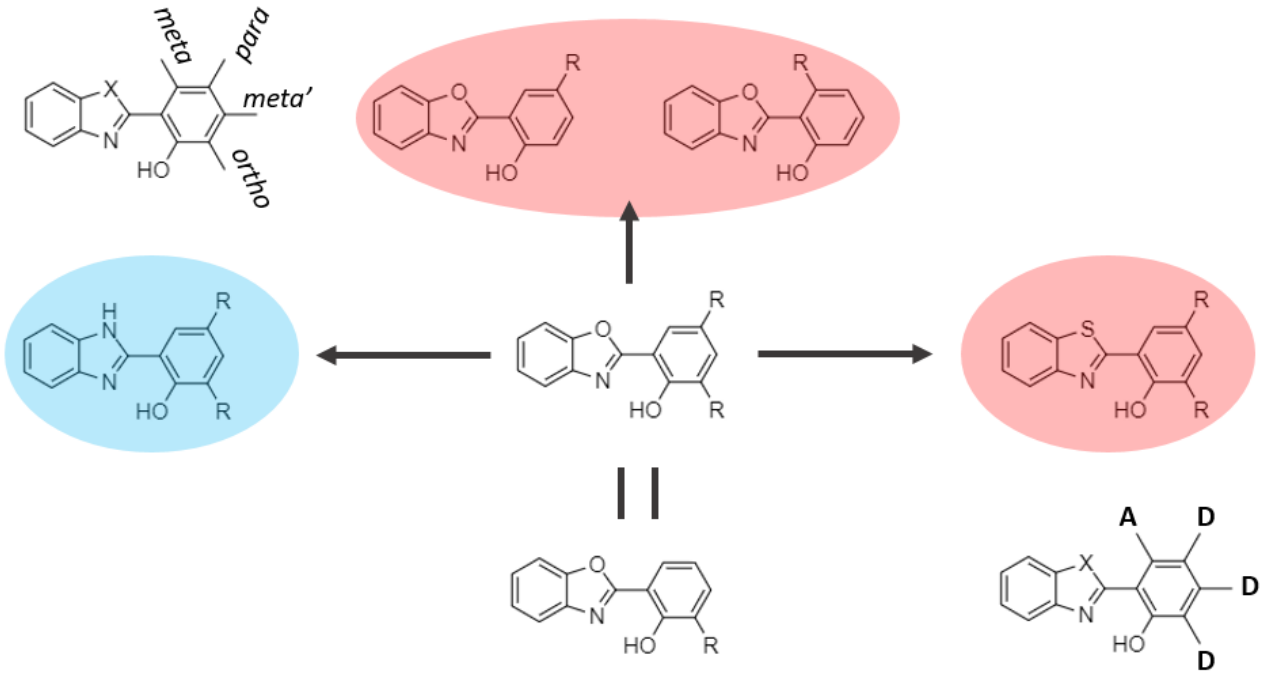

Figure 4: Représentation des différentes conclusions tirées de notre collaboration strasbourgeoise. En rouge et bleu sont représentés les décalages de la fluorescence selon la position des substituants et la nature de l'hétéroatome, comparé à la structure *ortho-para*-HBO. Les positions à caractère donneur (D) et accepteur(A) sont également représentées sur la structure en bas à droite.

para, *ortho*, et simultanément *ortho-para*) n'a mené dans le toluène qu'à une fluorescence certes intense mais de la forme céto uniquement. Cependant, en fonction de la position des substituants, des décalages systématiques des profils d'émission ont été observés, voir Figure 4. Les substitutions *ortho-para* et *ortho* conduisent à des signatures d'émission similaires tandis que les fluorescences résultant de systèmes avec des groupes *para* et *meta* sont similaires entre elles mais décalées vers le bleu par rapport aux précédents motifs. Cette tendance a été observée avec les deux cœurs HBO et HBI. De plus, un décalage notable vers le bleu de la fluorescence peut être noté lorsque l'hétéroatome X est un azote et non un oxygène. Le squelette HBT a été étudié avec des fragments en *ortho-para* uniquement et ce squelette a montré un décalage vers le rouge par rapport à ses équivalents HBO. Avec les tracés EDD, l'effet donneur du substituant placés aux positions *para* et *ortho* a été mis en évidence, une perte de densité de la triple liaison à l'état excité peut être observée. Cet effet est plus fort pour le groupe *para* que pour le groupe *ortho* même dans les systèmes bis-substitués. Le comportement opposé est observé en position *meta*: les liaisons simples bordant la triple liaison du substituant gagne de la densité lors de l'excitation. Ces différents effets peuvent être encore augmentés par des substitutions supplémentaires et exploités davantage pour contrôler la fluorescence, par exemple en ajoutant des groupes de donneurs supplémentaires aux substituants en *para* ou *ortho* ou des auxochromes accepteurs pour la position *meta*.

Pour chacune des séries étudiées, l'approche combinant i) une correction CC2 (méthode) et ii) une correction conjointes des modèles de solvant LR-PCM et cLR-PCM, dénotée CC2/LR+cLR, a donné les résultats les plus proches de l'expérience. C'est certainement satisfaisant du point de vue du théoricien que le modèle le plus " avancé " (théoriquement) utilisé soit également le plus précis (pratiquement). Comme on peut le constater avec la Figure 5, la TD-DFT est clairement l'approche donnant les écarts les plus importants par rapport aux valeurs expérimentales. Notons aussi que notre préférence va à la surestimation systématique des énergies d'émission (avec TD-DFT et CC2) plutôt qu'a une approche plus "erratique" [ADC (2)].

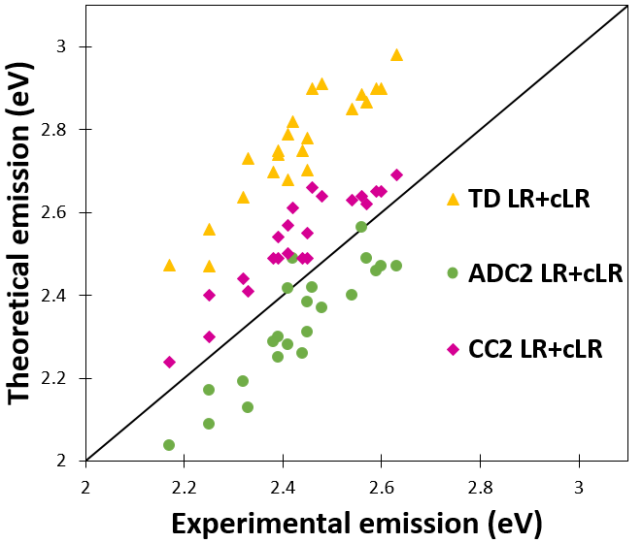

Figure 5: Comparaison d'énergies de fluorescence céto expérimentales et théoriques dans le toluène et benzène (eV) des colorants issues de notre collaboration avec l'équipe du Dr. Gilles Ulrich. Les énergies théoriques ont été calculées avec différentes approches théoriques avec une apporximarion verticale.

Parallèlement à cette collaboration, j'ai effectué la caractérisation des propriétés optiques et du mécanisme ESIPT d'un colorant triplement émissif.[14] Ce colorant est composé de deux sites ESIPT, offrant la possibilité d'obtenir une forme à double transfert de protons. Ce colorant présente en effet une triple émission, clairement attribuée expérimentalement aux trois tautomères possibles: la forme énol initiale (EE*), le tautomère énol-céto formé après le premier transfert de protons (EK*) et la structure céto-céto résultant du double transfert de protons (KK*), voir Figure 6.[15] L'étude de ce système a été l'occasion d'apprécier différentes approches théoriques combinant les méthodes TD-DFT et post-HF [ADC(2) et CC2] mais aussi, et peut-être de manière plus essentielle, un ensemble de modèles de continuum pour les états excités (LR, cLR, LR+cLR et VEM-UD PCM) afin d'obtenir la meilleure précision possible à un coût (de calcul) raisonnable. En effet, un modèle de solvant raffiné était évidemment nécessaire pour comprendre les incohérences entre les résultats des études théoriques précédentes, toutes réalisées au niveau théorique TD-DFT/LR-PCM,[16–20] et les résultats expérimentaux. Dans les systèmes ESIPT, les transitions électroniques sont généralement plus intenses (plus grand ϵ) pour les formes énol que pour les tautomères céto, et leurs moments dipolaires à l'état

excité diffèrent fortement. Par conséquent, l'utilisation de LR-PCM est insuffisante car ce modèle est plus adapté pour décrire les états ayant un caractère local et dipolairement permis. Toutefois, si les modèles de solvants *state-specific*, tels que le cLR, sont plus adéquats pour décrire l'état excité de la forme céto, il sont probablement moins efficaces pour l'isomère énol. Pour le colorant spécifiquement étudié (Figure 6), l'approche VEM-UD s'est avérée efficace pour décrire les formes céto à l'état excité de manière cohérente. Malheureusement, le processus d'auto-cohérence de VEM-UD rend cette approche gourmande en ressources calculatoires. La combinaison des corrections LR et cLR a également permis une description précise et équilibrée des formes E* et K*, en particulier lorsque CC2 est utilisé pour décrire la structure électronique. Avec les protocoles CC2/LR+cLR et CC2/VEM-UD, le système a pu être correctement décrit et les quatre pics d'émission expérimentaux attribués à un tautomère spécifique, les deux premiers pics résultant d'un fort couplage vibronique présent lors de l'émission de EE*, alors que la bande suivante est générée par les tautomères EK* et KK* comme décrit dans la publication expérimentale initiale. L'analyse des énergies relatives des différents ES et de leurs barrières ESIPT associées a en effet conforté cette attribution.

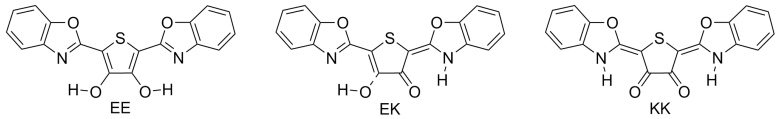

Figure 6: Représentation des différents isomères de **BBTP**. EE est la forme énol-énol, EK la forme énol-céto résultant d'un seul transfert de protons et KK la forme céto-céto résultant d'un double transfert de protons.

Dans une autre partie de ma thèse, j'ai choisi de tester la force du protocole CC2/LR+cLR, mis en place pour caractériser les colorants ESIPT, sur un système particulièrement complexe (Figure 7).[21] Ce composé a l'intérêt de présenter cinq couleurs différentes de luminescence selon l'environnement du composé.[22,23] Le colorant présente également une structure très flexible qui permet d'obtenir deux ESIPT différents grâce à des rotations moléculaires, qui peuvent être déclenchées par l'addition d'acide dans la solutions. Dans les publications expérimentales, une structure et un mécanisme ESIPT ont été proposé pour chaque couleur observée, sur la base des données disponibles (RMN et rayons X). Afin d'attribuer une structure aux fluorescences vertes, rouges et bleues observées, j'ai étudié et simulé: i) la stabilité, ii) la position des pics RMN, iii) les propriétés optiques, iv) les effets de la protonation, et v) les interactions avec les contre-ions des différents isomères et rotamères envisageables. Pour les deux premières espèces (verte et rouge), mes résultats étaient conformes aux conclusions expérimentales, voir Figure 7. Pour la fluorescence bleue, seules des hypothèses avaient été émises dans les articles originaux. Avec mes calculs, une nouvelle analyse plus robuste de cette structure a pu être proposée et j'ai pu montrer que l'emission bleue provenait très probablement d'une forme doublement protonée. Pour ce système, d'un point de vue plus technique, il a été montré que l'inclusion du contre-ion dans le calcul était nécessaire pour obtenir une tendance précise en accord avec les données expérimentales.

De nombreuses idées de nouveaux composés ESIPT pouvant montrer une émission double plus

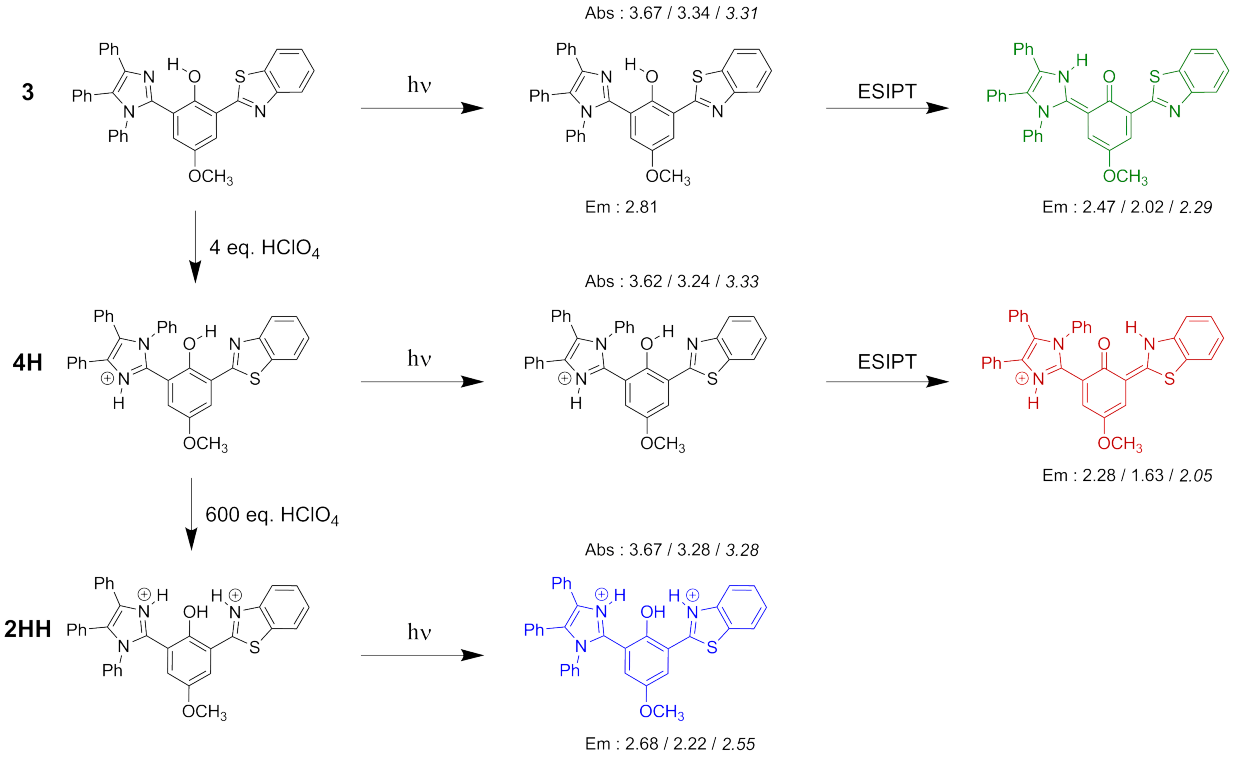

Figure 7: Configuration les plus stables d'après les calculs théoriques, en fonction des conditions acides et représentation des structures émettrices pour le fluorophore représenté en haut à gauche. Les énergies théoriques d'absorption et d'émission TD-DFT et ADC(2) (LR+cLR dans les deux cas) et expérimentales (en italique) sont données en eV. Les valeurs expérimentales sont extraites de la Réf. 23.

intense et/ou une fluorescence plus brillante restent à explorer avec nos collaborateurs. Beaucoup de ces systèmes intéressants restent à synthétiser, caractériser... et modéliser. Sur base de la découverte d'un effet accepteur du substituant placé en position *meta* sur le cœur HBX, une nouvelle série de fluorophores, avec un groupe d'attracteur d'électrons dans cette position, sera prochainement explorée. L'introduction d'un second groupe ESIPT pour obtenir une double émission est également envisagée.

Au cours de cette thèse, j'ai limité mes recherches aux colorants dans des solutions (principalement aprotiques). Cependant, les systèmes ESIPT sont remarquables pour leur luminescence brillante non seulement en solution mais également, et même plus spécifiquement, à l'état solide. La modélisation des propriétés optiques de ces colorants au sein de polymères serait clairement intéressante afin de mieux comprendre leurs comportements pour les applications " réelles" telles que les OLEDs et les portes logiques. Pour cela, des approches différentes doivent être utilisées. Pour étudier le mécanisme d'un colorant ESIPT dans un environnement solide, nous pouvons nous inspirer de travaux récents de plusieurs équipes.[24–26] Une approche permettant de prendre en compte la dynamique serait vraiment intéressante pour atteindre une compréhension plus approfondie des processus à l'état excité.

Une des limitations rencontrées lors de ces travaux a été la modélisation de l'impact de solvants protiques comme l'eau ou, dans le cas présent, l'éthanol, sur les stabilités relatives des formes énol et céto. Les résultats obtenus n'étaient pas vraiment convaincants. Avec le modèle PCM, les interactions

entre le soluté et le solvant sont décrites avec un modèle implicite principalement électrostatique, et les interactions intermoléculaires spécifiques entre le solvant et le colorant ne sont donc pas prises en compte, ce qui peut conduire à des erreurs dans les prédictions. Ici aussi, une approche dynamique, cette fois pour modéliser la dynamique du solvant, et pour décrire explicitement les molécules de solvant et leur impact sur le colorant pourrait être utilisée pour gagner en précision.[27,28]

L'une des approches innovantes de ce travail est l'exporation avec la TD-DFT des états de transition entre l'état excité céto et l'intersection conique pour rationaliser le rendement quantique expérimental de fluorescence. Cependant, si cette approche peut donner une idée globale des tendances dans une série donnée (ce qui n'est pas si mal!), cette approche est insuffisante pour estimer le rendement quantique de fluorescence de manière satisfaisante ou pour comparer différentes séries de composés. Pour résoudre ce problème, l'utilisation de méthodes multi-référence serait utile pour obtenir non seulement l'état de transition mais aussi une idée précise de la topologie de l'intersection conique.

Remerciements

Je souhaiterai tout d'abord remercier mon directeur de thèse, Denis Jacquemin, pour tout ce qu'il m'a apporté ces trois dernières années. Merci pour toutes les connaissances scientifiques que tu m'as permis d'acquérir, cette thèse en est le témoin. Merci de m'avoir montré les possibilités que le monde de la recherche peut offrir. Merci de m'avoir écoutée et conseillée lorsque je t'ai présenté mes interrogations sur la cohabitation entre vie privé et professionnel, de ne jamais m'avoir découragée dans mon projet de grossesse et même rassurée sur la compatibilité avec ma thèse. Merci beaucoup pour toutes tes qualités humaines qui ont rendu cette thèse agréable à vivre (la majeure partie du temps). Dans les moments où ma motivation était en baisse, tu t'es adapté et m'a proposé un suivi plus soutenu et tu m'as laissé une grande autonomie lorsque tout allait bien. J'ai vraiment beaucoup appris durant ces trois années sous ta direction. Merci !

Je voudrais également remercier Thomas Cauchy et Cloé Azarias qui m'ont tout deux beaucoup apporté. Merci à Thomas qui a été le premier à m'offrir la possibilité de découvrir la chimie théorique et les états excités au travers d'un stage. Même si j'ai parfois eu l'impression que tout s'enchainait trop facilement, je suis contente d'avoir suivi tes conseils. Quant à Cloé, elle a certainement joué un rôle important dans la réussite de cette thèse. Tu m'as chaleureusement accueillie dans l'équipe lors de mon stage de M2 réalisé en grande partie sous ta supervision. Après la fin de mon stage et durant ma thèse tu as toujours été là pour répondre à mes différentes questions. Je te remercie également pour les bons moments que nous avons pu passer ensemble en dehors du laboratoire.

Je souhaiterai remercier les docteurs Ilaria Ciofini, Morgane Vacher, Tangui Le Bahers, et Gilles Ulrich d'avoir accepté de faire partie de mon jury et d'évaluer mon travail.

Merci à Benjamin Lasorne et Arnaud Fihey qui ont pris le temps de suivre mes travaux et pour les pistes de réflexion proposées.

Une grande partie de cette thèse est le résultat de collaborations. Merci à Ciro Guido et Simon Budzak pour leur aide et leur temps (pour m'expliquer des concepts qui m'échappaient). Je souhaite

remercier l'équipe de Gilles Ulrich : Antoinette De Nicola, Julien Massue, Thibault Pariat et Maxime Munch pour la qualité et quantité des données expérimentales produites. Cette thèse et cette collaboration ont été financées par *l'Agence National de la Recherche* que je remercie pour leur contribution.

Je tiens à remercier les différentes personnes que j'ai pu côtoyer au sein du laboratoire notamment le directeur Jean-Michel Bouler. Merci à tous les membre de mon équipe pour les moments passés ensemble. Merci pour vos mots d'encouragements.

Je voudrais remercier plus particulièrement les non-permanents (Dani, Ciro, Cloé, Rui, Iyanar, Sergine, Amara, Neha, Manon, ...) pour les brunchs internationaux qui me manqueront et nos échanges quotidiens. Je souhaiterai plus particulièrement remercier mes amies Neha, Amara et Manon. Neha ma compagne de bureau qui par son enthousiasme et sa motivation a apporté une atmosphère positive à nos journées. Amara et son rire communicatif qui a égaillé la pause-café. Enfin Manon avec qui j'ai pu discuter geekerie et partager ma passion de la grenadine. Merci pour vos amitiés.

Un grand merci à ma famille pour leur soutien. Merci à mon père David, ma mère Sophie, ma sœur Juliette et mes frères Elliot et Roméo. Merci à Carole, Isa, Luc, Hélène et mon Papi. Merci aussi à Cécilia, Michèle, Thomas, et Gilbert. Chacun de vous m'a soutenue à sa manière et remotivée lorsque nécessaire. Merci à mes amis qui ont été là pour me soutenir et s'intéresser à mon travail, en particulier Justine (même depuis l'Australie tu étais là), Oriane, Fabien, Corentin, Mathilde, Camille, Nico, Max, Quentin (x3), et Damien (sur qui je peux toujours compter pour les discussions de comptoir).

Enfin je voudrais remercier la personne sans qui je n'aurais probablement pas entrepris cette thèse : Gabriel. Merci pour ton soutien sans faille. D'avoir eu confiance en moi lorsque je perdais pied. Merci d'avoir pris soin de moi particulièrement ces derniers mois lorsque la rédaction de ce manuscrit me paraissait une épreuve insurmontable. Cela n'a pas toujours été facile, mais tu as toujours été là pour m'aider à surmonter ces difficultés. Je suis heureuse de partager ma vie avec toi. Je t'aime.

Avec neuf étoiles, quatre doubles palmes, un cornue-et-ballon sur circulaire de satin violet, mon parcours étudiant s'arrête ici avec la satisfaction d'avoir été jusqu'au bout.

Contents

1 Introduction **1**

1.1 Absorption and Fluorescence 1

1.2 ESIPT process 3

1.3 A few applications of ESIPT dyes 3

1.3.1 OLED 4

1.3.2 Laser dyes 5

1.3.3 Logic gates 5

1.3.4 Fluorescent probes 5

1.3.5 Photostabilisers 6

1.4 Objectives of this thesis 6

2 Overview of the theoretical studies of ESIPT systems **11**

2.1 Dyes with one ESIPT center 12

2.1.1 SA - Salicylid acid derivatives 12

2.1.2 SDA - Salicylideneaniline 14

2.1.3 HBX 16

2.1.4 Rigidified ESIPT system 17

2.1.5 Green and blue fluorescent proteins 23

2.1.6 One ESIPT proton but two accepting sides 24

2.2 Double ESIPT systems 25

2.2.1 $BP(OH)_2$ - Bipyridine-diol 25

2.2.2 BBHQ - Bis-benzoxazolylhydroquinone 26

2.2.3 Double Schiff bases 28

2.2.4 Dihydroxydibenzophenazine 31

2.2.5 Bisflavonols 32

2.2.6 Compounds with two different ESIPT sites 33

2.3 Triple ESIPT systems 34

2.4 ESIPT studies from our team 35

2.5 A short summary . . . 36

3 Quantum chemistry: a short summary 39

3.1 Some common notions of quantum chemistry . . . 39
3.1.1 The Schrödinger equation . . . 39
3.1.2 The Born-Oppenheimer approximation . . . 40
3.1.3 Description of the wavefunction . . . 41
3.2 Ground state theories . . . 43
3.2.1 Hartree Fock . . . 43
3.2.2 Post-Hartree-Fock methods . . . 45
3.2.3 Density functional theory - DFT . . . 46
3.3 Excited state theories . . . 49
3.3.1 Second-Order Algebraic-Diagrammatic Construction - ADC(2) . . . 49
3.3.2 Second-Order Coupled Cluster - CC2 . . . 49
3.3.3 Time-Dependent DFT . . . 50
3.4 The environmental effects . . . 51
3.5 "Hybrid" approaches . . . 52
3.6 ESIPT characterisation . . . 54

4 Strasbourg's ESIPT dyes 57

4.1 Introduction . . . 57
4.2 Computational details . . . 58
4.3 Impact of the heteroatom on HBX cores . . . 59
4.4 HBX with an ethynyl aniline substituent . . . 63
4.4.1 Three different profiles in benzene . . . 64
4.4.2 A challenging interpretation of the fluorescence in DCM . . . 68
4.5 The HBO series . . . 72
4.6 HBX with mono- or bis-(tri-*iso* -propylsilyl)acetylene in toluene . . . 77
4.7 Substitution of a HBO scaffold by an ethynyl-tolyl moiety . . . 81
4.7.1 A full keto emission in toluene . . . 81
4.7.2 Keto and dual emissions with a touch of deprotonation in ethanol . . . 86
4.8 A personal conclusion: is one approach "better" than the others? . . . 90

5 A triply emissive dyes, BBTP 95

5.1 Introduction . . . 95
5.2 Computational details . . . 97
5.3 Exploration of the **BBTP** structure . . . 98
5.3.1 Geometries in gas phase . . . 98
5.3.2 Geometries in chloroform . . . 99

5.3.3 Relative stabilities . . . 100
5.3.4 Absorption . . . 103
5.3.5 Emission . . . 105
5.4 Design of potential quadruply fluorescent **BBTP** . . . 107
5.5 Conclusions . . . 111

6 Tuneable fluorescence of a full-colour dye, BTImP **113**
6.1 A full-colour dye . . . 113
6.2 Computational details . . . 115
6.3 The electronic ground state . . . 115
6.4 Optical properties . . . 123
6.4.1 Absorption of **BTImP** and protonated systems . . . 124
6.4.2 Green fluorescent **BTImP** structure: **3** . . . 125
6.4.3 Red fluorescent structure: **4H** . . . 126
6.4.4 Blue fluorescent structure: **2HH** . . . 128
6.5 Conclusions and Outlook . . . 128

7 General conclusions and perspectives **131**
7.1 Conclusions . . . 131
7.2 Perspectives . . . 135

Bibliography **139**
Appendix to Chapter 5 . . . A-1
Appendix to Chapter 6 . . . A-7

Chapter 1

Introduction

Contents

1.1 Absorption and Fluorescence 1

1.2 ESIPT process 3

1.3 A few applications of ESIPT dyes 3

1.3.1 OLED 4

1.3.2 Laser dyes 5

1.3.3 Logic gates 5

1.3.4 Fluorescent probes 5

1.3.5 Photostabilisers 6

1.4 Objectives of this thesis 6

The interactions between light and matter are everywhere around us. Colors are one of the most fascinating results of these interactions. Light can interact with the physical nature of matter. In this case, the physical colours are obtained by refraction (rainbow), diffusion (blue sky), interference (iridescence of soap bubbles), or diffraction (butterfly wings of *Morpho Menelaus*). But light can also interact more deeply with matter through its chemical nature. Indeed the photons can be absorbed by atoms and molecules. This phenomenon is responsible of the colour of dyes and pigments. Absorption can also be followed by luminescence, that is 'photon production'. Emissive compounds are used for applications such as OLED television or safety pictograms.[29] In this manuscript, we are strongly interested in luminescent systems and more specifically fluorescent dyes.

1.1 Absorption and Fluorescence

The photon absorption is a phenomenon explained only at the beginning of the 20th century with the apparition of quantum mechanics and the description of the quantified nature of electronic, vibrational, and rotational energy levels of molecules. Under irradiation, if the photon energy corresponds to the energetic difference between the ground state (GS), typically a singlet state, S_0, and an excited state (ES)

of the same spin symmetry, S_n (n≥1), this photon can be absorbed by the molecule. The probability of this phenomenon will depend on the dipolar coupling between these states. The energy received by the compound will promote an electronic excitation from S_0 to S_n. This electronic transition is almost instantaneous (10^{-15}s). As the molecular vibrations take place on a slower timescale (10^{-10}–10^{-12}s), absorption's time is too short to allow significant displacement of the nuclei. Therefore absorption can be described as a vertical process following the well-known Franck-Condon principle.[30,31]

The different subsequent pathways are summarised in Perrin-Jablonski diagram, see Figure 1.1. The system can return to the GS through radiative and non-radiative processes.[32,33] For most organic compounds the emission occurs from the S_1 to S_0 due to the empirical Kasha's law. If the system is excited in S_n (n>1), it will often reach the S_1 by vibrational relaxation (10^{-12}–10^{-10}s), VR, and/or internal conversion (10^{-11}–10^{-9}s), IC. The energy decrease coming with these processes is accompanied by a heat transfer to the environment. Once the system is at the S_1, non-radiative VR and IC can continue allowing to reach the S_0 or fluorescence can bring back the system to the GS. Fluorescence is a radiative process (10^{-10}–10^{-7}s) and corresponds to the transition between two states of same spin multiplicity (in this case singlet).[34]

If triplet T_n (n≥1) and singlet S_1 ES are close enough in energy, a non-radiative intersystem crossing (10^{-10}–10^{-8}s), ISC, can occur between these both states to populate a lower triplet state. From T_1, reverse ISC and VR can occur to go back to S_0 or phosphorescence can take place. Phosphorescence is a radiative process slower than fluorescence (10^{-6}–10^{0}s) and corresponds to the transition between two states of different spin multiplicities. As ISC is a spin-forbidden process, it typically occurs with low efficiency in organic compounds not containing heavy atoms and hence (almost) free of relativistic effects.

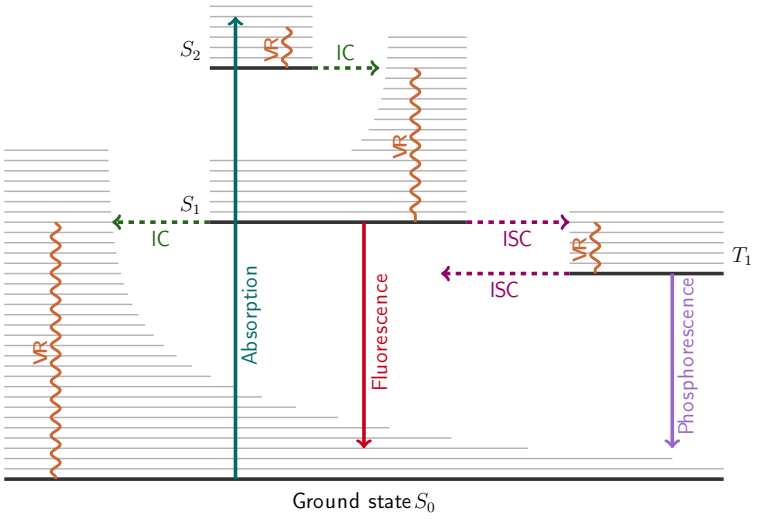

Figure 1.1: Simplified Perrin-Jablonski diagram.[35] Photon absorption and radiative processes are represented with full arrows whereas non-radiative processes are represented with dot and wavy arrows. IC: internal conversion, ISC: intersystem crossing, VR: vibrational relaxation.

1.2 ESIPT process

During my thesis, I have focused my research on a specific class of fluorescent dyes: the ESIPT systems, ESIPT meaning excited-state intramolecular proton transfer.[1–6] It is a process which mostly appears in molecules containing a five- or a six-member ring encompassing an intramolecular hydrogen bond. In this manuscript, all molecules include a 6-membered ring with a N$\cdots$HO interaction. Under photoexcitation, the hydrogen atom can be transferred between the two sites to yield a tautomer, generally called keto structure (K*), in contrast to the original enol (E) form that is typically predominant in the GS. The purpose of this process is to stabilise the excited-state. As illustrated in Figure 1.2, a further energy decrease can occur through the twisting of the interring (double) bond of the K* form, which leads to a conical intersection (CI) with the ground state. When this twisting process is limited, the K* form is a stable tautomer that can effectively emit light at long wavelength with a large Stokes' shift compared to the enol (E) absorption. The significant rearrangements of the electron density and hence of the geometry between the absorbing and emitting isomers (enol and keto, respectively) are responsible for the enhanced Stokes' shift, characteristic of ESIPT dyes.

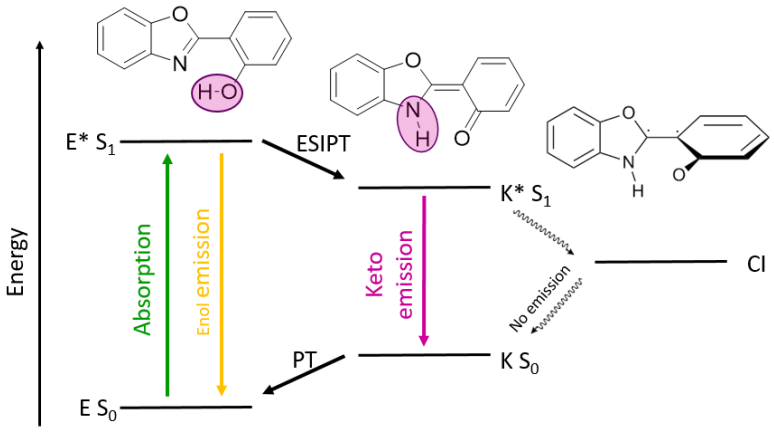

Figure 1.2: Typical ESIPT process: absorption of the stable enol form at the ground state is followed by ESIPT to obtain the keto excited state which can emit light. A twist of the K* can also occur leading to a conical intersection (CI) and a non-radiative relaxation to the ground state.

1.3 A few applications of ESIPT dyes

Since their discovery in the 50s,[1] ESIPT dyes have found useful applications in OLEDs,[36–40] laser dyes,[41–44] logic gates,[45,46]photostabilisers,[47] and fluorescent probes.[48–54] The interest in these dyes is mainly driven by their large Stokes' shift and emissions in the red region. In addition, the fluorescence spectra of ESIPT dyes are generally very sensitive to the environment, i.e., to the solvent polarity, the pH, and the presence of specific ions.[55–57] Indeed, those parameters allow to modulate the relative stabilities of the tautomers which subsequently tunes the emission. Below I give a few illustrative

examples of applications of ESIPT dyes.

1.3.1 OLED

For organic light-emitting diode (OLED) applications, an important property is the Stokes' shift: the energetic gap between the absorption and fluorescence as to be strong enough to avoid self-absorption. During the proton transfer, the system looses energy, therefore the K* emission is red-shifted compared to E* and the Stokes' shift increased. One of the current challenges in the field is to generate white light, which can be achieved using several strategies: i) by generating an anion in the excited state, leading to an additional emission band,[40,58] ii) by including several ESIPT centres in a single compound,[5,36,59] or iii) by obtaining a suitable ratio between E* and K* emissions.[60]

Using the second strategy, Park and co-workers have designed and reported a *'single-molecule-based white-light-emitting OLED'*,[36] see Figure 1.3a and 1.3b. The molecule is constituted of two noninteracting ESIPT chromophores which both emit fluorescence resulting form the K* tautomers. As the emitted lights are blue and yellow, their combination by the human eyes restores a white lighting.

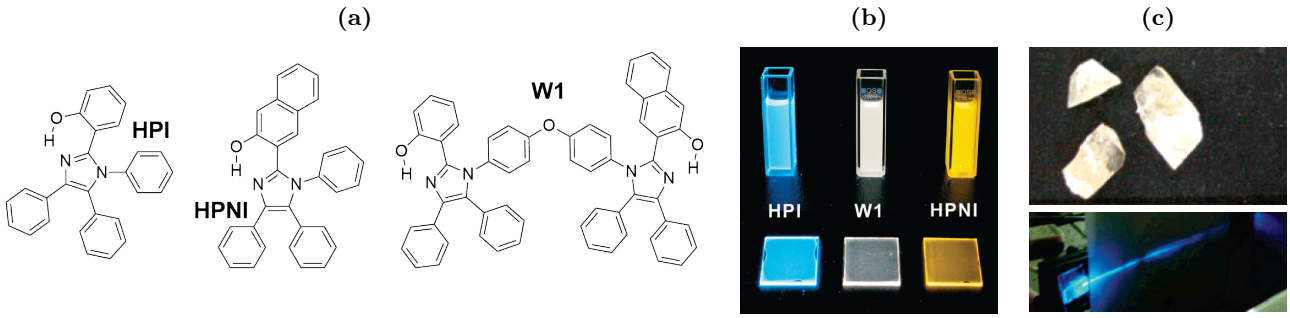

Figure 1.3: (a) Structure of white light emitter **W1** and its two distinct ESIPT compounds. (b) Photo- and electroluminescence from the white-light-emitting molecular dyads. (c) Single crystal of **HPI** (top) and photograph of a straight path of blue amplified spontaneous emission of **HPI** (bot). Photographs reprinted (adapted) with permission from Ref. 42 and 36 Copyright (2005) (2009) American Chemical Society.

In some cases, the E* and K* forms are almost isoenergetic which yields dual-emission as illustrated in Figure 1.2 with emissions from both E* and K* (third strategy described above).[12] More concretely, in Figure 1.4, the emission bands of the E* and K* around 480 and 580 nm, respectively, of an ESIPT dyes are clearly seeable. In this example by the Ulrich group, the ratio of these emission can be controlled by chemical tuning and leaded to white light emission.[38]

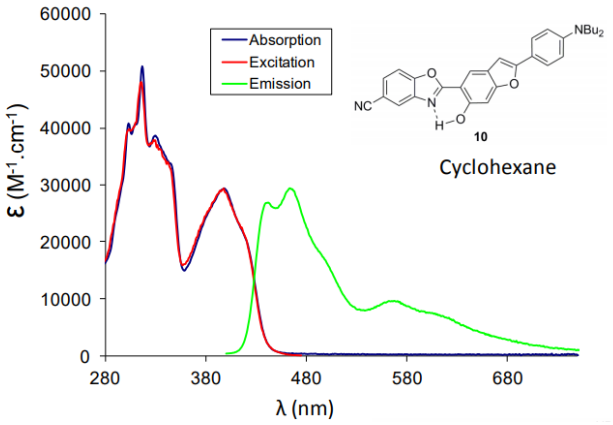

Figure 1.4: Absorption and emission spectra of an ESIPT dual emitter. Reproduced with permission from Ref 38 Copyright (2014) WILEY.VCH Verlag GmbH Co. KGaA, Weinheim.

1.3.2 Laser dyes

Similar properties as the one required for OLED are expected for laser dyes applications: strong Stokes' shift and hight quantum yield of fluorescence. With **HPI** derivatives, see Figure 1.3, Park and co-worker had also proposed laser dyes applications.[42] The emission of this compound results from the K* form. Single crystal of **HPI** with intense blue fluorescence and amplified spontaneous emission (ASE) can be obtain, see Figure 1.3c. At the solid state, non-radiative deactivation by intermolecular vibronic interactions or through accessible conical interaction are much reduced and therefore the fluorescence efficiency is enhanced, which is also an asset of ESIPT compounds in a large dye context.

1.3.3 Logic gates

Molecular logic gates respond to chemical and photonic inputs by generating output signals. With the possibility of emitting fluorescence from the enol or keto ES depending of the environment, ESIPT systems are interesting candidates for logic gates applications. Luxami and Kumar have reported a double ESIPT system reacting to acid/base stimuli but also to complexation with Cu^{2+} ions.[45,46] Depending on the environment, E* or K* fluorescence appears and this can be used to build logic operators.

1.3.4 Fluorescent probes

For fluorescence probes, the systems have to present a large Stokes' shift and long wavelength emission to avoid self-absorption. Indeed long wavelength emissions will be preferred for biological applications, long wavelength photons having deeper tissue penetration. An ESIPT system with a keto fluorescence presents all these characteristics. The strength of ESIPT derivative for fluorescence also comes from the possibility to modulate the stability of the E* and K* and therefore control the emission wavelength. In one valuable example, Liu and co-workers inhibited the ESIPT emission with an aromatic boronic

ester, see Figure 1.5.[61] This substituent is also the sensing unit to detect hydrogen peroxide (H_2O_2). In presence of H_2O_2, the aromatic boronic ester is released, and the remaining ESIPT system, not inhibited anymore, will emit an easily detectable hallmark K* fluorescence.

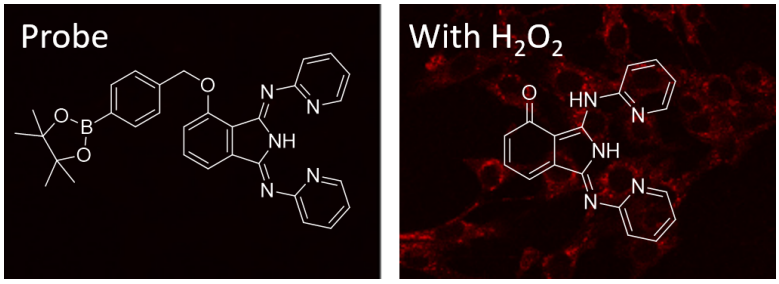

Figure 1.5: Probe fluorecence in presence (right) or absence (left) of H_2O_2 in living 4T1 cells. Adapted from Ref. 61, Copyright (2017), with permission from Elsevier.

1.3.5 Photostabilisers

If some ESIPT systems exhibit strong fluorescence, this latter can also be quenched by non-radiative decay. Indeed the excited state can be effectively deactivated by an accessible conical intersection between the GS and ES. This phenomenon makes ESIPT systems good candidates to develop photostabilisers, and is the key to the strong stability of the indigo dye.[62] At the GS, the dye is formally under a double keto form, see Figure 1.6. Under irradiation the proton transfer (PT) will occur and form the E* tautomer. With advanced theoretical calculations, Yamazaki and co-workers have shown that the associated PT is barrierless. In the enol configuration, the nature of central bond becomes single and not double as in the GS geometry. Therefore the enol tautomer wins in flexibility and can easily twist to reach the conical intersection which will bring back the dye at the GS non-radiatively.

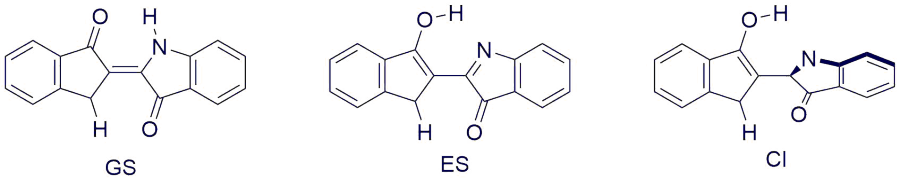

Figure 1.6: Illustration of ESIPT structures in indigo dye.

1.4 Objectives of this thesis

An important part of my thesis work has been performed in close collaboration with the team of Dr. Gilles Ulrich in Strasbourg. Indeed, my PhD funding is provided by the ANR (*Agence national de la recherche*) with the GeDEMi project, that is led by Dr. Gilles Ulrich and Pr. Denis Jacquemin. This project seeks to rationalise and optimise molecules presenting a dual emission using the ESIPT

mechanism. Let me sumarise the context of the project.

The selected backbones, detailed below, were anticipated to present large emission quantum yields both in solution and solid states.[11–13] Through a joint design by both teams, based on chemical feasibility and (my) results of accurate quantum modelling, fluorophores with enol and keto excited states presenting almost the same energy were supposed to be obtained. One should remember that the dual emission and more precisely the intensity ratio of the two emission bands can be perturbed by external stimuli, opening the way to new ratiometric fluorescent probes: the electronic interactions between an analyte and the molecular core could bring variations of the (relative) peak intensities.[3,63] Such probes are of great interest for the determination of pollutants in water or *in cellulo*, to help understand biological phenomena or to detect specific pathologies (by tracking and quantification of ions or metabolites).[52–54] In addition, the efficient luminescence of the selected group of compounds in the solid state makes them good candidates for incorporation in luminescent devices or as safety inks with unique optical signature.

The fundamental challenges of GeDEMi project were, on the one hand, the rational design of sophisticated luminophores with the help of *ab initio* calculations, and, on the other hand, the rapid synthetic implementation to ascertain the optical properties. The first theoretical goal has been attributed to Pr. Denis Jacquemin at the University of Nantes and led to my recruitment as PhD student. The second objective of synthesis and optical characterisation is carried out by Dr Gilles Ulrich, Dr. Julien Massue, and Dr. Antoinette De Nicola at the University of Strasbourg. It was also accompanied a PhD grant which was attributed to Thibault Pariat. As usual, the GeDEMi project has not totally followed the initial plan. Strongly emissive ESIPT dyes were obtained but most of them finally shown a single emission from the keto form. Nevertheless, some dual emitters have been explored but their optimisation to obtain ratiometric probes is unfinished at this stage. In Chapter 4, I present a part of the work (see Figure 1.7) that I have realised in the scope of this collaboration with the team of Dr Gilles Ulrich which has resulted in four publications, articles I-IV in the following list of my publications.

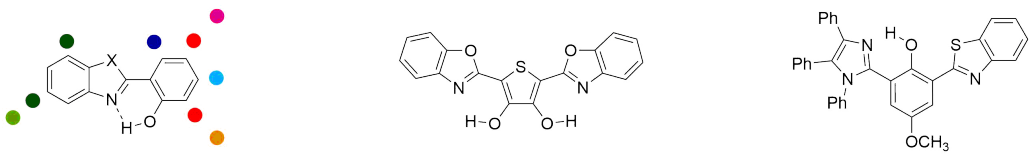

Figure 1.7: Representation of structures of the systems studied in the three chapters describing main results. In Chapter 4, different heteroatoms have been tested (X = O, S, NH) as well as positions for substituents (color dots).

In parallel to this work, I have performed the characterisation of optical properties and ESIPT

mechanism of a symmetric molecule composed of two ESIPT sites showing a triple experimental emission.[15] This study was the opportunity to test different levels of theory (TD-DFT and post Hartree-Fock approaches). The influence of the solvent was also investigated with three different schemes leading to the first application of a new solvent model. This work is described on Chapter 5 which is largely inspired of the publication V in the following list of my publications.

In another part of my thesis, I have chosen to test the strength of the protocol that was developed to characterise ESIPT dyes, on a complex system (rhs. of Figure 1.7). This compound is composed of benzothiazole and imidazole moieties. Depending of nature of the environment, Sakai and Tsuchiya (the designers of this system) have reported five different fluorescent colours.[22,23] I explored different isomers, protonation, and complexation with counter-ions to finally attribute a structure to each of the observed emission. This work has been published as well (article VI in the following list of my publications) and is presented in Chapter 6.

During this thesis, I also participated to the collaboration of my supervisor with Prof. Elisabeth New (Sydney University). For this 'side project', we performed calculations on naphthalimide based compounds to characterise absorption and emission spectra. Two series of 8 and 18 compounds each have been investigated. One of our goal were to explain the difference of quenching by tetrazine substituent depending of it position. The fluorescence quenching by tetrazine has been qualitatively rationalised by electronic energy transfer calculations. The results of this collaboration have not yet been published and are not discussed in the present manuscript which is focussed on ESIPT systems.

The manuscript is articulated as follows. I firstly review in Chapter 2, the diversity of the ESIPT systems and of the associated calculations, performed to characterise them, from 1980 to 2020. Secondly, the quantum methods that I used, are presented in Chapter 3. Thirdly, the results of my thesis are reported in the Chapters 4, 5 and 6. Finally general conclusions and outlook are given in Chapter 7. At the end of this manuscript, additional data to the results Chapters are reported in Appendix.

Bonne Lecture !

List of publications

Chapter 4, resulting directly from our collaboration with the team of Dr. Gilles Ulrich, contains unpublished results, but also data of two projects which have led to the publications I–IV. Chapters 5 and 6 have been strongly inspired by publications V and VI corresponding to each of these chapters. At the beginning of my thesis, I have also complete the work that I have performed during my final graduation internship already under the supervision of Prof. Denis Jacquemin, which led to the redaction of the corresponding publication (VII),

I. J. Massue, A. Felouat, P. M. Vérité, D. Jacquemin, K. Cyprych, M. Durko, L. Sznitko, J. Mysliwiec and G. Ulrich, *An Extended Excited-State Intramolecular Proton Transfer (ESIPT) Emitter for Random Lasing Applications*, Phys. Chem. Chem. Phys., **2018**, *20*, 19958–19963.

II. M. Munch, M. Curtil, P. M. Vérité, D. Jacquemin, J. Massue and G. Ulrich, *Ethynyl-Tolyl Extended 2-(2'-Hydroxyphenyl)benzoxazole Dyes: Solution and Solid-state Excited-State Intramolecular Proton Transfer (ESIPT) Emitters*, Eur. J. Org. Chem., **2019**, *2019*, 1134–1144.

III. J. Massue, A. Felouat, M. Curtil, P. M. Vérité, D. Jacquemin and G. Ulrich, *Solution and solid-state Excited-State Intramolecular Proton Transfer (ESIPT) emitters incorporating Bis-triethyl-or triphenylsilylethynyl units*, Dyes Pigm., **2019**, *160*, 915–922.

IV. J. Massue, T. Pariat, P. M. Vérité, D. Jacquemin, M. Durko, T. Chtouki, L. Sznitko, J. Mysliwiec and G. Ulrich, *Natural Born Laser Dyes: Excited-State Intramolecular Proton Transfer (ESIPT) Emitters and their use in Random Lasing Studies*, Nanomaterials, **2019**, *9*, 1093.

V. P. M. Vérité, C. A. Guido and D. Jacquemin, *First-Principles Investigation of the Double ESIPT Process in a Thiophene-Based Dye*, Phys. Chem. Chem. Phys., **2019**, *21*, 2307–2317.

VI. P. M. Vérité, S. Hédé and D. Jacquemin, *A Theoretical Elucidation of the Mechanism of Tuneable Fluorescence in a Full-Colour Emissive ESIPT Dye*, Phys. Chem. Chem. Phys., **2019**, *21*, 17400–17409.

VII. P. M. Vérité, C. Azarias, and D. Jacquemin, *Theoretical Spectroscopy of a NIR-Absorbing Benziphthalocyanine Dye*, Theor. Chem. Acc., (**2018**), *137*, 61.

Chapter 2

Overview of the theoretical studies of ESIPT systems

Contents

2.1 Dyes with one ESIPT center 12
2.1.1 SA - Salicylid acid derivatives 12
2.1.2 SDA - Salicylideneaniline 14
2.1.3 HBX 16
2.1.4 Rigidified ESIPT system 17
2.1.5 Green and blue fluorescent proteins 23
2.1.6 One ESIPT proton but two accepting sides 24
2.2 Double ESIPT systems 25
2.2.1 $BP(OH)_2$ - Bipyridine-diol 25
2.2.2 BBHQ - Bis-benzoxazolylhydroquinone 26
2.2.3 Double Schiff bases 28
2.2.4 Dihydroxydibenzophenazine 31
2.2.5 Bisflavonols 32
2.2.6 Compounds with two different ESIPT sites 33
2.3 Triple ESIPT systems 34
2.4 ESIPT studies from our team 35
2.5 A short summary 36

ESIPT dyes can be incorporated in a large panel of applications as stated in the previous Chapter. Therefore, ESIPT systems continue to attract the interest of a large community that designs and synthesises news dyes with optimal properties. To have an efficient design strategy as well as to obtain

an in-depth understanding of the observations, it is important to rationalise the properties. This has led to a huge number of theoretical investigations of the ESIPT phenomenon with a large diverse panel of modeling approaches. Theoretical calculations have started to be used as early as the 80s' to provide additional informations on ESIPT dyes. Until the 21st century, the majority of these calculations have been performed with semi-empirical methods such as PPP, CNDO, INDO, ZINDO, MNDO, AM1, and PM3.[64–86]. At the beginning of this century the DFT and TD-DFT methods started to become very popular. Therefore during the last 20 years, a large number of ESIPT works included calculations performed with TD-DFT and, as one could have expected, the famous B3LYP functional was generally used.[87–98] Other studies, using the refined CASSCF or CASPT2 methods, can also been found.[47,97–126]

2.1 Dyes with one ESIPT center

2.1.1 SA - Salicylid acid derivatives

The first experimental publication referencing an ESIPT process dates back from 1956.[1] The studied dye was a salicylic acid (SA), see Figure 2.1. Since this day, numerous studied have been performed on this compound and closely related derivatives with diverse methods.[102,108,119,125,127–133] Notably, TD-DFT has been employed to determine the nature of the absorbing and emitting forms by optimising the enol and keto tautomers at the GS and ES but also by performing potential energy surface (PES) scan of different SA dyes, see Figure 2.1.[128,130–132] The vibrational frequencies are a point of specific interest for this small compound, as one can highlight the role of the stretching of the OH bond in the proton transfer.

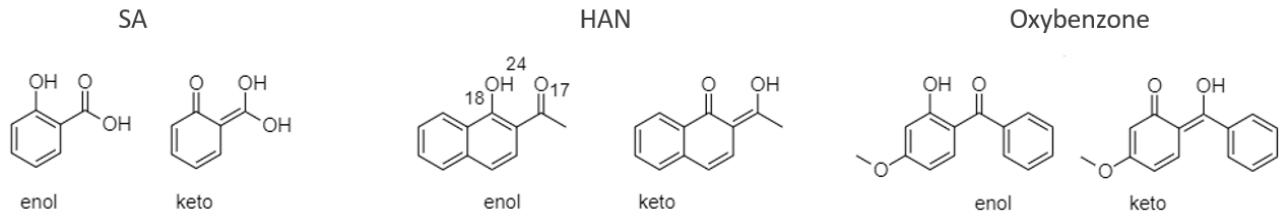

Figure 2.1: Representation of structures deriving from salicylic acid (SA): 1-hydroxy-2-acetonaphthone (HAN) and Oxybenzone.

Using TD-B3LYP and TD-M06-2X approaches with the TZVP basis set, the mechanism of ESIPT in 1-hydroxy-2-acetonaphthone (HAN) has been recently studied with adiabatic molecular dynamics simulations (500 trajectories of 200 fs with 0.5 fs time step).[133] The enol has been defined as the most stable form at the GS and the keto at the ES, see Figure 2.2a. With the dynamic simulation, the authors could observe the ESIPT reaction as traduced by the increase/decrease of the covalent/intramolecular H bonds of the enol tautomer, see Figure 2.2b, and determine an ESIPT speed of 37 fs, highlighting the speed of the process.

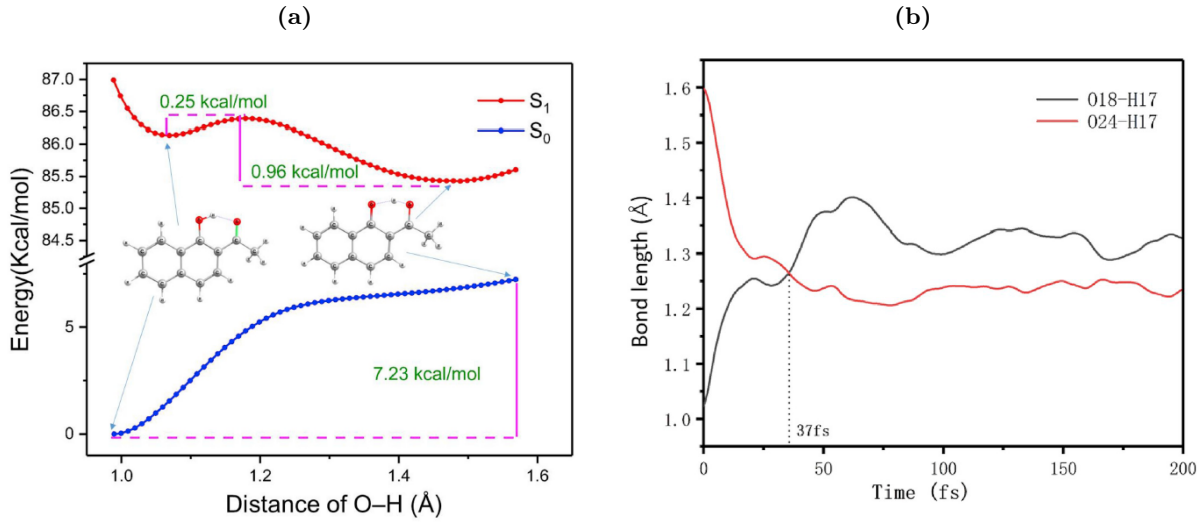

Figure 2.2: (a) PES of the S_0 and S_1 of HAN. (b) Time evolution of the O18–H17 and O24–H18 distances averaged over all the dynamic trajectories. See Figure 2.1 for atoms' label. Reprinted from Ref. 133, Copyright (2020), with permission from Elsevier.

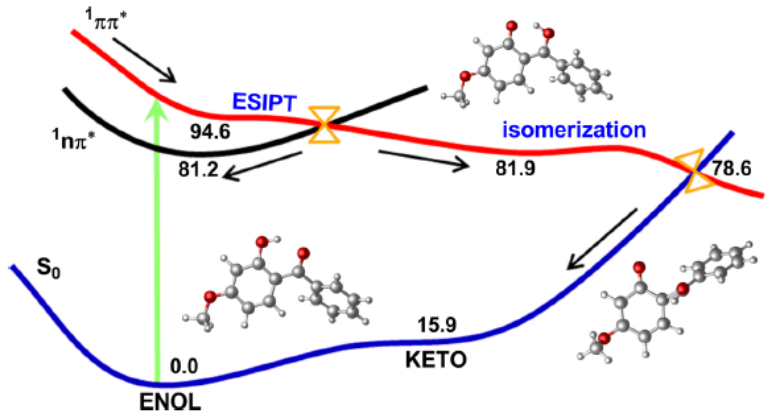

Figure 2.3: Photochemical mechanism (relative energy in kcal/mol) suggested based on static electronic structure calculations and nonadiabatic dynamics. Reprinted with permission from Ref. 119 Copyright (2016) AIP Publishing.

Using both CASSCF and CASPT2 static calculations and associated dynamic studies, Cui and co-workers identified two ultrafast excited-state deactivation pathways for the oxybenzone system, see Figure 2.3.[119] The S_0, S_1, and S_2 structures of the enol isomer as well as the S_0 of the keto tautomer were optimised together with the conical intersections and the minimum-energy reaction paths related to the ESIPT process. The first deactivation pathway is an internal conversion between the S_2 and S_1 of the enol form. The second one occurs after the ESIPT process occurred: a conical intersection between the GS and ES leads back to the initial enol form without emission. This system is used in application as sunscreens ans this theoretical study help to bring more light on it photoprotection

mechanism: as can be seen there are indeed efficient deactivation pathways from the lowest excited states to the ground state, ensuring photostability of the dye. In contrast, as no emission from the keto tautomer, such dye could not be used as a fluorescence probe.

2.1.2 SDA - Salicylideneaniline

Salicylideneaniline (SDA, Figure 2.4), is an ESIPT system with a weak fluorescence and a complex luminescent mechanism.[134]. This system belonging to the group of Schiff bases has been firstly studied with semi-empirical approaches (PPP, CNDO, INDO, MNDO, AM1, and PM3) to determine the presence (or absence) of the ESIPT process[65,66,77,80,135] as well as to investigate its mechanism.[81,136–142] DFT and TD-DFT studies have also been performed in order to characterise the ESIPT mechanism with an improved accuracy.[143–158] More recently studies relying on the post-HF FOMO-CASCI[159] or investigating explicitly the dynamics of the process[160] have been published. An important parts of theses modelling efforts have been made on SDA derivatives aiming not only to characterise their photophysical mechanisms but also to increase the quantum yield of fluorescence.[39,77,115,140–142,148,149,151–153,155,157,160–168] The challenge to characterise the fluorescent mechanism(s) of SDA comes from its intrinsic flexibility which allowed different *cis-trans* conformations, see Figure 2.4.

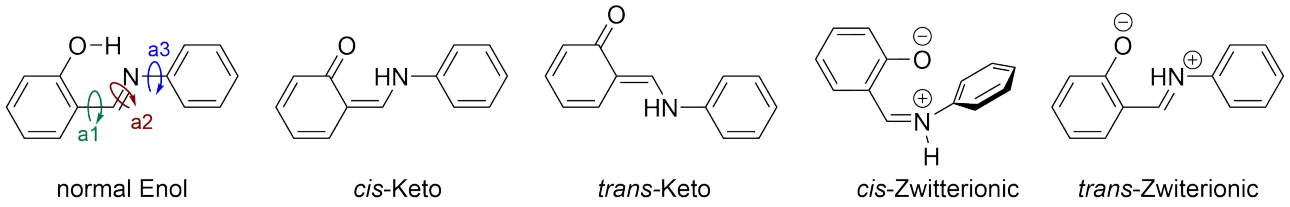

Figure 2.4: Possible isomers of Salicylideneaniline (SDA).

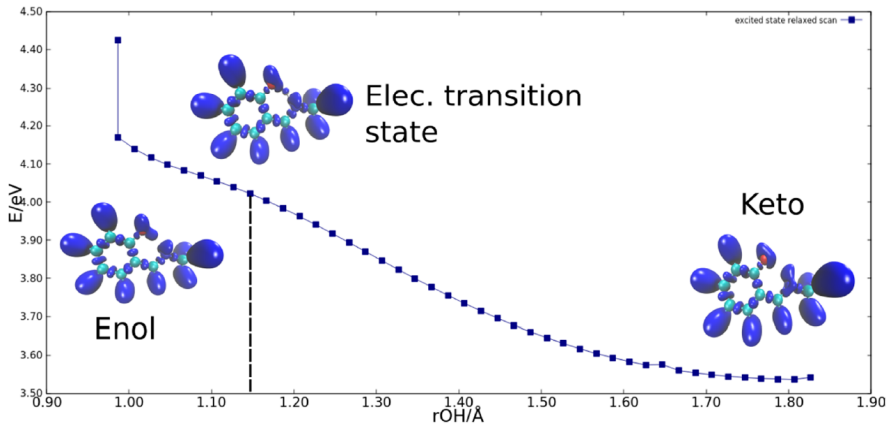

Figure 2.5: Potential energy surface along the internal reaction coordinate of the proton transfer in the first singlet excited state of salicylidene methylamine and ELF(0.8) isosurfaces. Reprinted with permission from Ref. 158 Copyright (2019) American Chemical Society.

Kletskii and co-workers have been the first to propose a twisted intramolecular charge transfer quenching of the fluorescence thanks to investigation of the PES of SDA.[81] The optimisation of the compounds' geometries were performed with PM3 method in this 1997 work. Based on AM1 and ZINDO calculations, Mitra and Tamai proposed a *cis*-Keto nature of the fluorescence. They also underlined the similar stability with the *cis*-Keto and *trans*-zwitterionic isomer which have a different charge distribution but similar geometric structures.[136,169] The *cis*-Keto will then twist to form the *cis*-zwitterionic form. Louant *et al.* have later investigated the *cis*-Keto ES with CC2, and found that this isomer was so close in energy from the *trans*-Keto GS, that the CC2 optimisation directly leads to a CI-like point.[156]

Maulèn and co-workers have explored the evolution of chemical bonds during the ESIPT in salicylidene methylamine with (TD-)DFT, and more precisely ωB97X-D/6-311+G(d,p), see Figure 2.5.[158] Their topological analysis relies on the electron localization function (ELF) approach. They observed an excess of electrons in the lone-pair of the nitrogen atom at the ES in the starting tautomer. This excess is attracting the proton and therefore, leads to the break of the O–H bond. This attraction between the proton and the lone pair of the nitrogen atom is described as the primary driving force of the barrierless ESIPT by Maulèn and corworkers. Previously, Guitiérrez-Arzaluz *et al.* had also explored the driving force of the ESIPT in SDA by investigating the aromaticity at the (TD-)τHCTH-hyb/6-311G++(d,p) level coupled to a quantum theory of atom in molecule (QAIM) analysis, and they reached similar conclusions as Maulèn and coworkers.[154]

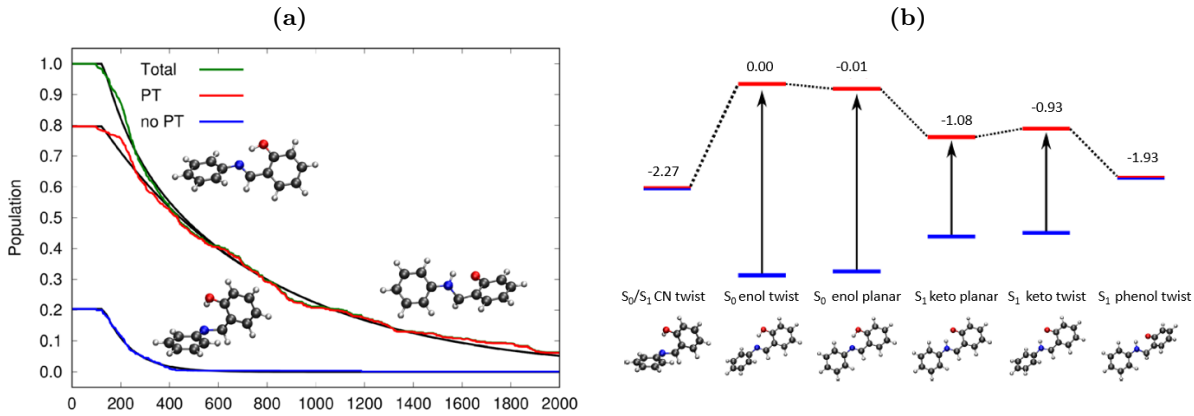

Figure 2.6: (a) Population of the S_1 electronic state for the first 2 ps following excitation (green). Trajectories exhibiting proton transfer are reported in red whereas those without PT are in blue. (b) Relative energies (eV) on the S_0 state are given relative to the Franck-Condon point (the S_0 enol twist geometry). Energies are computed with FOMO-CAS(2/2)-CI/6-31G** including a DFT correction from ωPBEh. Adapted with permission from Ref. 159. Copyright (2018) American Chemical Society.

Pijeau and co-workers performed a detailed study of SDA with non adiabatic simulation using a FOMO-CASCI Hamiltonian and applying a DFT-embedding correction to incorporate a part of of the dynamic electron correlation neglected by FOMO-CASCI approach.[159] AIMS simulations of the ES

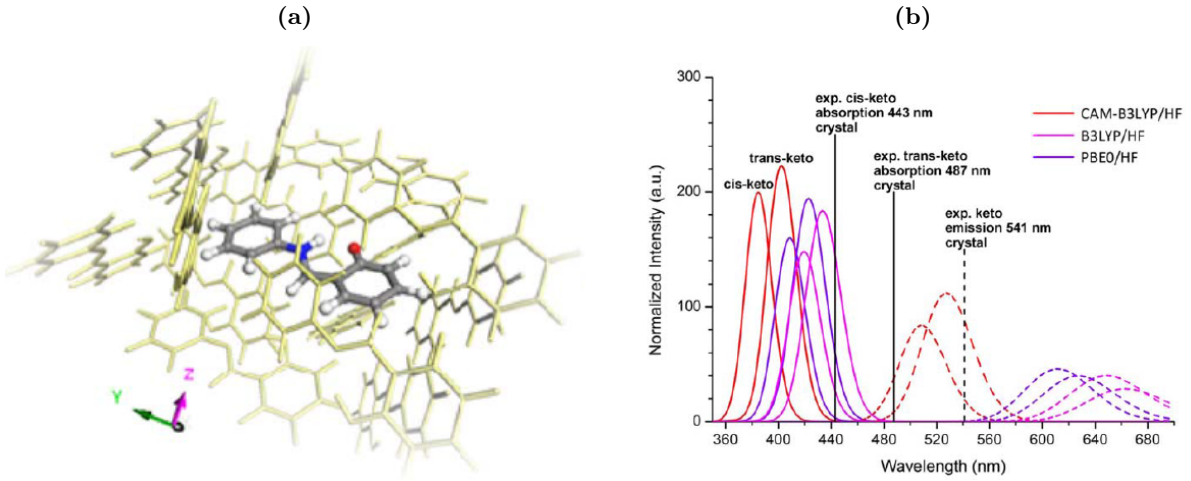

Figure 2.7: (a) Perspective view of the optimized S_1 CAM-B3LYP *cis*-keto cluster with surrounding molecules (yellow) in the enol form. (b) Simulated absorption (full line) and fluorescence (dashed line) spectra obtained using a QM/QM' approach and charge embedding model. Reprinted with permission from Ref. 25. Copyright 2016 Wiley Periodicals, Inc.

dynamics were also performed. This methodology allowed them to pinpoint a secondary photochemical pathway, see Figure 2.6. They concluded that the ESIPT process leading to a planar keto ES is the major pathways. Nevertheless, by investigating the conical intersection resulting from phenolic (a1), CN (a2) and anilic (a3) twists (see Figure 2.4), they proposed a minor pathway resulting from a frustrated proton transfer. This minor form is reached with CN twisting (a2) and associated to a much shorted ES lifetime in agreement with an internal conversion pathway.

Presti and co-workers used QM/QM' ONIOM calculations to study the effect of the crystalline environment on the ESIPT process.[24,25] The molecule of interest (the central SDA) was optimised with DFT B3LYP, PBE0 and CAM-B3LYP/6-31+G(d) whereas 14 others SA were added and treated at HF/STO-3G level of theory (see Figure 2.7). They concluded that this approach is given '*a fair description of the complex optical features of crystalline thermochromic SA*'. The enol form is defined as the most stable tautomer at the GS and the absorption features are well reproduced. In agreement with the experimental observation of *cis*-keto impurity in SA crystals, this form is less stable than the enol but still very close in energy. The *cis*-keto is found as slightly more stable than the *trans*-keto in the ES. Experimentally the emission of the *cis*-keto and *trans*-keto are not well separated therefore it was difficult to perform a comparison with theoretical data. The authors of these works also underline that the quality of their predictions are strongly dependent on the choice of functional, see Figure 2.7b.

2.1.3 HBX

The ESIPT dyes reported and discussed in the Chapters 4–6 are all based on the HBX scaffold; HBX being a generic abbreviation used to regroup 2-(2'-hydroxyphenyl)benzoxazole (HBO), 2-(2'-

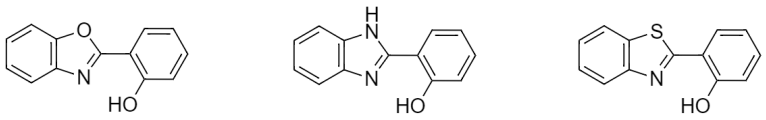

Figure 2.8: Representation of HBX structures, from left to right: HBO, HBI, and HBT.

hydroxyphenyl)benzimidazole (HBI), and 2-(2'-hydroxyphenyl)benzothiazole (HBT) compounds, see Figure 2.8. I will keep short here, as the reader has already have quite a few data to see for these systems in the forthcoming Chapters. This is not however meaning that we are the first to have interest in these systems. Indeed an extensive diversity of dyes based on HBO,[7,8,10–14,38,58,117,170–174] HBI,[9,47,107,114,126,175–183] and HBT[21,46,49,67,68,127,174,184–191] architectures have been investigated with theoretical methods in the literature.

It is noteworthy that more specific studies have also been performed on cores only,[73,75,88,89,127,192–197] a large share of which with TD-DFT. Different functionals have been tested to explore the properties of HBX cores: Tathle and co-workers[88] assessed M06-L, B3LYP, X3LYP, M06, and M06-2X, whereas Manojai and co-workers[89] upraised B3LYP, PBE0, M06, M06-2X, ωB97X-D, CAM-B3LYP, and LC-BLYP functionals. Both eventually discussed the results obtained with the B3LYP functional based on it accuracy to reproduce absorption spectra.

Estimations of the conical intersection with TD-DFT by optimisation of twisted keto structures around the interring bond (70–100°)[195] or of the pyramidalized keto ES[193] have been reported. Those structures were found more stable than the planar K* hinting as radiationless relaxation which can be directly related to the low quantum yield of fluorescence of these dyes. Using the PCM model, the impact of the solvent on the relative stabilities of the tautomers and the optical properties have been investigated for cyclohexanol, DMSO, DMF, ethanol, and water by Roohi *et al* for HBX core,[195] for hexane, methanol, acetonitrile, DMF, and water by Tathle and co-workers for the HBO structure only,[88] and for heptane, THF, DCM, methanol, and water by Duarte *et. al* for the HBT dye.[197] Prommin and co-workers performed dynamic calculations to estimate the influence of the solvent.[196] More in details, following the (TD-)DFT optimisation of the tautomers at the GS and ES, they performed dynamic calculations (25 trajectories of 500fs with 1fs time step) in ammoniac, methanol, and water for the HBI core. With this dynamic study, they observed different behaviour of the proton transfer (PT) reaction depending of the solvent. In methanol, the classic ESIPT process occurs, however in ammoniac the PT takes place through an intermolecular exchange involving the solvent, whereas in the water the intramolecular and intermolecular PT processes compete.

2.1.4 Rigidified ESIPT system

Quinolin derivatives

In quinolin derivatives, the core of the dyes is rather similar to one found in HBI compounds. However the central bond between the phenol and pyridine is rigidified by the presence of and extra bond

forming a six-member ring, see Figure 2.9. In such configuration the deactivation path through the conical intersection reach by rotation around the central bond is not possible anymore. The available theoretical characterisations of the 10-hydroxybenzo[h]quinoline (10-HBQ) have been mainly performed with TD-DFT using a static, and sometimes a dynamic approach.

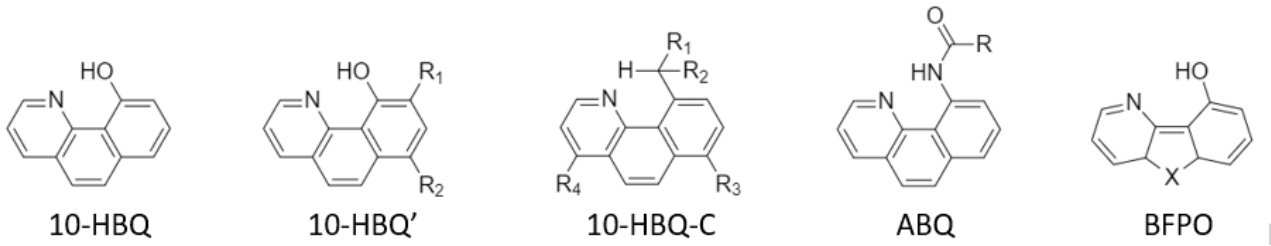

Figure 2.9: Representation of 10-hydroxybenzo[h]quinoline (10-HBQ) and derivatives (10-HBQ' and 10-HBQ-C), 10-aminobenzo[h]quinoline acylation (ABQ). Benzofuro[3,2-b]pyridin-9-ol (BFPO) is represented as well.

Schriever and co-workers have carried on a detailed investigation of the proton transfer process of the 10-HBQ as early as 2008.[198] Using the (TD-)DFT B3LYP/SVP and CC2/SVP levels of theory, the vertical excitation energies of the optimised GS and ES of the enol and keto tautomers have been investigated and vibrational frequencies computed. Using a normal modes analysis, four frequencies have been identified as involved in the proton transfer. Dynamic trajectories using a TD-DFT(B3LYP) approach have also been done in order to study the ESIPT process. From those different calculations coupled to the experimental data, they proposed an enol GS and a keto ES as the most stable forms. Given the agreement between their quantum and classical results, they concluded that the ultrafast proton transfer occur without tunneling.

Three years later, Paul and Guchait completed the theoretical characterisation of the 10-HBQ compound using (TD-)DFT/B3LYP but also HF and CIS calculations coupled with the 6-311+G(d,p) atomic basis set.[90] They performed PES scan to follow the ESIPT reaction and characterised the proton transfer by exploring the Muliken's charge distribution, which allowed evidencing the respective increase and decrease of the negative charges on the nitrogen and oxygen atoms after photoexcitation which is a favourable condition for the ESIPT to occurs. Their results are in agreement with the observation of a keto fluorescence.

Higashi and Saito performed another dynamic investigation of 10-HBQ using electronically embedded multiconfiguration Shepard interpolation(EE-MCSI).[199] This method, based on the QM/MM methodology, can be used to generate PES of a reaction in condensed phase. With this protocol, they have able to obtain 10 000 excited-state molecular dynamic trajectories on the S_1 PES for 10 ps by taking the coordinates and velocities from the ground-state equilibrium MD simulations as initial conditions.

One of the most recent theoretical study on the 10-HBQ system, realised by Yang and co-workers, was focussed on the detection mechanism of the phenylboronic acid, see Figure 2.10.[200] Using TD-DFT, and more precisely B3LYP/6-311+G(d,p), combined to non-adiabatic dynamics (trajectories of

300 fs and 100 fs with 1 fs time step), they confirmed the keto nature of the fluorescence in 10-HBQ and suggested that the phenylboronic acid is complexed with the 10-HBQ. In this latter configuration, the emission remains similar to the enol.

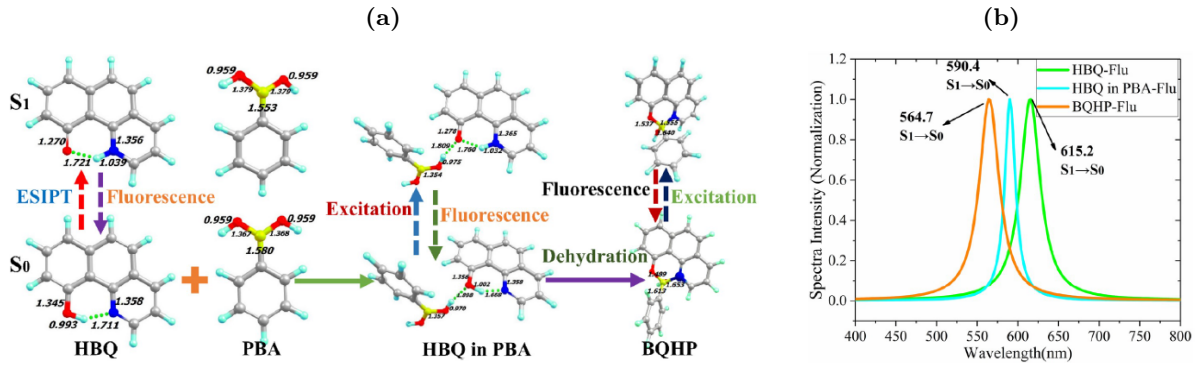

Figure 2.10: (a) Representation of fluorescence process of 10-HBQ (HBQ) alone, in presence of phenylboronic (PBA), and complexed with PBA (BQHP). (b) Fluorescence spectra of HBQ, HBQ+PBA, and BQHP. Reprinted from Ref. 200, Copyright (2020), with permission from Elsevier.

Using TD-DFT, different teams have been working on quantifying the impact of donor and acceptor substituents on the ESIPT process so as to control the enol-keto equilibrium not only in the ES but also in the GS.[201–208] The mostly used positions of substitution are reported in Figure 2.9 (10-HBQ'). In particular, different donor proton groups have been investigated by both Stasyuk[203] and An,[206] and their co-workers. The first team explored the CH–N ESIPT (10-HBQ-C) whereas a more classic NH–H ESIPT (ABQ) was investigated by An. Benzofuro[3,2-b]pyridin-9-ol (BFPO) are also another possibility to obtain more rigid ESIPT dyes based not on the combination of a benzene with a quinolin but with an indeno moiety. TD-DFT studies can also be found for these systems.[209,210] The normal form is determined as the most stable in the GS and the tautomer as the most stable in the ES. A small barrier between the normal and tautomer form is detected at the excited state allowing the emission from both forms.

7-hydroxy-1-indanone derivatives

Tang and co-workers have demonstrated the possibility to tune the normal/tautomer equilibrium in 7-hydroxy-1-indanone (7-HIN, see Figure 2.11) based dyes, depending of the size of the π-conjugated pathway.[211] In a combined experimental and theoretical study, they determined that the compound I is emitting from it keto ES, whereas II and III show dual emission from both E* and K*. The theoretical calculations performed at PCM-TD-B3LYP/6-311+G(d,p) level, indicate that enol ES is more stable in the case of the dual emitting dyes II and III based on ES calculations performed at the Franck-Condon structure.

Compound III has also been studied more in details by Zhang and collaborators.[91] They performed TD-DFT PCM-B3LYP/6-311+g(2d,2p) calculations to scan the PES along the proton transfer coor-

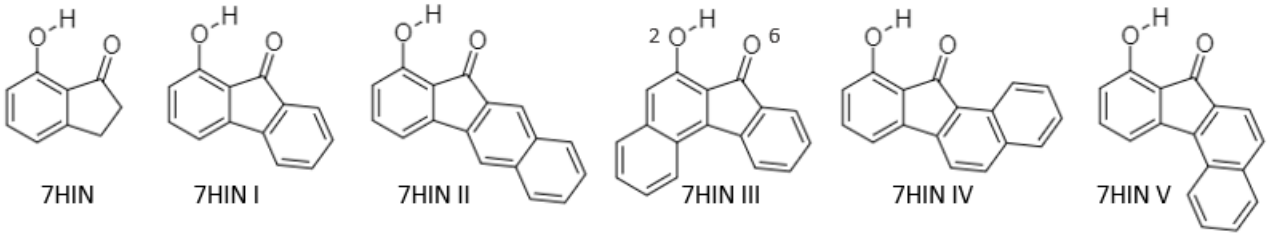

Figure 2.11: Representation of 7-HIN derivatives in their canonical form.[91,92,211,212]

dinate and fully optimises the GS and ES of both the normal and tautomer forms. The computed vibrational frequencies allows to observe a strengthening of the intramolecular hydrogen bond between E and E*, whereas the electron density repartition in E* and K* hint at a driving force for both the forward and backward ESIPT processes. Indeed, the group bearing the labile proton is always behaving as donor whereas the second can mainly be characterised as an acceptor. Therefore, independently of the nature of the ES, the conditions are favourable for ESIPT to occur, from the E* to the K* but also form the K* to the E*, which indicate that an equilibrium between the two tautomers is taking place, which translates into dual emission for that fluorophore.

Roohi and Alizadeh performed a TD-DFT study to investigated the modified 7HIN dyes II–V.[212] Their calculations made with the PBE0 and B3LYP functionals and the 6-311++G(d,p) atomic basis set account for solvent effects with cLR-PCM. In addition to localise the enol and keto minima for both the GS and ES, they also studied the vibrational frequencies and performed a scan of the PES. With the relative stability the systems have been defined as enol at the GS and ES. Depending of the compounds, differences in the 0.3–5.6 kcal/mol range between the enol and keto ES have been reported. An investigation of the solvatochromism, considering cyclohexane, acetonitrile, and water have been performed as well for both absorption and emission. A red-shift of both the absorption and emission when increasing the polarity of the solvent is observed. The E* and K* are stabilised by polar solvents with respect to the enol GS. Using QTAIM, the hydrogen bonding strength was studied to demonstrate the change of density of the proton. The covalent hydrogen bond, O2–H, in the enol form logically becomes an intramolecular hydrogen bond when the configuration is changing to keto, whereas the reverse is reported for the intramolecular bond, O6–H, that becomes covalent after ESIPT, see Figure 2.12.

Inspired by the study of Tang and collaborators[211] demonstrating that increasing the π-conjugated system allows the emergence of dual emitting dyes, Lei and co-workers proposed to couple 7HIN and diethienylethene (DTE) moieties in a single molecule, see Figure 2.13. Depending on the selected excitation energy, the ESIPT or the DTE moiety is excited. If the excitation is localised on the ESIPT moiety, the proton transfer can occur, whereas this process will be frustrated in the case of an excitation on the DTE part. This mechanism has been studied with theoretical tools only at this stage. The TD-DFT analysis has been performed using SMD-PBE0/6-31G(d) results although calculations with the B3LYP, B3P86, and M06-2X have also been performed. To explore the mechanism of this system

they studied the relative stability of the tautomers, as well as the transition state and vibrational frequencies. The dyad-o-n (open-normal) configuration is the most stable at the GS, and the dyad-c-t (closed-tautomer) at the ES., highlighting the interplay between the two units.

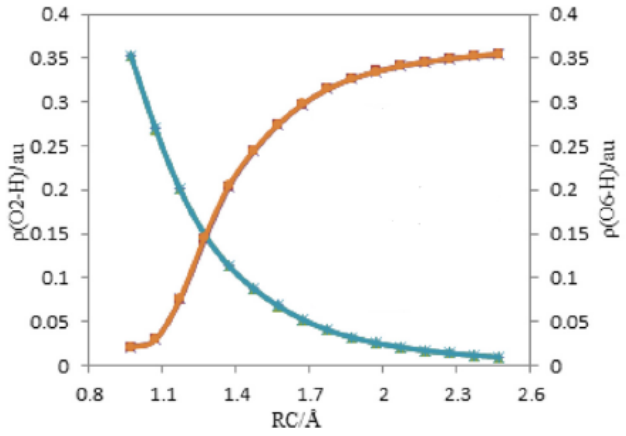

Figure 2.12: The change in the density ρ(r) at the O2–H as well as O6–H bond critical points *versus* reaction coordinate during the proton transfer reaction of 7HIN-III in the S_0 state. Reprinted from Ref. 212, Copyright (2018), with permission from Elsevier.

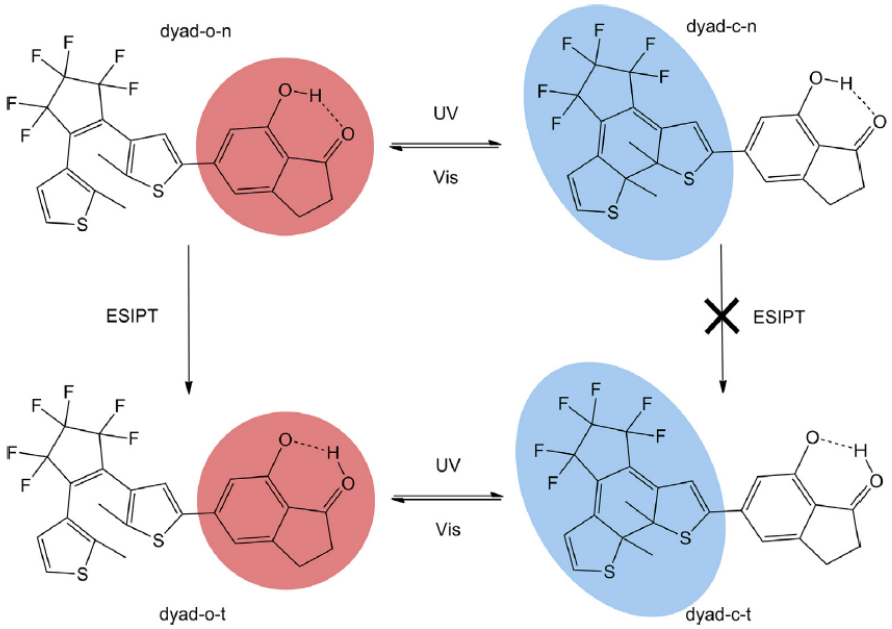

Figure 2.13: Representation of the mechanism to control the ESIPT process depending of the photoisomerisation of DFT. The excited part is represented by colours circles [localised on the ESIPT (red) or DTE (blue) parts]. Reproduced from Ref.[92], Copyright 2018 King Saud University. Production and hosting by Elsevier.

Hydroflavonol

Hydroflavonol derivatives present a 5-members ESIPT cycle and their fluorescence mostly results from the keto ES in non-polar solvent. However dual emission can also be observed in polar and protic solvents. TD-DFT studies have been performed on 3-hydroflavonol derivatives, see Figure 2.14.[173,213–215] The keto nature of the fluorescence and the ESIPT mechanism of 3HF-A,[173] 3HF-B,[213,216] 3HF-C[215] have been confirmed thanks to analyses of the IR spectra, PES scans, nature of MO, as well as calculations of the vertical absorption and emission energies.

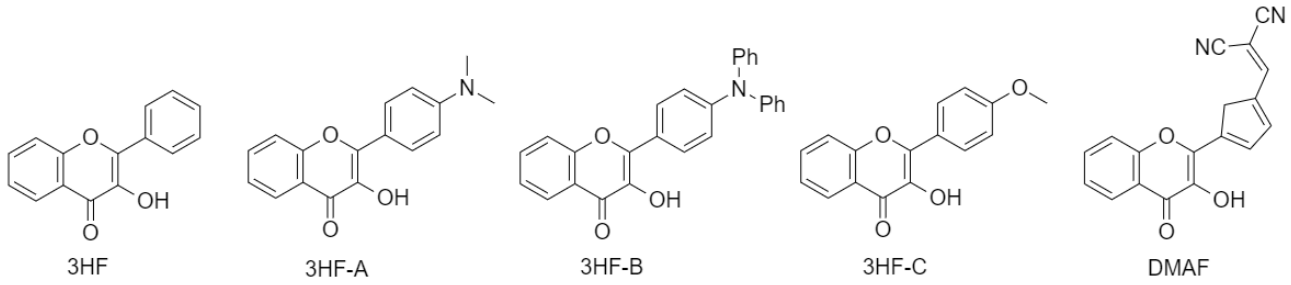

Figure 2.14: Representation of selected 3-hydroflavonol derivatives.

Loco and co-workers have performed modelling on these compounds, with a specific focus on solvent effects, that were evaluated using an atomistic description (QM/MM) approach, as well as continuum and hybrid strategies.[27,28] With this strategy, they were able to attribute the different experimental spectral signals to each of the possible forms of 3HF (enol, keto, and anionic). They demonstrated that the accuracy of the prediction of the solvent effects is increased when going to higher levels of theory. The 3HF-A dye has also been the subject of a classic molecular dynamic study by Hessz *et. al* aiming at accounting for the effect of the water environment. The MM conformation analysis was performed using the MMFF force field, whereas the stationary system was optimised at the (TD-)DFT PCM-M06-2X/6-31++G(d,p) level.[217] If 3HF-A is known for its dual fluorescence in organic medium, only the enol emission is observed in water. The MM study has demonstrated a decrease of the intramolecular H-interaction strength in favour of an intermolecular solvent-solute interaction. The latter is stronger in the ES than in the GS which is not offering favourable condition for the ESIPT to occur.

The DMAF dye (see Figure 2.14) presents an interesting behaviour theoretically unravelled by Yuan *et. al.*[124] The excitation of this system leads to the S_2 enol ES which can undergo two different pathways: an ultrafast ESIPT yielding the S_1 keto ES or an internal conversion to the S_1 enol ES. Thanks for TD-DFT, CASSCF, and CASPT2 optimisations of the different states and determination of the reaction barriers, the two process have been showed to be in competition, therefore a dual emission can be observed.

2.1.5 Green and blue fluorescent proteins

It is well known that Green Fluorescent Proteins (GFP) can be used as luminescent protein markers in living organisms. One of the GFP chromogen, 4-(2-hydroxybenzylidene)-1,2-dimethyl-1H-imidazol-5(4H)-one (*o*-HBDI), see Figure 2.15, contains an ESIPT center. The intramolecular H-bond rigidifies the system and allows emission from the keto tautomer. However the observed QY of fluorescence is extremely low which is not the case of the Blue fluorescent protein, that is based on the 4-(2-(amino)benzylidene)-1,2-dimethyl-1H-imidazol-5(4H)-one chromophore (*o*-ABDI). The ESIPT process of the latter, of its derivatives or modeled compounds, have been intensively investigated with TD-DFT, CASSCF, and CASPT2.[93,118,121,218–225]

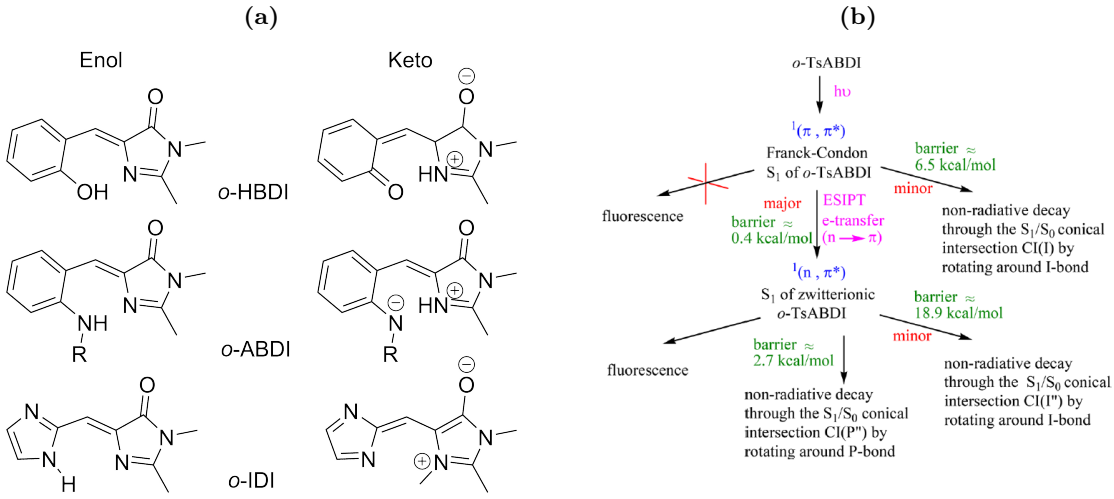

Figure 2.15: (a) Representation of the GFP and BFP structures *o*-HBDI,[93,121,218–220,222,223] *o*-ABDI,[224,225] and *o*-IDI.[118,221] (b) Proposed relaxation pathways of *o*-TsABDI (*o*-ABDI with R=CH_3PhSO_2) after photoexcitation, reprinted with permission from Ref. 224 Copyright (2018) American Chemical Society.

OH—N interactions : Green fluorescent protein

Hsieh and co-workers investigated with both CIS/6-31G(d) and PCM-B3LYP/6-31G(d), the enol and keto forms of *o*-HBI.[93] Based on the computed vibrational frequencies analysis, they reported a deformation of the systems helping the ESIPT transfer to occur. The vertical energies of the same derivatives were evaluated at different levels of theory: TD-DFT, CC2, and OM2/MRCI by Thiel's group.[219]. The best accuracy with respect to the experimental results were obtained with the OM2/MRCI and CC2 models. With CASSCF and CASPT2 calculations, the low QY of the GFP were rationalised by the existence of a conical intersection between the GS and ES in the keto form: the rotation around central bond is responsible for the rapid deactivation of o-HBDI.[121,220]

The team of Roohi explored different ESIPT systems[195,209,210,212,226] including *o*-HBI.[223] They performed their calculations with (TD-)DFT relying on either the PBE0 or M06-2X functional and took into account the environment effects with LR and cLR PCM. They explored the impact of electron

donating or withdrawing groups on the optical properties of *o*-HBI.

NH—N interactions : Blue fluorescent protein

Cui and co-worker have proposed a comparative study of the green and blue fluorescent proteins' chromohores *o*-HBDI and *o*-ABDI.[118] The main structural difference, the H-donor, induces, as stated above, a strong tuning of the optical properties: the QY is strongly decreased with an OH donor whereas dual emission is enhanced with the NH donor. Using CASSCF and CASPT2 approaches, the keto and dual fluorescence of *o*-HBDI and *o*-ABDI could be rationalised regarding the evolution of the barrier between the E^* and K^* tautomers. In addition, the higher barrier towards the conical intersection in BFP than in GFP explained the enhancement of the QY of the former. Similarly, Chen and co-workers used the TD-DFT and CASSCF to explore possibility of reaching a conical intersection in the BFP system but, in addition, they investigated zwiterrionic structures.[224] An increase of the intramolecular H-bond at the GS is observed in presence of acceptor substituents placed *para*. Electron-donor and withdrawing groups respectively induce a red-shift and blue-shift effect on the absorption. The enol emission can be observed with some electron withdrawing substituents (CN, NO_2) in polar solvents (acetonitrile, dicholoromethane). For the keto fluorescence in non-polar solvent (cyclohexane) a red-shift is observed with donor groups as compared to acceptors.

Using TD-DFT, Yuan *et. al* have highlighted a relationship between the decrease of the E^*/K^* barrier and the increase of the electron withdrawing strength of the substituting group.[225] In one other study, Hubin and collaborators found a failure of the TD-DFT for describing the equilibrium between the enol and keto ES of a model dye of *o*-ABDI, whereas they concluded that EOM-CC was suitable to obtain (more) accurate emission prediction.[221]

2.1.6 One ESIPT proton but two accepting sides

In some cases, the molecular scaffold offers the possibility for different conformers, all potentially ESIPT-active. Depending on the configuration of the intramolecular hydrogen bond in the GS, different ESIPT sites can be available, as illustrated in Figure 2.16. In this situation theoretical calculations are a specifically powerful tool to explore the different possible phenomena. The three compounds represented in Figure 2.16 have all been characterised by theoretical studies due to (from left to right) Qi and collaborators,[227] Yang *et. al*,[228] and Sobolewski[229]. Using TD-DFT the former group demonstrated that the ESIPT with the 6-members cycle (in blue) is favoured as compared to proton transfer the 5-members cycle (in red). The system reported by Sobolewski offers interesting applications in ultra-fast optical switching and data storage as the PT will occur first in the red region (Figure 2.16), but, once in the keto form, a rotation will take place to the second configuration, stabilised by a new intramolecular hydrogen interaction.

In Chapter 6, I also study one intriguing system with multiple configurations leading to different ESIPT sites (and colours) which can be activated by playing with the environment conditions.

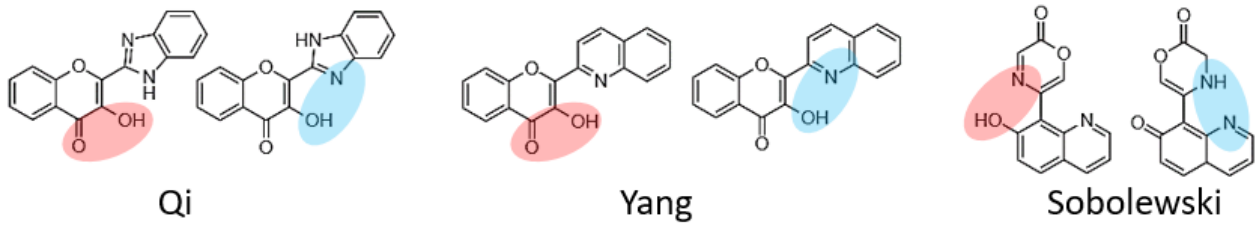

Figure 2.16: Representation of system with two possibilities of ESIPT process: 2-(benzimidazol-2-yl)-3-hydroxychromone (Qi), 2-(quinolin-2-yl)-3-hydroxychromone (Yang), and 7-hydroxy-(8-oxazine-2-one)-quinoline (Sobolewski).

2.2 Double ESIPT systems

The experimentally available double ESIPT (ESIDPT) systems have been reviewed by Serdiuk and Roshald three years ago.[5] The systems listed below are inspired of this previous publication, but with a focus on the theoretical studies here. The calculations realised on 2,5-bis(benzoxazol-2-yl)thiophene-3,4-diol (BBTP) structure are not discussed here as it has been one of my subject of interest. A full Chapter is dedicated to the study of this system (Chapter 5).

2.2.1 $BP(OH)_2$ - Bipyridine-diol

The simplest ESIDPT compound one can imagine is likely (2,2'-bipyridyl)-3,3'-diol [$BP(OH)_2$, see Figure 2.17]. The formation of the double proton transfer structure, i.e., the keto-keto form in both the GS and the ES, by concerted or step-wise transfer has been theoretically investigated with a large panel of approaches for this small compound.[69,70,74,78,230–236]

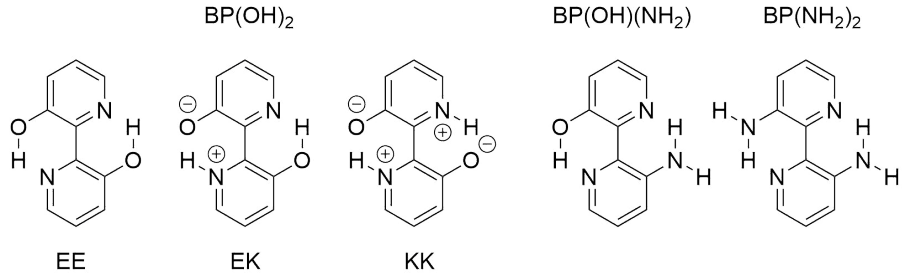

Figure 2.17: $BP(OH)_2$ tautomeric structures and amino derivatives.

At the HF/6-31G(d,p) level, Barone and Adamo have proposed the formation of the KK tautomer in the GS through a stepwise process.[230] However, they found that the EK and KK GS tautomers are transient species, and therefore only the enol-enol should be observed experimentally at the GS. To obtain these results, they optimised all the stationary points of the PES and characterised the PT mechanism with the so-called concerted large-amplitude path (CLAP) approach, see Figure 2.18. Sobolewski and Adamowicz confirmed this result with a PES study of the PT at the GS and ES respectively relying on the HF/3-21G and CIS/3-21G methods, accompanied by single-point CASSCF

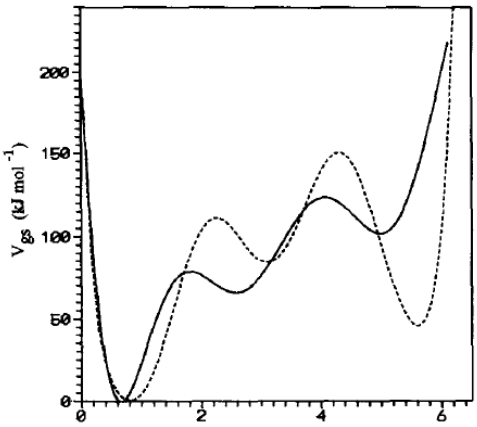

Figure 2.18: Concerted large-amplitude path (CLAP) for the stepwise tautmerization of $BP(OH)_2$ according to HF/6-31G(d,p) (full line) and AM1 (broken line) computations. Reprinted from Ref. 230, Copyright (1995), with permission from Elsevier.

and CASPT2 calculations.[231] They also ascribed the fluorescent species to the KK* form. Gelabert *et al.* investigated with (gas phase) DFT and TD-B3LYP/6-31G(d), the ESIPT mechanism although the ES energies are predicted using GS optimised structures. They concluded on the formation of the KK* through a step wise process.[233] Using CC2/TZVP and PCM-TD-B3LYP/SVP optimised PES calculations, adiabatic molecular dynamics simulations, and simulations of the spectral signatures, Plasser and co-workers also reported a step-wise process to form KK* but highlight the almost equivalent stabilities of EK* and KK* and the small barrier of 0.1eV separating both tautomers at the CC2 level.[236] Ortiz-Sánchez *et al.* performed (TD-)DFT B3LYP/6-31G+(d,p) and CASSCF calculations to describe the PT processes in $BP(OH)_2$, $BP(NH_2)_2$, and $BP(OH)(NH_2)$, see Figure 2.17.[234,235] For $BP(OH)_2$ and $BP(NH_2)_2$, they found two accessible paths to for the double PT tautomers: simultaneous and stepwise. They located the conical intersection to explain the quantum yield of fluorescence which is lower by four orders of magnitude in $BP(NH_2)_2$ as compared to $BP(OH)_2$. For the $BP(OH)(NH_2)$ hybrid, the double PT transfer can be reached with two different step-wise paths whereas the simultaneous PT implies a energetic barrier too high to be crossed.

2.2.2 BBHQ - Bis-benzoxazolylhydroquinone

The 2,5-bis(2-benzoxazolyl)hydroquinone (BBHQ, see Figure 2.19) has been intensively studied during the last 40 years.[64,71,170,237–249] The strong interest for this compound comes from the speed of ESIPT mechanism, 10–20 ps,[250] which is unusually slow for an ESIPT process. To understand the mechanism of BBHQ, theoretical calculations have been realised, in part, to understand the laser induced fluorescence results.[242]

The first calculations on BBHQ have been performed by Mordzinski and co-workers in 1983: they used a INDO/S Hamiltonian to predict the vertical transition energies. Only the single proton transfer process was retained by Mordzinski whereas 18 years later Weiß *et al.*[239] concluded on the possibility

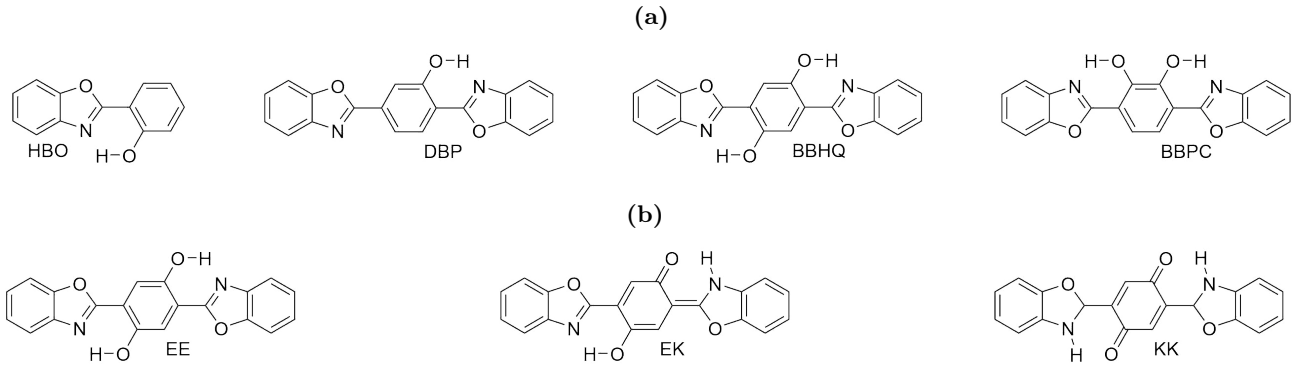

Figure 2.19: (a) Structures of BBHQ and derivatives and (b) representation of the three tautomers enol-enol (EE), enol-keto (EK), and keto-keto (KK).

of a double ESIPT by using semiempirical electronic Hamiltonians: AM1, PM3 and SAM1.

The next studies have all been performed with (TD-)DFT, using the B3LYP functional and atomic basis sets ranging from 6-31G(d) to 6-31+G(d,p).[170,241–247] Typically these works report a potential energy surface (PES) relaxed scans, optimizing the geometry of the system at various (fixed) O-H bond length. The different rotamers have been explored by Luzina *et al.*,[241] Sepioł and co-workers,[242] and the Sekar group.[246,247] They all concluded on a more favourable N$\cdots$O–H than O$\cdots$O–H intramolecular interactions.

The results of the gas phase calculations of Syetov yield a result contradicting experiment:[243] the enol-enol ES (EE*) is found to be the most stable form whereas a favoured EK* tautomer was expected. This clearly underlines the need to account for environmental effects when simulating ESIPT. In the publications including the environment by using the PCM model, the most stable form is indeed the enol-keto ES (EK*),[170,244,246,247] although some works also foresee the possibility of a double proton transfer.[170,244] BBHQ could reach a keto-keto ES (KK*) through a simultaneous double transfer (with a barrier around 6.9 kcal/mol only) or through a stepwise process (with a barrier of 3.3 kcal/mol for EE*→EK* and 3.6 kcal/mol for EK*→KK*).[170] However the KK* emission has never been recorded experimentally, as, according to theory it should appear at 1020 nm, which is clearly too red-shifted to come with a non-trifling fluorescence quantum yield.[170]

In the most recent publication dedicated to BBHQ at this day, a dynamical approach has been used to study the double ESIPT process of BBHQ in presence or not of two explicit water molecules.[249] Excited-state dynamic simulations of the systems relied on a TD-DFT B3LYP/SVP Hamiltonian and a microcanonical ensemble using Born-Oppenheimer energies and gradients was used. Twenty-five trajectories as a representative set for each system have been simulated using a time step of 1 fs with a maximum duration of 300 fs. The probability of observing a single or double proton transfer is only 40% when the water molecules are not included. When two solvent molecules are present in the system, the single proton transfer probability becomes 60%. The probability of a double proton transfer is also increased with explicit solvent (seven times larger than before). Such a study therefore confirms the key role played by the environment on the ESIPT process.

2.2.3 Double Schiff bases

ESIPT process in Schiff bases systems have been largely studied with theoretical tools for single PT as we discuss in the Section 2.1.2. Combination of two Schiff bases paves the way to ESIDPT, a possibly that has also been investigated for some compounds such as N,N'-bis-(salyciidene)-*p*-phenylenediamine (BSP),[94,135] 1,3-bis(2-pyridylimino)-4,7-dihydroxyisoindole (BPD),[251,252] one derivative of BPD (YT),[253] salicylidenesal-3,4-benzophen (SAB),[254] or Pigment Yellow 101, see Figures 2.20 and 2.21a.

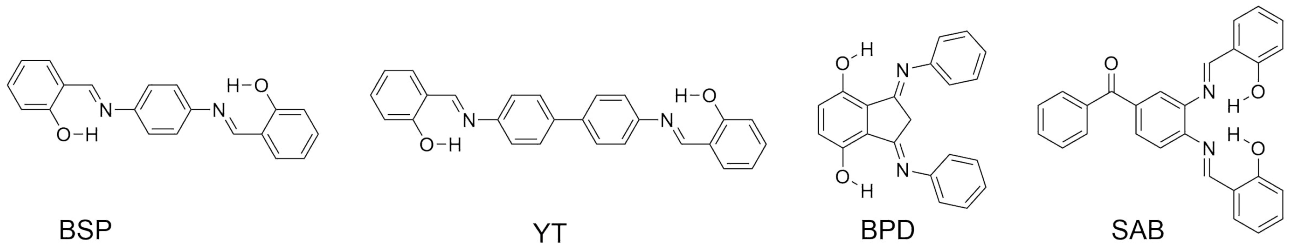

Figure 2.20: Double Schiff base structures (Refs: 94,135,251–254).

The BSP structure was explored for the first time by INDO calculations of the transition energies.[135]. This dye can be viewed as a double salicylideneaniline (SDA) and similar trends have been reported for SDA and BSP which led the authors to conclude on a single PT in BSP.[135]. (Much) latter the optimisation of the EE, EK, and KK with (TD-)DFT PM-B3LYP/TZVP at GS and ES was performed at the (TD-)DFT PCM-B3LYP/TZVP level, together with PES scans, infrared spectra simuylations, and vertical transitions energies calculations.[94] It was concluded that the KK* form is the most stable and responsible from the observed emission, and that this ESIDPT tautomer can be form by both a simultaneous or a stepwise ESIPT process.

For all the systems displayed in Figure 2.20, (TD-)DFT PCM-B3LYP calculations have been performed to determine the geometries of EE, EK, and KK in both electronic states, as well as to predict the vertical transitions energies. Based on these informations simultaneous or stepwise processes were again found accessible to form the KK* tautomer in YT.[253] For SAB, the KK* is not stable enough to be formed but two differents EK* can be obtained, which could explain the presence of two emission bands in the experimental spectrum. In the BPD structure, the keto-keto form has been described as the most stable at the GS and ES by Ma and co-workers,[252] whereas the calculations of Su yielded the normal enol-enol tautomer as favoured in the GS,[251] the double process occurs only at the ES to form KK* stepwisely. It is noteworthy that the latter work used both linear-response and state-specific solvation models.

2,2-dihydroxy-1,1-naphthalazine or Pigment Yellow 101 (PY101), see Figure 2.21, is the only commercially available yellow pigment exhibiting fluorescence.[255] This pigment is used, e.g., for the mass coloration of viscose, for printing inks and for artists' colours. The fluorescence mechanism of this pigments have been theoretical studied with (TD-)DFT by several groups.[95,96,256–264]

Dreuw *et al.* have been the first to theoretically investigate the mechanism of PY101.[95,96,256–258] Sixteen conformers have been investigated with three different functionals (BP86, B3LYP and BHLYP).

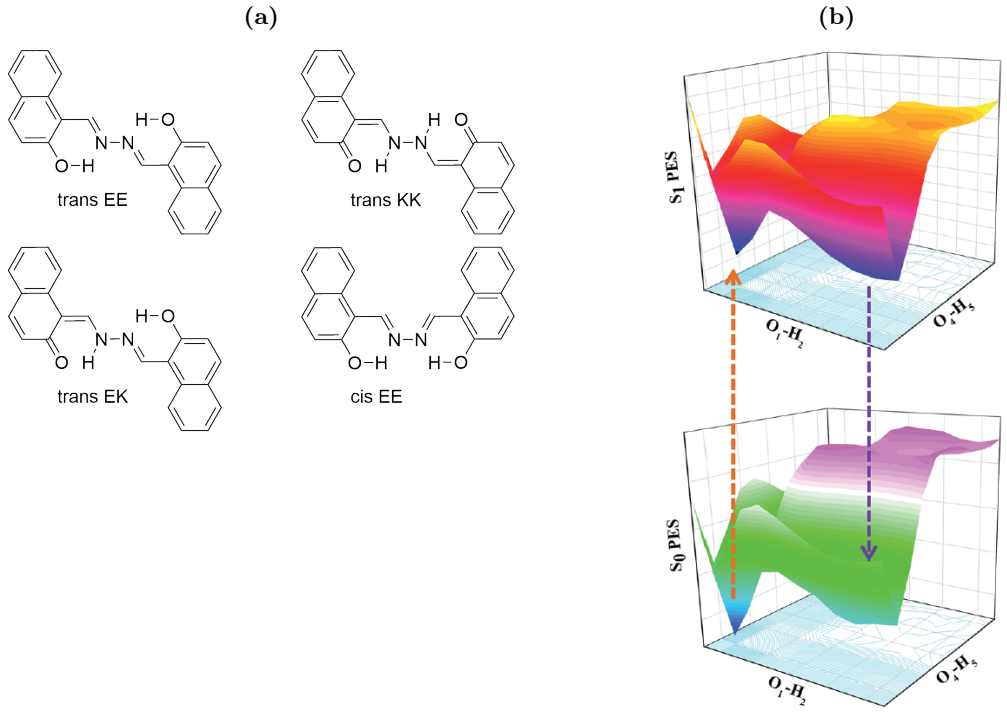

Figure 2.21: (a) Isomers of PY101 (b) potential energy surface (PES) reproduced from Ref. 262 with permission from The Royal Society of Chemistry.

Interestingly with BP86 and B3LYP, an artificially twisted structure around the N–N bond, resulting from the well-known charge-transfer failure of TD-DFT, is reported.[258] The compound present a static dipole moment of 10 Debye with BP86 in the planar configuration and it is increased to 17 D in the twisted form. Using a functional with a large share of Hartree Fock exchange was unsurprisingly found be the solution to bypass this issue. Therefore, based on their BHLYP results, the Dreuw group concluded to an emission resulting for the *trans* keto form although they did not excludes the possibility of an *trans–cis* isomerization which would lead to an emission from the equivalent *cis* keto tautomer. In one of their publications, they also explored the numerous deactivations patways explaining the exceptional photostability and colour fastness of PY101.[257]

With DFT B3LYP/6-31+G(d,p) calculations, Du and co-workers have evaluated the density properties of the dye and compared them with high resolution X-Ray data and obtained an excellent agreement between both.[261] They highlight the remarkably strong character of the intramolecular N-H...O H-bonds in PY101. To our knowledge, the first study including the environment has been carry on by Zhang and collaborators.[262] Using PES scans performed at the PCM-B3LYP/TZVP level of theory, they concluded that the enol-enol form is the most stable at both the GS and ES, see Figure 2.21b. However the barrier between the ES enol-enol and enol-keto tautomers is relatively small, 3.26 kcal/mol, therefore both EE* and EK* can be formed. These two structures emit at 540 nm an 551 nm respectively, according to these calculations, whereas the experimental emission takes place at 551 nm. The stronger deviations between theoretical and experimental optical properties found earlier,[257] with

gas-phase single point CC2/DZP calculations performed in TD-DFT BP86/DZP optimized geometries can likely explained by the neglect of environmental effects in that earlier work.

The most recent study of PY1010 has been performed with TD-DFT gas-B3LYP/6-311G(d,p) by Shen *et al.*.[264] Two possible pathways to reach a keto-keto structures by a stepwise process have been investigated, one with a torsion around the N–N bond but which is not possible in solid and another one with a simple PT but leading to an unstable tautomer, see Figure 2.22. They explain therefore the observed experimental dual emissions by the presence of two different single keto structures. Some derivatives of the PY101 have been explored as well by Satam,[260], Shreyka[263] and Hao[214] and their co-workers, all works relying on PCM-TD-B3LYP/6-31G(d) calculations. They concluded that all these structures can show only one ESIPT.

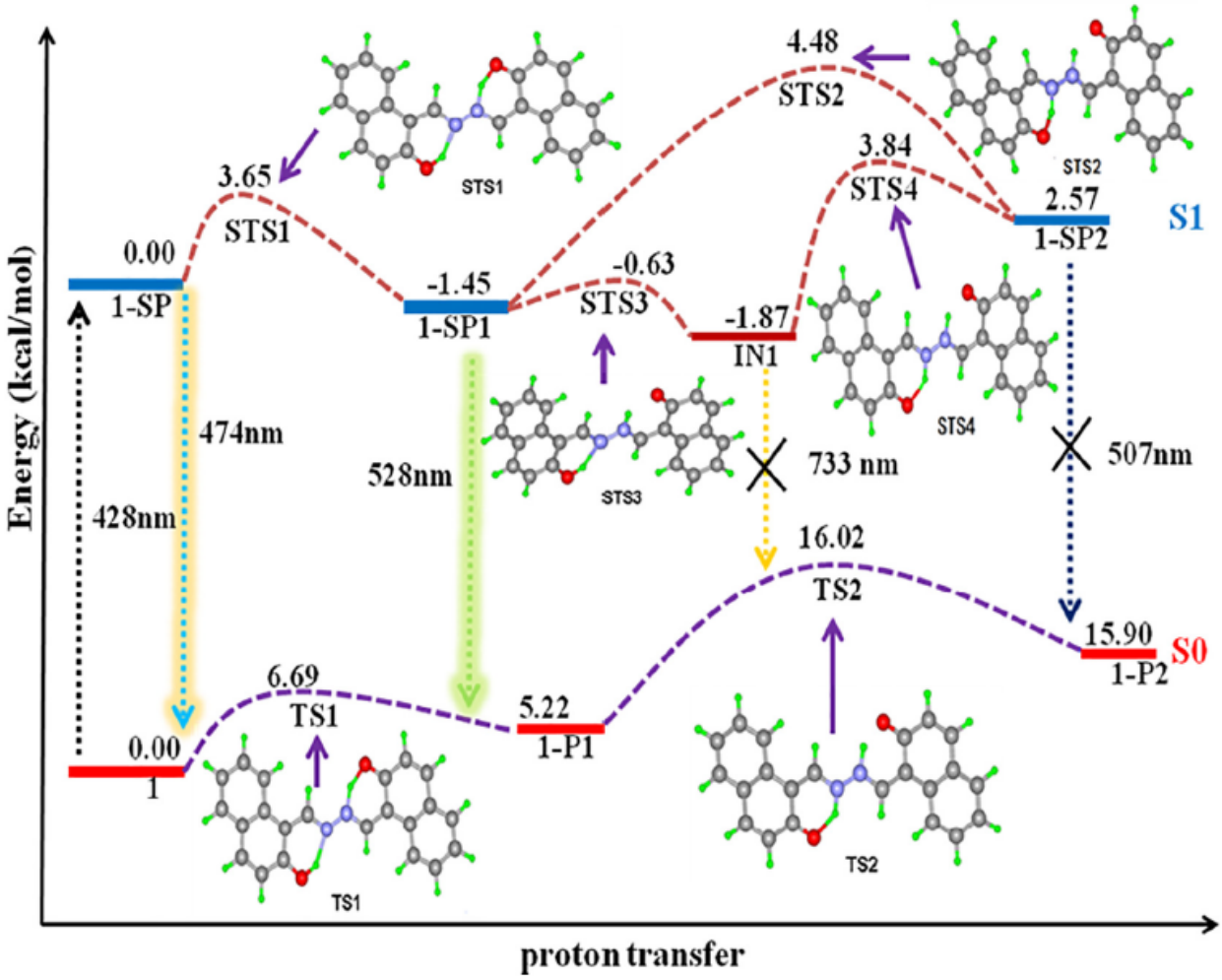

Figure 2.22: Calculated relative energies (kcal/mol) and wavelengths (nm) of vertical excitation and emission of PY101. Reprinted from Ref. 264, Copyright (2019), with permission from Elsevier.

2.2.4 Dihydroxydibenzophenazine

Xiao,[265,266] Zhang[98,177] and their collaborators both described the proton transfer in 1,8-dihydroxydibenzo[a,c]phenazine (**DHBP-c**) and 1,8-dihydroxydibenzo[a,h]phenazine (**DHBP-h**) dyes with TD-DFT and post-HF approaches (see Figure 2.23). The **DHBP-h** system has also been studied in another work.[43]

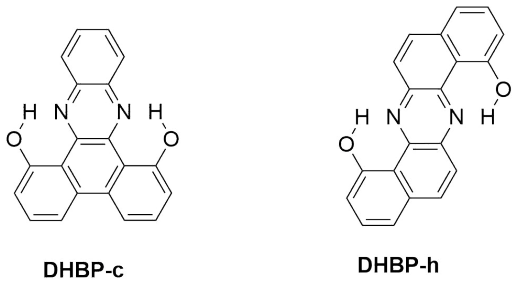

Figure 2.23: Dihydroxydibenzeophenazine structures

Using (TD-)DFT B3LYP and ωB97X-D/6-311++G(d,p) to optimize the structures and explore the pathways through IRC, as well as CC2/cc-pVDZ single point energy calculations, Xiao *et al.* described the EK* tautomer of **DHBP-c**, see Figure 2.23, as the most stable form and concluded on the possibility to obtain the KK* through a step-wise or simultaneous PT.[265] Latter Zhang and collaborators completed the study of this system by attributing the experimental emission to the EK* tautomer.[98] With (TD-)DFT PCM-B3LYP/6-311+G(d,p), CASSCF, and CASPT2 constrained energy profiles (CEP) searches from EE* to KK* combined to vertical transition energies, these authors indeed reported EK* as the most stable tautomer. They also studied **DHBP-h** with a similar approach in another work.[177] Zhao and collaborators also explored the (TD-)DFT PCM-B3LYP/6-31+G(d) PES of **DHBP-h** to estimate the minima and transition states.[43] From their results, they concluded that step-wise or simultaneous double PT could take place to form KK*. This latter tautomer is described as the most stable one but the experimental emission is attributed to the EK*. In Ref. 177, the emission is also attributed to the EK* but this form is the computed as the most stable tautomer. Regarding the energy profiles, simultaneous or stepwise PT can lead to the KK* but this latter tautomer is less stable than the EK*„ and a reverse ESIPT can easily happen. **DHBP-h** have also been investigated by Xiao with a (TD-)DFT B3LYP, CAM-B3LYP and ωB97X-D/6-311++G(d,p) approaches together with CASSCF/6-31G(d) calculations.[266] In this compounds, EK* is found to be the most stable form. The conical intersection obtained by CASSCF indicates that there is a strong barrier protecting the systems from non-radiative decay after ESIPT. Inter-system crossing between the third triplet ES T_3 and the first singlet ES S_1 has also been explored and found to be the likely cause of the fluorescence quenching.

2.2.5 Bisflavonols

1,4-bis-(3-hydroxy-4-oxo-4H-chromen-2-yl)-benzene (bisflavonol-A) and 3,7-dihydroxy-2,8- diphenyl-4H,6H-pyrano[3,2-g]chromene-4,6-dione (diflavonol-B) are constituted of two 5-members ESIPT sites, ses Figure 2.24. The proton transfers have been studied for these systems as well.[267–271]

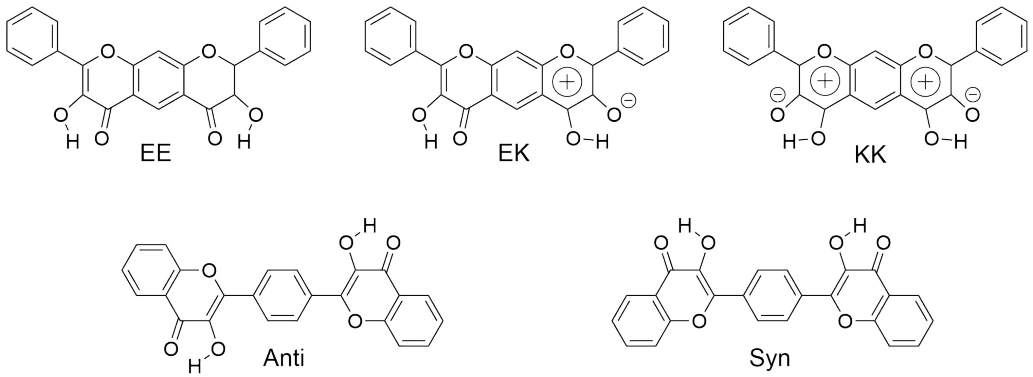

Figure 2.24: bisflavonol-A tautomers (top) and Bisflavonol-B anti and syn isomers (bot).

Bisflavonol-A

Using COSMO-AM1 and PCM-B3LYP/6-31G(d,p) calculations, Roshal *et al.* proposed an emission from the EK* form for the bisflavonol-A.[269] The same attribution has also been deduced by Falkovskaia and co-workers on the basis of CIS and B3LYP/6-31G(d,p) computations and scans of the PES scan.[267,268] Using a PCM-TD-B3LYP/cc-pVTZ protocol, Moroz *et al.* optimized the EE, EK and KK tautomers at the GS and ES and determined their vertical transitions energies.[270] Based on these results they concluded to an emission resulting from the EE* and EK* tautomers. This team also explored the impact of different substituents on neutral or anionic structures. For the latter structure, the complexation with methanol was taken account by the addition of explicit solvent molecules in the calculations. They found that complexation has a stabilising effect on the KK* isomer.

Bisflavonol-B

With B3LYP and CAM-B3LYP/TZVP calculations accounting for solvent effects through the PCM model, Zhao and co-workers performed PES scan and determined the vibrational frequencies, as well as Gibbs energies of all possible tautomers of Bisflavonol-B.[271] They also performed Born-Oppenheimer molecular dynamics (BOMD) for the ES starting from the transition state of the ESIPT process with a timestep of 0.5 ps. Both Anti and Syn configurations have been explored, as they both coexist at the GS. As illustrated in Figure 2.25, the EK* forms is the most stable with similar energies for the Anti and Syn configurations. The BOMD calculations allowed to concluded that the single PT process is the only possible process in this compound.

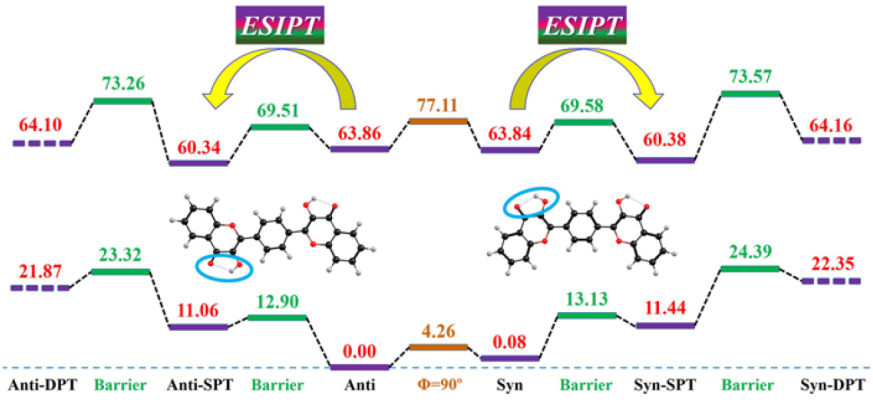

Figure 2.25: Calculated relative energies of reaction pathsn both GS and ES for Anti and Syn conformation of Bisflavonol-B. Reproduced from Ref.[271] with permission from The Royal Society of Chemistry.

2.2.6 Compounds with two different ESIPT sites

We report here systems with two different ESIPT sites, see Figure2.26.[272,273] In this situation theoretical calculations are a powerful tool to predict in which part of the dye the PT is likely to happen The two systems are composed of a salicyladheyde (6-members ring) or hydroxy-chromone (5-members ring) sites.

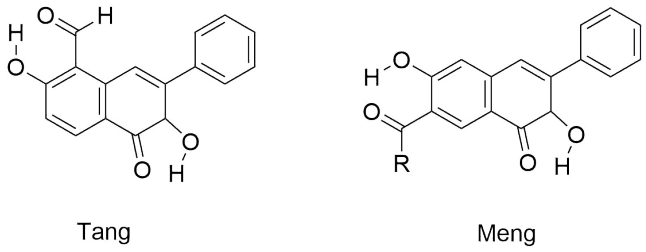

Figure 2.26: Compounds with two different ESIPT sites studied by Tang[272] and Meng[273] teams.

At the PCM-B1B95/TZVP level of theory, Tang and co-workers optimised the tautomers of the system represented in Figure 2.26, determined their vibrational spectra, investigated frontier MO, the molecular electrostatic potential surfaces (MEPS), PES, and performed populations analyses with two charge models. The PES, see Figure 2.27a indicates the strong stability of the EK* when the PT occurs in the hydroxy-chromone moiety (type 1) whereas a single PT transfer in the salicyladheyde part (type 2) leads to a less stable ES than the intial EE*, see Figure 2.27b. Due to the stronger stability of the EK* of type 1 and low oscillator strength of emission associated to the other EK* and KK* structures, only the emission from this first ES should be detected experimentally.

With a similar approach, PCM-CAM-B3LYP/6-31+G(d,p), Meng and co-workers characterised the second system represented in Figure 2.26.[273] Interestingly, in this system it is also a single ESIPT in the hydroxy-chromone part which yields to the most stable tautomer and is therefore responsible of the emission.

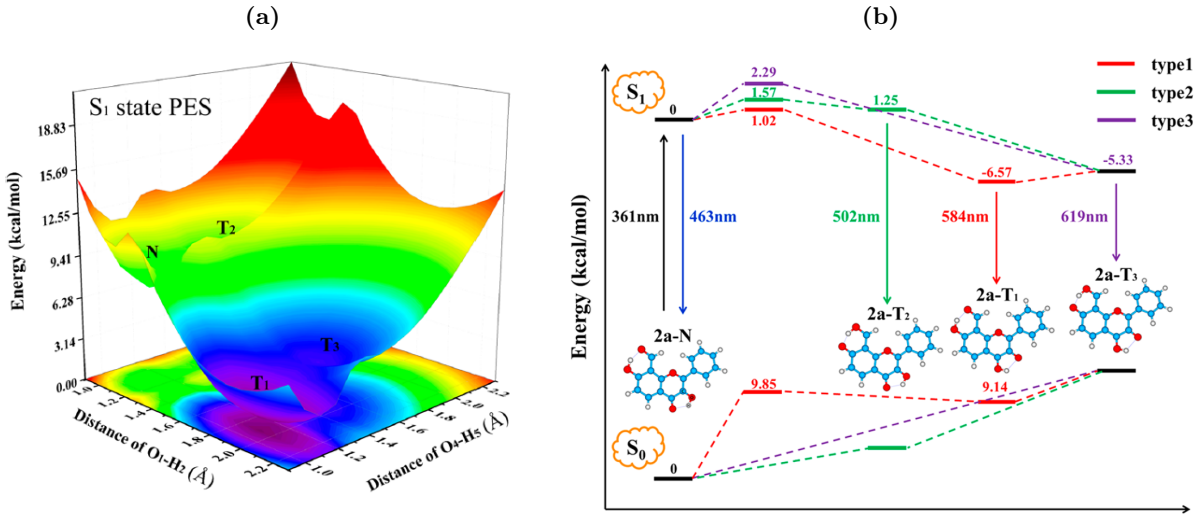

Figure 2.27: PES (a) and ESIPT process of dyes studied by Tang. Reprinted with permission from Ref[272] Copyright (2017) American Chemical Society.

2.3 Triple ESIPT systems

The tris(2-hydroxyphenyl)triazasumanene (OHPhTAS) dye exhibits single and dual emissions in solution and in the solid state, respectively, see Figures 2.28 and 2.29. Sartyounggkul and co-workers have investigated this system to understand the non-radiative pathways in solution.[274] Using PCM-CAM-B3LYP/6-31+G(d,p), they reported the vertical emission energies and adiabatic energies of the four envisageable tautomers, see Figures 2.28 and 2.29, the frontiers molecular orbitals, and PES of the radiative and non-radiative decay pathways. From their results, it can be concluded that a twist leading to a conical intersection but also the crossing point between T_1 ans S_0, both appearing after the first proton transfer, are responsible for the radiationless decay in solution. In solid state the twist of the compound will be prohibited and therefore the emission form the EEK* restored.

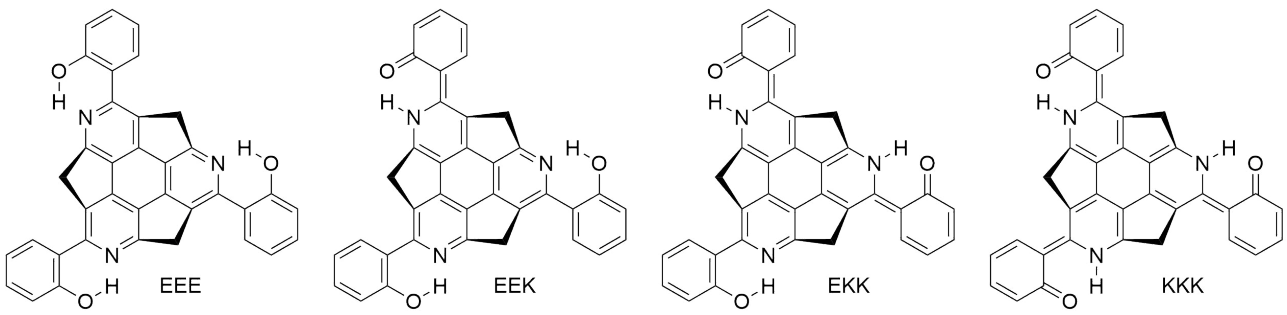

Figure 2.28: Possible tautomers of OHPhTAS.

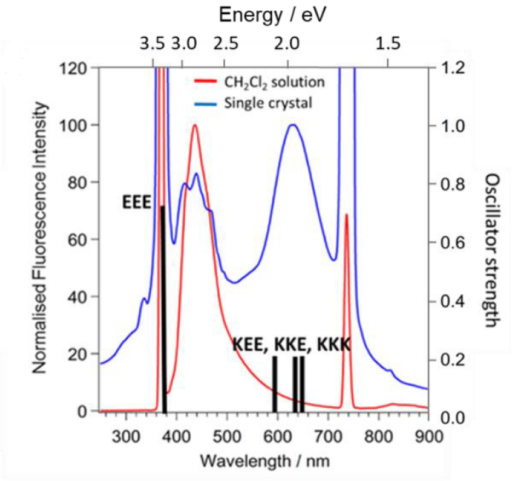

Figure 2.29: Experimental emission spectra of OHPhTAS (Red: in CH_2Cl_2 solution, Blue: single crystalline solid) and vertical transitions energies calculated by the PCM-CAM-B3LYP/6-31+G(d,p) level. The length of the bars corresponds to the calculated oscillator strengths. Reprinted with permission from Ref[274] Copyright (2020) American Chemical Society.

2.4 ESIPT studies from our team

Eventually, the Nantes' group has been investigated ESIPT systems since 2013 which has lead to a quite significant series of publications. Several of these publications are in close collaboration with the strasbourg's team,[6–13,38,171,183] my thesis being a direct results of this collaboration, whereas some other works are purely theoretical studies of ESIPT systems.[14,21,175,221,275–279] A representation of the variety of compounds studied can be found in Figure 2.30.

I will only go briefly on the main results obtained here. It was demonstrated that theoretical calculations are strongly recommended to characterize ESIPT system.[275,276] Indeed, the attributions of the emission to the K* tautomer on the basis of the observation of a large Stokes' shift can provide incorrect conclusions. The Stokes' shift is increased by ESIPT but charge transfer can have a similar effect as demonstrated for the systems noted 'Laurent' in Figure 2.30. As we will see afterwards, such possible confusion between a CT and ESIPT fluorescence was also a problem for some of the systems I investigated.

A important work focussed on obtaining dual emission using a single ESIPT emitter has been performed by Azarias, a previous PhD student in the group.[12] In this analysis, the relative energies of the tautomers in the ES, as computed by theory, can be used to predict the presence of enol, dual, or keto emissions. In more than 85% of the cases, this analysis yields the correct prediction, but solvent effects were clearly difficult to restore.

Since September 2018, a second PhD grand dedicated to ESIPT has been obtained which has led to the recruitment of Amara Chrayteh. Her work is focused on zwiterrionic ESIPT system, such as the system displayed in Figure 2.30.[279]

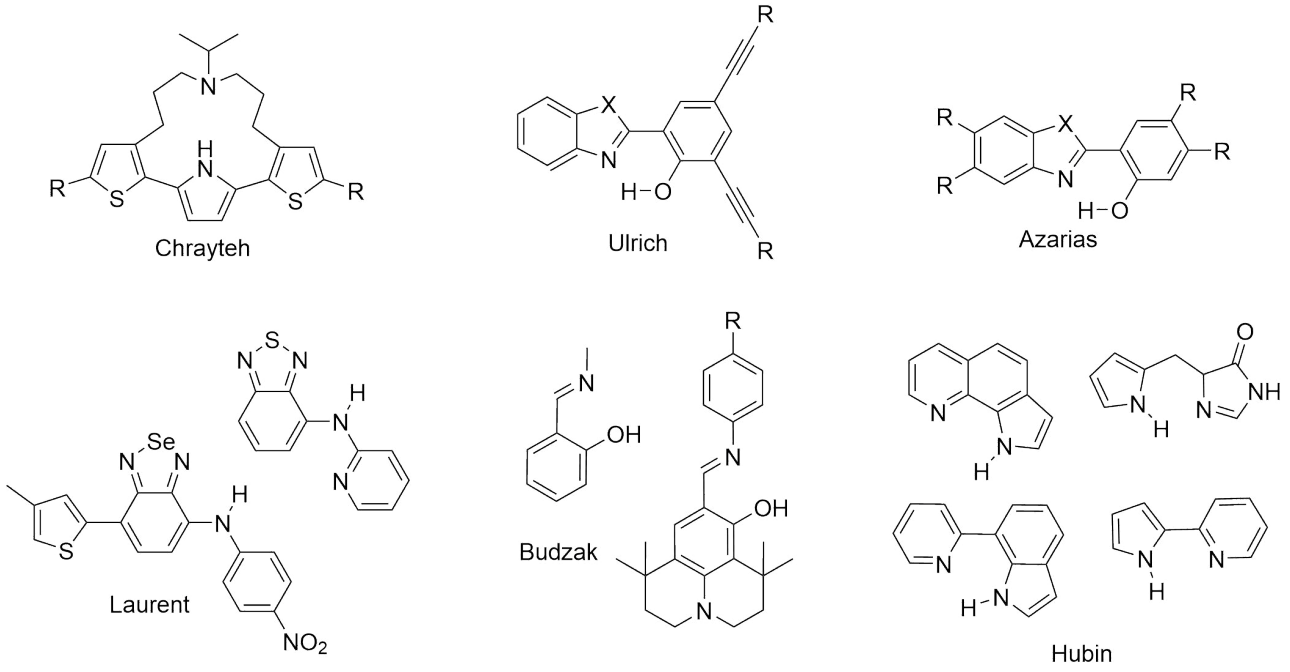

Figure 2.30: Some of ESIPT systems studied by our group.[6–12,221,275–279,279]

2.5 A short summary

To investigate the properties of ESIPT dyes a quite large panel of theoretical approaches can and has been employed. Obviously, the choice of the approach is mainly driven by the accuracy/cost ratio needed to determine the properties of interest, and, along the years, there has clearly been an improvement of the quality of the methods used. Amongst all, (TD-)DFT remains clearly the most frequently used as it offers an important range of tools to characterise these systems. First the geometry of enol and keto tautomers can be optimised at reasonable cost with or without inclusion of environment effects, a task that can be performed with various models (PCM, SMD, or COSMO, all in a linear-response or state-specific approach) for both the ground and excited states. From the literature, we see that the relative stability of the various forms is a strong indicator of the ESIPT phenomenon, and hence of the nature of the emission. To go further in the understanding of the ESIPT mechanism, potential energy surface scans can be performed to achieved the barrier between the tautomers and the different pathways. Some more rare studies have also chosen to directly optimise the transitions states. As expected, these optimisations have often been coupled to a vibrational frequency calculations to determine true minima (only positive frequencies) or transition state (one imaginary frequency). Infrared vibrational frequencies are also used to determine the normal modes involved in the proton transfer, sometimes in close comparison with experiment. As in all theoretical analyses, the topology of the molecular orbitals has been used as a visual tool to observe the density rearrangements during excitations and ESIPT. Less often representations of the electron difference of density between the ES and GS have been reported. The quantum theory of atom in molecule (QTAIM) or the electron

localization function (ELF) have also been used to follow the evolution of density of the hydrogen bonding during the process, or to visualise the excess of electron on the proton-acceptor.

Vertical transition energies and geometries can be determined with post Hartree-Fock models such as ADC(2), CC2, EOM-CCSD, CASSCF, and CASPT2. However they come with an increase of the computational cost as compared to TD-DFT. As can be seen from the literature examples listed in the present Chapter, CASSCF and CASPT2 have mostly been used to describe cases in which TD-DFT becomes unsuited, such as regions of the PES near conical intersections. Almost all the studies involving these two methods have indeed set a focus on defining the deactivation pathways of the ESIPT dyes through some rotations.

As TD-DFT offers an important panel of tools to characterise ESIPT systems at a reasonable computational cost, we used this method, in our studies discussed in the Chapters 4-6. Nevertheless, given the above, we added some corrections to the total and transition energies obtained by ADC(2) and CC2 calculations. Of course, we reach some limit point that more expensive approaches could have lifted but altogether we have been able to describe reasonably well our systems.

Chapter 3

Quantum chemistry: a short summary

Contents

3.1 Some common notions of quantum chemistry 39
3.1.1 The Schrödinger equation 39
3.1.2 The Born-Oppenheimer approximation 40
3.1.3 Description of the wavefunction 41
3.2 Ground state theories 43
3.2.1 Hartree Fock 43
3.2.2 Post-Hartree-Fock methods 45
3.2.3 Density functional theory - DFT 46
3.3 Excited state theories 49
3.3.1 Second-Order Algebraic-Diagrammatic Construction - ADC(2) 49
3.3.2 Second-Order Coupled Cluster - CC2 49
3.3.3 Time-Dependent DFT 50
3.4 The environmental effects 51
3.5 "Hybrid" approaches 52
3.6 ESIPT characterisation 54

This Chapter briefly presents the different theoretical methods used during my thesis. As I have not developed methods myself, this Chapter does not contain "unprecedented" materials, and Sections 3.1 to 3.4 have been inspired by various books, lectures, and articles.[280–289]

3.1 Some common notions of quantum chemistry

3.1.1 The Schrödinger equation

The aim of my thesis is to characterise some ESIPT systems. We are interested in their optical properties as well as the relative stabilities of various isomers at the ES. These properties are obviously

dependent on the electronic structure of the dyes. This structure can be determined by solving the Schrödinger equation.[290] This equation has an easily-accessible exact solution only for the mono-electronic problem. However the systems of interest here are poly-electronic and various approximations have to be made to solve the equation. Therefore diverse quantum chemical approaches, presented in the following of this Chapter, have been used. In its simplest form, for a stationary system, the Schrödinger equation reads:

$$H\Psi(x) = E\Psi(x) \tag{3.1}$$

with Ψ the wavefunction (WF) depending on the particle coordinates x, H the Hamiltonian of the system, and E the total quantified energy of the system. Ψ encompasses all of what should be known of the system and describes the collective behaviour of the studied system. For a time dependent system this equation can be written as:

$$H\Psi(x,t) = i\hbar\frac{\partial\Psi(x,t)}{\partial t} \tag{3.2}$$

with $\hbar$ the reduced Planck constant and t the time. The Schrödinger equation is an eigenvalue equation. The H operator acts on the wavefunction to restore the latter multiplied by a scalar, the energy: the WF is an eigenfunction and the energy an eigenvalue.

For an isolated non-relativistic molecular system, the Hamiltonian of a molecular system is composed of i) kinetic operators, describing the movements of the nuclei (T_{N}) and electrons (T_{e}), and ii) potential operators describing the Coulombic attraction between nuclei and electrons (V_{Ne}) as well as the complementary repulsions between electrons (V_{ee}), and nuclei (V_{NN}):

$$H = \quad T_{\mathrm{N}} \quad + \quad T_{\mathrm{e}} \quad + \quad V_{\mathrm{Ne}} \quad + \quad V_{\mathrm{ee}} \quad + \quad V_{\mathrm{NN}} \tag{3.3}$$

$$H = -\sum_{A=1}^{M}\frac{1}{2M_A}\nabla_A^2 - \sum_{i=1}^{N}\frac{1}{2}\nabla_i^2 - \sum_{A=1}^{M}\sum_{i=1}^{N}\frac{Z_A}{r_{iA}} + \sum_{i=1}^{N}\sum_{j>i}^{N}\frac{1}{r_{ij}} + \sum_{A=1}^{M}\sum_{B>A}^{M}\frac{Z_A Z_B}{R_{AB}} \tag{3.4}$$

with M_A the mass of the nucleus A in a.u., Z_A and Z_B the atomic number of the nuclei A and B, R_{AB} the distance between the nuclei A and B, r_{iA} the distance between the electron i and the nucleus A, and r_{ij} the inter-electronic separation.

3.1.2 The Born-Oppenheimer approximation

In 1927, Professor Max Born and his PhD student Robert Oppenheimer published a paper that became the basis of the first approximation typically used to resolve the Schrödinger equation.[291] Based on the significant difference of masses between nuclei and electrons, they proposed to uncouple their respective displacements.[30,31] With this approximation the Schrödinger equation can be split into two parts. The first is the electronic component which is described with fixed nuclei (electrons are so fast that they are considered to instantly adapt to any change of position of the nuclei) whereas, in the second nuclear part, the electronic energy contributes as a potential energy.

This implies that the electronic component of the Schrödinger equation, describing the electrons WF, depends explicitly on the electron positions but parametrically on the nuclear coordinates (fixed nuclei):

$$H = H^{\text{elec}} + T_{\text{N}} + V_{\text{NN}} \tag{3.5}$$

$$H^{\text{elec}}\Psi^{\text{elec}}(x) = E^{\text{elec}}\Psi^{\text{elec}}(x), \tag{3.6}$$

$$H^{\text{elec}} = T_{\text{e}} + V_{\text{Ne}} + V_{\text{ee}} = -\sum_{i=1}^{N}\frac{1}{2}\nabla_i^2 - \sum_{A=1}^{M}\sum_{i=1}^{N}\frac{Z_A}{r_{iA}} + \sum_{i=1}^{N}\sum_{j>i}^{N}\frac{1}{r_{ij}} \tag{3.7}$$

For the electrons, the nuclei are fixed, hence $T_{\text{N}} = 0$ and V_{NN} is a constant that can be added to E^{elec} at the end of the calculation. The first two terms in Eq. (3.7) are mono-electronic, however the third term, V_{ee}, explicitly depends on the positions of two electrons. Finding an approach to efficiently approximate this latter potential operator is at the center of the approaches described below. The general idea of these approximations is to transform the N-electron equation into a series of N mono-electronic equations, and also to describe the N-electron WF as a combination of 1-electron WF, that is, a combination of orbitals.

3.1.3 Description of the wavefunction

The antisymmetry or Pauli Exclusion Principle

H^{elec} depends only on the spatial coordinates of the electron. However a complete description of the electron also requires to know its spin, e.g., two electrons can have the same spatial position only if they present opposite spin. The four coordinates of electrons (three spatial and one spin-related) can be denoted by generalizing x as: $x = r, \omega$, with r describing the Cartesian coordinates and ω the spin (α or β). With the spin included into the wavefunction, a N-electrons WF is written $\Psi(x_1, x_2, \ldots, x_N)$. To respect the antisymmetry or Pauli exclusion principle, the WF has to change of sign when two electrons are interchanged, that is,

$$\Psi(x_1, x_2, \ldots, x_i, \ldots, x_j, \ldots, x_N) = -\Psi(x_1, x_2, \ldots, x_j, \ldots, x_i, \ldots, x_N) \tag{3.8}$$

Slater determinant

As stated above, the orbital is typically as one-electron WF, that is a mathematical function describing the behaviour of an individual electron. In the practice of quantum chemistry, molecular orbitals are used to describe the molecular electronic structure. To take into account of the spin, spin orbitals are used. They are the product of a spacial molecular orbital ($\phi(r)$), depending on the position vector r and describing the spacial distribution of an electron, and a function of the spin ($\sigma(\omega)$):

$$\Psi(r, \omega) = \phi_i(x) = \phi_i(r)\sigma(\omega) \tag{3.9}$$

To satisfy Pauli's principle, the antisymmetric WF can be written as a Slater determinant:[292]

$$\Phi(x_1,\ldots,x_N) = \frac{1}{\sqrt{N!}} \begin{vmatrix} \phi_1(x_1) & \cdots & \phi_N(x_1) \\ \vdots & \ddots & \vdots \\ \phi_1(x_N) & \cdots & \phi_N(x_N) \end{vmatrix} \tag{3.10}$$

or simply $\Phi(x_1,\ldots,x_n) = |\phi_1 \ldots \phi_N\rangle$. In Eq. (3.10), $\frac{1}{\sqrt{N!}}$ is a normalization factor, ensuring that integration of the square of the WF over all space would restore the number of electrons. By using a Slater determinant to describe the WF, one also ensures that Pauli's exclusion principle is satisfied. In the so-called single-reference approaches described below, the WF is described as a single Slater determinant. Multi-reference methods would use a combination of various determinants to build the WF.

Atomic basis sets

It is a common practice that the molecular orbitals $\phi_i(r)$ are constructed as a Linear Combinations of Atomic Orbitals (LCAO):

$$\phi_i(r) = \sum_{\mu} c_\mu \chi_\mu(r) \tag{3.11}$$

with c_μ the (LCAO) coefficients describing how the known χ_μ atomic functions (usually called atomic orbitals) are combined to form the molecular orbital. The atomic orbitals are fixed during the calculations, and hence, one has "only" to find the numerical c_μ, that is the "best" possible numerical combination of known functions. The ensemble of χ_μ is called the atomic basis set. This latter can be build with Slater-type orbitals (STOs) or Gaussian-type orbitals (GTOs), which show $e^{-\zeta r}$ and $e^{-\alpha r^2}$ spatial dependence, respectively. The STOs appear more accurate to build the molecular orbitals as they originate from the exact solution of the Schrödinger equation for the hydrogen atom. However, their mathematical form makes them less suitable for running high-performance computations on complex molecules, and it is the GTOs that are mostly applied. Indeed, GTOs, have the advantage to allow fast calculations of two-electron multi-center integrals. From the forms of these two functions major deviations obviously occur at $r = 0$ and large r. At $r = 0$, the Slater s function shows a peak whereas its Gaussian counterpart is flat. At the opposite site, at large r, the Gaussian function decays too rapidly compared to the Slater function. In order to correct these non-optimal dependencies of the GTOs, contracted functions are build using primitive Gaussian functions, so as to restore a STO-like topology.

From the size of the basis set depends the accuracy of the description of the system. But extending the basis set has a cost that one can clearly observe on the computational time. Therefore compromise choices have to be made depending of the expectations. In this manuscript, the calculation have been mostly performed with two Pople's basis sets[293] 6-31G(d) and 6-311+G(2d,p), and three Dunning's basis sets[294] cc-pVTZ, *aug*-cc-pVDZ, and *aug*-cc-pVTZ.

In the 6-31G(d) basis set the core electrons are described with one contracted basis function composed of 6 Gaussian primitives (**6**). The valence electrons are treated with two (double-ζ) functions encompassing 3 and 1 Gaussian primitives (6-**31**), respectively. In addition a polarization function is added to the non-hydrogen atom [6-31G(**d**)]. The more extended 6-311+G(2d,p) basis set presents one additional contracted function composed of one primitive to describe the valence electrons (6-**311**). Polarization effects are now described with two sets of *d* functions for heavy atoms, and the H atoms are polarized with *p* functions [6-311+G(**2d,p**)]. A diffuse (flatter) function is also added on all non-hydrogen atoms represented by the (+). Without entering into details, 6-311+G(2d,p), is probably extended enough to provide values rather near basis set convergence for the properties and systems under investigation in my thesis, i.e., it is unlikely that using an even more extended basis set would significantly modify the obtained conclusions.

The correlation-consistent (cc) basis sets of Dunning have been designed to recover the electronic correlation in a consistent manner. The general notation is cc-pVXZ basis set meaning correlation-consistent (cc) polarized valence (pV) for double (DZ) or triple (TZ) ζ basis set. All these bases therefore contain an increasing number of polarization functions, whereas the prefix *aug-* can be added to denote the addition of diffuse functions. The basis sets of Dunning do not have the restriction of Pople's bases in which equal exponents for *s-* and *p-* functions have been imposed. Globally, they are more flexible but also more expensive computationally. For the carbon atom with the *aug*-cc-pVTZ, the description of the basis set is written: (11s,6p,3d,2f) $\rightarrow$ [5s,4p,3d,2f] – the number of primitive functions is given in parenthesis whereas the number of final contracted functions obtained is written between brackets. To compare, the 6-311+G(2d,p) description for the carbon atom is (12s,6p,2d) $\rightarrow$ [5s,4p,2d]. Obviously, *aug*-cc-pVTZ is a very large basis set and it can be used as a *de facto* reference in the vast majority of quantum chemical calculations.

3.2 Ground state theories

3.2.1 Hartree Fock

Hartree Fock (HF) is the simplest *ab initio* theory and the "historic" method of quantum chemistry. It has been developed to solve the Schrödinger equation for a poly-electronic system. With HF, one uses a single Slater determinant, and the true Schrödinger Hamiltonian is approximated by (a combination of) Fock operators which allows transforming the Schrödinger equation into a set of (coupled) mono-electronic equations, which paves the way to very efficient computations, but at the cost of loosing accuracy.

Besides, the use of single Slater determinant, the central HF approximation is to consider that each electron is interacting with the average electric field created by the other electrons (Mean-Field Approximation) rather than with each other electrons individually. In other words, the repulsive interaction between electrons is approximated, and one neglects the so-called electron-correlation effects.

The one-electron HF Hamiltonian is the Fockian:

$$f(i) = h(i) + \sum_{j}^{N}(J_j(i) - K_j(i)) \tag{3.12}$$

This one-electron operator *f(i)* describes the kinetic energy of an electron and its electrostatic attraction with the nuclei as previously [*h(i)*] whereas the repulsion of the considered electron, i, with all the other electrons is divided into two operators: a Coulombic operator, $J_j(i)$, describing the classical Coulombic repulsion and the exchange operator, $K_j(i)$, describing the correlations between electrons of the same spin due to Pauli's anti-symmetry principle. This latter term is therefore a non-classical contribution, that is, in part, responsible for the formation of chemical bonds. These two operators can be written as :

$$J_j(r_1)\phi_i(r_1) = \left[\int \phi_j(r_2)\frac{\phi_j(r_2)}{r_{12}}dr_2\right]\phi_i(r_1), \quad \text{and} \tag{3.13}$$

$$K_j(r_1)\phi_i(r_1) = \left[\int \phi_j(r_2)\frac{\phi_i(r_2)}{r_{12}}dr_2\right]\phi_j(r_1) \tag{3.14}$$

The mono-electronic Fock equations can be written as:

$$f(i)|\phi_i\rangle = \epsilon_i|\phi_i\rangle \tag{3.15}$$

where ϵ_i is the energy of the spin-orbital i. The total HF energy can be obtained following:

$$E_{\mathrm{HF}} = \sum_{i}^{N}\langle\phi_i|h_i|\phi_i\rangle + \frac{1}{2}\sum_{i}^{N}\sum_{j}^{N}\langle\phi_j|J_i|\phi_j\rangle - \langle\phi_j|K_i|\phi_j\rangle \tag{3.16}$$

While all seems well if one accepts the mean-field approximation, it should be noted in Eqs. (3.12) and (3.13) the orbitals describing all the other electrons than i enter in the calculation of the Fock operator of that electron. This means that the HF equations depend on their own results and one needs to set up an iterative process, the Self Consistent Field (SCF) approach, to resolve the HF problem. The final solution, that is the HF wavefunction, corresponds to the minimal energy of the system that is found through the SCF process. In practice, SCF consists in finding the best set of molecular orbitals describing the system, that is, the LCAO coefficients leading to the smallest possible energy. The main advantages of the method are: i) its efficiency, as only one-electron equations have to be solved; ii) its variational character: the obtained energy is always larger than the exact energy.

However, in practice, the HF results are sometimes not accurate enough for chemical applications. What is missing in the HF solution, is the so-called electron correlation. Indeed, the correlation energy (E_{corr}) has been defined by Löwdin[295] as the difference between the exact energy of a system (E_{exact}) and the Hartree-Fock solution:

$$E_{\mathrm{corr}} = E_{\mathrm{exact}} - E_{\mathrm{HF}} \tag{3.17}$$

Correlation effects can be qualitatively separated into two components. The first is the static (or strong) correlation, related to the use of a single Slater determinant, which prevents the accurate HF

description of cases in which more than one electronic configuration plays a role (bond formation and breaking, crossing of electronic states...). The second is the dynamic (or weak) correlation related to the fact that the interplay between electron movements is not properly accounted for, due to the use of the mean-field approximation, which typically affects the quality of the estimated spectroscopic properties.

3.2.2 Post-Hartree-Fock methods

Using Hartree-Fock, the best possible single-determinant WF, one generally recovers ca. 99% of the total electronic energy. Therefore, some methods called post-HF approaches have been developed to incorporate (a part of) the correlation by using the HF result as a starting point. I briefly summarize the two I used below.

Møller-Plesset pertubation theory

The Møller-Plesset approach[296] consists in using perturbation theory to introduce electron-correlation, considering the HF solution as the unperturbed solution and the difference between the mean field HF operator and the real two-electron operator as the pertuber. As detailed below, one can therefore estimate what would be the obtained energy would the exact two-electron operator been used. The perturbation order can be increased to improve the share of electron-correlation energy that is recovered. Only the (simplest) second-order approach, MP2,[296,297] has been considered during my PhD work. Starting from the HF wavefunction and energy, a perturbation V is applied to the system, following:

$$H|\Psi_i\rangle = (H_0 + \lambda V)|\Psi_i\rangle = E_i|\Psi_i\rangle \tag{3.18}$$

with $0 < \lambda < 1$ a parameter and H_0 the sum of the one-electron Fock operators. The energies and wavefunctions can be expanded in a Taylor series in λ:

$$E_i = E_i^{(0)} + \lambda E_i^{(1)} + \lambda^2 E_i^{(2)} + \dots \tag{3.19}$$

$$|\Psi_i\rangle = |\Phi_i^{(0)}\rangle + \lambda|\Phi_i^{(1)}\rangle + \lambda^2|\Phi_i^{(2)}\rangle + \dots \tag{3.20}$$

The first correction to the energy including the electronic correlation effects is the second-order term,

$$E_{\mathrm{HF}} = E^{(0)} + E^{(1)} \tag{3.21}$$

$$E^{(2)} = \frac{1}{4}\sum_{a,b}^{\mathrm{occ}}\sum_{r,s}^{\mathrm{virt}} \frac{[\langle\phi_a\phi_b|\phi_r\phi_s\rangle - \langle\phi_a\phi_b|\phi_s\phi_r\rangle]^2}{\epsilon_a + \epsilon_b - \epsilon_r - \epsilon_s} \tag{3.22}$$

$$E_{\mathrm{MP2}} = E_{\mathrm{HF}} + E^{(2)} \tag{3.23}$$

where a and b (r and s) refer to occupied (virtual) molecular ϕ orbital of ϵ energy (as obtained at the HF level). MP2 is therefore quite simple to apply as very efficient implementations of Eq. (3.22) are available in many computational codes. For ground-state properties like geometries and interaction energies, MP2 yields theoretical estimation that are vastly improved as compared to HF. It is also noteworthy that MP2 is a size-consistent method but does not yield a variational energy.

Coupled Cluster

In the coupled cluster (CC) methods, the (dynamic) correlation is estimated differently through the incorporation of an exponential excitation (or cluster) operator T that generates additional contributions as compared to HF. More precisely, the CC WF can be written as:

$$\Psi^{\mathrm{CC}} = e^{T}\Psi^{\mathrm{HF}} \quad \text{with} \tag{3.24}$$

$$e^{T} = \sum_{k=0}^{\infty} \frac{1}{k!}T^{k} = 1 + T + \frac{1}{2}T^{2} + \frac{1}{6}T^{3} + \ldots = 1 + T_1 + (T_2 + \frac{1}{2}T_1^2) + \ldots \tag{3.25}$$

in which $T = T_1 + T_2 + T_3...$, with T_x the cluster operator generating all the (excited) determinants in which x occupied molecular orbitals of the starting HF WF have been replaced by x virtual orbitals. For the coupled clusters single and doubles (CCSD) method, the exponential excitation operator reads:

$$e^{T_1+T_2} = 1 + T_1 + (T_2 + \frac{1}{2}T_1^2) + (T_2T_1 + \frac{1}{6}T_1^3) + (\frac{1}{2}T_2^2 + \frac{1}{2}T_2T_1^2 + \frac{1}{24}T_1^4) \tag{3.26}$$

With the combination of single and double excitations appears not only singly and doubly excited determinants but also triply and quadruply excited determinants. This "trick" allows the CC approaches to remain size consistent (but not variational) irrespective of the expansion order. The CC2 method, which has been used in this thesis, is derived from CCSD.[298] In CC2, it is not the proper double excitation which is included but only the double contributions arising from the lowest (non-zero) order, i.e., from T_1^2. With this simplification, CC2 can be viewed as both a cost-effective approximation to CCSD and also as an improvement over the perturbative MP2. As for MP2, there exist several efficient implementations of CC2, allowing it to be used on compounds of large size (ca. 50–80 atoms) with a large improvement of accuracy as compared to HF.

3.2.3 Density functional theory - DFT

The density functional theory, DFT, that can be viewed as a mean-field alternative to HF, is undoubtedly the most commonly used approach to perform quantum calculations on large organic and inorganic molecules. The DFT principles have been defined by two theorems introduced in 1964 by Hohenberg and Kohn (HK).[299] The first indicates that for all systems under an external potential, here a set of nuclei, the external potential is described by a unique functional of the electron density $\rho(r)$. With this theorem, the resolution of $4N$ variables N-electrons WF is replaced by the three Cartesian coordinates of the density, the connexion between the two being provided by Born's equation:

$$\rho(r) = \Psi^{*}(r)\Psi(r) = |\Psi(r)|^{2} \tag{3.27}$$

In other words, rather than determining the WF, one can "simply" work with density that contains all the relevant information. All contributions to the energy (kinetic, electron-nuclei attraction...) can be, in principle, written as functionals of the density. With their second theorem, HK demonstrated the variational character of the functional. The functional, which describes the ground-state energy

delivers the lowest possible energy if and only if the input density is the true ground state (GS) one. With this theorem, energies obtained with approximate densities are always superior or equal (in an ideal scenario) to the exact energy of the system. This means, that the most accurate density (i.e., the one the closest from the true density) can be obtained by minimizing the energy functional with a SCF-like approach.

One year after the HK theorems, Kohn and Shan (KS) introduced the eponymous formalism.[300] The KS formalism allows to split the determination of the energy problem into two parts: a first part for which an exact formulations of the functionals is known and a second smaller component for which such exact formulation is lacking. The first includes: i) the kinetic energy of electrons described with a single Slater determinant, $T_e[\rho(r)]$, ii) the interaction potential between the electrons and nuclei, $V_{Ne}[\rho(r)]$, and iii) the Coulomb term, $J[\rho(r)]$ corresponding to classical electron-electron repulsions. The remainder is packed into a single term, the so-called exchange-correlation functional (XCF), $\epsilon_{xc}[\rho(r)]$. In equation terms, this translates as

$$E^{\text{HK-KS}} = \epsilon[\rho(r)] = T_e[\rho(r)] + V_{Ne}[\rho(r)] + J[\rho(r)] + \epsilon_{xc}[\rho(r)] \text{ with} \tag{3.28}$$

$$\epsilon_{xc}[\rho(r)] = (T[\rho(r)] - T_e[\rho(r)]) + (V_{ee}[\rho(r)] - J[\rho(r)]) \tag{3.29}$$

$\epsilon_{xc}[\rho(r)]$ is constituted of two terms, the first being the difference between the true kinetic energy and the one estimated with a Slater determinant, the second, often dominant, being the difference between quantum and classical electron-electron interactions. As $\epsilon_{xc}[\rho(r)]$ is unknown, one has to use a specific approximation for it. This approximation is the only one added to the traditional ones of quantum-chemistry (Born Oppenheimer, LCAO...). In practice, one has to choose an XCF and in doing so, one selects the approximation that will be used to describe the total energy functional, and to determine the density, $[\rho(r)]$. There is a vast amount of available $\epsilon_{xc}[\rho(r)]$.[301]

Exchange-correlation functionals

Although this is not a formal requirement, the exchange-correlation functional is usually separated into two functionals (exchange and correlation). The exchange functional, ϵ_{x}, takes into account the interaction between electrons with the same spin. The remaining interactions between electrons (mixed-spin interactions) are included in the correlation functional ϵ_{c}:

$$\epsilon_{\text{xc}}[\rho(r)] = \epsilon_{\text{x}}[\rho(r)] + \epsilon_{\text{c}}[\rho(r)] \tag{3.30}$$

The XCF are grouped in different categories. The simplest XCFs rely on the local density approximation (LDA). In this approach the XC contribution is computed considering a formula based on uniformly distributed density (electron gas model):

$$\epsilon_{\text{xc}}^{\text{LDA}}[\rho(r)] = \int \epsilon_{\text{xc}}[\rho(r)]\rho(r)dr \tag{3.31}$$

However this approach gives (very) poor results for organic molecules and is no more used for molecular calculations. With the generalized gradient approximation (GGA) the variations of electronic density

are introduced in the XCF with the normalized gradient $s_\sigma(r)$,

$$\epsilon_{\mathrm{xc}}^{\mathrm{GGA}}[\rho(r)] = \int f[\rho(r), s_\sigma(r)]dr \tag{3.32}$$

$$s_\sigma(r) = \frac{|\nabla\rho_\sigma(r)|}{\rho_\sigma^{4/3}(r)} \tag{3.33}$$

The GGA XCF can be further improved by the addition of a dependency to the kinetic energy density, $\tau_{(r)}$. This family of XCF is called *meta*-GGA.

$$\epsilon_{\mathrm{xc}}^{meta-\mathrm{GGA}}[\rho(r)] = \int f[\rho(r), s_\sigma(r), \tau(r)]dr \tag{3.34}$$

$$\tau_{(r)} = \sum_{i=1}^{\mathrm{occ}} |\nabla\phi_i(r)|^2 \tag{3.35}$$

Many different mathematical forms, based on various considerations and optimization approaches, have been derived over the years for both GGA and *meta*-GGA, e.g., the famous Becke formulation (B88 or simply B)[302] and the 1996 Perdew-Burke-Ernzerhof (PBE) alternative,[303] remain two of the most popular more than 25 years after their formulation. All these three families (LDA, GGA, *meta*-GGA) are *pure* DFT XCF, and if one often notices an improvement of the quality of the results in increasing the complexity of the XCF, it remains that the final accuracy remains rather poor especially for π-conjugated systems for which the all pure XCF typically exaggerate the electron delocalization.

The XCFs, from which come functionals selected to perform our calculations here, are called *hybrid* functionals. The main idea of this class is to combine the strength of HF and DFT approaches, or to state it less positively to rely on some error cancellation between the two approaches. In hybrid XCFs, a fraction of the so-called *exact* exchange (of HF form) is included in the exchange part, e.g., in the simplest approach:

$$\epsilon_{\mathrm{xc}}^{\mathrm{hybrid}}[\rho(r)] = \lambda\epsilon_{\mathrm{x}}^{\mathrm{HF}}[\rho(r)] + (1-\lambda)\epsilon_{\mathrm{x}}^{\mathrm{DFT}}[\rho(r)] + \epsilon_{\mathrm{c}}^{\mathrm{DFT}}[\rho(r)] \tag{3.36}$$

This idea was introduced by Becke in 1993,[304] and was soon recognized as extremely valuable for chemists. Indeed, with hybrid XCFs, the description of many molecular properties, as for instance absorption and emission, is (much) improved as compared with other functionals (LDA, GGA, and *meta*-GGA).[301,305] However the accuracy reached with those XCFs still strongly depends on the fraction of exact exchange introduced. In our calculations, the M06-2X[306] functional which contains 54% of exact exchange is mainly used based on previous ESIPT studies.[11–13,162,175,275,276] Occasionally the seminal B3LYP[307] XCF (20% of HF exchange) has been employed. One of the limits of these two XCFs is that the inter-electronic interaction at long range is only partially described, which can be an issue for our purposes. One solution of this problem is provided by the range-separated hybrid (RSH) XCFs. In this subclass of hybrid XCFs, the percentage of *exact* exchange increases with the inter-electronic distance, allowing to recover a more correct physical description of long-range effects. In Chapter 5, the ωB97X-D[308] RSH which includes 100% of exact exchange at long range and 22% at short range, has been employed.

3.3 Excited state theories

3.3.1 Second-Order Algebraic-Diagrammatic Construction - ADC(2)

The second-order Algebraic-Diagrammatic Construction, ADC(2), can be seen as an extension of the MP2 method to (electronic) excited states, but with a self-consistent building up of the latter.[309]

In more details, ADC(2) is based on propagator theory using many-body Green's function theory.[310] The different properties of the ES can be obtained by applying the associated propagator. The two-particle Green's function, the related particle-hole (p-h) response function and the polarization propagator, also known as p-h propagator are applied in this method. The second order ADC approach, that I have used during my work, accounts for both the p-h and 2p-2h excitations. The polarization vector can be written with the Lehmaann representation as:

$$g_{pq,rs}(\omega) = \sum_{n>0} \frac{\langle\psi_0|C_q^* C_p|\psi_n\rangle\langle\psi_n|C_r^* C_s|\psi_0\rangle}{\omega + E_0^{\mathrm{N}} - E_n^{\mathrm{N}}} + \sum_{n>0} \frac{\langle\psi_0|C_r^* C_s|\psi_n\rangle\langle\psi_n|C_q^* C_p|\psi_0\rangle}{-\omega + E_0^{\mathrm{N}} - E_n^{\mathrm{N}}} \tag{3.37}$$

with ψ_0 is the electronic many-body ground-state wavefunction of the molecule with the associated E_0^{N} energy and ψ_n the excited state of total energy E_n^{N} . The creation C^* and annihilation C operators describe respectively the addition and removal of an electron in the corresponding one-electron state. The energies of ES are obtained at the poles, when the external frequency is equal to the excitation energy: $\omega = \omega_n = E_0^{\mathrm{N}} - E_n^{\mathrm{N}}$.

In practice, ADC(2) requires to solve a Hermitian matrix ($\mathbf{M}$): $\mathbf{MY} = \mathbf{Y}\Omega$ and $\mathbf{Y}^*\mathbf{Y}=1$, Ω being the diagonal matrix of vertical excitation energies ω_n. As ADC(2) is a Hermitian approach, it has several advantages over CC theories, but as it is based on a MP2 ground state, it tends to become less suited when the gap is too small. In terms of computed transition energies, ADC(2) can globally be viewed as providing excitation energies with a ca. 0.15 eV accuracy, similar to the one obtained with the corresponding second-order CC approach, but for a smaller computational cost.[311,312]

3.3.2 Second-Order Coupled Cluster - CC2

The linear second-order coupled cluster (CC2) approach is solved, as ADC(2), with the addition of propagator operator at the ES.[298,313] However, a Jacobian matrix ($\mathbf{A}$) is used in this case. This matrix is non-symmetric and therefore the right and left eigenvalues differ : $\mathbf{AR} = \Omega\mathbf{R}$ and $\mathbf{LR} = \mathbf{R}\Omega$, with $\mathbf{R}$ and $\mathbf{L}$ the matrices with the right and left eigenvectors corresponding respectively to the rows and columns of the Jacobian matrix. This is clearly a weak point as compared to ADC(2). However, CC2 has the advantage to rely on a self-consistent ground state and is therefore generally more robust to compute transition energies of compounds presenting a small gap. As stated above, the "expected accuracy" of CC2 is ca. 0.15 eV for valence excitations in organic molecules.[311,312]

3.3.3 Time-Dependent DFT

The Kohn-Sham DFT approach described in Section 3.2.3 is limited to time-independent systems, that is ground electronic states. To describe excited state properties with a DFT-based approach, this model has been extended to a time-dependent (TD) formalism, called time-dependent DFT (TD-DFT). The analogue time-dependent theorem to the first Hohenberg-Kohn principle has been developed by Runge and Gross (RG) in 1984.[314] The RG theorem shows a one-to-one mapping between the TD density, $\rho(r,t)$, and the TD potential, $\mathrm{V}_{ext}(r,t)$ for a fixed initial wavefunction.

$$\rho(r,t) = \Psi^*(r,t)\Psi(r,t) = |\Psi(r,t)|^2 \tag{3.38}$$

To calculate electronic absorption, the linear response (LR) of the TD GS density submitted to an external electric field has to be calculated. The vertical excitation and oscillator strengths are determined by solving the LR equation at the poles of the polarizability. Using a matrix formalism the LR TD-DFT equation can be presented as:[287]

$$\begin{pmatrix} \mathbf{A} & \mathbf{B} \\ \mathbf{B}^\star & \mathbf{A}^\star \end{pmatrix} \begin{pmatrix} \mathbf{X} \\ \mathbf{Y} \end{pmatrix} = \omega \begin{pmatrix} \mathbf{1} & 0 \\ 0 & \mathbf{-1} \end{pmatrix} \begin{pmatrix} \mathbf{X} \\ \mathbf{Y} \end{pmatrix} \tag{3.39}$$

where (X, Y) is the linear response vector, ω the excitation energies, whereas the elements of matrices **A** and **B** read:

$$A^{\mathrm{TD-DFT}}_{ar,bs} = \delta_{rs}\delta_{ab}(\epsilon_r - \epsilon_a) + (ar|bs) + (ar|f_{\mathrm{xc}}|bs), \tag{3.40}$$

$$B^{\mathrm{TD-DFT}}_{ar,bs} = (ar|sb) + (ar|f_{\mathrm{xc}}|sb) \tag{3.41}$$

with $\delta_{rs}\delta_{ab}(\epsilon_r - \epsilon_a)$, the difference of energies of the orbitals a (occupied) and r (virtual), $(ar|bs)$ and $(ar|sb)$ the antisymetrised two-electrons repulsion integrals (derived from the linear response of the Coulomb and exchange operators), $(ar|f_{\mathrm{xc}}|sb)$ the response of the chosen exchange-correlation potential, and f_{xc} the so-called exchange-correlation kernel, that, within the usually applied adiabatic approximation, does not depend on the time:

$$f_{\mathrm{xc}}[\rho](r,r') = \frac{\partial v_{\mathrm{xc}}[\rho_t](r)}{\partial \rho_t(r')} = \frac{\partial^2 E_{\mathrm{xc}}[\rho_t](r)}{\partial \rho_t(r')\partial \rho_t(r)} \tag{3.42}$$

It should be noted that the latter approximation is quite strong and has an important impact: the results obtained with TD-DFT are highly dependent on the selected XCF (globally more than for the ground state).[315] A typical and well-known example is that charge-transfer excited states can hardly be accurately modeled with global hybrid functionals. Therefore, benchmarks and "educated choices" are sometimes needed prior to performing TD-DFT calculations.[315]

3.4 The environmental effects

The dyes studied in this thesis have all been experimentally characterized in solution. Therefore to reproduce, with accuracy, their properties, the environmental effects have to be taken into account during the theoretical calculations. Let me recall that, on the one hand, the enol and keto tautomers have significantly different polarities in most ESIPT compounds, and, on the other hand, that the measured fluorescence spectra are obviously highly dependent on the selected solvent (more than in "traditional" chromophores).[2,13,38,316,317] As a consequence, it seems indeed natural to include solvation effects during the calculations.

The solvent effects can be incorporated with either implicit or explicit methods. With an explicit method, the system is surrounded by multiple solvent molecules treated at a given level of theory. All solute-solvent interactions can be, in principle, accurately modeled with such strategy but one generally needs a preliminary dynamical search to generate snapshots that will all be studied, before an averaging procedure is carried out. In other terms, this is a quite expensive procedure, computationally speaking. The second possibility, which has been applied herein, is to describe the environment with an implicit model. With such approach, the solvent is treated as a homogenous and structureless material presenting the macroscopic properties of the real medium. The calculations do not require the (painful) dynamical search but specific solute-solvent interactions, such as hydrogen bonds or ion pairing, can not be described accurately. For ESIPT systems, this type of interaction is mostly important in protic solvent such as ethanol (in this specific case, the model reaches its limits, see Chapter 4, Section 4.7) but most of the molecules have been experimentally measured in aprotic solvent, such as the toluene. In aprotic solvents, the main interactions between the solvent and the solute are of electrostatic nature. The implicit model applied during our calculations is the well-known polarizable continuum model (PCM),[318] in which the solute is located in a molecular-shaped cavity. The solvent effects are then represented as a dielectric field through an apparent surface charge (ASC) approach, that is, charges are placed on the cavity surface. In more details, the environment polarization is represented by a sum of partial charges influenced by the electrostatic potential of the solute. The solvent and solute exert a mutual polarization on each others and the surface charges are self-consistently determined.[319]

For excited state calculations, some more specific questions have to be answered. Indeed, at the GS, the solvent-solute interactions are equilibrated: both the nuclear and electronic degrees of freedom of the solvent are adapted to match the electronic density of the solute.[320] During an electronic transition of the solute following photon absorption, only the electronic degrees of freedom of the solvent can immediately respond to the new electronic density of the solute. This process considered as a vertical transition is simply too fast for the nuclei to reorganize themselves according to Franck-Condon principle.[30,31] In such scenario, the solvent-solute interactions are considered to be in the so-called *non-equilibrium* limit, meaning that the effective dielectric constant for the non-equilibrium state is ϵ_∞ rather than ϵ_r. To determine the absorption transition energy, the solvent is considered in equilibrium with the GS but in non-equilibrium with the ES. In a slow process, i.e., when the nuclei of

the solvent have time to adapt to the ES density of the solute, one is in the so-called *equilibrium* limit. This is the case for instance when relaxing the ES geometry of a fluorescent molecule. However, for the vertical emission, one is back in a non-equilibrium case, but with an ES that is in equilibrium and a GS in non-equilibrium. I have systematically accounted for non-equilibrium effects in the computations of our emission energies in the following of the thesis, and this is not further specified.

In addition, it should be noted that different schemes can be used to combine PCM and TD-DFT; one can distinguish the linear-response[320] (LR) model and the state-specific (SS) schemes such as the corrected LR[321] (cLR) and the vertical excitation methods[322,323] (VEM). In the LR model, the solvent response is dependent on the transition density (or transition dipole moment). This model is adapted to describe ES with a local and (strongly) dipole-allowed characters. In contrast, if the electronic excitation involves a large density rearrangement in the solute (like in a CT state), the LR model is insufficient as the density dependent relaxation of the solvent polarization is not included. In such cases, state-specific models are more appropriate. In the cLR model, the response of the solvent polarization to the excitation is determined pertubatively from the difference of electrons densities of the initial and final states (or, more simply, excited state dipole moment). The VEM model rests on the same concept but its response is the result of an iterative process between the solvent and solute. The VEM model is quite expensive and has been applied in Chapter 5 only. In ESIPT systems, the electronic transitions are typically brighter in the enol than in the keto tautomers, and their ES dipole moments strongly differ. Therefore, is it not straightforward to *a priori* select a LR or a SS model, and this aspect will be discussed in more details in the forthcoming Chapters dedicated to the results. To take into account both LR and SS effects, one can combine the approaches with the so-called LR+cLR scheme. In practice, the LR+cLR energies are the sum of the total LR and cLR energies subtracted by ω_0, the excitation energy due to the ground state frozen polarization (to avoid obvious double counting). To my knowledge, I have been one of the first to extensively use this LR+cLR model, and I wish to underline that this effective approach was proposed by Dr. Ciro Guido during his post-doctoral stay in Nantes.

3.5 “Hybrid” approaches

The exploitation of our data has been realised using combined approaches as we wished to increase the accuracy of our results while maintaining a reasonable computational cost. With these mixed strategies one is taking into account corrections provided by higher levels of theory for various calculation aspects, e.g., basis sets, solvent, or even methodological effects for a relatively low cost.

Free energy

The free energy, G, is extremely useful to determine the relative stabilities of different isomers of a system for practical applications, as G drives the experimental response. To compute G one needs not only the total electronic energy of the system but also a series of (quantitatively) smaller corrections,

e.g., the zero-point vibrational energy (ZPVE), the thermal contribution and the entropy. These smaller corrections can be grouped in a "thermodynamical correction" which requires the calculation of the vibrational frequencies. However, this type of calculation can rapidly become expensive when the level of theory is improved. Therefore we have chosen to perform it with a rather basic protocol, i.e., with a small basis set (SBS) and the LR-PCM solvent model, and to determine the total energy of the system with a higher level of theory.

In Eq. (3.43), the free energy, $G^{\mathrm{cLR}}_{\mathrm{LBS}}$, is the sum of the total energy, $E^{\mathrm{cLR}}_{\mathrm{LBS}}$, determined with a large basis set (LBS) and the cLR-PCM solvent model, and the thermodynamic correction, $\Delta E^{\mathrm{thermo}}$, determined at simplest SBS-LR level.

$$G^{\mathrm{cLR}}_{\mathrm{LBS}} = E^{\mathrm{cLR}}_{\mathrm{LBS}} + \left(G^{\mathrm{LR}}_{\mathrm{SBS}} - E^{\mathrm{LR}}_{\mathrm{SBS}}\right) \tag{3.43}$$

$$G^{\mathrm{cLR}}_{\mathrm{LBS}} = E^{\mathrm{cLR}}_{\mathrm{LBS}} + \Delta E^{\mathrm{thermo}} \tag{3.44}$$

With this approach, post-HF corrections can also be included to obtain the free energy. As our post-HF calculations are performed in gas phase, a solvent correction is added as well, following,

$$G^{\mathrm{cLR}}_{\mathrm{post-HF}} = E^{\mathrm{gas}}_{\mathrm{post-HF}} + \left(G^{\mathrm{LR}}_{\mathrm{SBS}} - E^{\mathrm{LR}}_{\mathrm{SBS}}\right) + \left(E^{\mathrm{cLR}}_{\mathrm{LBS}} - E^{\mathrm{gas}}_{\mathrm{LBS}}\right) \tag{3.45}$$

$$G^{\mathrm{cLR}}_{\mathrm{post-HF}} = E^{\mathrm{gas}}_{\mathrm{post-HF}} + \Delta E^{\mathrm{thermo}} + \Delta E^{\mathrm{cLR}} \tag{3.46}$$

Those approaches can be applied to determine the free energy at the GS and ES. As stated in the previous Section, different models have been used to take into account the solvent effects: LR, cLR, VEM and LR+cLR. In the previous equations, the cLR corrections are included, but one could also apply:

$$G^{\mathrm{LR+cLR}}_{\mathrm{LBS}} = E^{\mathrm{LR+cLR}}_{\mathrm{LBS}} + \left(G^{\mathrm{LR}}_{\mathrm{SBS}} - E^{\mathrm{LR}}_{\mathrm{SBS}}\right) \tag{3.47}$$

$$G^{\mathrm{LR+cLR}}_{\mathrm{post-HF}} = E^{\mathrm{gas}}_{\mathrm{post-HF}} + \left(G^{\mathrm{LR}}_{\mathrm{SBS}} - E^{\mathrm{LR}}_{\mathrm{SBS}}\right) + \left(E^{\mathrm{LR+cLR}}_{\mathrm{LBS}} - E^{\mathrm{gas}}_{\mathrm{LBS}}\right) \tag{3.48}$$

or similarly,

$$G^{\mathrm{VEM}}_{\mathrm{LBS}} = E^{\mathrm{VEM}}_{\mathrm{LBS}} + \left(G^{\mathrm{VEM}}_{\mathrm{SBS}} - E^{\mathrm{VEM}}_{\mathrm{SBS}}\right) \tag{3.49}$$

$$G^{\mathrm{VEM}}_{\mathrm{post-HF}} = E^{\mathrm{gas}}_{\mathrm{post-HF}} + \left(G^{\mathrm{VEM}}_{\mathrm{SBS}} - E^{\mathrm{VEM}}_{\mathrm{SBS}}\right) + \left(E^{\mathrm{VEM}}_{\mathrm{LBS}} - E^{\mathrm{gas}}_{\mathrm{LBS}}\right) \tag{3.50}$$

Absorption and emission

For the vertical absorption and emission, combined approaches are also used extensively into include solvent and post-HF corrections in the forthcoming Chapters of this thesis. The different transitions energies are defined as:

$$E^{\mathrm{gas}}_{\mathrm{abs,TD}} = E^{\mathrm{gas}}_{\mathrm{ES}} - E^{\mathrm{gas}}_{\mathrm{GS}} \tag{3.51}$$

$$E^{\mathrm{solv}}_{\mathrm{abs,TD}} = E^{\mathrm{solv,neq}}_{\mathrm{ES}} - E^{\mathrm{solv}}_{\mathrm{GS}} \tag{3.52}$$

$$E^{\mathrm{solv}}_{\mathrm{abs,post-HF}} = E^{\mathrm{gas}}_{\mathrm{ES,post-HF}} - E^{\mathrm{gas}}_{\mathrm{GS,post-HF}} + E^{\mathrm{solv}}_{\mathrm{abs,TD}} - E^{\mathrm{gas}}_{\mathrm{abs,TD}} \tag{3.53}$$

with the energies taken at the ground state geometry and

$$E^{\text{gas}}_{\text{em,TD}} = E^{\text{gas}}_{\text{ES}} - E^{\text{gas}}_{\text{GS}} \tag{3.54}$$

$$E^{\text{solv}}_{\text{em,TD}} = E^{\text{solv,eq}}_{\text{ES}} - E^{\text{solv,neq}}_{\text{GS}} \tag{3.55}$$

$$E^{\text{solv}}_{\text{em,post-HF}} = E^{\text{gas}}_{\text{ES,post-HF}} - E^{\text{gas}}_{\text{GS,post-HF}} + E^{\text{solv}}_{\text{em,TD}} - E^{\text{gas}}_{\text{em,TD}} \tag{3.56}$$

with the energies taken at the excited state geometry.

3.6 ESIPT characterisation

In Chapter 1 (Figure 1.2), the general ESIPT process has been described, whereas I present here the different calculations steps that we have performed to characterise this process, see Figure 3.1.

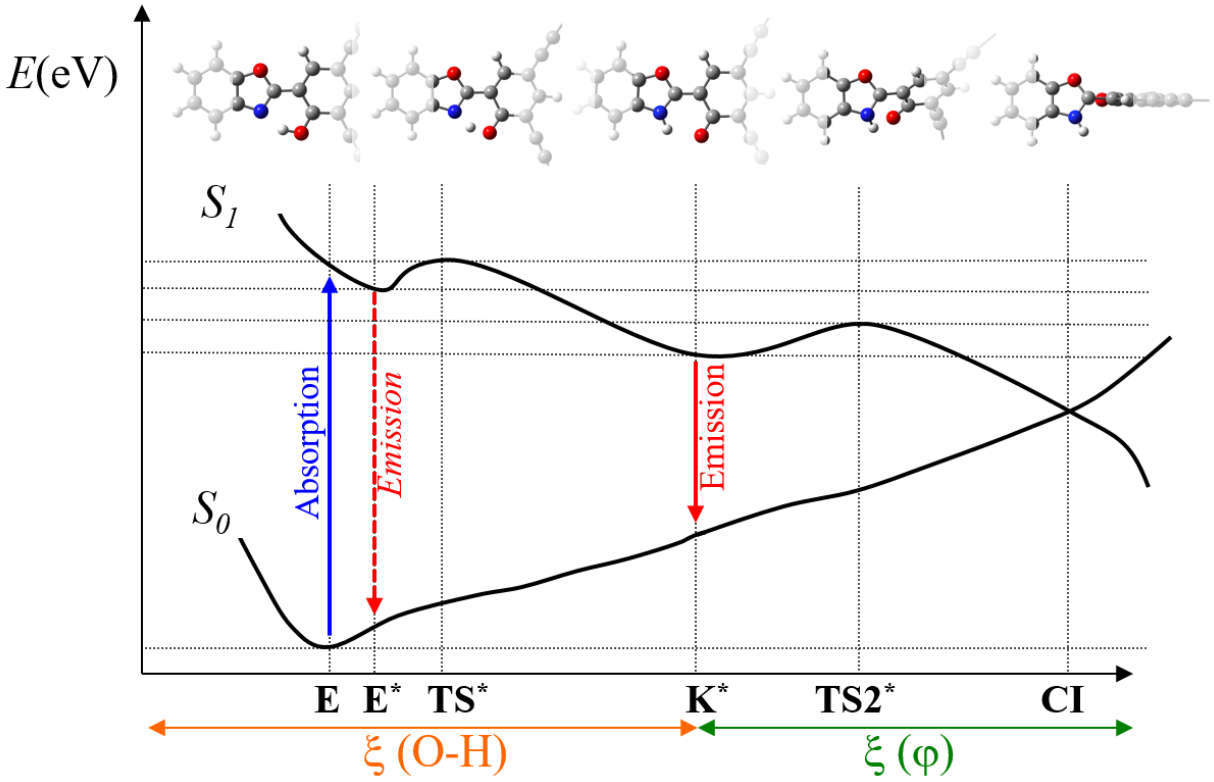

Figure 3.1: Representation of the potential energy surface (PES) during ESIPT process. The coordinates correspond to ESIPT (in orange) and the twisting between the two moieties after proton transfer (in green). For these two processes, the transition states are denotes TS* and TS2* respectively. The conical intersection (CI) point is depicted as well but was not explicitly explored during my work.

First, the enol structure at the GS is optimised. Note that each of our optimisation is coupled with frequency calculations to confirm the nature of geometry, true minima (no imaginary frequencies) or, when computed, transition state (one imaginary frequency corresponding to the expected

nuclei change). In Chapter 2, many studies on ESIPT are reviewed. From these previous works, it appears that the enol form is the most stable form at the GS, except in some very specific cases. The systems studied during my thesis in collaboration with the Strasbourg's group do not belong to this strongly exotic category. Therefore the GS nature has been assumed to be enol rather than keto without optimising the GS geometry of the latter tautomer. From the enol GS structure, I obtain vertical absorption estimates as well as electron density difference (EDD) to represent the change in the repartition of the density induced by light absorption. Next, the enol and keto tautomers are optimised at the ES and their (vertical) emission energies calculated. The relative stability of these forms is evaluated to define which one is the most stable and will likely produce fluorescence. The proton transfer can be modulated by the barrier between the two tautomers. This barrier is not estimated by a PES scan but by the optimisation of the true transition state between E^* and K^*, called TS^*. In practice, the proton is placed between its enol and keto position as starting point to perform the transition state optimisation. The imaginary frequency associated to TS^* has to represent the transfer of the proton between oxygen and nitrogen atoms. Finally, the transition state between K^* and the conical intersection, called $TS2^*$, has been optimised. The conical intersection between S_0 and S_1 is a clear multi-reference situation which can not be properly treated with TD-DFT but requires (more expensive) calculations, e.g., CASTP2.[324–326] To avoid this issue, we estimated the barrier leading to the CI by optimising a transition state which generally presents a twist between the two halves of the molecules of ca. 30–50°. With this barrier we can qualitatively evaluate the probability of non-radiative decay by reaching this CI and link it with the experimental quantum yield of fluorescence. Test calculations performed by Dr. Budzak of Matej Bel University have shown that the estimated relative energies of $TS2^*$ and K^*, as obtained with our TD-DFT base approach are in good agreement with CASPT2 values for model systems.

Chapter 4

Strasbourg's ESIPT dyes

Contents

4.1 Introduction 57

4.2 Computational details 58

4.3 Impact of the heteroatom on HBX cores 59

4.4 HBX with an ethynyl aniline substituent 63

4.4.1 Three different profiles in benzene 64

4.4.2 A challenging interpretation of the fluorescence in DCM 68

4.5 The HBO series 72

4.6 HBX with mono- or bis-(tri-*iso* -propylsilyl)acetylene in toluene 77

4.7 Substitution of a HBO scaffold by an ethynyl-tolyl moiety 81

4.7.1 A full keto emission in toluene 81

4.7.2 Keto and dual emissions with a touch of deprotonation in ethanol 86

4.8 A personal conclusion: is one approach "better" than the others? 90

4.1 Introduction

This Chapter discuss the results obtained during collaboration with the team of Dr. Gilles Ulrich in Strasbourg. This work has been realised in the framework of the GeDEMi project funded by the ANR (*Agence national de la recherche*). A description of this project which has supported my PhD grant is given in Chapter 1. Four publications have emerged from this collaboration[7–10]

Chronologically (see Figure 4.1), we have started by studying the **A** series in which mono- or bis-(trialkylsilyl)acetylene substituent are added at different positions of a 2-(2'-hydroxyphenyl)benzoxazole (HBO) scaffold. The next group of systems, the **B** series, was created to investigate the impact of the position of an ethynyl tolyl moiety on an HBO core. In the same time, the impact of the heteroatom

(X= O, S, and NH) on the ESIPT properties of those cores has been more specifically studied both experimentally and theoretically. In the **C** and **D** series, the impact on the spectral properties of HBO, 2-(2'-hydroxyphenyl)benzimidazole (HBI), and 2-(2'-hydroxyphenyl)benzothiazole (HBT) cores of an ethynyl aniline and a bis-(tri-*iso*-propylsilyl)acetylene substituent has been studied.

In this Chapter, I have chosen to present the HBX cores first, to continue with **C**, then to discuss **A** and **D** in close association, and finally to go to **B** series, which is therefore not exactly the ordering in which I performed the calculations. Of course I report the experimental data for comparisons but I did not measured myself these data, all come from Strasbourg's team.

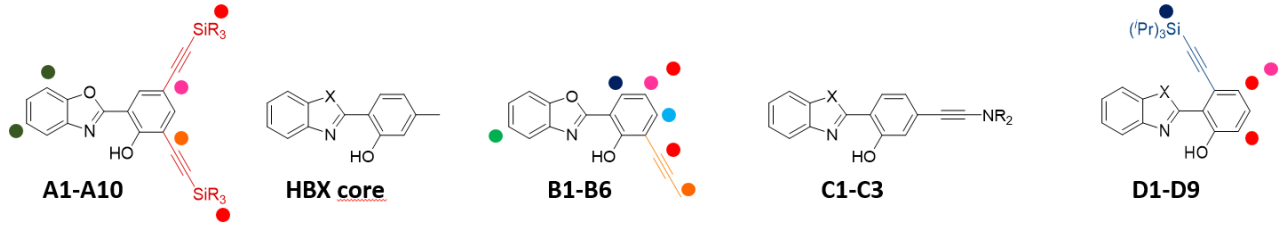

Figure 4.1: Overview of the structures discussed in the present Chapter. X= O, S, and NH. The colour points represent the positions of the investigated substitutions.

4.2 Computational details

The same global calculation protocol has been applied to all compounds presented in this Chapter: a composite approach combining the results of TD-DFT and post Hartree-Fock methods, ADC(2)[309] and CC2,[327] is used. This composite approach is described in Chapter 3: the geometries and vibrations are obtained with TD-DFT,the energies with second-order models, and the environmental effects with the PCM model. All DFT/TD-DFT calculations are performed by using Gaussian 16 software,[328] whereas all ADC(2)/CC2 calculations are performed by using Turbomole 6.4 and 6.6.[329]

For all DFT/TD-DFT calculations, we use the M06-2X *meta*-GGA exchange-correlation functional.[306] For geometry optimisations, the compact 6-31G(d) atomic basis set is used, whereas the more extended 6-311+G(2d,p) atomic basis set is applied for TD-DFT transition-energy calculations. The optimised structures of ground and excited states are confirmed by frequency calculations by computing analytical Hessian for both states, which result in no imaginary frequency for the enol GS (E), enol ES (E*), and keto ES (K*), see Figure 3.1 in Chapter 3. To achieve numerical stability in the results, we use a tightened self-consistent field (10^{-10} a.u.) and geometry optimisation (10^{-5} a.u.) convergence criteria and the so-called *ultrafine* (99,550) DFT-pruned integration grid in all our TD-DFT calculations.

For **C3-H** in DCM, a convergence problem pushed us to increase the level of theory during the optimisation and to use the so-called *superfine* DFT integration grid.

Counterpoise correction[330] calculations are realised in gas phase with the 6-311+G(2d,p) atomic basis set for **B1-B6** systems to estimate complexation energies with ethanol molecules.

Geometry optimisations and Hessian calculations of the excited states take advantage of the linear-response (LR)[320] polarizable-continuum model (PCM) approach, whereas for transition energies the more elaborate corrected LR scheme (cLR)[321] is used to take into account the change in the cavity polarization upon electron excitation by calculation of excited-state one-electron density. We also account simultaneously for both effects in the so-called LR+cLR model (see details in Chapter 3). During gradient and Hessian TD-DFT calculations, we apply the equilibrium regime of PCM solvation (slow processes), whereas absorption and fluorescence are treated as fast nonequilibrium processes. Toluene, ethanol, benzene, DMF, and DCM are used as solvent depending on the experimental solubility.

The density difference plots ($\Delta\rho$) used to characterise the nature of the enol GS, are obtained from the difference of total densities of excited and ground states (LR-PCM-TD-DFT calculation). A contour threshold of 0.0008 a.u. is used for the representation.

The *aug*-cc-pVTZ atomic basis set is used for ADC(2) and CC2 calculations. The CC2 calculations use the Resolution-of-Identity (RI) technique. Default Turbomole parameters were used to perform these calculations. CC2 optimisations are realised with the def2-TZVP atomic basis set for the GS and ES of **HBO'**, **HBT'**, and **HBI'** systems.

4.3 Impact of the heteroatom on HBX cores

All the compounds investigated with our partners are based on a HBX scaffold. HBX is a general abbreviation regrouping 2-(2'-hydroxyphenyl)benzoxazole (HBO), 2-(2'-hydroxyphenyl)benzimidazole (HBI), and 2-(2'-hydroxyphenyl)benzothiazole (HBT), see Figure 4.2a.

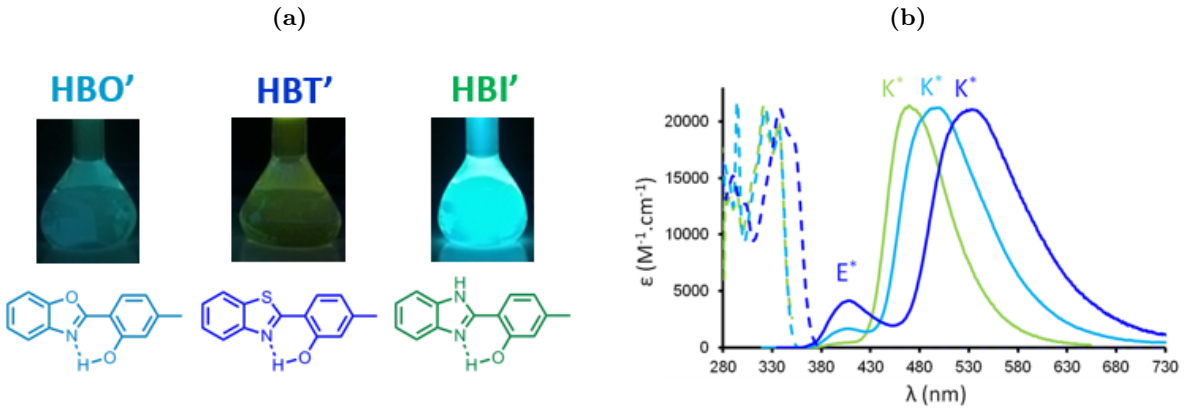

Figure 4.2: (a) Fluorescent solutions and structures of **HBO'**, **HBT'**, and **HBI'** ; (b) their measured absorption and emission spectra in toluene.

Before studying the influence of substituents on the fluorescence, it is important to explore the

properties of these cores and understand the impact of heteroatom. I have therefore performed analyses for these three cores and more precisely the three synthesised structures displayed in Figure 4.2a. Interestingly, the three systems give different spectral and photophysical properties: the influence of the heteroatom can be observed, see Figure 4.2 and Table 4.1.

Table 4.1: Experimental photophysical data in aerated toluene solution at room temperature of **HBO'**, **HBT'**, and **HBI'** and the QY of fluorescence in solid state. In bracket are reported the weak enol emission band values.

	$\lambda_{abs}{}^a$	$E_{abs}{}^b$	ε^c	$\lambda_{em}{}^a$	$E_{em}{}^b$	ΔS^d	QY^e	QY^e solid
HBO'	324	3.83	20800	(404)/500	(3.07)/2.48	10900	0.03	0.17
HBT'	339	3.66	21200	(401)/532	(3.09)/2.33	10700	0.01	0.60
HBI'	321	3.86	21200	471	2.63	9900	0.36	0.12

[a]Maximum absorption and emission wavelengths (nm) , [b]Maximum absorption and emission energies (eV), [c]Molar absorption coefficient ($M^{-1}cm^{-1}$), [d]Stokes' shifts (cm^{-1}) , [e]QY of fluorescence

Absorption

Absorption spectra of the three compounds have similar shapes with an intense band at 321–339 nm (3.86–3.66 eV), see Figure 4.2b. A small red-shift of -0.17 eV is observed for **HBT'** compared to **HBO'**, an effect nicely reproduced with CC2/LR+cLR calculations (-0.23 eV), see Tables 4.1 and 4.2.

Table 4.2: Absorption and emission energies (eV) computed in toluene of **HBO'**, **HBT'**, and **HBI'** with TD/LR+cLR, ADC(2)/LR+cLR, and CC2/LR+cLR approaches. Oscillator strengths obtained with TD-DFT are reported as well.

	HBO'				**HBT'**				**HBI'**			
	f	TD	ADC2	CC2	f	TD	ADC2	CC2	f	TD	ADC2	CC2
E	0.82	4.23	4.02	4.08	0.74	4.02	3.79	3.85	0.84	4.24	4.03	4.08
E*	0.97	3.62	3.40	3.52	0.83	3.54	3.30	3.42	0.98	3.64	3.43	3.53
K*	0.42	2.91	2.37	2.64	0.43	2.73	2.13	2.41	0.50	2.98	2.47	2.69

Electronic density difference

The electronic density difference (EDD) plots for these dyes are displayed in Figure 4.3. For the three HBX, a strong decrease of the electronic density of the hydroxyl of the phenol group (in blue) can be observed whereas an increase of the density on the nitrogen atom (in red) appears. This changes of acidity/basicity when going from the GS to ES is obviously favourable to induce the transfer of the proton from the phenol to the nitrogen atom in the excited state, and therefore to form the keto tautomer. In this condition, a (quantitative) ESIPT process should occur.

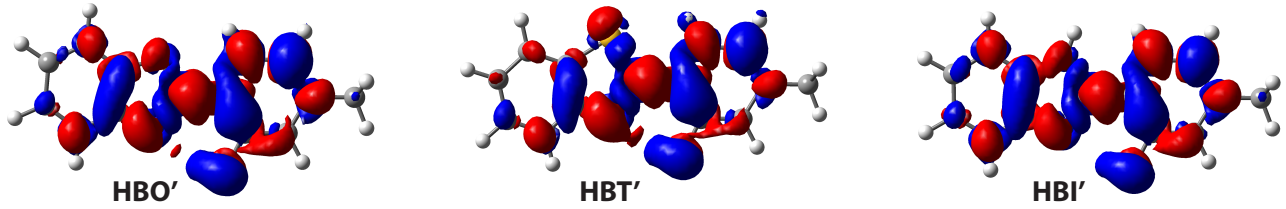

Figure 4.3: Electron density difference plots (isovalue = 0.0008 a.u.) for HBX core structures in toluene. Blue (red) regions indicate decrease (increase) of the density upon absorption of light.

Relative stabilities

The three systems exhibit a fluorescence associated to the K* form only, although a small enol band is also observed for **HBT'**. With our calculations, Table 4.3, we determine K* as the most stable form for the three compounds consistently with the experimental observation of a strong Stokes' shift. Indeed the E* → K* driving force for the ESIPT is between -0.12 eV and -0.52 eV depending on the level of theory and compound considered. In addition the E* → TS* barrier for the ESIPT is always negative (on the free energy scale) with the wavefunction approaches: ESIPT is barrierless. Nevertheless, for **HBT'**, we expected a smaller difference between E* and K* or a small barrier between both structures as a weak enol emission band appears experimentally. None of our approaches is able to reproduce such trend.

Table 4.3: Difference of free energies of E* and K*, and corresponding transition state energies for the compounds of Figure 4.2a. All values are in eV and obtained with TD-DFT/LR+cLR correction (toluene) applied at the TD-M06-2X/6-311+G(2d,p), ADC(2/)*aug*-cc-pVTZ, and CC2/*aug*-cc-pVTZ levels of theory.

	HBO'			**HBT'**			**HBI'**		
	TD	ADC(2)	CC2	TD	ADC(2)	CC2	TD	ADC(2)	CC2
E* → K*	-0.12	-0.30	-0.26	-0.30	-0.52	-0.45	-0.23	-0.38	-0.37
E* → TS*	0.04	-0.13	-0.16	-0.18	-0.32	-0.34	-0.03	-0.14	-0.18
K* → TS2*	0.17	0.09	0.03	0.05	0.04	0.01	0.16	0.24	0.13

Emission

With CC2/LR+cLR approach, we can reproduce keto emissions with a mean absolute deviation (MAD) of 0.10 eV, as compared to experiment (Table 4.2). However the deviation is bigger for E*, with errors of 0.45 eV for **HBT'** and 0.33 eV for the small enol shoulder in **HBO'** spectrum. With ADC(2)/LR+cLR, the description of the K* emission is reasonable but there is an underestimation of 0.16 eV approximately whereas the E* fluorescence is overestimated by 0.39 eV. With TD/LR+cLR, the deviation between the experiment and theory is more constant, the enol and keto emission energies are overestimated by 0.50 and 0.39 eV, respectively. Regarding these approaches, the description of the K*

seems therefore more accurate than the one of E*. If we consider the E^{0-0} between the ES and GS, which can be directly compared to the absorption and emission crossing point (AFCP), we obtain a better accuracy with our combined methods, see Table 4.4.[331,332] With post-HF/LR+cLR approaches the deviations are in the 0.10–0.18 eV range whereas with TD/LR+cLR, the errors are 0.37–0.43 eV. Clearly this illustrates the difficulties to reach accurate description of all data at the same time with a "cheap" computational approach.

The HBX cores are small enough to consider a CC2 optimisation of the ES. Unfortunately none

Table 4.4: Calculated E^{0-0} and experimental AFCP of **HBO'**, **HBT'**, and **HBI'**. All values are in eV. The E^{0-0} are obtained with TD-DFT/LR+cLR correction (toluene) applied at the TD-M06-2X/6-311+G(2d,p), ADC(2/)*aug*-cc-pVTZ, and CC2/*aug*-cc-pVTZ levels of theory. The AFCP of **HBI'** could not be properly determine with the experimental data and is therefore not reported here.

E^{0-0}	TD	ADC(2)	CC2	AFCP
HBO'	3.83	3.56	3.61	3.46
HBT'	3.74	3.44	3.49	3.31
HBI'	3.82	3.56	3.61	-

of the E* structures could be obtained with the (gas) CC2 optimisation, the systems systematically twist around the central bond. Same behaviour happens with **HBT'** K*. In order to compare the CC2 K* structures of **HBO'** and **HBI'** to TD-DFT, we optimised the K* in gas and with the same TZVP basis set in TD-DFT. Then, we used these CC2 and TD-DFT gas structures to perform the calculations of transition energies at higher levels of theory [ADC(2)/aug-cc-pVTZ, CC2/aug-cc-pVTZ and TD(gas)/6-311+G(2d,p)]. The results are reported in Table 4.5.

Table 4.5: Emission energies (eV) of **HBO'**, **HBT'**, and **HBI'** computed in gas with TD/LR+cLR, ADC(2)/LR+cLR, and CC2/LR+cLR approaches on CC2/TZVP and TD(gas)/TZVP structures.

	HBO'			**HBT'**			**HBI'**		
Geometry	TD	ADC2	CC2	TD	ADC2	CC2	TD	ADC2	CC2
TD-DFT	2.94	2.39	2.66	2.67	2.04	2.33	2.97	2.45	2.67
CC2	2.81	2.02	2.38	-	-	-	2.77	2.02	2.32

The trend of emissions obtained on the TD-DFT geometries in gas are similar as we previously reported with the LR+cLR corrections. TD-DFT has the stronger deviations and CC2 the most accurate results whereas intermediate values are obtained with ADC(2) that underestimate the experimental transition energies. The emissions obtained on the CC2 geometries are always smaller than the ones based on TD-DFT structures. An estimation of the fluorescence energies based on full post-HF calculations is not a solution for a better accuracy in the present case. The deviations obtained with ADC(2) and CC2 are increased when CC2 optimised structures are used.

Quantum yield of fluorescence

Interestingly, a strong quantum yield of fluorescence (QY) is observed in **HBI'** (36%) whereas **HBO'** and **HBT'** have much weaker emissions (QY of 3 and 1% respectively) in solution, see Figure 4.2. The three keto are all bright states, with oscillator strengths between 0.42 and 0.50, Table 4.2. Therefore the radiative path is unlikely sufficient to explain this difference. Changes of the non radiative relaxation should be mainly responsible for the difference in QY. A twist of the molecule around the central (formally double) bond linking the two parts of the ESIPT centre can lead to a conical intersection and therefore back to the GS without fluorescence,[47,333] see Chapter 3. A protective barrier of this twisted CI can be theoretically estimated (TS2*), see Figure 3.1. Different trends are obtained for this barrier depending on the selected theoretical approaches, see Table 4.3. With TD-DFT/LR+cLR the barrier is stronger for **HBO'** and **HBI'** whereas with ADC(2)/LR+cLR, only **HBI'** has a barrier of more than 0.15 eV. One would expected a similar bright emission of **HBO'** and **HBI'** based on TD results and an intermediate emission for **HBI'** based on ADC(2), but it is not in agreement with the experimental observations. Fortunately, with CC2/LR+cLR, our "best" model, the strongest barrier (0.13 eV) is determined for **HBI'** which is the most emissive dye whereas almost barrierless deexcitation ($K^* \rightarrow TS2^*$ under 0.03 eV) are predicted for the two other dyes that have QY under 3% experimentally. In this case, the CC2/LR+cLR model is clearly the most appropriate to describe the HBX core systems. With our calculations, we have no access to the information concerning the solid state, therefore no investigation have been done to explain the strong enhancement of the QY of **HBO'** and **HBT'** and the degradation of the one of **HBI'** in going from solution to solid-state matrices.

With the joint theory-experiment investigation of the HBX cores, we observe that HBT core (X=S) is more favourable to yield dual emission whereas HBO (X=O) yields keto fluorescence. At this point, the introduction of nitrogen as heteroatom (HBI) seems to be a good approach to enhance the QY in solution. Through diverse series we explore the evolution of those properties under the influence of substituents in the following of this Chapter.

4.4 HBX with an ethynyl aniline substituent

In this first series, an ethynyl aniline moiety is added in *meta* of the hydroxy in an effort to enhance the quantum yield of fluorescence. The studied structures are shown in Figure 4.4. Experimentally, the absorption spectra of HBX **C1-C3** dyes display an intense band spanning from 357 to 383 nm (3.47–3.24 eV) in benzene and DCM with absorption coefficients in the 41400–61000 $M^{-1}cm^{-1}$ range, see Figure 4.5 and Table 4.6. In benzene, three different emission profiles are obtained. A full keto emission can be observed for HBI **C2-H** and HBT **C3-H** whereas their methylamino equivalent, **C2-Me** and **C3-Me**, generate dual fluorescence. The two HBO **C1** dyes have apparently a single enol emission profile. In DCM, the shape of the spectra suggests a single emission with a Stokes' shift of 5500–7200 cm^{-1} for all dyes. As we discuss in the following, it is not that straightforward to pinpoint

the emissive tautomer in DCM by "just" looking at the spectra.

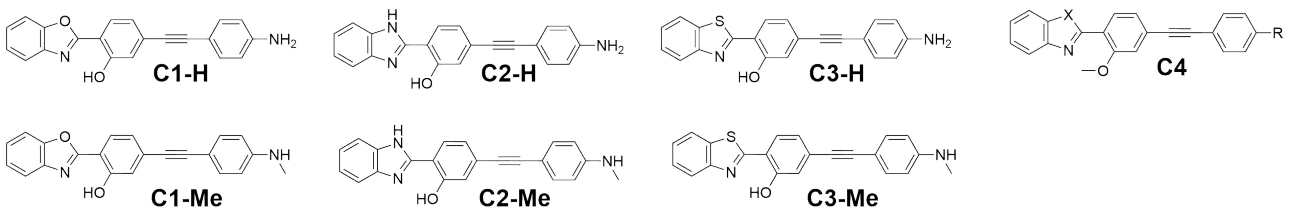

Figure 4.4: Structures of HBX **C1**–**C3** series.

The addition of a substituent to the HBX core restores high quantum yields of fluorescence for HBO and HBT based dyes, the QY changes from under 3% for the unsubstituted core in toluene to 18–76% for **C1** and **C3** in benzene. We have to notice that we compare two different solvents but the dielectric constant of the benzene and toluene are really close, $\epsilon_r = 2.3$ and 2.4, respectively, so such comparison is quite reasonable. If the luminescence of HBI remains when adding the etynyl aniline, the QY being divided per two for **C2** compared to the non-substituted case.

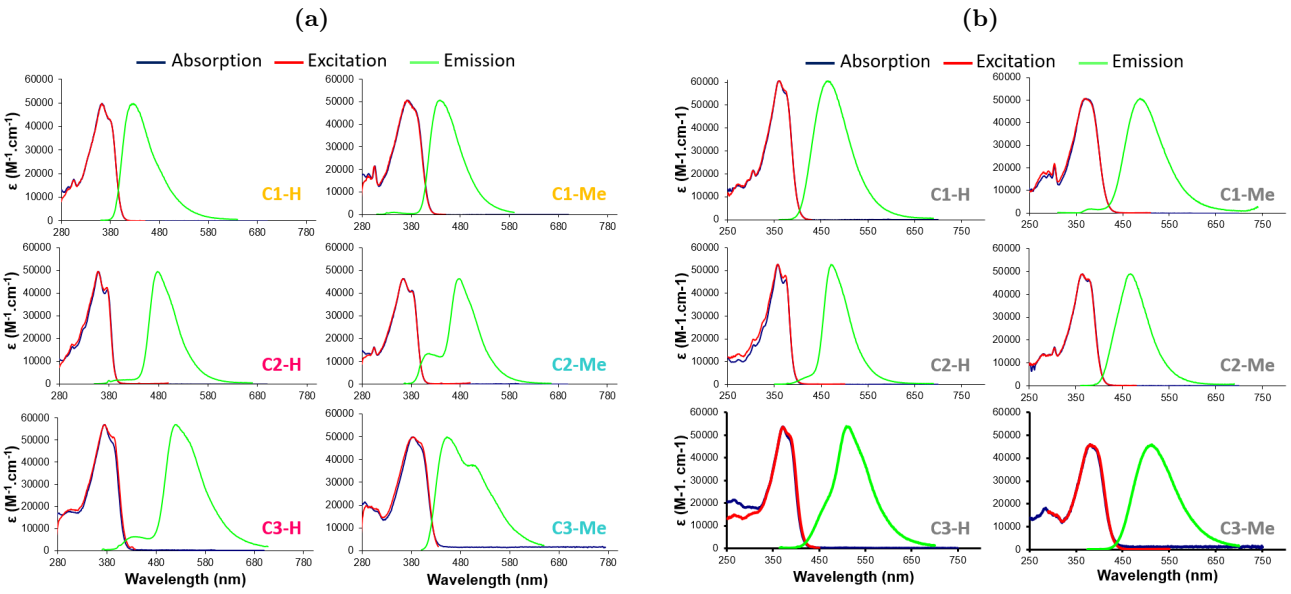

Figure 4.5: Experimental absorption and emission spectra of **C1**–**C3** measured in (a) benzene and (b) DCM.

4.4.1 Three different profiles in benzene

To build our theoretical analysis we like to start, in most of the cases, by exploring the relative stability of both enol and keto tautomers at the excited state to have an idea of their probability of co-existing. A look at the electronic density difference can also give a qualitative representation of the favourable (or not) dyes for the ESIPT to proceed. Next, we compare our fluorescence predictions to the experiment to test the accuracy of our model and the consistency with the computed relative energies of the tautomers. Finally, we try to rationalise the quantum yield of fluorescence by a comparison with the

Table 4.6: Experimental photophysical data in aerated solution at room temperature of **C1**-**C3**. See Figure 4.4 for structures representations. In brackets are reported the weak enol emission observed.

solvent	$\lambda_{abs}{}^a$	$E_{abs}{}^b$	ε^c	$\lambda_{em}{}^a$	$E_{em}{}^b$	ΔS^d	QY^e	τ^f
				C1-H				
Benzene	364	3.41	50000	430	2.88	4300	0.62	0.95
DCM	360	3.44	61000	465	2.67	6500	0.68	1.53
				C1-Me				
Benzene	372	3.33	51100	438	2.83	4100	0.76	1.1
DCM	372	3.33	50500	487	2.55	6400	0.68	2.02
				C2-H				
Benzene	359	3.45	41400	478	2.59	5600	0.15	0.92
DCM	357	3.47	46100	471	2.63	5500	0.15	0.82
				C2-Me				
Benzene	364	3.41	46000	420/480	2.97/2.60	3700	0.17	0.75
DCM	364	3.41	49300	467	2.65	6200	0.36	0.99
				C3-H				
Benzene	373	3.32	57000	(435)/519	(2.85)/2.39	7100	0.18	-
DCM	371	3.34	53700	509	2.44	7200	0.18	-
				C3-Me				
Benzene	383	3.24	49800	455/509	2.72/2.44	4000	0.20	-
DCM	380	3.26	45900	513	2.42	6800	0.30	-

[a]Maximum absorption and emission wavelengths (nm) , [b]Maximum absorption and emission energies (eV), [c]Molar absorption coefficient ($M^{-1}cm^{-1}$), [d]Stokes' shifts (cm^{-1}) , [e]QY of fluorescence, [f]fluorescence lifetime (ns)

protective barrier between K^* and the conical intersection. The relative stabilities of **C1**–**C3** dyes, calculated in benzene, are reported in Table 4.7. The theoretical fluorescence of these compounds can be found in Table 4.8.

Relative Stabilities

If we have a look at the TD/LR+cLR calculations only, the enol form is systematically the most stable tautomer in the ES and should be the emitting form, see Table 4.7. However it is not the case, dual and keto emissions are observed in benzene as illustrated in Figure 4.5a. By including CC2 corrections, we are able to obtain a better match between experiment as the relative energies allow to predict the measured trends more accurately.

C1-Me and **C1-H** have their enol forms determined as the most stable by respectively 0.12 and 0.28 eV compared to the keto tautomer, with a positive barrier of more than 0.05 eV to reach the keto tautomer. This means that the back ESIPT is barrierless and that the K^* tautomer is unstable. This

Table 4.7: Difference of free energies of E* and K*, and corresponding transition state energies for **C1**–**C3** dyes in benzene. All values are in eV and obtained with TD-DFT/LR+cLR correction applied at the TD-M06-2X/6-311+G(2d,p), ADC(2)/aug-cc-pVTZ, and CC2/aug-cc-pVTZ levels of theory. See Figure 4.4 for structure representations.

	TD	ADC(2)	CC2	TD	ADC(2)	CC2	TD	ADC(2)	CC2
		C1-H			**C2-H**			**C3-H**	
E* → K*	0.36	0.08	0.12	0.16	-0.09	-0.08	0.18	-0.10	-0.03
E* → TS*	0.38	0.08	0.05	0.21	-0.03	-0.07	0.19	-0.07	-0.08
K* → TS2*	0.30	0.19	0.15	0.30	0.34	0.31	0.15	0.12	0.11
		C1-Me			**C2-Me**			**C3-Me**	
E* → K*	0.51	0.24	0.28	0.27	0.04	0.05	0.26	0.00	0.06
E* → TS*	0.47	0.20	0.17	0.26	0.03	-0.01	0.21	-0.04	-0.05
K* → TS2*	0.25	0.14	0.12	0.29	0.33	0.31	0.17	0.14	0.13

is in line with the observation of single emission with a small Stokes' shift attributed to the E* form in Figure 4.5a. For **C2-H** and **C3-H** it is the keto form which is the most stable by -0.08 and -0.03 eV, respectively, and this time the forward ESIPT transition should be barrierless. It is consistent with the observation of a quantitative keto emission and the absence of enol fluorescence in the experimental spectra. Indeed to observe a dual emission, the enol and keto tautomers have to be close in energy without a strong barrier separating them. This is the case for both **C2-Me** and **C3-Me**: the enol is the most stable by 0.05 eV only and no significative barrier blocks the transfer, which fits reasonably experiment.

Electronic density difference

With the EDD, we can observe a strong delocalisation of the density over the full system, see Figure 4.6. The donor character of the aniline moiety is clear with a strong loss of density (in blue) on this part of the system. By taking a look at the EDD, the conditions seem not so favourable for the ESIPT to occur. The nitrogen atom gains density but the loss of density on the hydroxy is weak in every cases. For **C1** in which the emission comes from the enol form, this is consistent to have a blocked ESIPT. But in the two other dyes the ESIPT is occurring experimentally which is not obvious from the EDD, highlighting the limits of such representation.

Spectroscopic properties

Let me now discuss the theoretical spectroscopic properties summarised in Table 4.8. **C1-H** and **C1-Me** have an experimental enol emission profile well reproduced by the relative energies. For the calculated emissions, the TD/LR+cLR approach gives the smallest deviations to experiment when taking the keto emission which is obviously inconsistent. In contrast, with post-HF/LR+cLR, the

largest deviations are obtained with the keto structure which is consistent with the measurements. With ADC(2), the three trends (enol, dual, and keto) of the dyes are reproduced but the energies of the keto emissions are underestimated compared to their experimental equivalents. Indeed, the ADC(2)/LR+cLR method seems to reproduce well the enol fluorescence (**C1**, **C2-Me**, and **C3-Me**) with deviations around 0.05 eV but to underestimate the keto one by -0.1 to -0.2 eV (**C2** and **C3**). Eventually, with CC2, the keto character of **C2-H** and **C3-H** emissions is clearly highlighted by deviations of less than 0.1 eV compared to the experimental data. For their methylamine counterparts with dual emissions, enol and keto transitions energies have a deviation of less than 0.15 eV with an accurate attribution of the emission bands. All these data confirm the quality of the CC2/LR+cLR approach in the present case. In contrast to ADC(2), "constant" deviations ranging from 0.06 to 0.17 eV are observed with CC2 independently of the nature of the system.

Table 4.8: Vertical emission energies (eV) in benzene of E* and K* forms of **C1**–**C3** with TD/LR+cLR, ADC(2)/LR+cLR, and CC2/LR+cLR approaches and difference with experimental fluorescence maxima. ADC stands for ADC(2). For **C2-Me** and **C3-Me**, the difference is computed between the first experimental band (smallest Stokes' shift) and E* theoretical prediction whereas the second band is associated with theoretical K*.

	TD	ADC	CC2	ΔTD	ΔADC	ΔCC2	TD	ADC	CC2	ΔTD	ΔADC	ΔCC2
				C1-H						**C1-Me**		
E*	2.98	2.96	3.05	0.10	0.07	0.17	2.93	2.89	2.97	0.10	0.06	0.14
K*	2.87	2.41	2.64	-0.01	-0.47	-0.25	2.88	2.43	2.65	0.05	-0.40	-0.18
				C2-H						**C2-Me**		
E*	3.06	3.04	3.13	0.46	0.45	0.53	3.00	2.97	3.05	0.05	0.02	0.10
K*	2.90	2.46	2.65	0.31	-0.13	0.06	2.90	2.47	2.65	0.32	-0.12	0.07
				C3-H						**C3-Me**		
E*	2.90	2.84	2.93	0.51	0.45	0.54	2.85	2.78	2.86	0.12	0.05	0.14
K*	2.75	2.25	2.49	0.36	-0.14	0.10	2.75	2.26	2.49	0.31	-0.18	0.06

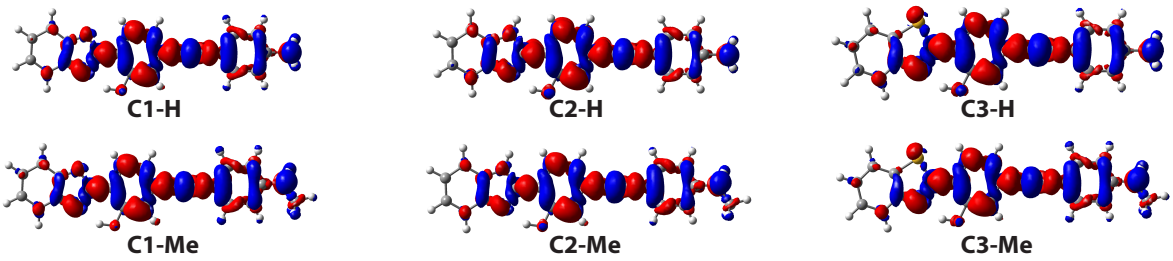

Figure 4.6: Electron density difference plots (isovalue = 0.0008 a.u.) of **C1**–**C3** structures in benzene. Blue (red) regions indicate decrease (increase) of the density upon absorption of light.

Interestingly, the substituent affects more significantly the emission energy of the enol band than the position of its keto counterpart. Indeed the dyes substituted by a methylamine group have their enol band experimentally red-shifted by -0.05 eV in **C1** and -0.13 eV for **C3** as compared to the amino dyes For the keto forms blue-shifts of 0.01 and 0.05 eV are measured for **C2** and **C3**, respectively. This effect is even more marked in our theoretical results. The enol emission energy is systematically decreased by -0.07 eV between NH_2 and NHMe substitutions whereas the keto emission remains unchanged, see Table 4.8. The computed excited state dipole moment of the enol form are significantly larger (11.7–13.6 Debye) than the one of the keto tautomers (3.8-5.6 D) and this stronger polarity explains the stronger impact of terminal group on the E^* than K^* fluorescence. This large dipole of the E^* form is consistent with a charge-transfer (CT) character of the electronic transition, see Figure 4.6.

Protective barriers to the CI between 0.11 and 0.31 eV (CC2/LR+cLR) have been computed, consistent with the measured high quantum yield of fluorescence (15-76%), see Table 4.7. The QY trend is however not reproduced. **C2** and **C3** dyes have similar QY (15–17%) but the barrier is higher for the first dye (0.3 and 0.1 eV respectively). **C1** is the most emissive dye (QY: 62–76%) but does not show the largest barrier, this is however irrelevant as this dye is emitting through its enol form and therefore the emission is not affected by the path to reach the CI from the K^*.

4.4.2 A challenging interpretation of the fluorescence in DCM

Although the analysis of the relative stabilities is an interesting starting point, we are opening the discussion with the optical properties for this specific case because we think this is more enlightening in the present case.

Spectroscopic properties

In DCM, the fluorescence is observed between 2.42 and 2.67 eV experimentally, see Figure 4.5b. For **C1-H** and **C1-Me**, the fluorescence energies decrease by -0.21 and -0.28 eV, respectively when switching from benzene to DCM, see Table 4.9. This could be the result of a change of tautomer (a keto emisison), or of a strong solvatochromic effect for the enol band due to the aforementioned CT character: we have indeed found very large ES dipole moment for E^*. For **C2** and **C3** when moving in DCM, the emission is weakly changed compared to the keto fluorescence in benzene, and can be attributed to a keto form or, once again, to a strongly red-shifted E^* emission. From these experimental observation we are not able to conclude on the nature of the fluorescence and we will try to rationalise it with the help of theoretical calculations!

With TD/LR+cLR, the enol form has an emission smaller than its keto tautomer (Table 4.10) which is unusual for an ESIPT system and illustrates the very high polarity of the E^* isomer. Indeed

Table 4.9: Experimental and CC2/LR+cLR energy difference between the E* and K* emissions in benzene and undefined DCM fluorescence. All results are in eV.

	Experimental		CC2/LR+cLR			
	E_{benz}-X_{DCM}	K_{benz}-X_{DCM}	E_{benz}-E_{DCM}	K_{benz}-K_{DCM}	E_{benz}-K_{DCM}	K_{benz}-E_{DCM}
C1-H	0.21	-	0.31	0.07	0.48	-0.10
C1-Me	0.28	-	0.31	0.07	0.39	-0.01
C2-H	-	-0.04	0.26	0.07	0.55	-0.22
C2-Me	0.32	-0.05	0.26	0.06	0.46	-0.14
C3-H	(0.41)	-0.05	0.30	0.08	0.52	-0.14
C3-Me	0.30	0.02	0.31	0.07	0.44	-0.06

Table 4.10: Vertical emission energies (eV) in DCM of E* and K* forms of **C1**–**C3** with TD/LR+cLR, ADC(2)/LR+cLR and CC2/LR+cLR approaches and difference with experimental fluorescence. ADC stands for ADC(2).

	TD	ADC	CC2	ΔTD	ΔADC	ΔCC2	TD	ADC	CC2	ΔTD	ΔADC	ΔCC2
				C1-H						**C1-Me**		
E*	2.67	2.64	2.74	0.01	-0.02	0.07	2.61	2.57	2.66	0.07	0.02	0.11
K*	2.80	2.35	2.57	0.14	-0.31	-0.10	2.81	2.36	2.58	0.26	-0.18	0.03
				C2-H						**C2-Me**		
E*	2.79	2.78	2.87	0.16	0.15	0.23	2.74	2.71	2.79	0.08	0.05	0.14
K*	2.82	2.40	2.58	0.19	-0.23	-0.05	2.83	2.40	2.59	0.17	-0.25	-0.07
				C3-H						**C3-Me**		
E*	2.60	2.53	2.63	0.16	0.10	0.19	2.54	2.46	2.55	0.12	0.05	0.13
K*	2.66	2.18	2.41	0.22	-0.25	-0.02	2.66	2.19	2.42	0.24	-0.23	0.00

the TD/gas emissions calculated on the same geometries give the expected trend: a smaller K* fluorescence energy than E* energy. As an example, here are the vertical emission energies of E* and K* respectively for **C1-H** in gas: 3.16 and 2.95 eV, and with solvent correction LR: 2.78 and 2.82 eV, cLR: 2.96 and 3.00 eV, and LR+cLR: 2.67 and 2.80 eV. The impact of the solvent correction is huge for the enol form that possess a strong ES dipole moment (17.1 D as compared to 4.5 D for the keto tautomer). With the addition of post-HF corrections, we come back to the general trend for ESIPT systems, the K* emission is red-shifted compared to E* but with quite small differences with according to CC2. We have found earlier that TD/LR+cLR and ADC(2)/LR+cLR approaches are describing with larger errors the keto emissions than the enol ones in benzene. In the present case we need to make the difference between E* and K* emission but we don't have clear-cut experimental fluorescence data to use. This is why we discuss only the CC2/LR+cLR results below as this method yielded the most consistent trends.

With CC2, the computed E* and K* energies surround the experimental fluorescence and the deviation is smaller when considering the K*, but for **C1-H**. This would naively hint at K* emission. However, the deviations of CC2 K* values compared to experimental peak positions are mostly negative whereas the K* fluorescence energy is overestimated by 0.1–0.2 eV in benzene. If such overestimation is considered here, then the computed enol emission is better matching with the experimental fluorescence.

We have discussed above (in benzene) the impact of the substituent on the luminescence, and highlighted its strongest effect on the E*. Therefore a strong change between the emission of C-H and C-Me species could be linked to an enol nature for the fluorescence. Experimentally this behaviour is well observed for **C1** with a shift of -0.12 eV, letting us suppose that we are indeed in presence of E* emission for the **C1** species, consistent with their emissions in benzene and the large measured QY. For **C2** and **C3**, the shift is still negative but smaller (-0.02 eV) and it is therefore tricky to conclude on this basis. At this stage we are honestly a bit stuck in our analyses.

Relative stabilities

The relative stabilities in DCM indicate that the enol ES is the most stable tautomer, with a difference of 0.1 eV or more with the K* except for **C2-H**, see Table 4.11. For this latter compound the stability of the enol and keto tautomers is not clearly defined, TD-DFT, ADC(2) and CC2 yielding different conclusions. With TD-DFT, the enol form of **C2-H** is defined as the most stable tautomer (0.22 eV) as the other dyes whereas the two wavefunctions models are predicting almost equal K* and E* energies (-0.02 eV with ADC(2) and 0.00 eV with CC2). On such basis, it seems reasonable to conclude at E* for **C1** and **C3** at the very least.

Table 4.11: Difference of free energies of E* and K*, and corresponding relative transition state energies for dyes **C1**-**C3** in DCM. All values are in eV and obtained with TD/LR+cLR correction applied at the TD-M06-2X/6-311+G(2d,p), ADC(2)/aug-cc-pVTZ, and CC2/aug-cc-pVTZ levels of theory. See Figure 4.4 for structure representations.

	TD	ADC(2)	CC2	TD	ADC(2)	CC2	TD	ADC(2)	CC2
		C1-H			**C2-H**			**C3-H**	
E* → K*	0.49	0.23	0.27	0.22	-0.02	0.00	0.30	0.05	0.12
E* → TS*	0.46	0.17	0.13	0.26	0.01	-0.03	0.32	0.06	0.04
K* → TS2*	0.29	0.17	0.14	0.24	0.31	0.29	0.10	0.08	0.07
		C1-Me			**C2-ME**			**C3-Me**	
E* → K*	0.51	0.28	0.32	0.31	0.10	0.11	0.31	0.08	0.14
E* → TS*	0.41	0.16	0.11	0.29	0.07	0.02	0.25	0.02	0.00
K* → TS2*	0.30	0.17	0.14	0.27	0.33	0.31	0.13	0.19	0.11

Conclusions

Lets us now put all those data together. For more clarity, the conclusions obtained with each criteria discussed above are summarised in Table 4.12. If we have faith in CC2/LR+cLR model, we have coherent results between the relative stability and emission in benzene and DCM. First in the non-polar solvent, the results are rather clear. In DCM based on the standard deviations due to approximations of the CC2/LR+cLR model and on the relative stabilities of the dyes, the fluorescence of the six dyes can be attributed to the enol form. The strong Stokes' shift experimentally reported would be, in this hypothesis, due to the solvatochromic behaviour of E^* consistently with its large ES dipole moment (15.4–17.1 D). For **C1**, this attribution is also consistent with the auxochromatic effect on the emission. For **C2** and **C3** we have however to underline that even if the deviation "trend" obtained with CC2/LR+cLR is in favour of E^* emission, the smallest deviation with the experimental luminescence is with K^* and the relative stability of **C2-H** does not indicate any tautomer as the most stable. In this framework, the conclusion of frustrated ESIPT and therefore enol emission in DCM have to be carefully advanced. Extra experimental tests would be welcome to build a more robust conclusion on the nature of the ES. Perhaps the synthesis of the system with frustrated ESIPT as dye **C4** in Figure 4.4 could help, as the emission spectrum of a frustrated ESIPT system should be closest to the one of an enol emitting system.[15] We have confirmed this hypothesis for **C1-H**, the theoretical frustrated ESIPT emission is predicted to be 3.00 eV and 2.70 eV in benzene and DCM respectively whereas the E^*/K^* emissions of the standard dye are 2.98/2.87 eV and 2.67/2.80 eV. Therefore depending of the gap between this new system of reference and the enigmatic one, we could conclude more definitely on the nature of the fluorescence.

Table 4.12: Tautomer attributed to the emission of **C1-C3** dyes in benzene and DCM, based on: E^*/K^* relative stability (Stab.), systematic CC2 deviation of 0.1–0.2 eV with experiment (Em. trend), smallest deviation between CC2 and experiment (Δ_{Em}), and experimental difference of emission depending on terminal amino moiety (Δ_{H-Me}).

	benzene				**DCM**			
	Stab.	Em. trend	Δ_{Em}	Δ_{H-Me}	Stab.	Em. trend	Δ_{Em}	Δ_{H-Me}
C1-H	E	E	E	E	E	E	E	E
C1-Me	E	E	E	-	E	E	K	-
C2-H	K	K	K	K	?	E	K	?
C2-Me	D	D	D	-	E	E	K	-
C3-H	K	K	K	(D) K	E	E	K	?
C3-Me	D	D	D	-	E	E	K	-

4.5 The HBO series

New ESIPT emitters based on the HBX scaffold, mainly HBO, incorporating mono- or bis-(trialkylsilyl)-acetylene substituent(s) have been synthesised through an expedite two-steps synthetic route by our collaborators of the University of Strasbourg. Structures of this series are sketched in Figure 4.7. The

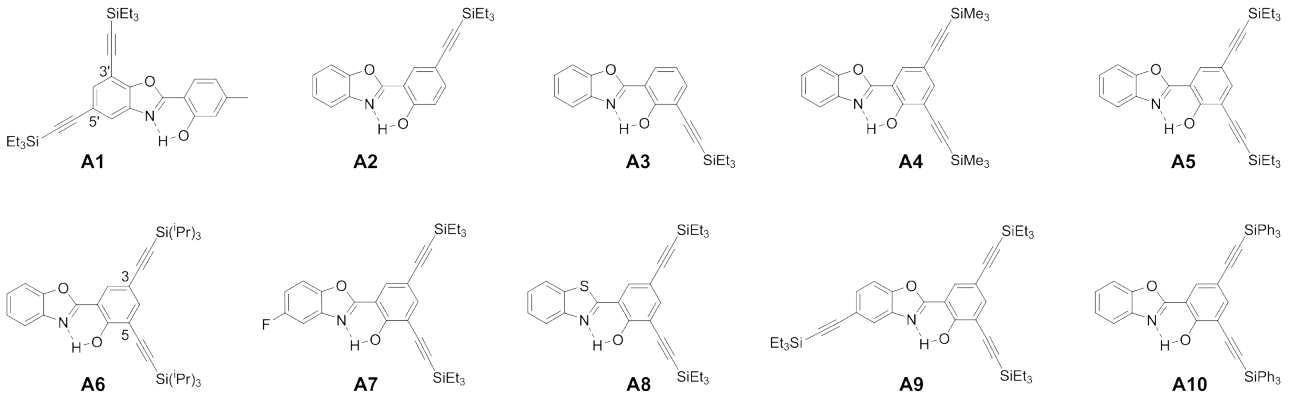

Figure 4.7: Structures of substituted HBX scaffolds presenting mono- or bis-(trialkylsilyl)acetylene segments.

absorption spectra of HBX dyes **A1**–**A10** all exhibit an intense band spanning from 340 to 378 nm (3.65–3.28 eV) with absorption coefficients in the 11700–34800 $M^{-1}cm^{-1}$ range, see Table 4.13 and Figure 4.8. In toluene, upon excitation an intense single emission band appears in the 508–570 nm (2.44–2.18 eV) range, see Figure 4.8. This band is a clear proof of ESIPT and it can be assigned to the K* tautomeric species. Therefore ESIPT appears to be a quantitative process in all dyes displayed in

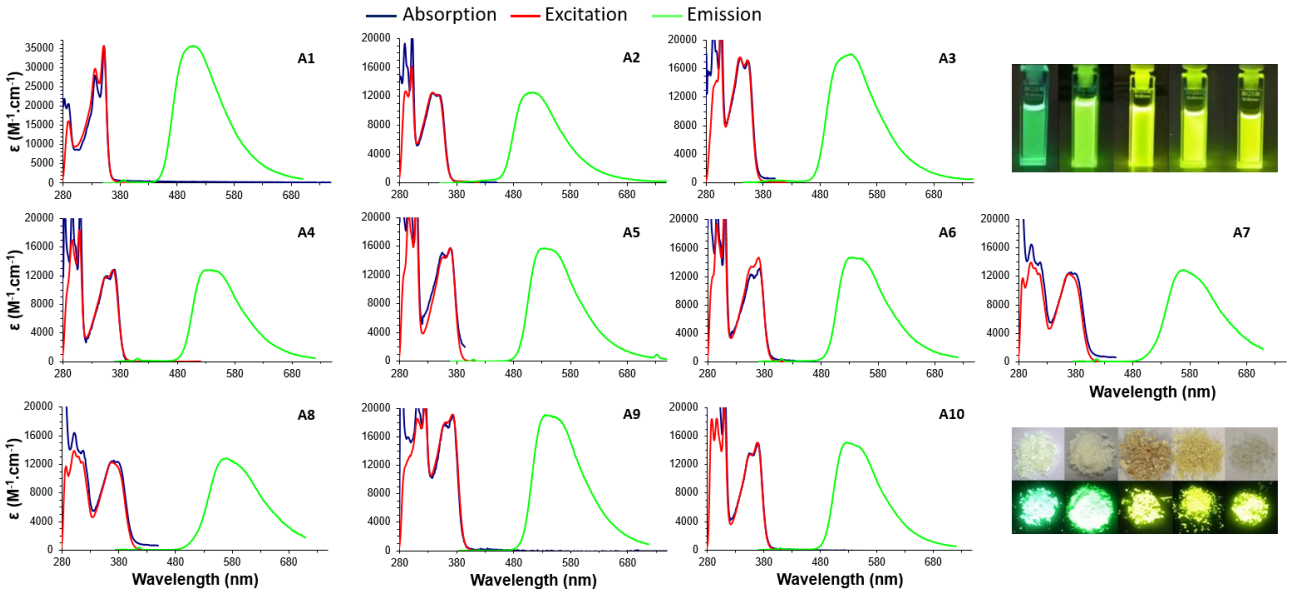

Figure 4.8: Experimental absorption and emission spectra of **A1**-**A10** in toluene. Photographs of **A2**-**A5** (from left to right) under irradiation in toluene solution, and as powders under daylight (top) and under irradiation (bottom).

Figure 4.7, leading to red-shifted single emitters with Stokes' shifts larger than 8000 cm^{-1}. This is confirmed by our calculations discussed below. The fluorescent lifetimes are all monoexponential, in the nanosecond range, confirming the singlet nature of the excited-state. Importantly, the solution-state

Table 4.13: Experimental photophysical data in aerated toluene solution at room temperature of **A1**–**A10**.[7,9,10] See Figure 4.7 for structures representations.

	$\lambda_{abs}{}^a$	$E_{abs}{}^b$	ε^c	$\lambda_{em}{}^a$	$E_{em}{}^b$	ΔS^d	QY^e	τ^f
A1	352	3.52	34800	508	2.44	8700	0.05	0.5
A2	345	3.59	11900	513	2.42	9500	0.11	3.9
A3	340	3.65	17000	538	2.30	10800	0.28	2.9
A4	368	3.37	12800	539	2.30	8600	0.49	3.9
A5	371	3.34	12500	537	2.31	8300	0.38	3.7
A6	371	3.34	13800	535	2.32	8300	0.32	3.8
A7	373	3.32	11700	551	2.25	8700	0.43	3.3
A8	378	3.28	12000	570	2.18	8900	0.22	2.5
A9	374	3.32	19200	535	2.32	7900	0.34	3.6
A10	370	3.35	15000	530	2.34	8200	0.52	4.5

[a]Maximum absorption and emission wavelengths (nm) , [b]Maximum absorption and emission energies (eV), [c]Molar absorption coefficient ($M^{-1}cm^{-1}$), [d]Stokes' shifts (cm^{-1}) , [e]QY of fluorescence, [f]fluorescence lifetime (ns)

fluorescence QY of ESIPT emitters HBX **A2**–**A10** are found to be drastically enhanced compared to the unsubstituted HBX reported and discussed in Section 4.3 which feature QY between 1 and 2%. Indeed, with the notable exception of HBO **A1**, all HBX emitters display high QY in toluene (11–52%), highlighting the beneficial influence of the 3 and 5 ethynyl substitutions of the phenol ring on the optical properties.

These fluorophores remain highly emissive in the solid-state, as dispersed in KBr pellets or doped in PMMA films (QY up to 77% and 60% respectively). Such behaviour indicates that this kind of system is very promising and attractive in the context of aggregation induced light enhancement such as random lasing.[36,44,211] This collaborative work has been published in *Phys. Chem. Chem. Phys.*,[7] *Dyes Pigm.*,[9], and *Nanomaterials*[10] and my contributions are more specifically described below.

In order to shed more light onto the emission spectra of HBX **A1**–**A10** and probe the nature of the ES, all systems have been studied with *ab initio* approaches, considering toluene as medium. Table 4.14 lists the free energy difference calculated with TD-DFT and corrected with ADC(2). In Table 4.15 absorption and emission energies at the TD/LR+cLR and ADC(2)/LR+cLR are reported. Note that CC2 calculations were beyond reasonable computational reach for theses systems when these calculations have been performed.

Relative stabilities

First, for all dyes except **A1**, the K* form is more stable than the E* form by more than 0.2 eV, which hints at a quantitative ESIPT process in all cases.[12] Only the K* emission should be observed, a conclusion consistent with experimental observation where a single emission band with a large Stokes's shift is observed, see Figure 4.8. For **A1**, depending of the model used, we can predict a possible dual emission or a pure keto fluorescence. With TD/LR+cLR, K* is more stable than E* by 0.04 eV only and a small barrier of 0.10 eV has to be crossed which would indicate dual emission but as for the other dyes, K* is more stable by (0.23) eV with a barrierless E* → K* transition when applying the ADC(2)/LR+cLR method. For **A1**, the ADC(2)/LR+cLR profile therefore clearly provides the best match with experiment highlighting the limits of TD-DFT. In the electronic density difference plots, Figure 4.9, one also notes the usual topology favourable for ESIPT with loss and gain of densities on the H donor and acceptor, respectively.

Table 4.14: Difference of free energies of E* and K*, and corresponding transition state energies for dyes **A1**–**A10** (Figure 4.7). All values are in eV and obtained with TD-DFT/LR+cLR correction applied at the TD-M06-2X/6-311+G(2d,p) and ADC(2)/aug-cc-pVTZ levels of theory.

	TD	ADC(2)	TD	ADC(2)	TD	ADC(2)	TD	ADC(2)
	A1		**A2**		**A3**		**A4**	
E* → K*	-0.04	-0.23	-0.19	-0.26	-0.22	-0.30	-0.22	-0.26
E* → TS*	0.10	-0.07	-0.06	-0.14	-0.02	-0.10	-0.01	-0.08
K* → TS2*	0.19	0.11	0.22	0.12	0.27	0.18	0.27	0.20
	A5		**A6**		**A7**[a]		**A8**	
E* → K*	-0.24	-0.29	-0.26	-0.31	-0.21	-0.26	-0.25	-0.35
E* → TS*	-0.04	-0.11	-0.03	-0.09	-0.04	-0.03	-0.03	-0.05
K* → TS2*	0.32	0.23	0.31	0.23	-	-	0.13	0.20
	A9[a]		**A10**[a]					
E* → K*	-0.16	-0.21	-0.31	-0.35				

[a]Transition states could not be optimised (only TS2* for **A7**).

Absorption

Secondly, a reasonable agreement between theoretical TD/LR+cLR and experimental absorption and emission energies is found, see Table 4.15. HBO dye **A1** displays a significantly blue-shifted absorption band as compared to other HBX dyes (3.52 eV vs. 3.28–3.37 eV, for HBO **A1** and HBX **A4**–**A10**, respectively), see Table 4.13. This shift is also found theoretically with TD/LR+cLR (4.04 eV vs. 3.74–3.90 eV, for HBO **A1** and HBX **A4**–**A10**, respectively), see Table 4.15. The absorption energies of mono-substituted HBO dyes **A2** and **A3** are hypsochromically shifted as compared to their bis–substituted analogues **A4**–**A10** (3.59–3.65 eV for HBO **A2**–**A3**). Indeed, **A2** and **A3** are the most blue-shifted dyes of this series and this hold both experimentally and theoretically. These observations

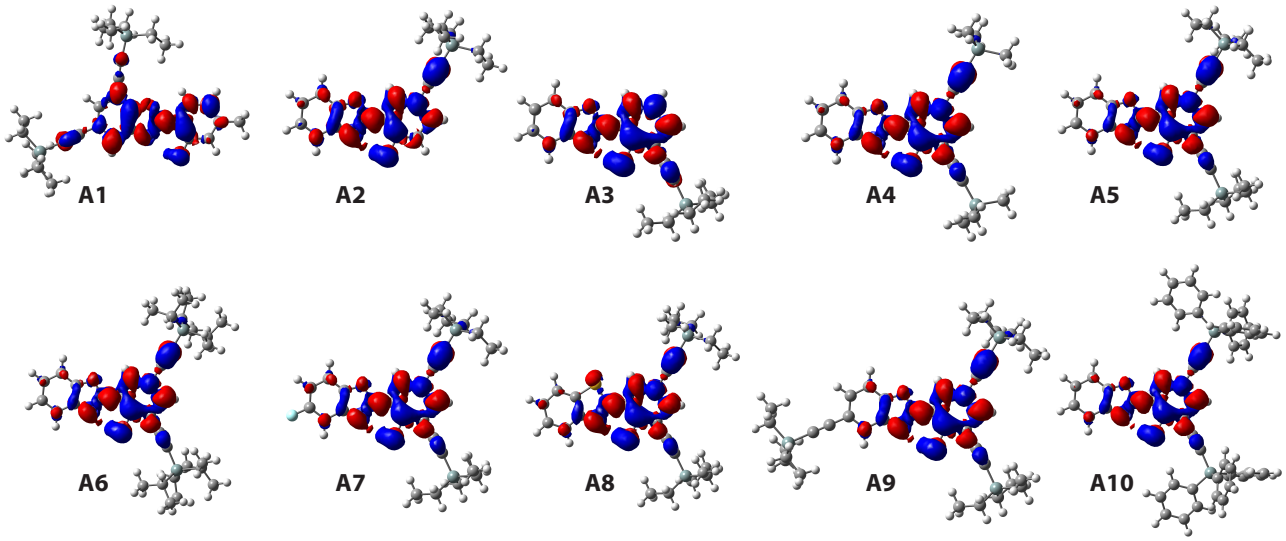

Figure 4.9: Electron density difference plots (isovalue = 0.0008 a.u.) of **A1**–**A10** structures in toluene. Blue (red) regions indicate decrease (increase) of the density upon absorption of light.

highlight the fact that a second trialkylsilylalkynyl unit is necessary to induce a red-shifted absorption regardless of the position of the first unit on the π-conjugated molecular core. Among the 3,5 bis-substituted series, no drastic change is observed in terms of (shape and) position of the absorption band upon increasing the length of the alkyl chain (Me, Et, ^{i}Pr, or Ph). Indeed, a variation of 0.05 eV or 0.03 eV only is seen both experimentally and theoretically (TD/LR+cLR). This is consistent with the EDD plots of Figure 4.9: these alkyl groups do not play a direct role in the absorption process, as expected.

With ADC(2), these absorption effects (blue-shift of **A1**–**A3** and similar absorption independently of the alkyl chain length) are also well described. The mean absolute, maximum, and minumum deviations are actually smaller with ADC(2) than TD-DFT: with ADC(2)/LR+cLR we obtain a MAD of 0.30 eV; MaxD of 0.34 eV and MinD of 0.20 eV, whereas with TD/LR+cLR we obtain MAD = 0.51 eV, MaxD = 0.55 and MinD = 0.42 eV.

Emission

The huge deviations between the experimental and calculated E* emissions confirm the keto nature of the observed fluorescence. Indeed the mean absolute deviation obtained with TD-DFT or ADC(2) as compared to experiment is much larger for E*, 1.10/0.84 eV, than for K*, 0.34/0.12 eV. With ADC(2), the keto fluorescence is underestimated, the MaxD and MinD being -0.16 eV and -0.07 eV, respectively. Larger deviations are obtained with TD-DFT that overestimates the emission energies (MaxD = 0.43 eV, MinD = 0.28 eV). We choose to use the TD/LR+cLR approaches to discuss the luminescence in the following. We prefer to overestimate the emission energies rather to underestimate them, as with ADC(2). However ADC(2)/LR+cLR could also been used, all the effects described below can also be

Table 4.15: Vertical absorption and emission energies (eV) in toluene of the various tautomer forms of **A1**–**A10** with the LR+cLR solvent model and TD-DFT, ADC(2), and CC2 transition energies. Oscillator strengths obtained with TD-DFT are reported as well.

	f	TD	ADC(2)	f	TD	ADC(2)	f	TD	ADC(2)	f	TD	ADC(2)
		A1			**A2**			**A3**			**A4**	
E	0.90	4.04	3.86	0.47	4.06	3.85	0.49	4.07	3.85	0.48	3.89	3.68
E*	1.07	3.55	3.35	0.57	3.51	3.28	0.72	3.53	3.28	0.53	3.38	3.15
K*	0.53	2.84	2.31	0.45	2.79	2.33	0.56	2.70	2.23	0.51	2.64	2.20
		A5			**A6**			**A7**			**A8**	
E	0.48	3.88	3.67	0.48	3.87	3.66	0.48	3.85	3.64	0.49	3.74	3.51
E*	0.53	3.38	3.13	0.52	3.43	3.19	0.51	3.34	3.09	0.53	3.14	2.85
K*	0.51	2.61	2.17	0.51	2.60	2.16	0.51	2.58	2.13	0.52	2.47	1.97
		A9			**A10**							
E	0.58	3.85	3.64	0.52	3.90	3.67						
E*	0.62	3.47	3.23	0.57	3.40	3.14						
K*	0.59	2.75	2.31	0.54	2.63	2.18						

observed with this method.

The HBO fluorophores **A2** and **A3**, functionalized with a single triethylsilylalkynyl unit at the 5 or 3 positions of the phenol cycle, display maximum experimental emission energies at 2.42 and 2.30 eV respectively, Table 4.13. Functionalization in the *ortho* position of the hydroxy group as in HBO **A3**, leads to a sizeable red-shift of the emission, as compared to the *para* substitution as in HBO dye **A2** (ΔE_{A2-A3} = -0.12 eV exp. and -0.09 eV theo, see Table 4.15). The introduction of a second trialkylsilylalkynyl moiety onto the HBO scaffold triggers only a further slight bathochromic shift of the emission as compared to mono-substituted dye **A2** but yields comparable emission energies as **A3**. The presence of a fluorine atom at the 3' position in HBO **A7** induces a slightly red-shifted emission band as compared to HBO **A5** (2.25 eV vs. 2.31 eV for **A7** and **A5** respectively) which is qualitatively reproduced by our calculations. The substitution of the oxygen atom for a sulphur in HBT **A8** leads to a pronounced bathochromic shift in emission, as compared to HBO **A5**. Expectedly and similarly to the absorption case, the nature of the alkyl or aryl groups attached to the silicon atom has a very little impact on the emission profile, as evidenced by the similar emission energies of HBO dyes **A4** (Me), **A5** (Et), **A6** (Pr), and **A10** (Ph). Variation covering the tiny range of 0.04 eV can be detected for the emission energies of these four latter dyes (exp. and theo.). No significant change of density on the silicon atoms can indeed be seen in Figure 4.9. These alike density patterns can explain the very little impact of the substitution of the silicon on the absorption and emission maxima. Similarly, the presence of an additional triethylsilyl ethynyl substituent at position 3' as in HBO **A9** leads to similar emission energy as in HBO **A5** and the EDD plot directly explain this outcome. Indeed as can be seen on Figure 4.9, the additional ethynyl segment does not play a role in the ES and has therefore

no influence on the emission energy. Nevertheless in that specific case TD-DFT does exaggerate the impact of the additional substituent (Table 4.15).

Quantum yield of fluorescence

Thirdly, in the hope to rationalise the QY, we have estimated the protective barriers between the K* and the CI. As a general observation, we can see that with a low-limit of 0.27 eV with TD/LR+cLR, the associated QY are higher than 28%. Unfortunately for the most emissive dye **A9** and **A10**, and also for **A7**, we could not obtain an optimised transition state to estimate the barrier. For **A7** and **A10**, the optimisation leads back to a planar configuration whereas for **A9** the calculation is looking for a TS2* with an angle of more than 60°, which is obviously too twisted for TD-DFT.

The quantum yields of fluorescence of the double substituted HBO series **A4**–**A6** are important (32–49%) with a slight drop upon increase of the length of the silylalkyl chain; the barrier for these three dyes are similar, around 0.3 and 0.2 eV with TD and ADC(2) respectively. The twisting deactivation pathway is not the reason for the change of QY when increasing the alkyl size and this feature could be explained by the additional vibrational pathway triggered by the flexible unsaturated arms.

4.6 HBX with mono- or bis-(tri-*iso* -propylsilyl)acetylene in toluene

Given the promising properties of **A2**–**A10** for luminescent applications, similar compounds have been synthesised. In particular, a nitrogen atom is incorporated as heteroatom in order to try to enhance the QY (**D1**–**D4** series). One dye with a HBT core has also been studied for a thorough comparison (**D9**). For this new **D1**–**9** series the substituents is systematically a tri-*iso*-propylsilylacetylene. Different positions for this moiety have been explored, see Figure 4.10. All the compounds **D1**–**D9** present a full keto emission between 2.17 and 2.57 eV with a Stokes' shift of 7400-11600 cm^{-1} in toluene, see Figure 4.11 and Table 4.16. High QY are also registered experimentally (7–54%).

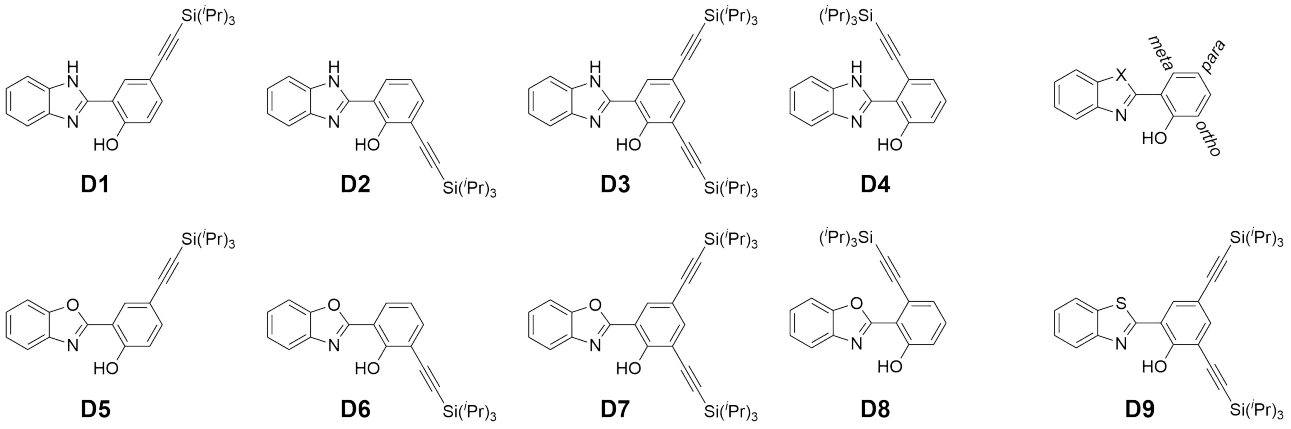

Figure 4.10: Structures of **D1**–**D9** series, (**D7** = **A6**).

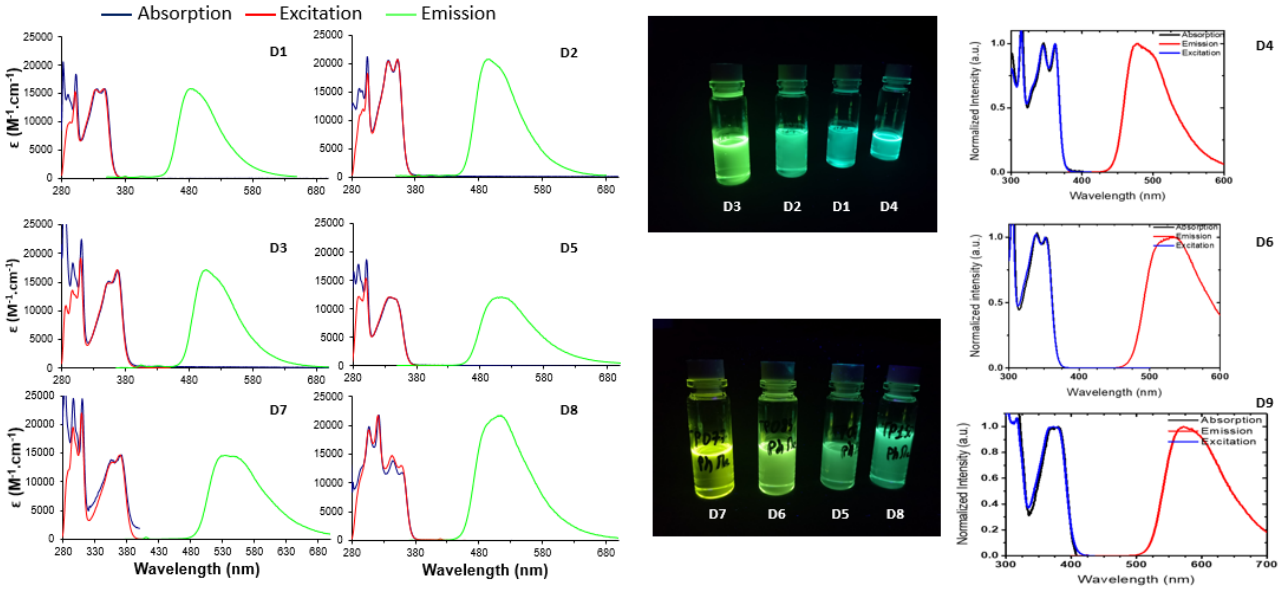

Figure 4.11: Experimental absorption and emission spectra of **D1**-**D9** in toluene. Photographs of **D1**-**D8** under irradiation in toluene solution.

Table 4.16: Experimental photophysical data in aerated toluene solution at room temperature of **D1**–**D9**.

	$\lambda_{abs}{}^a$	$E_{abs}{}^b$	ε^c	$\lambda_{em}{}^a$	$E_{em}{}^b$	ΔS^d	QY^e	τ^f
D1	347	3.57	15860	483	2.57	8100	0.54	4.6
D2	353	3.51	20731	507	2.45	8600	0.51	4.5
D3	368	3.37	17104	507	2.45	7400	0.53	4.9
D4	346	3.58	18158	485	2.56	8300	0.45	4.7
D5	340	3.65	12000	515	2.41	10000	0.11	3.9
D6	340	3.65	14000	520	2.38	10100	0.13	3.2
D7	371	3.34	14657	535	2.32	8300	0.32	4.0
D8	322	3.85	22000	513	2.42	11600	0.15	4.6
D9	375	3.31	11700	570	2.17	9200	0.15	-

[a]Maximum absorption and emission wavelengths (nm) , [b]Maximum absorption and emission energies (eV), [c]Molar absorption coefficient ($M^{-1}cm^{-1}$), [d]Stokes' shifts (cm^{-1}) , [e]QY of fluorescence, [f]fluorescence lifetime (ns)

With our theoretical model, the **D1**–**D4** structures could not be optimised. In fact, the *iso*-propyl is rotating preventing the convergence of the calculation. However, we have seen that the length of the alkyl chain has no significant influence on the optical properties when comparing **A4**, **A5**, and **A6**. Therefore, to be consistent and allow meaningful comparisons, we simplify all structures in this Section by replacing the alkyl chains by methyl groups.

Relative Stabilities

The relative stabilities of ES that we computed indicate that the K* is favoured, see Table 4.17. Indeed this tautomer is more stable by 0.16—0.43 eV than the E* in all dyes. The proton transfer is also barrierless, except for **D4** with TD/LR+cLR. This barrier is 0.06 eV only but becomes negative when adding post-HF corrections. These relative stabilities correspond to a quantitative keto fluorescence consistently with the experiment.

Table 4.17: Difference of free energies between E* and K*, and corresponding transition state energies of dyes **D1**–**D9**. All values are in eV and obtained with TD-DFT/LR+cLR correction applied at the TD-M06-2X/6-311G+(2d,p) and ADC(2)/aug-cc-pVTZ levels of theory. See Figure 4.7 for structure representations.

	TD	ADC(2)	CC2	TD	ADC(2)	CC2	TD	ADC(2)	CC2
		D1			**D2**			**D3**	
E* → K*	-0.32	-0.36	-0.35	-0.34	-0.37	-0.34	-0.42	-0.43	-0.41
E* → TS*	-0.05	-0.10	-0.13	-0.06	-0.09	-0.10	-0.07	-0.09	-0.10
K* → TS2*	[a]	[a]	[a]	[a]	[a]	[a]	0.36	0.45	0.38
		D4			**D5**			**D6**	
E* → K*	-0.16	-0.24	-0.24	-0.22	-0.29	-0.26	-0.27	-0.34	-0.28
E* → TS*	0.06	-0.01	-0.05	-0.03	-0.12	-0.14	-0.04	-0.12	-0.13
K* → TS2*	0.36	0.52	0.49	0.23	0.14	0.08	0.29	0.20	0.13
		D7			**D8**			**D9**	
E* → K*	-0.22	-0.26	-0.22	-0.17	-0.26	-0.23	-0.32	-0.39	-0.32
E* → TS*	-0.01	-0.08	-0.10	-0.04	-0.15	-0.17	-0.04	-0.37	-0.30
K* → TS2*	0.27	0.20	0.12	[a]	[a]	[a]	0.15	0.22	0.15

[a] TS2* could not been optimised.

Electronic density difference

As previously, the EDD of Figure 4.12 provid a qualitative representation of the favourable conditions for the ESIPT to occur. The difference of density is well marked between the hydroxy which is losing density at the excited state and the nitrogen atom which *a contrario* is gaining density. An interesting impact of the substitution position is also appearing with these EDD plots. The (tri-*iso*-propylsilyl)acetylene moiety has a donor effect on the systems, the triple bond loosing density at the ES, expect when it is linked to the core in *meta* position (**D4** and **D8**). In this latter configuration the ethynyl substituent acts like an electron-withdrawing group, a gain of density is visible on the single bonds bordering the triple linkage, this effect is stronger for HBI **D4** than **D8**. We can also notice that the donor effect of the triple bond is stronger in *para* position than *ortho* even in bis-substituted systems. This interesting behaviour of the substituent depending of its position can be tuned by the addition of an extra donor group to the *para* or *ortho* moiety or by an acceptor group in *meta*.

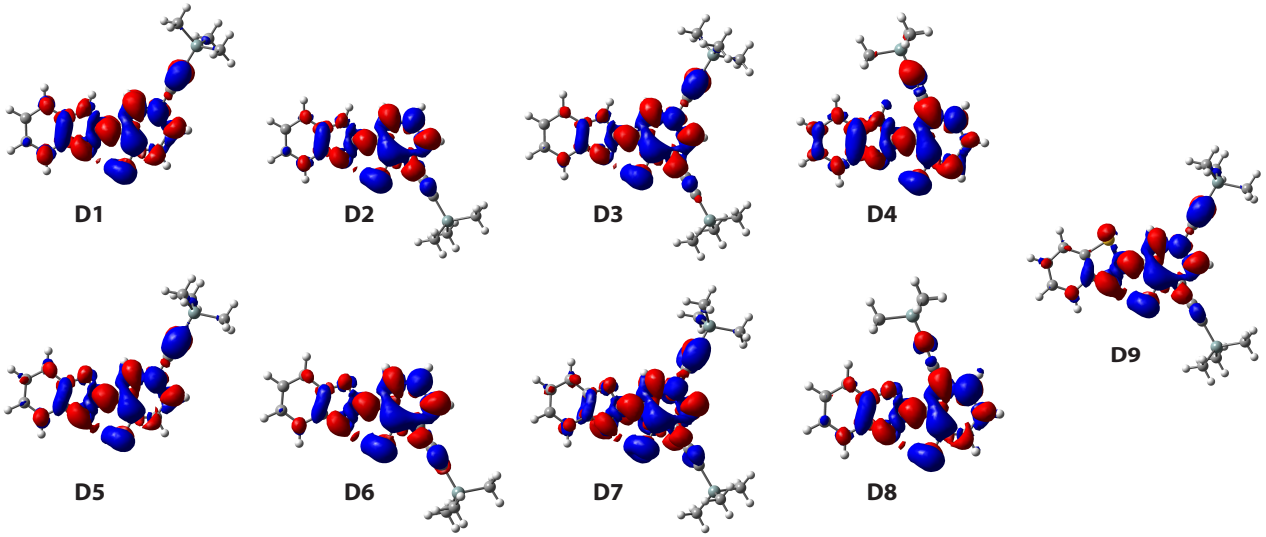

Figure 4.12: Electron density difference plots (isovalue = 0.0008 a.u.) of **D1**–**D9** structures in toluene. Blue (red) regions indicate decrease (increase) of the density upon absorption of light.

Fluorescence

Another proof of the K* nature of the luminescence is the better match of the experiment with the computed K* vertical transition energies than with E*, see Table 4.18. The MAD with CC2/LR+cLR is clearly smaller for K*, 0.12 eV than E*, 0.88 eV. This comes as no surprise at this stage of the thesis. **D3**, **D7**, and **D9** have the same architecture, only the heteroatom is changing. Experimentally and theoretically, **D9** with its sulphur atom is the most red-shifted (2.17/2.24 eV exp/CC2) and HBI **D3** the most blue-shifted (2.45/2.49 eV exp/CC2), which basically reproduces the trends of the unsubstituted core, see Section 4.3.

Table 4.18: Vertical emission energies (eV) in toluene of E* and K* forms of **D1**–**D9** with LR+cLR corrected approaches (TD, ADC(2) and CC2). Oscillator strengths obtained with TD-DFT are reported as well.

	f	TD	ADC(2)	CC2	f	TD	ADC(2)	CC2	f	TD	ADC(2)	CC2
			D1				**D2**				**D3**	
E*	0.70	3.57	3.48	3.42	0.80	3.54	3.41	3.38	0.61	3.42	3.25	3.25
K*	0.52	2.87	2.49	2.62	0.64	2.78	2.38	2.55	0.58	2.70	2.31	2.49
			D4				**D5**				**D6**	
E*	0.70	3.40	3.42	3.29	0.58	3.51	3.44	3.37	0.72	3.53	3.40	3.37
K*	0.48	2.88	2.57	2.64	0.45	2.79	2.42	2.57	0.55	2.70	2.29	2.49
			D7				**D8**				**D9**	
E*	0.53	3.38	3.24	3.23	0.73	3.46	3.48	3.33	0.53	3.16	2.95	2.97
K*	0.51	2.64	2.19	2.44	0.42	2.82	2.49	2.61	0.53	2.47	2.04	2.24

D5, **D6**, and **D7** have similar structures as **A2**, **A3**, and **A5** respectively, the difference is only the

alkyl chain which is an *iso*-propyl for **D** series and an ethyl in series **A**. However we remind that we replaced the *iso*-propyl by methyl in our calculations. Experimentally the emission maxima of both series are matching with less than 0.02 eV of difference with the notable exception of **D6**–**A3** in which a large change (0.08 eV) is found. In the same time, for this three couples the TD/LR+cLR vertical emission energies are perfectly matching. Looking closer at the experimental shapes of **D6** fluorescence spectrum in Figure 4.11, we can notice the large and flat band which can induced some uncertainty in the definition of the maximum.

For HBI **D1**–**D4** and HBO **D5**–**D8**, the impact of the position of the substituent is independent of the heteroatom. Therefore the same trend as for **A2**, **A3**, and **A5** is found. The doubly substituted structures are the most red-shifted, and *para* and *meta* groups yield a hypsochromic effect on the position of the luminescence, this effect being stronger with the *meta* position.

Quantum yield of fluorescence

Incorporating a nitrogen as heteroatom strongly enhances the emission with QY in the 51–54% range for HBI **D1**–**D3** whereas the QY of HBO **D5**–**D7** is 11–32% only. As a reminder the QY of **HBI'**, **HBO'**, and **HBT'** are 32%, 3% and 1%, respectively. The oscillator strength is in the 0.42–0.58 range for all the dyes, these small differences can not explain the reported variations of QY. We have therefore looked at the protective twisting barrier, see Table 4.17. In the present case, the largest barriers are found for HBI compounds ($>$ 0.38 eV) whereas the less emissive HBO dyes have barriers between 0.08 and 0.13 eV in agreement with the QY trends. The protective barrier is also quite low for **D9** (0.15 eV) which has one of the lowest QY in this series.

4.7 Substitution of a HBO scaffold by an ethynyl-tolyl moiety

Another HBO-based series synthesised by our collaborators is presented in this Section. This time, an ethynyl tolyl moiety is introduced on the HBO scaffold in an effort to enhance the quantum yield of fluorescence, see Figure 4.13. The diverse positions of substituents lead to tunable emission. Depending on the solvent, single or dual fluorescence from enol and/or keto tautomers or even from the anionic form, are experimentally observed. To go further in the understanding of the optical properties, we have ran *ab initio* calculations with different levels of success depending on the solvent. This collaborative work has been published in *Eur. J. Org. Chem.*[8]

4.7.1 A full keto emission in toluene

The photophysical properties of these compounds, measured in solution, are reported in Figure 4.14 and Table 4.19. The absorption spectra of the HBO derivatives **B1**–**B6** in toluene feature similar trends such as a broad, rather unstructured band assigned to the S_0-S_1 transition, with a wavelength of maximal absorption located between 332 and 368 nm (3.73–3.37 eV). The molar absorption coefficients

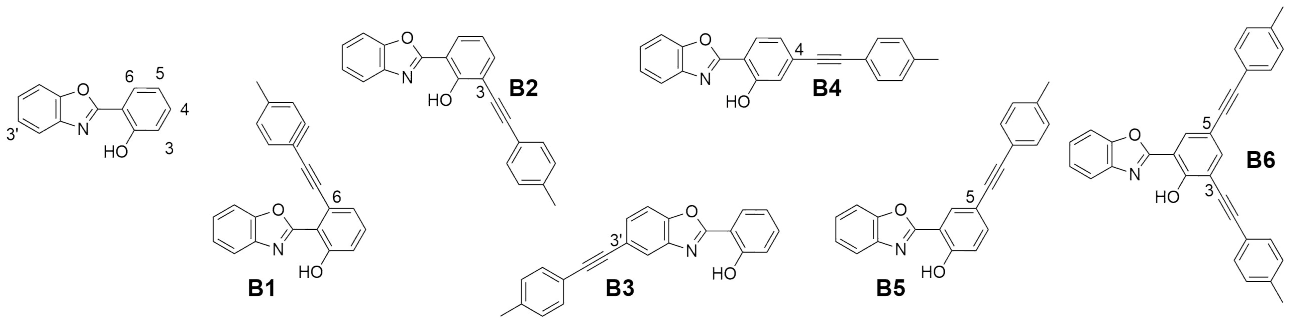

Figure 4.13: Representation of the **B1**–**B6** structures.

Table 4.19: Experimental photophysical data in aerated solution at room temperature of **B1**–**B6**.[8] See Figure 4.13 for structures representations.

solvent	$\lambda_{abs}{}^a$	$E_{abs}{}^b$	ε^c	$\lambda_{em}{}^a$	$E_{em}{}^b$	ΔS^d	QY^e	τ^f
				B1				
Toluene	332	3.73	27000	519	2.39	11000	0.23	3.2
Ethanol	328	3.78	11000	402/508	3.08/2.44	5600	0.20	0.5/1.2
				B2				
Toluene	349	3.57	19000	550	2.25	10000	0.32	2.3
Ethanol	342	3.63	19000	538	2.30	10100	0.17	1.6
				B3				
Toluene	332	3.73	30200	504	2.46	10000	0.04	2.1
Ethanol	329	3.77	28400	398/489	3.12/2.54	5300	0.02	3.3
				B4				
Toluene	349	3.55	45700	489	2.54	8200	0.19	1.8
Ethanol	345	3.59	28800	398/485	3.12/2.56	3900	0.16	1.4
				B5				
Toluene	347	3.57	37200	397/514	3.12/2.41	3600	0.10	1.3
Ethanol	345	3.59	11500	389/450/505	3.19/2.76/2.46	3300	0.04	0.5/3.1
				B6				
Toluene	368	3.37	15600	550	2.25	9000	0.30	3.4
Ethanol	371	3.34	14700	540	2.30	8400	0.24	3.2
DMF	361	3.43	30600	388/495	3.20/2.50	1000	0.23	3.3/3.5
DMF	460	2.70	21100	495	2.50	1500	0.49	3.3/3.5

[a]Maximum absorption and emission wavelengths (nm) , [b]Maximum absorption and emission energies (eV), [c]Molar absorption coefficient ($M^{-1}cm^{-1}$), [d]Stokes' shifts (cm^{-1}) , [e]QY of fluorescence, [f]fluorescence lifetime (ns)

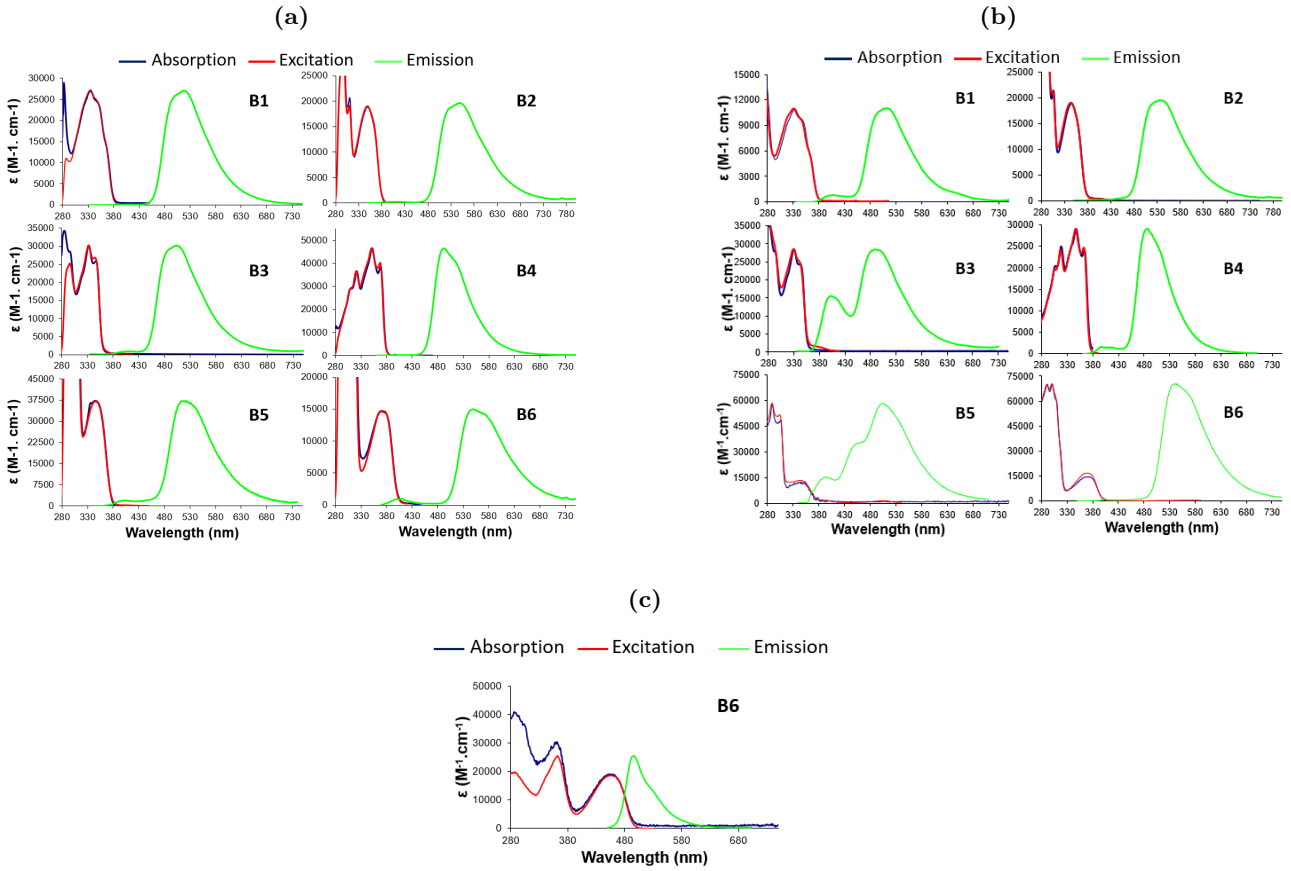

Figure 4.14: Experimental absorption and emission spectra of **B1-B6** in (a) toluene, (b) ethanol and (c) DMF.

are in the 15000 to 46000 $M^{-1}cm^{-1}$ range, which is typical for compact polyaromatic dyes, see Figure 4.14a. The absorption spectra in ethanol display very similar features as those observed in toluene, see Figure 4.14b, indicating that the optical properties at the ground state geometry are not strongly influenced by the substitution pattern nor by the nature (polarity) of the solvent. Upon excitation, HBO dyes **B1**–**B6** display a single intense emission band with a maximum spanning from 489 to 550 nm (2.54–2.25 eV) depending on the position of the ethynyl tolyl substituent(s) on the HBO core. The Stokes' shifts are in the range 8000–11000 cm^{-1} which is (again) typical of ESIPT emitters. These Stokes' shifts values, larger than in standard organic fluorophores, are consistent with the formation of the keto tautomer in the excited-state.

Relative Stability

Experimentally the shape of fluorescence spectra in toluene clearly hints at a full emission from the K*, but for **B5** for which a small additional enol band appears. Therefore, we expect a K* isomer more stable than its E* counterpart as well as a (nearly) barrierless proton transfer. To obtain this trend, post-HF corrections are necessary, see Table 4.20. Without these corrections, i.e, with "simple"

Table 4.20: Free energy difference between the E* and K* tautimers, and corresponding transition state energies calculated in toluene and ethanol of **B1**–**B6**. All values are in eV, and the LR+cLR solvent correction is applied on TD-DFT and CC2 energies. See Figure 4.13 for structure representations.

	Toluene		Ethanol		Toluene		Ethanol		Toluene		Ethanol	
	TD	CC2	TD	CC2	TD	CC2	TD	CC2	TD	CC2	TD	CC2
	B1				**B2**				**B3**			
E* → K*	0.00	-0.21	-0.04	-0.22	-0.22	-0.24	-0.35	-0.35	-0.09	-0.20	-0.15	-0.23
E* → TS*	0.08	-0.24	0.09	-0.24	-0.03	-0.14	-0.07	-0.18	0.05	-0.13	0.06	-0.12
K* → TS2*	0.33	0.12	0.18	-0.07	0.33	0.12	0.26	0.02	0.21	0.06	0.14	-0.04
	B4				**B5**				**B6**			
E* → K*	0.14	-0.06	0.10	-0.11	-0.17	-0.20	-0.26	-0.27	-0.26	-0.26	-0.34	-0.32
E* → TS*	0.17	-0.13	0.25	-0.06	-0.03	-0.13	-0.03	-0.14	-0.08	-0.17	0.17	-0.06
K* → TS2*	0.28	0.10	0.28	0.12	0.27	0.08	0.17	-0.06	0.37	0.17	0.27	0.04

TD-DFT calculations, one would predict that the E* form is the most stable isomer for **B1** and **B4** which would not be consistent with the experimental observations. For **B5**, all approaches yield a quantitative emission from K* with a barrierless transition whereas experimentally a weak fluorescence from the E* is also observed. For all other dyes of this series, CC2/LR+cLR correctly gives the K* form most stable than E* by -0.06 to -0.26 eV. As stated previously a difference of -0.20 eV coupled to a barrierless transition for the E* → K* reaction is typical of "pure" ESIPT dyes.[12]

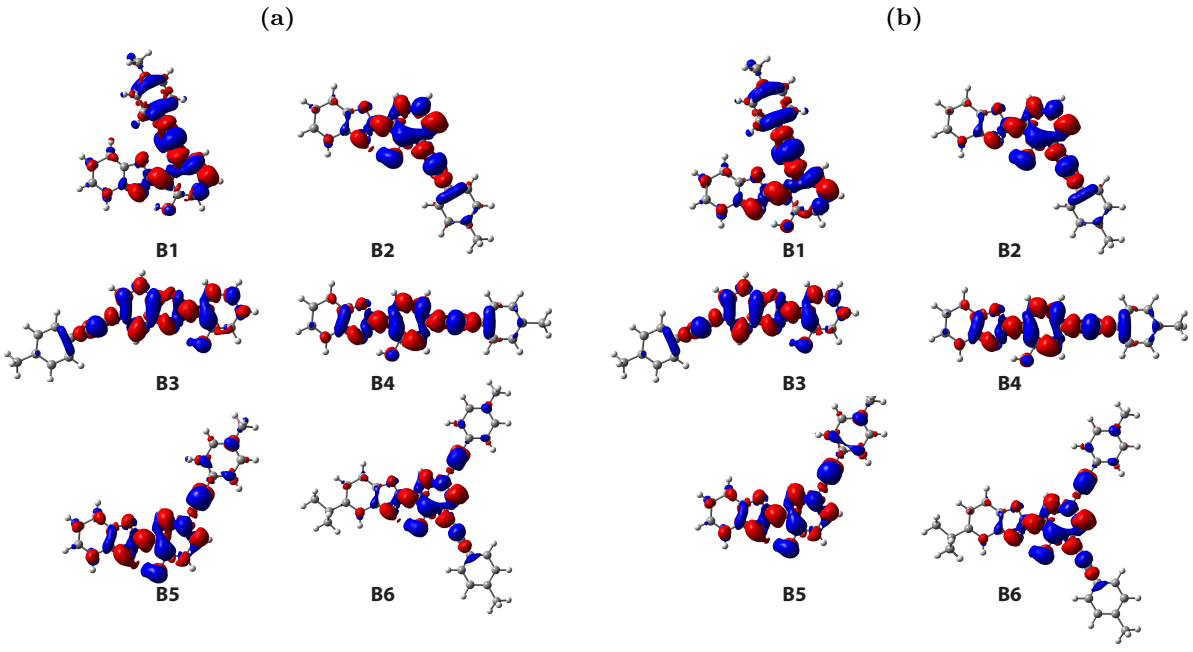

Figure 4.15: Electron density difference plots (isovalue = 0.0008 a.u.) for **B1**–**B6** in (a) toluene and (b) ethanol. Blue (red) regions indicate decrease (increase) of the density upon absorption of light.

Electronic density difference

The EDD of this series are typical of ESIPT systems, see Figure 4.15a. A strong decrease (increase) of electronic density on the phenol (nitrogen) is found: the acidity of the proton increases while the basicity of the nitrogen atom decreases after excitation. The density charge is strongly delocalised in **B1** whereas it is more localised in **B6**.

Emission

With the CC2/LR+cLR approach, we are able to reproduce the position of the keto emission with an MAD of 0.12 eV, see Table 4.21. We recall that such comparisons are made neglecting vibronic couplings and are therefore inherently limited. **B3** and **B4** are the two most blue-shifted dyes, both experimentally and theoretically, whereas **B2** and **B6**, which have a substituent in position 3, are the most red-shifted. The theoretical enol and keto ES energies of **B5** match the two experimental maxima in the dual fluorescence spectrum with a similar deviation, 0.24 and 0.27 eV, respectively, clearly indicating that the computed band separation is accurate.

Table 4.21: Emission energies (eV) in toluene and ethanol of E* and K* forms of **B1**–**B6** with LR+cLR corrected approaches (TD and CC2). Oscillator strengths obtained with TD-DFT are reported as well.

	Toluene			Ethanol			Toluene			Ethanol		
	f	TD	CC2	f	TD	CC2	f	TD	CC2	f	TD	CC2
	B1						**B2**					
E*	0.71	3.18	3.28	1.00	3.01	3.10	0.95	3.34	3.25	1.27	3.29	3.22
K*	0.49	2.74	2.54	0.66	2.65	2.46	0.72	2.56	2.40	0.83	2.52	2.38
	B3						**B4**					
E*	1.40	3.55	3.94	1.55	3.40	3.32	2.13	3.16	3.24	2.33	2.98	3.06
K*	0.60	2.90	2.66	0.74	2.81	2.58	0.62	2.85	2.63	0.84	2.75	2.53
	B5						**B6**					
E*	0.48	3.36	3.24	0.73	3.25	3.14	0.66	3.19	3.08	0.84	3.11	3.01
D*	-	-	-	2.81	0.95	2.59	-	-	-	-	-	-
K*	0.16	2.68	2.50	0.65	2.61	2.43	0.13	2.47	2.30	0.77	2.41	2.26

Interestingly, comparable results are obtained for **A2**–**B5**, **A3**–**B2**, and **A5**–**B6**, see Table 4.22. Those couples in the **A** and **B** series are substituted at the same position, only the nature of substituent is changed. The experimental emissions are close in each pair whereas a difference of more than 0.1 eV is predicted by TD/LR+cLR. The deviation between experiment and theory is bigger in the **A** series than in its **B** counterpart. The stronger flexibility of the substituent in the former group could be an explanation for this difference. Most probably, the presence of silylalkyl moieties in the **A** series induce larger errors. Nevertheless, the trends within each series remains nicely reproduced.

Table 4.22: Experimental and theoretical (TD/LR+cLR) keto emission in toluene of sytems substituted in 3 and 5 positions, see Figures 4.7 and 4.13.

	A5	**B6**	**A2**	**B5**	**A3**	**B2**
Exp.	2.31	2.25	2.42	2.41	2.30	2.25
Theo.	2.61	2.47	2.79	2.68	2.70	2.56

Quantum yield of fluorescence and protective barrier from the CI

The fluorescence quantum yields in solution are generally limited by the presence of efficient non-radiative routes. Indeed, as can be seen in Table 4.21, all dyes present large oscillator strengths, only very bright states are at play. For ESIPT dyes, we recall that one of the most well-known deactivating pathway is the twisting around the central interring bond after proton transfer (see Chapter 3), that can ultimately lead to a conical intersection with the ground state, and hence the emission quenching. To obtain first insights into that pathway, the transition state characterizing this twisting mode from the K* tautomer was determined. As can be seen in Table 4.20, positive barriers between 0.06 and 0.17 eV (CC2/LR+cLR) are systematically obtained, consistent with the presence of fluorescence experimentally. The barriers associated with the lowest QY, which are **B3** (4%) and **B5** (10%), are under 0.1 eV whereas, for the other dyes, larger barriers are computed and QY of 19% and more have been measured. Only a qualitative estimation of the QY can be obtained with this approach, the trends are not properly reproduced in details when the experimental variations are small.

4.7.2 Keto and dual emissions with a touch of deprotonation in ethanol

In ethanol, a protic solvent, the enol ES is stabilised and fluoresces jointly with the keto tautomer in dyes **B1**, **B3**, **B4**, and **B5**. However the enol emission remains extremely weak in **B1** and **B4**. For **B2** and **B6**, the emission spectrum shows a single peak with a Stokes' shift exceeding 8000 cm^{-1} hinting at the keto nature of band. Dyes **B5** stands out by the presence of an additional emission band at 450 nm (2.76 eV) (i.e., between the enol and keto ones), see Figure 4.14b. This band is attributed to the deprotonated conjugated base D*, thanks to additional experiments, that is to the direct addition of base in the solution to form the deprotonated species.[8]

Relative stability

Given the computed relative stabilities of the E* and K*, we are not obviously able to reproduce the experimental dual emission in ethanol. Indeed, the CC2/LR+cLR method describes enol tautomers as less stable by more than 0.11 eV than their keto counterparts with barrierless transitions. With TD/LR+cLR the enol tautomer is also less stable by more than 0.04 eV than the K*, but for **B4**. However the enol form is also incorrectly found to be the most stable form in toluene for **B4**. The

most stable K* are determined for **B2** and **B6** (> 0.3 eV), consistently with the observation of an associated keto fluorescence. For the dual emitting form, regarding the ratio between the enol and keto emission, the relative stability between E*/K* should be smaller for **B3** and **B5** than **B1** and **B4** to partially reproduce this ratio. However the opposite trend is observed, K* is more stable for **B3**/**B5** than **B1**/**B4**. Therefore these results are not very satisfying but we have used here a continuum approach to model the solvent, which is certainly not totally suited for a protic solvent.

To reproduce this dual emission, calculations including one to three explicit solvent molecules have been performed for **B1**, **B2**, and **B3**. We tried different positions for the ethanol molecules, the optimised structures obtained for **B1** are represented in Figure 4.16. Similar configuration are obtained for **B2** and **B3**, however their ES with three explicit ethanol molecules could no be obtained. The solvent molecules regroup around the ESIPT center but the calculation failed to converge to a proper minimum.

Table 4.23: (a) Total complexation energy (kcal/mol) computed at the (gas)-M06-2X/6-31G(d) level on the GS LR-PCM(ethanol)-M06-2X/6-31G(d) structures depending of the number of surroinding EtOH molecules for **B1**-**B3**. Counterpoise corrections are applied. (b) Relative stability (eV) of E* → K* at LR-PCM(ethanol)/M06-2X/6-31G(d) level. See Figure 4.16 for structures representation.

(a)

EtOH	**B1**	**B2**	**B3**
1	-6.42	-8.50	-6.29
1-N	-15.39	-6.38	-6.10
1-O	-4.39	-4.07	-4.10
2	-11.47	-12.24	-12.14
3	-23.48	-21.69	-25.06

(b)

EtOH	**B1**	**B2**	**B3**
0	-0.07	-0.36	-0.17
1	-0.10	-0.42	-0.26
1-N	-0.20	-0.50	-0.30
2	-0.18	-0.49	-0.34
3	-0.21	/	/

The complexation energy is stronger when the ethanol molecule is close to the phenol and to the nitrogen atom, especially for **B1**, see Table 4.23a. The addition of three solvents molecules is weakly increasing the complexation energy (per solvent molecule)), from 6.4/6.3 kcal/mol with one to ca. 7.7/8.3 kcal/mol per EtOH molecule with three solvent molecules for **B1** and **B3**, respectively. However the inverse effect is observed for **B2**. No clear energetic trend depending on the amount of solvent molecules can be drawn from our calculations.

In those configurations including explicit solvent molecule(s), the relative stabilities of the tautomers are still in favour of a more stable K*, see Table 4.23b, the enol remaining relatively less stable by more than 0.10 eV in each of the cases. We can also note a small increase of the stabilisation of the keto tautomer when increasing the number of solvent molecules in the system. Therefore H-bonds between the solute and the solvent molecules are insufficient to explain the theoretical shortcomings.

With CC2/LR+cLR, a negative barrier to the CI is found for **B3** and **B5** which have the smallest QY (2 and 4%, respectively), but also for **B1** which has a QY of 20%, see Tables 4.19 and 4.20. Even considering a ca. 10% error margin for the measured QY, a negative barrier for **B1** is not compatible with its measured QY. With TD/LR+cLR, we obtained positive protective barriers for all dyes but again the trends are incorrect for **B1** and **B5**. In this case, it does not seem possible to conclude on the difference of the QY of these dyes based on their twisting barriers.

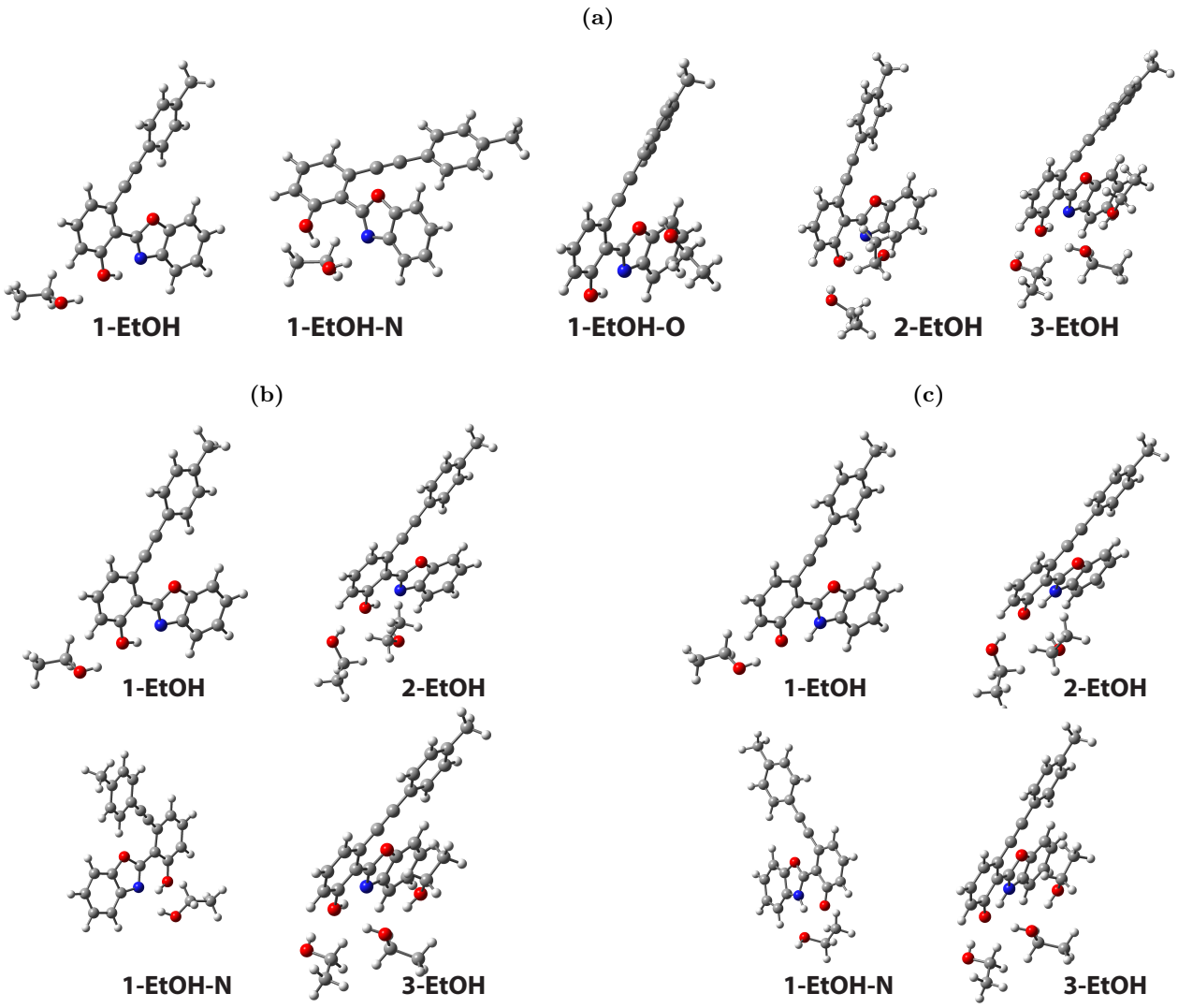

Figure 4.16: Optimised LR(ethanol)-M06-2X/6-31G(d) structures of **B1** at (a) GS, (b) E*, and (c) K* considering a few explicit solvent molecules. The first position of the label denotes the number of ethanol molecules. The 1-EtOH label is attributed to structures where the ethanol is close of the phenolic oxygen atom. In 1-EtOH-N the ethanol molecule is in interaction with the nitrogen atom whereas in 1-EtOH-O the ethanol is located close to the oxygen atom of the benzoxazole.

Emission

The positions of the dual and keto emissions are nicely reproduced with CC2/LR+cLR (MAD = 0.06 eV), see Table 4.21. However the computed deviations are not very consistent. Whereas we find deviations between +0.05 and +0.20 eV in toluene, errors spanning from -0.06 to +0.20 eV are found in ethanol. As we can see, negative deviations are found for **B4**–**B5**.

In ethanol, as in toluene, **B3** and **B4** have the most blue-shifted fluorescence, this fact is reproduced with CC2/LR+cLR calculations even if the energy is underestimated for **B4**. However in ethanol **B3** and **B4** exhibit dual emission (as **B1** and **B5**); **B2** and **B6** are the only dyes conserving their pure keto fluorescence in ethanol. They are also the most red-shifted dyes both experimentally and theoretically, see Table 4.21.

Thanks to its extended conjugation at the *para* position of the hydroxy group, **B5** displays a triple E*/D*/K* (enol, deprotonated, and keto ES) emission behaviour but with a strong quenching of the fluorescence (QY of 4%). Theoretically, the deprotonated emission wavelength is also surrounded by the enol and keto counterpart as experimentally observed. However the CC2/LR+cLR error is significantly larger for D* (0.17 eV) than for E* and K* (0.05 and 0.03 eV, respectively). It is interesting to note that this triple emission is not observed in **B6** dye which also presents a *para* substitution. In order to shed more light on the photophyscial properties of these *para*-substituted dyes, the optical properties of **B6** has been studied in DMF. Theoretically, only **B6** has been investigated when this study has been originally performed.

For **B6** in DMF, in addition to the usual absorption band (361 nm, 3.43 eV), an extra one (460 nm, 2.70 eV) appears, see Figure 4.14c. This latter lowest-energy band has been assigned to the stabilisation of the anionic species formed by deprotonation of **B6**. Indeed DMF which is the most basic of the solvent studied here. Theoretically, we can confirm this attribution, with TD/LR+cLR, the enol and anionic forms of **B6** absorb at 3.70 and 3.05 eV, respectively.

In DMF, upon photoexcitation in the absorption band assigned to D, a distinctive intense blue emission is observed at 495 nm (2.50 eV), attributed to the emission of the excited deprotonated species D* whereas a bright green/yellow emission at 550–540 nm (2.25–2.30 eV) is found in toluene and ethanol. Interestingly, for the anionic form of **B6** in DMF, we predict a very bright emission (f=1.00) at 2.60 eV, that is in between the E* (3.14 eV) and K* (2.44 eV) band, which nicely fits the experimental value (2.50 eV), and therefore confirms the experimental assignment (CC2/LR+cLR vertical energies are given here).

4.8 A personal conclusion: is one approach "better" than the others?

Experimental and theoretical conclusions

The main goal of this collaboration with the team of Dr. Gilles Ulrich was the synthesis and study of dual emissive systems. More precisely, my task was to rationalise the properties of the synthesised compounds. The systems reported in this Chapter, are all based on the HBX scaffold (HBO, HBT and HBI) and include one ESIPT site only. Therefore dual luminescence can only result from the coexistence of two forms, the enol and the keto tautomers (or alternatively an anion) at the excited state. For reaching dual emission, the HBT core (X=S) has shown very promising results, however its quantum yield of fluorescence is very weak (1%). To enhance the QY, diverse substitutions have been explored. This strategy has also been applied to HBO (X=O) and HBI (X=NH) cores to modulate their E^*/K^* emission ratio. Indeed, the HBI scaffold can be viewed as a more valuable starting point due to its quite large QY (36%).

The introduction of an ethynyl aniline in *meta* position (leading to linear compounds) of the hydroxy group allows recovering the three different emission profiles (enol, keto, and dual) in benzene, all with high QY (>15%). Depending on the substituent nature, keto or dual emissions have been observed with the HBT and HBI scaffolds (keto with aniline, dual with methylamine). The substitution in *meta* of HBO by an ethynyl aniline strongly stabilises the enol ES which becomes the emissive ES. This stabilisation by the *meta* substitution has not been obtained with other substituting moieties, such as, an ethynyl tolyl moiety (studied in toluene). The only difference between these two moieties is the presence or not of a terminal electron donor, an effect evidenced by the electron density difference plots.

While several substituents (trialkylsilyl-acetylene and tolyl-acetylene) and positions (*meta*, *para*, *ortho*, and both *ortho-para*) have been tested for the HBO core, only bright keto fluorescence was obtained in toluene with these groups. However, depending on the positions of the substituents, systematic tuning effects of the emission profiles have been observed. The *ortho-para* and *ortho* substitutions lead to similar emission signatures whereas the fluorescences resulting from systems with *para* and *meta* groups are similar and blue-shifted as compared to the other patterns. This trend has been observed in both HBO and HBI emitters. In addition, comparing the two latter, a notable blue-shift of the HBI fluorescence can be noted. The HBT skeleton has been studied with *ortho-para* moieties only, and it showed red-shifted emission compared to its HBO equivalents. With the EDD plots, the donor effect of the substituent in *para* and *ortho* positions was evidenced, the triple bond loosing density at the ES. This effect is stronger for the *para* than for the *ortho* group even in bis-substituted systems. The opposite behaviour is observed in *meta* position, the single bonds bordering the triple linkage gain density in the ES. These different effects can be further increased through additional chemical substitutions and further exploited to tune the fluorescence, e.g. by adding extra donor group(s) to

the *para* or *ortho* moiety or an acceptor group in *meta*.

The influence of the solvent has been difficult to capture with our calculations. In DCM, the enol ES is probably stabilised for the ethynyl aniline substituted dyes, and this effect is coupled to a stronger solvatochromic effect and increased Stokes' shift, due to the stronger CT nature of these dyes. However, additional experiments would be required to obtain a more solid conclusion regarding the exact nature of the emission in this case. On the bright side, we can state that theory helped pinpointing that the interpretation of the experimental optical signatures was likely not straightforward for these compounds. On the dark side, theory was indeed unable to yield a definitive answer. Experimentally, ethanol often induces a stabilisation of the enol form. However, as expected, the description of the solvent effects through a continuum model is not able to reproduce this effect. Moreover, the addition of a few explicit molecules in a mixed implicit/explicit solvation approach was not very satisfying either, and clearly the simulations would gain in being improved here. Indeed, ethanol can be a medium of choice to obtain dual emission.

In short, from the 34 compounds that have been jointly studied experimentally and theoretically, keto fluorescence was found in most cases, whereas the desired dual emission appeared in only a limited number of cases. However, some extremely bright ESIPT emitters were found during this work (some of the largest QY in solid-state with ESIPT dyes were observed). More globally, we also increased our knowledge regarding the relationship between, on the one hand, the substitution pattern and the nature of the heteroatom in the dye's scaffold, and, on the other hand, the fluorescence wavelength and QY for this class of fluorophores.

Limits of our models

For the majority of the systems presented here, our theoretical strategy (relative stability, EDD, and transitions energies) used to determine the nature of the excited state gives a conclusion in agreement with the experimental data. Of course, given the large number of compounds made by the Strasbourg's group, compromise had to be made in the computational approach. However in some cases, the limits of this approach have to be highlighted. For the **C** series, described in Section 4.4, most of the theoretical parameters evaluated indicate an emission resulting from the enol form in DCM solution, however the possibility of a keto emission is difficult to discard considering the match of this form with the CC2 values and the large Stokes' shifts. In this kind of inconclusive situation, already mentioned above, we have to be careful not to present results biased by the "expected" conclusions. Another obvious limit is the modelling of protic solvent effects. In our calculations, the environment is modelled by a dielectric continuum and the intermolecular interactions between the solvent and solute are not taken into account. In the case of ethanol, Section 4.7, we were not able to account for the impact of this intermolecular interaction on the ESIPT process in a satisfying way. We tried to include explicit molecules of solvent in our calculations, but the frustration of the ESIPT could not been reproduced. For this issue, QM/MM calculations would perhaps be a valuable path for improvement. For all the systems, I have tried to rationalise the quantum yield of fluorescence by comparison with the barrier

protecting from the conical intersection, an approach that I recognise as crude, but that has the merit of efficiency. If we could obtain an overview of the compounds with smallest and biggest QY, this model is not accurate enough for reaching a fine understanding nor to predict QY.

Choosing the "best" approach

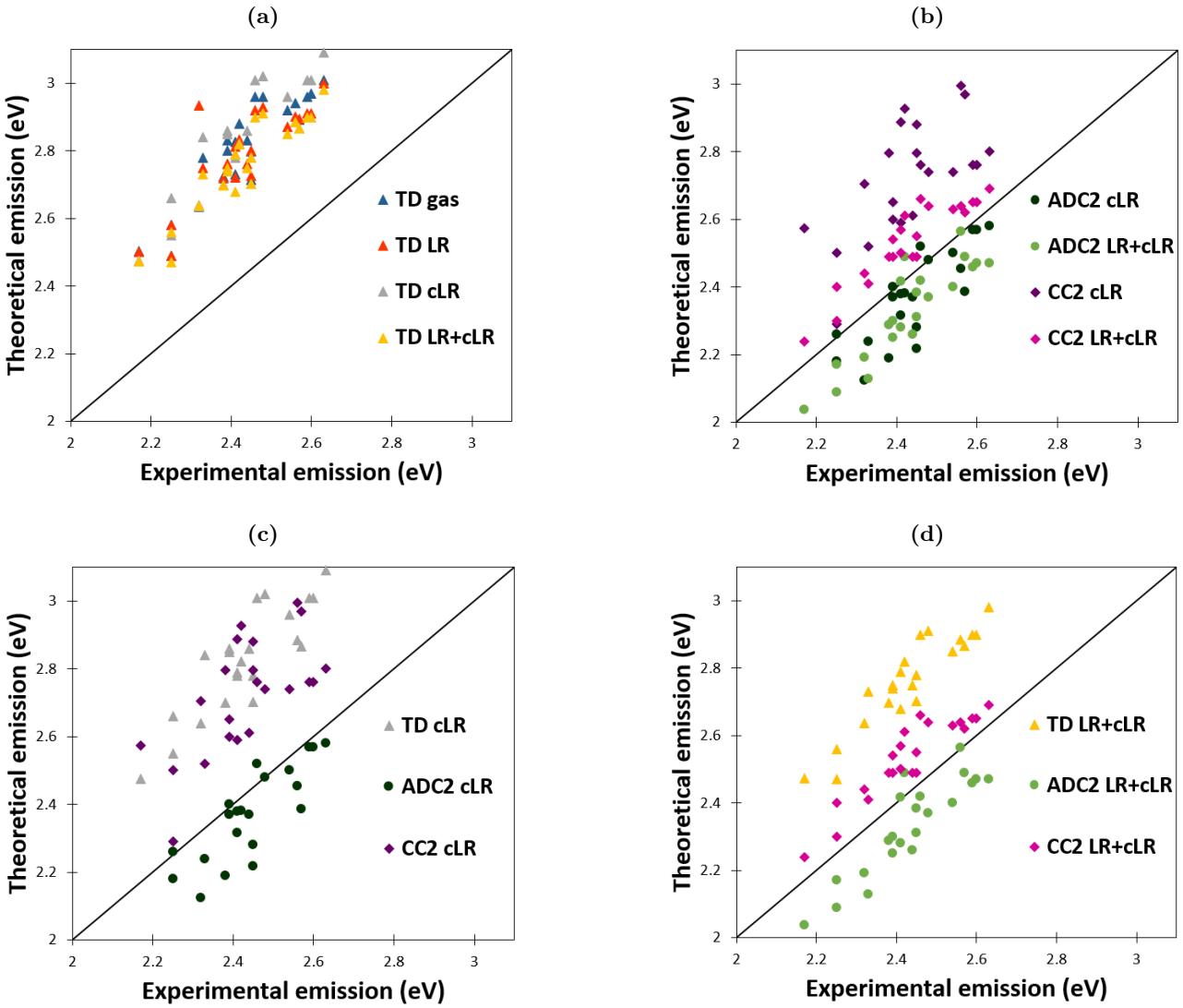

Figure 4.17: Comparison between the theoretical and experimental toluene and benzene keto emission energies (eV) of dyes previously discussed in this Chapter. The central lines indicate a perfect theory/experiment match. I report, the emission calculated with (a) TD-DFT and various solvent models, (b) post-HF levels and cLR or LR+cLR solvent models, (c) cLR solvation for various levels of electronic structure calculation, and (d) LR+cLR solvation for various levels of electronic structure calculation.

For each of the investigated series, the CC2/LR+cLR approach has given the results best fitting experiment, and it is certainly satisfying from the theoretician's point of view that the most "advanced" model used (theoretically) is also the most accurate (practically). I note that the emission is mostly

provided by the keto tautomer in the investigated emitters and that the diversity between the enol, keto, and dual fluorescence is not large enough to be able to determine a CC2/LR+cLR stability range leading to E* , K* or dual fluorescence as performed in Azarias' publication for a much more diverse set of dyes.[12] In some sense, investigating compounds showing subtle differences is also more challenging for theory. Nevertheless the accuracy of the combined hybrid approach to describe the keto emission can be evaluated. Only the results for K* luminescence in benzene and toluene have been selected for this purpose here. We are confident that the conclusions can be transferred to other aprotic solvents. To be coherent in the discussion, the **A** series has been excluded because the CC2 transition energies are not available for this group. The comparison between experimental and theoretical K* emissions is reported in Figure 4.17 and Table 4.24. In Figure 4.17a is illustrated the deviation between

Table 4.24: MAD, MSD, MaxD, MinD and standard deviation (SD) of the vertical emission energies compared to experiment depending on the level of theory for all the dyes with a K* emission in toluene or benzene.

		TD-DFT			ADC(2)		CC2	
	gas	LR	cLR	LR+cLR	cLR	LR+cLR	cLR	LR+cLR
MAD	0.37	0.37	0.39	0.33	0.10	0.10	0.31	0.11
MSD	0.37	0.37	0.39	0.33	-0.09	-0.09	0.31	0.11
MaxD	0.50	0.61	0.55	0.44	0.06	0.07	0.51	0.20
MinD	0.24	0.24	0.25	0.22	-0.23	-0.20	0.04	0.04
SD	0.07	0.08	0.09	0.06	0.09	0.07	0.12	0.05
MAD (with **A** series)	0.36	0.37	0.40	0.34	0.08	0.11	–	–

experimental and theoretical keto emission, obtained with TD-DFT depending on the solvent model. The variations are in a close range, with MAD changing by 0.05 eV only between the different schemes. With the LR+cLR model, the smallest deviations are found, with errors in the 0.22–0.44 eV range. The post-HF results are represented in Figure 4.17b. The underestimation of the K* emission by ADC(2) can clearly be noticed. If this method gives the best accuracy (MAD of 0.10 eV with cLR and LR+cLR) it is also the only one showing both negative and positive deviations. With CC2/cLR, the MAD is larger than with its ADC(2)/cLR equivalent (0.31 eV) but the LR+cLR corrections yield similar MAD for both models (0.11 eV). In Figures 4.17c and 4.17d, the deviations depending on the electronic structure approach with cLR or LR+cLR solvent corrections are reported. In these figures, TD-DFT is clearly the approach with the strongest deviations whereas ADC(2) gives accurate results in both cases. Results close to the experimental values are also obtained with CC2/LR+cLR. Our preference goes to the systematic overestimation of the emission energies (with TD-DFT and CC2) rather than with a more "erratic" approach [ADC(2)]. In particular we note that CC2/LR+cLR gives the smallest SD. In short, given both the predictions in terms of emitting species and the accuracy/consistency of the predicted emission wavelengths, the CC2/LR+cLR approach appears as the method of choice. Once more, one should recall that these comparisons are made without accounting for vibronic couplings and that this introduced a bias.

Chapter 5

A triply emissive dyes, BBTP

Contents

5.1 Introduction 95

5.2 Computational details 97

5.3 Exploration of the BBTP structure 98

5.3.1 Geometries in gas phase 98

5.3.2 Geometries in chloroform 99

5.3.3 Relative stabilities 100

5.3.4 Absorption 103

5.3.5 Emission 105

5.4 Design of potential quadruply fluorescent BBTP 107

5.5 Conclusions 111

5.1 Introduction

We focus here on a symmetric molecule unusually showing triple emission experimentally: the 2,5-bis(benzoxazol-2-yl)thiophene-3,4-diol, **BBTP**, see Figure 5.1. This Chapter is based in one of our publication that appeared in *Phys. Chem. Chem. Phys.*[14] **BBTP** has been synthesised and experimentally characterised by Hao and Chen in 2016.[15] This compound shows an absorption of the enol ground state (EE) between 340 and 400 nm. With the help of modified dyes presenting frustrated ESIPT centres, methoxy group are introduced instead of hydroxy, the emission spectrum of the **BBTP** has been shown to result from the emission of the EE*, EK*, and KK* forms, with fluorescence peaking at ca. 412, 475, and 550 nm, respectively. The lack of ultra-fast time-resolved data did, however, not allow the experimental group to draw conclusions regarding the exact mechanism of the double proton transfer. Five theoretical studies, summarised in Table 5.1, have subsequently been carried out to gain insights into this mechanism, typically through scans of the potential energy surface performed with

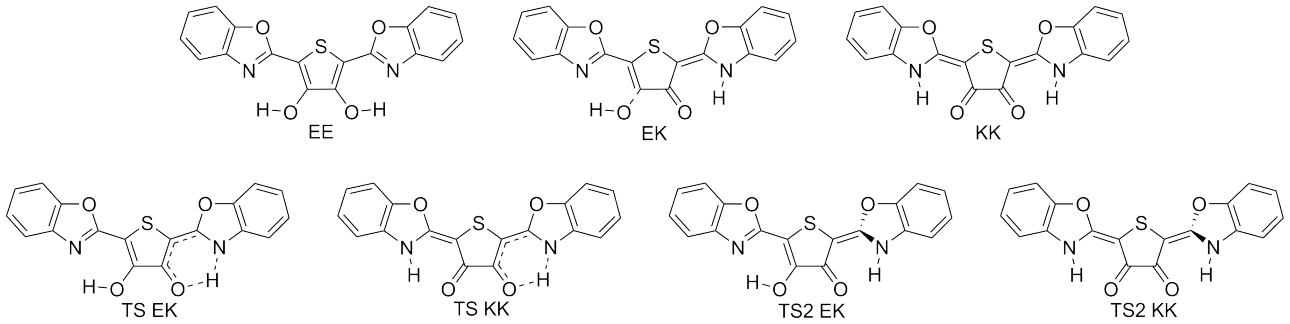

Figure 5.1: Representation of the different isomers of **BBTP** and their transition states. EE is the Enol-Enol form, EK the Enol-Keto form resulting from a single proton transfer, and KK the Keto-Keto form resulting from a double proton transfer. TS EK is the ESIPT transition state between EE and EK and TS KK the one between EK and KK. TS2 EK (KK) is the transition between the EK (KK) form and its associated conical intersection with the ground state (rotation around the double bond).

TD-DFT. Based on the energy barriers between the three tautomeric forms, four studies have concluded that the EE*→ KK* process is stepwise[16,18–20] whereas another has suggested the possibility of a simultaneous transfer of the two protons,[17] *i.e.*, a one-step EE* to KK* transformation. Divergent conclusions were also reached for the relative stabilities of the EE*, EK*, and KK* tautomers, *e.g.*, Jia[16] and Huang[17] reported that EE* is the most stable structure, whereas the studies of Lan[19] and Zhao[18] concluded that KK* is the most stable ES tautomer. The stability ordering given in two of the five studies[16,17] seems to disagree with the fact that the experimental emission spectrum presents three bands: it seems unlikely that ESIPT would take place if EE* is the tautomer presenting the lowest energy. Let us underline that all these works used different TD-DFT protocols (Table 5.1) which might explain their divergent conclusions. Indeed, as discussed in Chapter 3, it is well-known that the selected functional has often a large impact on the computed TD-DFT energies.[315] Huang and co-workers also studied the various conformers that can be envisaged. They concluded that the N$\cdots$H–O interaction are stronger than the O$\cdots$H–O ones which is corroborated by similar studies in other double ESIPT systems.[243,246] The N$\cdots$H–O hydrogen bond was also examined by Lan and co-workers using a reduced density gradient analyses, which allowed to visualise the strength of the non-covalent interaction. The hydrogen bond revealed itself stronger in the enol (N$\cdots$H–O) than in the keto (N–H$\cdots$O) form. Zhao and Zheng have additionally studied the impact of an external electric field on the ESIPT process.[18]

Due to the contradictory conclusions of these previous studies, we investigate in this Chapter the ESIPT mechanism and the related optical properties of **BBTP** with higher levels of theory. We optimise the different phototautomers not only with TD-DFT but also with post-Hartree-Fock methods, *i.e.*, the second-order algebraic diagrammatic construction[309] and the second-order coupled cluster[327] approaches. The transition states of the ESIPT processes as well as those leading to the twisted structure allowing for non-radiative deactivation (see Chapter 3) are determined to estimate all relevant barriers, *i.e.*, we do not use scans of the potential energy surfaces (PES) but actually

Table 5.1: Summary of the previous theoretical results obtained for **BBTP**: predicted stability ranking of the three tautomers and energy barriers for the various ESIPT processes (in kcal/mol). The method used is given in the rightmost column.

	Stability ranking	Barriers			Method
Ref		EK*–EE*	KK*–EE*	KK*–EK*	
16	$E_{EE^*} < E_{EK^*} < E_{KK^*}$	7.20	6.27	13.09	PCM/B3LYP/6-31++(d,p)
19	$E_{KK^*} < E_{EK^*} < E_{EE^*}$	8.66	5.79	16.71	PCM/B3LYP/6-31(d)
20		7.40	4.98	15.30	PCM/B1B97/def-TZVP
18	$E_{KK^*} < E_{EK^*}$	7.21	4.58	14.30	PCM/B3LYP/TZVP
17	$E_{EE^*} < E_{EK^*} < E_{KK^*}$	6.76	5.50	6.91	COSMO/B3LYP/TZVP

determine true transition states. The vibronic spectra are additionally calculated as well to validate our model and to allow additional comparisons with the experimental data. Importantly, we examine the influence of the solvent using three different schemes to describe the excited states in the framework of the polarizable continuum model (PCM): : the linear response approach[334] (LR), the corrected LR scheme (cLR-PCM),[321] and the vertical excitation model (VEM) in its unrelaxed density (UD) approximation.[322,323] These methods have been described in Chapter 3. Our goals are to lift the previous inconsistencies in the theoretical analyses and to reach more definitive conclusions. Finally, we investigate the effects of several chemical substitutions on the fluorescence and ESIPT mechanisms in a more prospective part of our study.

5.2 Computational details

All VEM-UD[322,323] calculations are performed with a locally modified version of Gaussian, whereas for all the other (TD-)DFT (gas, LR, and cLR) and post-HF calculations, the Gaussian16[328] and Turbomole 6.6 program[329] are respectively used. During all Gaussian calculations we use improved energy (10^{-10} a.u. for GS and 10^{-8} a.u. for ES), and geometry optimisation (10^{-5} a.u.) convergence thresholds and apply the *ultrafine* DFT integration grid. ADC(2) calculations use the so-called ADC(2)-s formalism[309] and both ADC(2) and CC2 calculation are performed applying the resolution of identity (RI) technique.[327,335]

For DFT [Post-HF] geometry optimisations, the 6-31G(d) [cc-pVTZ] atomic basis set is used, whereas a larger 6-311+G(2d,p) [*aug*-cc-pVTZ] atomic basis set is applied during the TD-DFT [ADC(2) and CC2] calculations of total and transition energies. An exception has to be noted: (TD-)DFT optimisations in gas phase rely on the cc-pVTZ basis set to allow a fair comparison with post-HF optimised structures (*vide infra*). For the gas phase optimisation, B3LYP,[307] M06-2X,[306] and ωB97X-D[308] exchange-correlation functionals are used. The two latter XFCs are also employed in calculations including solvent effect. The environmental effects are included with PCM using chloroform as solvent. As stated above, three different schemes are used:[336] the LR formulation, where the response of the

solvent dynamic polarisation to the excitation is a functional of the transition density,[334] and two state specific approaches,[336–338] where the same polarisation is determined by the difference of the electron densities of the initial and final states: perturbative cLR[321] and the self-consistent VEM-UD[322] approaches, see Chapter 3. To consider the influence of the solvent approach on the geometry, the LR and VEM-UD models are used to optimise and calculate the vibrational frequencies of the ES. Optimisation and frequency calculations are made using the *equilibrium* limit of PCM whereas vertical absorption and fluorescence energies are determined within the *non-equilibrium* limit, according with the different time scale of the considered processes.

Calculations of the analytic (or numeric for VEM-UD) vibrational frequencies are performed with the atomic basis set used during optimisations [6-31G(d)] for all the GS and ES structures.

The density difference plot, $\Delta\rho$, are obtained from the difference in the total density of the ES and the GS considering the total relaxed density for the ES. A contour threshold of 0.0004 a.u. is used for the representation.

Vibrationally resolved absorption spectra are computed using the FCclasses program.[339] The Franck-Condon approximation is employed as we consider only significantly dipole-allowed transition.[340,341] The reported spectra are simulated by applying the so-called adiabatic Hessian (AH) approach[342] and using convoluted Gaussian functions that present a half-width at half-maximum (HWHM) that is adjusted to allow accurate comparisons with experimental results (values specified in captions). A maximum number of 25 overtones for each mode and 20 combination bands on each pair of modes are included in the calculation.

5.3 Exploration of the BBTP structure

The number of observed emission bands is linked to the existence of different tautomers in the ES, possible vibronic fine structures and the relative stabilities of the various isomers. We therefore explore below the different structures resulting from single and double ESIPT, and their corresponding transition states (Figure 5.1). However one needs a trustworthy protocol to achieve accurate estimations. Indeed, as discussed above, the selected method has a significant impact on the relative stabilities for **BBTP**. We therefore start our study with a methodological investigation.

5.3.1 Geometries in gas phase

First, we optimise the GS of the EE isomer and the ES of the three tautomers with three functionals: B3LYP, M06-2X, and ωB97X-D. In the absence of X-ray structure, these results are compared to CC2 calculations, in order to have a benchmark value. Our results are listed in Table 5.2.

For the GS, the maximal positive deviation ($MaxD^+$) between DFT and CC2 is related to the description of the N$\cdots$H–O hydrogen bond length. This distance is significantly overestimated by DFT as compared to CC2. The largest $MaxD^+$, mean absolute deviation (MAD), and largest negative deviation ($MaxD^-$) are all obtained with M06-2X whereas ωB97X-D and B3LYP deliver more accurate

Table 5.2: Mean absolute deviation (MAD), mean signed deviation (MSD), maximum positive and negative deviations ($MaxD^+$ and ($MaxD^-$) in Å for the bond lengths of the EE, EE*, EK*, and KK* forms obtained with (TD-)DFT using CC2 as reference. All the optimisations are in gas phase and use the cc-pVTZ atomic basis set.Details of bond lengths are available in Tables A-1 and A-2 in Appendix

	EE			**EE***		
	B3LYP	M06-2X	ωB97X-D	B3LYP	M06-2X	ωB97X-D
MAD	0.012	0.019	0.016	0.016	0.019	0.017
MSD	0.008	0.007	0.002	0.010	0.007	0.003
$MaxD^+$	0.076	0.120	0.076	0.106	0.130	0.092
$MaxD^-$	-0.010	-0.019	-0.018	-0.017	-0.022	-0.023
	EK*			**KK***		
	B3LYP	M06-2X	ωB97X-D	B3LYP	M06-2X	ωB97X-D
MAD	0.020	0.024	0.023	0.025	0.025	0.023
MSD	0.010	0.007	0.004	0.017	0.013	0.010
$MaxD^+$	0.225	0.230	0.222	0.192	0.198	0.179
$MaxD^-$	-0.027	-0.033	-0.034	-0.023	-0.036	-0.028

estimates. To settle between these two latter functionals, the ES structures of the three tautomers have been optimised in gas phase with the same basis set. For the ES, the intramolecular hydrogen bond gives the MaxD that goes from 0.092 to 0.230 Å, see Table 5.2. M06-2X is again the functional leading to the largest deviation with respect to the CC2 reference. Selecting the "best" functional is not an easy choice: ωB97X-D and B3LYP deliver, in the present case, rather similar results. We selected ωB97X-D in the following for three reasons: i) the N$\cdots$H–O bond is in the heart of the ESIPT process, and ωB97X-D yields a better accuracy for this H-bond; ii) previous benchmarks have shown that this range-separated hybrid offers a very good balance for many families of ES whereas B3LYP is often less accurate for charge-transfer cases;[343] and iii) studies of the delicate interplay between the solvation response scheme and the exchange-correlation functional, showed that range-separated hybrids are providing more accurate results when using state-specific approaches.[338]

5.3.2 Geometries in chloroform

For the calculations including solvent effects, the ωB97X-D results are discussed when no additional details are provided. The impact of the solvent model on the ES geometry is rather limited (Table 5.3). Indeed, the MAD does not exceed 0.008 Å between the LR and VEM-UD optimised structures. Nevertheless, we notice that using VEM-UD increases the difference with the gas geometry as compared to the LR approach. This is obviously related to the fact that SS approaches, such as VEM-UD, are sensitive to large density reorganisations.[338] From a simplified point of view, the link between the VEM-UD effect and the magnitude of the density can be seen in the correlation between the MAD

given in Table 5.3 and the ES dipole moments of the different tautomers. Indeed, the ES dipole moment is larger in EK* (9.31D) and KK* (6.92 D) than in EE* (4.43 D), these quite large dipole could also be qualitatively related to significant solvatochromic effects.[15] Again, the largest deviations for the EK* and KK* tautomers are related to the intramolecular H-bond interaction between hydrogen and oxygen atoms in the keto configuration.

With a quick look on the impact of the solvent model coupled to M06-2X XCF, an increase of the maximum deviation between VEM-UD and LR is observed, see Table 5.3. However the MAD still does not exceed 0.015 Å. If the M06-2X XCF is not the optimal one (see above), reasonable trends could probably be obtained with it.

Table 5.3: MAD, MSD, MaxD$^+$, and MaxD$^-$ in Å for the bond lengths of EE*, EK*, and KK* tautomers between TD-DFT gas, LR, and VEM-UD with ωB97X-D/6-31G(d) and M06-2X/6-31G(d) optimised structures. Details of bond lengths are available in Tables A-3, A-4, and A-5 in Appendix.

	ωB97X-D XCF								
	VEM-UD versus LR			gas versus LR			gas versus VEM-UD		
	EE*	EK*	KK*	EE*	EK*	KK*	EE*	EK*	KK*
MAD	0.002	0.008	0.008	0.002	0.008	0.009	0.001	0.013	0.014
MSD	0.000	-0.002	-0.005	0.000	0.004	0.006	0.000	0.007	0.010
MaxD$^+$	0.004	0.012	0.010	0.006	0.045	0.072	0.006	0.071	0.130
MaxD$^-$	-0.004	-0.028	-0.059	-0.003	-0.010	-0.006	-0.001	-0.013	-0.011
	M06-2X XCF								
	VEM-UD versus LR			gas versus LR			gas versus VEM-UD		
	EE*	EK*	KK*	EE*	EK*	KK*	EE*	EK*	KK*
MAD	0.010	0.014	0.012	0.002	0.014	0.015	0.010	0.007	0.012
MSD	0.000	-0.007	-0.004	0.000	-0.007	-0.007	0.000	0.004	-0.001
MaxD$^+$	0.029	0.015	0.024	0.004	0.013	0.029	0.021	0.009	0.053
MaxD$^-$	-0.017	-0.092	-0.053	-0.006	-0.092	-0.091	-0.030	-0.054	-0.071

5.3.3 Relative stabilities

To determine the relative free energies of the different forms, our composite TD-DFT/post-HF approaches can be used. An important numbers of combinations has been tested in order to evaluate the impact of the corrections implemented using different basis sets, post-HF methods and solvent models. The detail of the equations to obtain the various free energies are given in the Chapter 3, Eqs 3.43 to 3.50. We recall that the wavefunction calculations systematically use the *aug*-cc-pVTZ basis set here. Amongst all these protocols, the most refined and, therefore presumably the most accurate, is the latter (post-HF/VEM) as it combine a coupled-cluster description of the electronic structure to advanced solvation approach.

Experimentally, three emission bands corresponding to the emission from the different tautomers are observed with relative intensities of 0.2 (EE*), 1.0 (EK*), and 0.9 (KK*).[15] Without experimental quantum yields available and hence without the radiative (k_r) and non-radiative (k_{nr}) constants, let us first take a look at the computed oscillator strengths, although quantitative comparisons are not possible. The oscillator strengths are 1.6 , 0.4, and 0.1, for EE*, EK*, and KK*, respectively at the TD-ωB97X-D level. Similar values are obtained with CC2 : 1.5, 0.3 and 0.1 respectively. Therefore, in first qualitiative approximation one can expect a smaller k_r for KK* and EK* than for EE*. Given that the intensity of the EE* band is very small experimentally, it is therefore reasonable to expect that the EE* tautomer is significantly less stable than the two other forms, and that the transition state corresponding to the first ESIPT process is (very) low. In addition, as both the EK* and KK* bands appear experimentally, there should be a non-zero barrier for the second ESIPT process. Indeed, if the EK* $\rightarrow$ KK* transition was barrierless, only the KK* fluorescence band would likely be present in observed spectra. This analysis therefore gives a global idea of the expected trends that are used in the following to assess the theoretical results.

Table 5.4: Difference of free energies of EE*, EK*, and KK* of **BBTP** and corresponding transition state energies. TD-DFT calculations use the ωB97X-D XCF. All values are in eV, see Figure 5.1 for structure representations.

LR geometries	$\Delta G^{\mathrm{LR}}_{\mathrm{SBS}}$	$\Delta G^{\mathrm{cLR}}_{\mathrm{LBS}}$	$\Delta G^{\mathrm{LR+cLR}}_{\mathrm{LBS}}$	$\Delta G^{\mathrm{cLR}}_{\mathrm{ADC(2)}}$	$\Delta G^{\mathrm{LR+cLR}}_{\mathrm{ADC(2)}}$	$\Delta G^{\mathrm{cLR}}_{\mathrm{CC2}}$	$\Delta G^{\mathrm{LR+cLR}}_{\mathrm{CC2}}$
EE* $\rightarrow$ EK*	0.01	-0.13	-0.05	-0.17	-0.09	-0.20	-0.12
EE* $\rightarrow$ KK*	-0.11	-0.26	-0.17	-0.10	-0.01	-0.18	-0.09
EK* $\rightarrow$ KK*	-0.12	-0.13	-0.12	0.07	0.08	0.02	0.03
EE* $\rightarrow$ $\mathrm{TS_{EK^*}}$	0.25	0.18	0.22	-0.05	-0.01	-0.08	-0.04
EK* $\rightarrow$ $\mathrm{TS_{KK^*}}$	0.15	0.10	0.12	0.13	0.15	0.08	0.10
EK* $\rightarrow$ $\mathrm{TS2_{EK^*}}$	0.27	0.25	0.31	0.28	0.34	0.23	0.30
KK* $\rightarrow$ $\mathrm{TS2_{KK^*}}$	0.39	0.37	0.44	0.39	0.46	0.29	0.36
VEM geometries	$\Delta G^{\mathrm{VEM}}_{\mathrm{SBS}}$	$\Delta G^{\mathrm{VEM}}_{\mathrm{LBS}}$	$\Delta G^{\mathrm{VEM}}_{\mathrm{ADC(2)}}$	$\Delta G^{\mathrm{VEM}}_{\mathrm{CC2}}$			
EE* $\rightarrow$ EK*	-0.16	-0.14	-0.20	-0.23			
EE* $\rightarrow$ KK*	-0.43	-0.42	-0.23	-0.30			
EK* $\rightarrow$ KK*	-0.27	-0.28	-0.03	-0.07			
EE* $\rightarrow$ $\mathrm{TS_{EK^*}}$	0.19	0.18	-0.03	-0.05			
EK* $\rightarrow$ $\mathrm{TS_{KK^*}}$	0.15	0.10	0.13	0.08			
EK* $\rightarrow$ $\mathrm{TS2_{EK^*}}$	[a]	[a]	[a]	[a]			
KK* $\rightarrow$ $\mathrm{TS2_{KK^*}}$	[a]	[a]	[a]	[a]			

[a] Calculation of the VEM-UD TS2 EK* and KK* did not converged

As can be seen in Figure 5.2 and deduced from Table 5.4, significant divergences are observed between the results of the different protocols. Despite these discrepancies, all tested methods predict quite large protective barriers for the twisting motion leading to the conical intersection (TS2 in Table

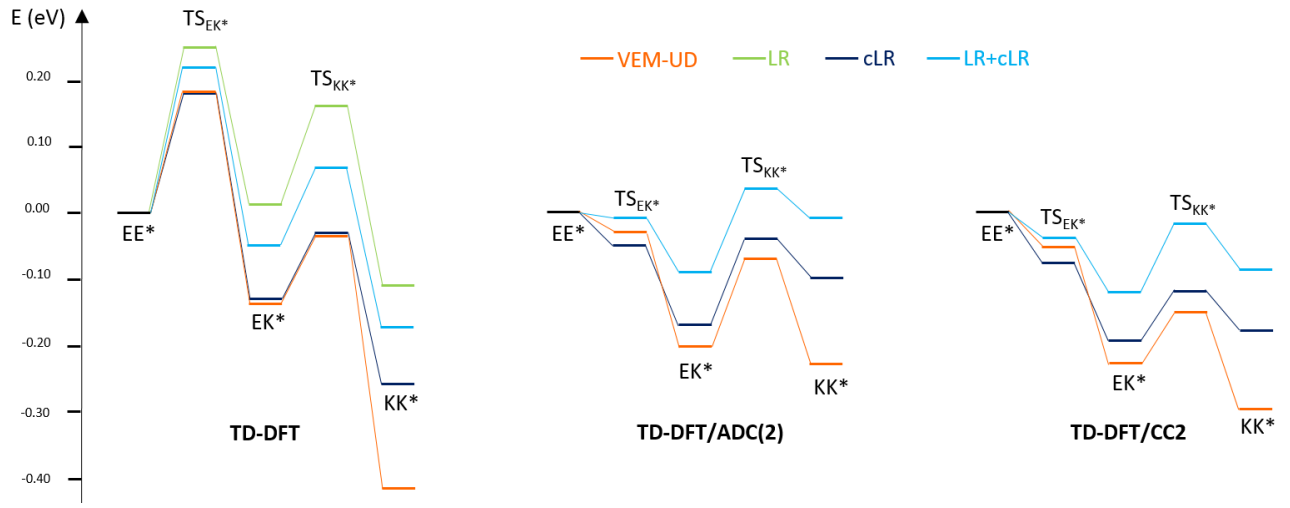

Figure 5.2: ES potential energy surface for the various tautomers of **BBTP** as a function of the selected level of theory.

5.4), and we therefore first focus on the other processes. Amongst all the tested approaches, LR/TD-DFT is the only one predicting a similar energy for EE* and EK*, which is not consistent with the experimental outcomes and allows to exclude LR/TD-DFT from the trustworthy approaches. This is not surprising : as stated above, the ES dipole moments are large and therefore one expects state-specific solvation effects to be non negligible. This also explains why many previous analyses led to inconsistent results.[16–20] With cLR/ADC(2) and LR+cLR/ADC(2) calculations, the trend seems also incorrect for the KK* form: ADC(2) makes the KK* tautomer less stable than EK*, which contradicts the measurement of nearly equal EK* and KK* intensities although the latter has a smaller oscillator strength and is also more red-shifted. Why would a second ESIPT process take place if the final tautomer is less stable ? In contrast, VEM-UD optimisations clearly (and correctly) yield KK* as the most stable tautomers irrespective of the selected electronic structure approach. The formation of EK* (from EE*) is barrierless according to post-HF results but a sizeable barrier is calculated with TD-DFT between these two tautomers which is again inconsistent with experiment (small EE* emission despite a very large oscillator strength). When comparing the cLR/TD-DFT and composite cLR/CC2 approaches, two differences can be observed. First cLR/CC2 gives similar stabilities for EK* and KK* whereas cLR/TD-DFT predicts KK* to be more stable than EK* by 0.13 eV. Without experimental quantum yields available, it is difficult to predict the relative stabilities of these two tautomers and, consequently, to determine which method is the most accurate. The second discrepancy is the height of the computed barrier between EE* and EK*. With cLR/TD-DFT, the barrier is rather large, 0.18 eV, whereas CC2 gives a barrierless transition. Nevertheless, both methods predict the EK* and KK* to be more stable than EE* by more than 0.13 eV, which is the correct trend. Consequently, a more complete description of the solvation effects is reached, as explored in Chapter 3, by adding LR and cLR solvent corrections together, the effects due to the dynamical response of the environment to the quantum-mechanical charge density oscillating at the Bohr frequency, and those due to the rear-

rangement of the electronic density are taken into account simultaneously. Indeed, the LR+cLR/CC2 method, the most complete tested, gives the best overall match with experimental data with a good driving force for the first ESIPT, nearly isoenergetic EK* and KK* and a sizeable barrier between these two tautomers (see Table 5.4). On the one hand, this result is quite gratifying for theory, as the "best" model it indeed the most accurate. On the other hand, is indicates quite obviously that the previous calculations performed with LR-PCM/TD-B3LYP (see Section 5.1),[16,18,19] were most probably not the final call for the present system.

Up to now only the stepwise process was studied. The transition state corresponding to the simultaneous ESIPT at the two centers has also been investigated, but only the stepwise process could lead to a valid transition state. This is in agreement with the conclusions of the theoretical studies of Jia's,[16] Lan's,[19] Lu's,[20] and Zhao's[18] groups: the process should be stepwise because the barrier for synchronous transfer is too high. Furthermore, as stated above, the twisting barriers between the keto states and the conical intersection (TS2) are located ca. 0.3 eV higher than the emissive tautomers, which is relatively high, and translates into an experimentally weak efficiency for this non-radiative deactivation pathway, consistent with efficient fluorescence. Unfortunately, the VEM-UD/TD-DFT optimisations did not converge for the TS2. Additionally we note that VEM-UD TD-DFT calculations are significantly more demanding than the composite LR+cLR/CC2 approach, and we therefore stick to the later in the following.

5.3.4 Absorption

With the electron density difference plots ($\Delta\rho$) (Figure 5.3d), a qualitative estimation of the probability to observe ESIPT can be obtained as discussed in Chapter 3. For the **BBTP**, the $\Delta\rho$ is typical of an ESIPT compound: upon excitation, the density increases on the nitrogen atom whereas a small drop of the density can be observed on the hydroxyl oxygen. Such topology is favourable for ESIPT and consistent with the relative stabilities of the tautomers discussed above.

The computation of the vibrationnally resolved spectrum allows well-grounded comparison between measured and computed data. Indeed the calculated shape and intensity of all peaks can be directly correlated to the experimental spectrum[342,344,345]. The theoretical 0-0 energy, E^{0-0}, can also be compared to the experimental absorption and fluorescence crossing point, AFCP.[342,346–348] The 0-0 energy, E^{0-0}_{CC2}, is evaluated using the adiabatic energy from CC2 calculations corrected by the zero-point and solvent corrections from TD-DFT as follows:[331]

$$\begin{aligned} E^{0-0}_{CC2} &= E^{adia}_{TBE} + \Delta ZPVE \\ &= E^{adia}_{CC2} + \Delta E_{solv.\ correct.} + \Delta ZPVE \\ &= E^{adia}_{CC2} + E^{adia}_{TD\ solvent} - E^{adia}_{TDgas} + \Delta ZPVE \end{aligned} \tag{5.1}$$

Table 5.5: 0-0 and adiabatic energies of EE/EE* given in eV. Energies are determined with composite protocols, see Eq. (5.1).

		ωB97X-D		M06-2X	
E^{0-0}	cLR	LR + cLR	VEM-UD	cLR	VEM
TD-DFT	3.31	3.08	3.25	3.29	3.24
ADC(2)	3.09	2.86	3.04	3.09	3.03
CC2	3.17	2.94	3.18	3.16	3.10
		ωB97X-D		M06-2X	
E^{adia}	cLR	LR + cLR	VEM-UD	cLR	VEM
TD-DFT	3.40	3.17	3.38	3.38	3.33
ADC(2)	3.18	2.95	3.18	3.18	3.12
CC2	3.26	3.03	3.25	3.25	3.20

For EE the experimental energy of AFCP is ca. 3.07 eV whereas the theoretical values are given in Table 5.5. The differences between theory and experiment are in the range of the errors typical of such calculations,[342,346–348] with deviations in the 0.1–0.2 eV domain when CC2 is used. As represented in the Figure 5.3a, the ωB97X-D vibronic spectrum (very) accurately reproduces the shape of the experimental absorption of the starting tautomer, with the presence of three peaks and a shoulder. The quality of the simulation is similar with both solvation schemes: the relative positions of the maxima are nearly perfectly reproduced, whereas the relative intensities are also accurate but for a slight underestimation of the 0-0 band compared to experiment independently of the solvent model applied. An impact of the XCF is observed on the adiabatic and 0-0 energies with VEM model. The energies are decreased with M06-2X especially when post-HF corrections are implemented and E^{0-0} becomes closer from the experimental AFCP. However, no significant change can be observed on the shape of the vibronic spectrum as can be seen in Figure 5.3b.

In the ωB97X-D absorption spectrum, the most important vibronic contributions responsible for the specific topology of the band come from two vibrational modes of the ES. The first at 194 cm^{-1} (A), involves a breathing mode of the thiophene which shortens the H$\cdots$N distance (Figure 5.4a), whereas the second at 1711 cm^{-1} (B) corresponds to an effective conjugation mode, changing the double/single bond character mainly in the central thienyl unit, but also involves wagging of the alcohol hydrogens (Figure 5.4b). Both modes are clearly favourable for trigger ESIPT, as they induce changes of the H-bond lengths, while being strongly coupled to the electronic transition. The four major vibronic peaks appear at 3.33 eV (372 nm), 3.52 eV (352 nm), 3.54 eV (350 nm), and 3.73 eV (332 nm) and respectively correspond to modes A, B, A combined to B (1906 cm^{-1}), and resonant B (harmonic at 3422 cm^{-1}) (those energies values do not match with those displayed on Figure 5.3a, they correspond to the computed energies whereas the spectrum is shifted by 0.186 eV in the Figure 5.3a).

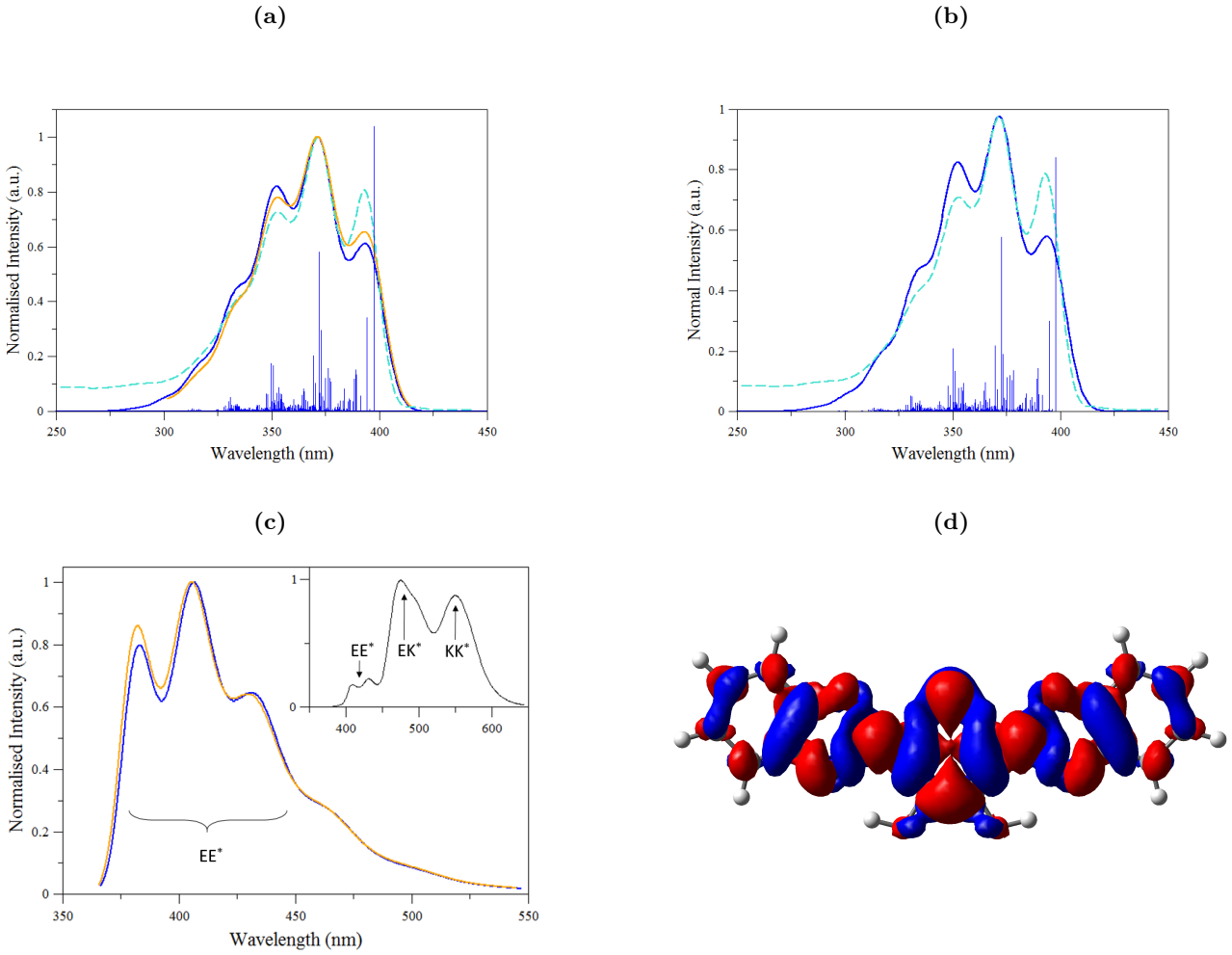

Figure 5.3: Vibrationally-resolved ωB97X-D (a) and M06-2X (b) $S_0 \rightarrow S_1$ absorption spectrum of **EE** and (c) ωB97X-D emission spectrum of **EE***. The theoretical spectrum is in full-line (blue: LR; orange: VEM-UD) and the experimental absorption in dash-line for absorption and shown as an inset for emission. A Half Width of Half Maximum (HWHM) of 0.060 eV and a red-shift of 0.186 eV (a), 0.046 eV (b) have been applied on the theoretical curve. The LR stick spectra are shown as well. Experimental spectra extracted from Ref 15 with permission of Elsevier. (d) Electron density difference plots (isovalue = 0.0004 a.u.) for the **BBTP** derivatives, blue (red) regions indicate decrease (increase) of the density upon absorption of light.

5.3.5 Emission

Experimentally, four maxima appear in the experimental fluorescence spectrum, and they are respectively located at 3.01 eV, 2.87 eV, 2.61 eV, and 2.25 eV. They have been attributed to EE* (two first peaks), EK*, and KK* (see inset in Figure 5.3c).[15] With the help of the calculation of the vibrationnally resolved emission spectrum with ωB97X-D, we indeed confirm that the two first maxima are vibronic bands of the lowest electronic state of EE*, see Figure 5.3c. We note that the ES solvation scheme used to optimise the GS and ES geometries has a trifling impact on the shape of the spectrum,

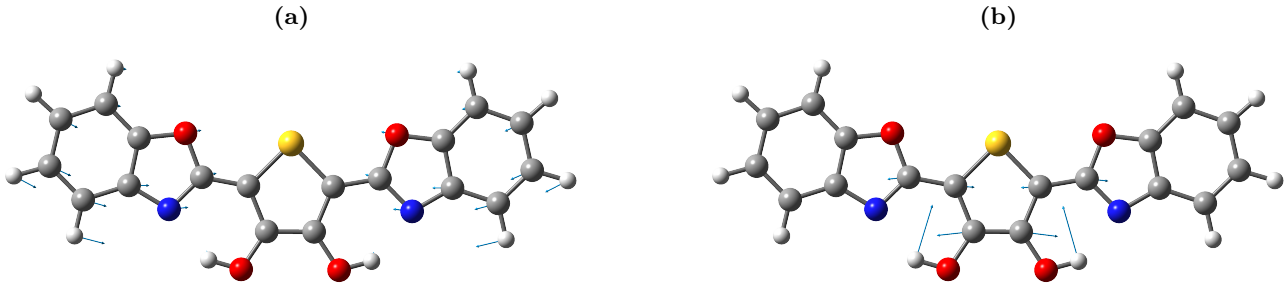

Figure 5.4: Representation of the vibrational modes contributing the most in vibrationally-resolved ωB97X-D absorption spectrum of **EE**. In (a), the frequency A of the ES appearing at 194 cm^{-1} which corresponds to a breathing mode of the central thiophene and in (b), the frequency B of the ES appearing at 1711 cm^{-1} which is a conjugation mode coupled to a wagging of the hydroxy hydrogen atoms.

and that the E_{CC2}^{adia} are almost the same with cLR and VEM-UD, see Table 5.5. This is consistent with the fact that only a moderate influence of the solvation approach on the optimised structural parameters was noticed. The global topology of the vibronic emission obtained with theory nicely explains the presence of two experimental bands in the EE* species. The energy gap between the two lowest energy peaks is 0.18 eV according to theory, nicely fitting the 0.14 eV experimental value. The third band, computed at ca. 425 nm and the shoulder at ca. 455 nm in Figure 5.3c, do not appear in the experimental spectrum, probably because they are buried under the emission of the keto forms. This overlap between the emission of several tautomers is common in multi-ESIPT emitters and hints that only the total emission quantum yield could likely be experimentally determined

Let us now turn toward a comparison of the emission energies of the three tautomers. Based on the previous analyses of the different methods, we go for the LR+cLR/CC2 approach (LR geometries) to compare experimental emission maxima to theoretical vertical transition energies. With this method that neglected vibronic couplings, the gaps between each peaks are nicely reproduced as well as the positions of the peaks which are only underestimated of 0.1 eV, see Table 5.6. Although some error compensation mechanism is likely at play, these agreement between experimental and theoretical results is one more hint that the selected level of theory is valid.

From a more methodological point of view, we interestingly note that the fluorescence energy difference between EK* and KK* is well described by all tested methods at the exception of LR+cLR/ADC(2) whereas the gap between the EE* and EK* emissions strongly depends upon the selected protocol, it goes from 0.15 eV with cLR/TD-DFT to 0.65 eV with VEM-UD/ADC(2) ! By comparing the cLR/TD-DFT and VEM-UD/TD-DFT results, one notes that the fluorescence energies are nearly identical for EE* but larger for EK* and KK* with cLR than with VEM-UD. This is because VEM is a self-consistent and variational scheme. Indeed, the trend in emission energies follows the ES dipole moments (see Section 5.3.2): the largest is μ^{ES}, the largest is the cLR/VEM difference.

The vertical results obtained with the VEM-UD model are closer from the experimental positions of the maxima. With the LR+cLR correction, the description of EK* and KK* is improved compared

Table 5.6: Emission energies from the excited states of all possible tautomers of **BBTP** given in eV, as obtained experimentally,[15] ΔE_{exp}, or calculated with the ωB97X-D functional or post-HF approaches combined with cLR, LR+cLR, and VEM-UD solvent models. The oscillator strengths obtained with cLR/TD-DFT and CC2 are also reported.

	Exp	LR PCM						
	ΔE_{exp}	$\Delta E^{\text{gas}}_{\text{LBS}}$	$\Delta E^{\text{cLR}}_{\text{LBS}}$	$\Delta E^{\text{LR+cLR}}_{\text{LBS}}$	$\Delta E^{\text{LR+cLR}}_{\text{ADC(2)}}$	$\Delta E^{\text{LR+cLR}}_{\text{CC2}}$	f_{cLR}	f_{CC2}
EE*	3.01	3.06	3.04	2.81	2.81	2.91	1.64	1.58
EK*	2.61	2.90	2.89	2.74	2.31	2.52	0.43	0.33
KK*	2.25	2.52	2.50	2.36	1.85	2.11	0.15	0.09
EE* - EK*	0.40	0.16	0.14	0.06	0.59	0.48		
EK* - KK*	0.36	0.38	0.39	0.38	0.46	0.41		
		VEM-UD						
		$\Delta E^{\text{gas}}_{\text{LBS}}$	$\Delta E^{\text{VEM}}_{\text{LBS}}$		$\Delta E^{\text{VEM}}_{\text{ADC(2)}}$	$\Delta E^{\text{VEM}}_{\text{CC2}}$	f_{VEM}	f_{CC2}
EE*		3.10	3.05		3.04	3.14	1.31	1.57
EK*		2.89	2.65		2.20	2.41	0.24	0.36
KK*		2.52	2.27		1.77	2.01	0.06	0.09
EE* - EK*		0.21	0.32		0.65	0.55		
EK* - KK*		0.39	0.37		0.42	0.38		

to the separate LR or cLR results Once again, on the theory side, we note that the VEM-UD approach yields trustable results although the self consistent procedure is more expensive in terms of computational cost. The LR+cLR alternative reveals itself interesting to more rapidly obtain results fitting experiment, especially when coupled to a CC2 calculation. However, we recall, that analytical gradients are not available for LR+cLR, and hence only energies can be straightforwardly obtained which is clearly a limit. No significant variations are observed between ωB97X-D (Table 5.6) and M06-2X (Table 5.7) vertical emission energies obtained with LR geometries. However with the VEM model, the EE* and EK* energies are decreased of 0.1 eV to 0.2 eV with M06-2X, giving less accurate prediction of the fluorescence.

5.4 Design of potential quadruply fluorescent BBTP

In this Section, five substituted dyes are studied. By substituting **BBTP**, we aim at modulating the emission energies and, possibly, to reach quadruply fluorescent compounds by creating less symmetric structures. To this end we evaluated the impact of one electron-withdrawing group (EWG), the cyano group, and one electron-donor group (EDG), the dimethyamino moiety. The studied structures are displayed in Figure 5.5.

Above, we have demonstrated the stepwise character of the double ESIPT process in **BBTP**, and this character is assumed to pertain for the substituted compounds. However, with the introduction of new groups, symmetry is sometimes lost and the number of paths to form KK* increases: two non-

Table 5.7: Emission energy (eV) from the excited-states of EE*, EK*, and KK* of **BBTP**, ΔE_{gas} , $\Delta E_{\text{cLR neq}}$, $\Delta E_{\text{ADC(2)}}$, and ΔE_{CC2} calculated with TD-M06-2X cLR and VEM solvent models. f are the corresponding oscillator strengths.

				LR PCM			
	$\Delta E^{\text{gas}}_{\text{LBS}}$	$\Delta E^{\text{cLR}}_{\text{LBS}}$	$\Delta E^{\text{LR+cLR}}_{\text{LBS}}$	$\Delta E^{\text{LR+cLR}}_{\text{ADC(2)}}$	$\Delta E^{\text{LR+cLR}}_{\text{CC2}}$	f_{LR}	f_{CC2}
EE*	3.05	3.03	2.79	2.80	2.90	1.68	1.58
EK*	2.88	2.85	2.70	2.30	2.51	0.51	0.35
KK*	2.49	2.47	2.33	1.87	2.12	0.11	0.09
				VEM-UD			
	$\Delta E^{\text{gas}}_{\text{LBS}}$	$\Delta E^{\text{VEM}}_{\text{LBS}}$		$\Delta E^{\text{VEM}}_{\text{ADC(2)}}$	$\Delta E^{\text{VEM}}_{\text{CC2}}$	f_{VEM}	f_{CC2}
EE*	3.06	2.84		2.82	2.93	0.91	1.55
EK*	2.86	2.55		2.13	2.34	0.26	0.38
KK*	2.49	2.21		1.75	1.99	0.06	0.10

equivalent starting paths for the ESIPT processes have to be considered, see Figure 5.6. All results presented below for these new dyes have been obtained with the method found to be the most effective for the unsubstituted compound, that is $\Delta G^{\text{LR+cLR}}_{\text{CC2}}$ for the stability and $\Delta E^{\text{LR+cLR}}_{\text{CC2}}$ for the emission energies .

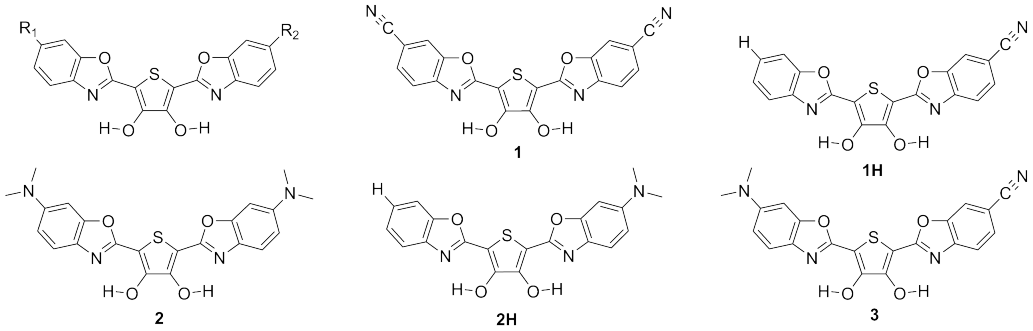

Figure 5.5: Representation of the substituted **BBTP**. **1** : $R_1 = R_2 = CN$; **1H** : $R_1 = H$ and $R_2 = CN$; **2** : $R_1 = R_2 = NMe_2$; **2H** : $R_1 = H$ and $R_2 = NMe_2$; **3** : $R_1 = NMe_2$ and $R_2 = CN$.

The electron density difference plots ($\Delta\rho$) of the different systems are displayed in Figure 5.7. In the case of **1** and **1H**, we find very similar topologies as the original **BBTP** (which as a favourable EDD for ESIPT) for the lowest excited states. For **1H**, which is non-symmetrical, the favourite side (see below) can be intuited: the loss of density is stronger for the oxygen atom of the non-substituted moiety. In **2**, both the nitrogen and oxygen atoms undergo an increase of the density at the excited state which could block the ESIPT process. In contrast, in **2H** and **3**, the density decreases on the oxygen atom of the EDG side. Of course these $\Delta\rho$ plots offer only qualitative pictures of the actual processes and we now turn towards an analysis of the relative energies.

For the five considered compounds, the protective barrier preventing the access to the conical intersection is high enough (between 0.3 - 0.5 eV) to limit the non-radiative deactivation taking place

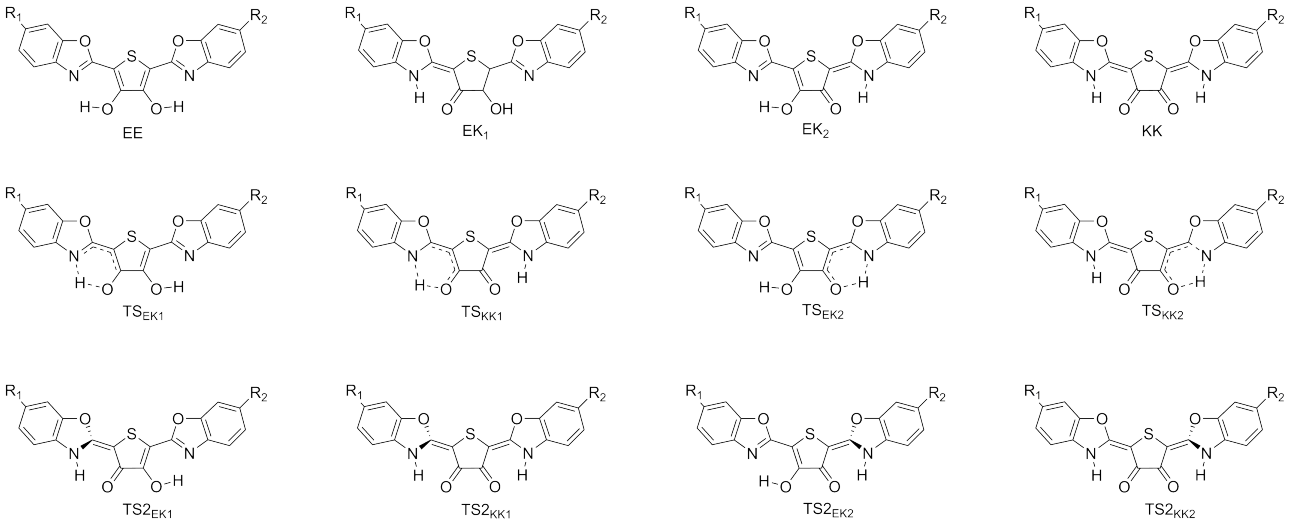

Figure 5.6: Representation of the different tautomers and associated TS and TS2 for substituted **BBTP**.

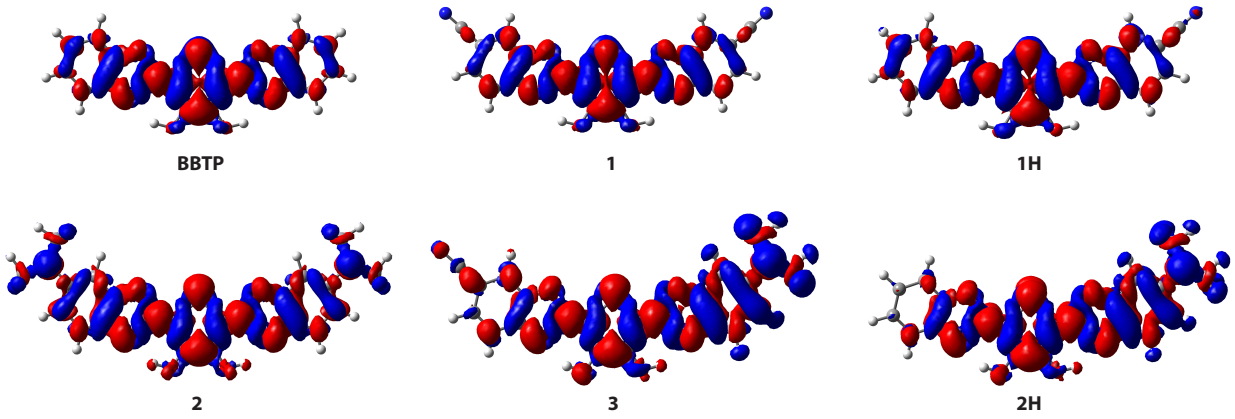

Figure 5.7: Electron density difference plots (isovalue = 0.0004 a.u.) for the (non-)substituted **BBTP** derivatives. Blue (red) regions indicate decrease (increase) of the density upon absorption of light.

through interring rotation in the keto tautomers, and the emission quantum yield is therefore not limited by such phenomena.

The effects of the electro-active groups are significant and depend on the exact substitution pattern. In **1**, the substitution at the *para* position of both benzoxazole groups by a cyano moiety does not change significantly the relative energies of the tautomers and their associated TS compared to the non-substituted **BBTP**, see Tables 5.4 and 5.8. Indeed, EE* remains the least stable tautomer and the relative stabilities of the different ES are of the same order as in unsubstituted **BBTP**, with almost isoenergic EK* and KK* according to LR+cLR/CC2. However the substitution has a small impact on the fluorescence wavelength, with a red-shift of 0.1 eV compared to **BBTP**, see Table 5.9. Such red-shift is often a desired property in practical applications as OLED, fluorescent probes or laser dyes, and we therefore predict that **1** would be advantageous compared to the unsubstituted **BBTP**. By breaking the symmetry of **1** (replacing a cyano group by an hydrogen atom leading to **1H**) two

Table 5.8: Difference of free energy, ΔG_{CC2}^{LR+cLR} , of EE*, EK* and KK* in substituted **BBTP** and corresponding transition state barriers. All values are in eV, see Figure 5.6 for structure representations.

	1	**1H**	**2**	**2H**	**3**
$EE^* \rightarrow EK_1^*$	-0.11	-0.15	0.23	0.32	0.25
$EE^* \rightarrow KK^*$	-0.08	-0.06	0.53	0.41	0.38
$EK_1^* \rightarrow TS_{EK_1^*}$	-0.65	-0.03	0.16	0.17	0.19
$EK_1^* \rightarrow TS_{KK_1^*}$	0.10	0.21	0.35	0.26	0.22
$EK_1^* \rightarrow TS2_{EK_1^*}$	[a]	0.38	0.50	0.41	0.53
$KK^* \rightarrow TS2_{KK_1^*}$	0.44	0.46	0.33	0.37	0.62
$EE^* \rightarrow EK_2^*$	[b]	0.02	[b]	0.24	0.44
$EK_2^* \rightarrow TS_{EK_2^*}$	[b]	0.04	[b]	0.16	0.22
$EK_2^* \rightarrow TS_{KK_2^*}$	[b]	-0.06	[b]	0.15	0.17
$EK_2^* \rightarrow TS2_{EK_2^*}$	[b]	0.24	[b]	0.40	0.45
$KK^* \rightarrow TS2_{KK_2^*}$	[b]	0.37	[b]	0.37	0.54

[a] Calculation of TS2 EK_1^* did not lead to a physical transition state

[b] By symmetry $EK_1^* = EK_2^*$, $TS_1^* = TS_2^*$ and $TS2_1^* = TS2_2^*$

Table 5.9: Emission energy in eV computed for the EE*, EK*, and KK* tautomers of substituted **BBTP**, ΔE_{CC2}^{LR+cLR}, together with the calculated oscillator strengths.

	1		**2**		**1H**		**2H**		**3**	
	ΔE	f_{LR}	ΔE	f_{LR}	ΔE	f_{LR}	ΔE	f_{LR}	ΔE	f_{LR}
EE*	2.86	1.89	2.34	1.95	2.85	1.76	2.34	1.74	2.17	1.82
EK_1^*	2.42	0.37	2.31	1.64	2.37	0.41	2.35	1.61	2.18	0.84
EK_2^*					2.55	0.36	2.33	0.89	-0.27	1.58
KK*	2.02	0.16	2.14	0.17	2.05	0.15	2.11	0.19	1.93	0.20

different single ESIPT can occur. The relative stabilities of the EK_x^* tautomers indicate that ESIPT on the non-substituted side of the compound as EK_1^* is favoured, which is consistent with the $\Delta\rho$ analysis. Nevertheless, accessing EK_2^* should remain possible : its stability is close to EE*(0.02 eV) and the difference with the most stable form is 0.17 eV only. The barrier to populate EK_2^* is negligible and the second ESIPT to reach KK* is also computed to be barrierless. Therefore, only a small (or null) emission from the EK_2^* can be expected, the majority of the EK_2^* should be rapidly converted into KK*. In **1H**, all tautomers present clearly different emission energies which should allow experimental detection of the various bands, though the EK_2^* emission could be absent. The effects of EDG (here an amino group) on similar systems have been characterised as leading to a systematic stabilisation of the enol form.[12] It is effectively the trend observed for **2**, **2H**, and even for the "push-pull" **3**. The keto tautomers are less stable than their enol counterparts, the associated barriers for ESIPT are also

above 0.2 eV in most cases. For these three **BBTP** substituted by at least one EDG, only the enol form will emit, and no ESIPT will take place. If this is no good news for the design of multi-emissive compounds, one positive conclusion is that the fluorescence is red-shifted of 0.5 eV compared to the non-substituted system.

5.5 Conclusions

We successfully characterised the ESIPT processes occurring in a **BBTP** dyes encompassing two ESIPT centres. The four experimental emission bands have been attributed to the three tautomers generated by the two possible ESIPT. Indeed, the strong vibronic couplings present in the EE* form explain the observation of the two first experimental fluorescence peaks (showing small Stokes shifts), whereas the bands with larger Stokes shifts can be attributed to the single- and double-ESIPT products. This analysis is well corroborated by the calculations of the free energies and ESIPT barriers of all tautomers. It should also be underlined that the topology of the excited-state of the enol-enol form, as well as the vibrational modes strongly coupling with the absorption are all favourable to trigger the proton transfer. The investigation of the barriers, protecting from the twisting motion leading to the conical intersection suggests that the non-radiative relaxation is not the main issue limiting fluorescence. Between the different patterns explored, only the stepwise ESIPT transfer process has lead to valid transition states, and we have excluded the possibility of concerted (double) ESIPT, in agreement with the conclusion of Jia[16], Lan[19], Lu[20] and Zhao[18]. Eventually, we designed five substituted compounds through the introduction of cyano and/or amino groups. Only the structures free of amino groups (**1** and **1H**) fullfil the stability criteria required for ESIPT dyes. For **1H**, it is not unreasonable to hope for a triple or quadruple fluorescence due to the symmetry breaking, but with small intensity for half of the bands. To our knowledge, such quadruply-emissive ESIPT dye was not reported to date.

From a methodology point of view, a refined model has to be used to accurately model the ESIPT process taking place after absorption in **BBTP**. Indeed, in the framework of polarisable models, one needs to use solvent polarisation schemes taking into account state-specific effects as well as a couple-cluster approach to obtain energies consistent with experimental findings, whereas, in contrast, "standard" TD-DFT calculation do not provide an accurate picture. Therefore, low cost calculations, e.g., performed with TD-DFT combined to a linear-response solvent model, can easily lead to a wrong interpretation of the data, as exemplified by the relative stabilities of the EE* and EK* forms, incorrectly predicted to be very similar. The VEM-UD approach has been shown to be effective in the present case, which is consistent with the large excited-state dipole moments of the keto forms. Unfortunately the self-consistency process of VEM-UD makes it computationally expensive. An alternative to correct the excitation energies is to combine LR and cLR corrections which allows to obtain results consistent with experiment, especially when CC2 is used to describe the electronic structure. Eventually, in contrast to many known cases, we found here rather significant differences between the

ADC(2) and CC2 descriptions of the relative energies.

Chapter 6

Tuneable fluorescence of a full-colour dye, BTImP

Contents

6.1 A full-colour dye . . . 113

6.2 Computational details . . . 115

6.3 The electronic ground state . . . 115

6.4 Optical properties . . . 123

6.4.1 Absorption of **BTImP** and protonated systems . . . 124

6.4.2 Green fluorescent **BTImP** structure: **3** . . . 125

6.4.3 Red fluorescent structure: **4H** . . . 126

6.4.4 Blue fluorescent structure: **2HH** . . . 128

6.5 Conclusions and Outlook . . . 128

6.1 A full-colour dye

Let us now towards another complex ESIPT case that we have helped in-solving with theory. This Chapter is based on our recent publication on *Phys. Chem. Phys.*.[21] In contrast to the previous Chapter in which a double ESIPT in a symmetric compound was the core of the investigation, we study here a system with several non-symmetric ESIPT centres. This work was also for me the opportunity to supervise a master student, Simon Hédé, during his stay in the group.

Indeed, reaching a highly tunable emission spectrum with the ESIPT strategy has been successfully achieved by Sakai and Tsuchiya with their 2-(1,3-benzothiazol-2-yl)-4-methoxy-6-(1,4,5-triphenyl-1H-imidazol-2yl)phenol (**BTImP**) compound which is able to emit five different colours depending on it environment.[22,23] As seen in Figure 6.1, this fluorophore is composed of benzothiazole (BT) and

imidazole (Im) moieties linked together by a central phenol. The hydrogen atom of the hydroxy group can be switched to form intramolecular interaction with either BT or Im moieties. Depending on the orientation, the observed emissions differ. Taking advantage of this specificity, Sakai and Tsuchiya achieved the control of the emitted colour. More in details, the change of ESIPT site can be induced by the protonation of the compound and, different emission colours are observed has a function of the amount of acid added: green, red, white, and blue (Figure 6.1).

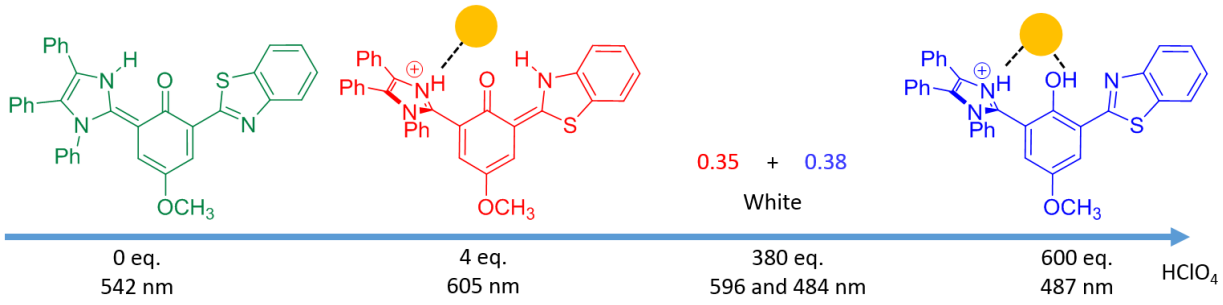

Figure 6.1: Structure proposed by Tsuchiya and co-workers for each observed emission colour as a function of the amount of acid added. The orange circle represents the counter-ion.

In the seminal 2016 BTImP paper,[22] a switch of the ESIPT between the Im and BT parts was reported to give green and orange fluorescences, respectively. The authors attributed the green emission to the K* form resulting from an ESIPT with the Im moiety, whereas the orange fluorescence, observed in acidic conditions, was ascribed to an ESIPT taking place with the BT part. This assignment was supported by X-Ray analysis of the structure before and after protonation. In 2018, the same group published an in-depth study of the protonation effects on the optical properties of **BTImP**.[23] They investigated the impact of the amount of acid, the solvent, and the nature of the counter-ion on the structure and optical properties of the dye. The protonation was shown to be localised on the Im side at the ground state thanks to X-ray and NMR (^{1}H and ^{15}N) studies. With a small addition of acid in dioxane, the emission turns red due to an ESIPT with the BT moiety, whereas a huge amount of acid yields blue fluorescence. They explained this second emission by an interaction between the phenol and the anion, blocking the ESIPT process. White emission can be observed as well when a proper balance between blue and red emitting species is reached. We stress that the only presumed difference between the red and blue emissions is the binding mode of the anion to the dye, see Figure 6.1.

The group of Yuan[349] previously used DFT and TD-DFT to investigate some isomers to identify the forms involved in the emission. This former theoretical study did not took into account the effects of the complexation with anions, which was an highlight in the experimental work published by the Tsuchiya group.[23] Prior to our work there was, to the best of our knowledge, no other investigations of this compound with ab inito tools. In the present Chapter, we explore all possible conformers of **BTImP** an its protonated forms to provide deeper insights into the experimental results. The effect of three anions (BF_4^-, ClO_4^-, and Cl^-), are modelled with (TD-)DFT and wavefunction approaches. We aim at an improved understanding of the observed diversity of the fluorescence by studying the stability and

spectroscopic properties of all isomers. All our calculations take into account of solvent effects through the use of the polarizable-continuum model (PCM) with 1,4-dioxane (DOX) and tetrahydofuran (THF) as solvents, whereas anions are explicitly added. The strength of the theoretical protocol used for ESIPT systems previously has once more been tested on this new challenging compound.

6.2 Computational details

All DFT and TD-DFT calculations are performed using the Gaussian16[328] program. During the DFT calculations we use improved energy (10^{-10} a.u. for ground-state, GS, and 10^{-8} a.u. for excited state, ES), and geometry optimisation (10^{-5} a.u.) convergence thresholds and apply the so-called *ultrafine* DFT integration grid. All (TD-)DFT calculations are performed with the M06-2X XCF. The GS and ES are optimised with the 6-31G(d) atomic basis set whereas more extended atomic basis set, 6-311+G(2d,p), is used for the TD-DFT transition-energy calculations. Below, we refer to these two bases as SBS (small) and LBS (large) respectively. Relaxed scans have been performed with the 6-31G(d) atomic basis set when needed to identify all conformers. The bulk environment effects are modelled with the PCM model applying the standard linear-response[334] scheme in its equilibrium limit for the DFT and TD-DFT geometry optimisation and frequency calculations, and the corrected LR[321] scheme in its non-equilibrium limit for the computation of the vertical absorption and fluorescence. The LR and cLR corrections are also simultaneously accounted for, this model gives interesting results as seen in previous Chapters 4 and 5. Calculations of the analytic frequencies are performed with the same atomic basis set [6-31G(d)] for all the GS and ES structures To investigate the nature of the transitions, density difference plots, $\Delta\rho$, are obtained from the difference in the total density of the ES and GS. A contour threshold of 0.001 a.u. is used for the representation. NMR shielding of ^{1}H and ^{15}N are computed at the GIAO-B3LYP/cc-pVTZ level in solution (PCM), using TMS and ammonium as references, respectively.

All post-HF calculations [MP2, ADC(2), and CC2] are realised using Turbomole 6.6[329] program. ADC(2) calculations rely on the so-called ADC(2)-s formalism[309] and both post-HF methods use the resolution of identity technique.[327,335] The *aug*-cc-pVDZ atomic basis set is applied for post-HF transition-energy calculations. The electronic MP2 and CC2 energies of the system at the GS are also calculated, with *aug*-cc-pVTZ.

6.3 The electronic ground state

The **BTImP** molecule presents different possible ESIPT sites. To determine which form is associated to each emission colour, the stability of the different possible isomers in the ground electronic state is first investigated. Rotations around the bonds between i) the phenol and the benzothiazole (**1** and **3** ; **2** and **5** in Figure 6.2), and ii) the imidazole and the phenol (**2** and **4**) can be used to build different conformers. This list is completed by testing two possible hydrogen bonding patterns (**1** and **2**). As

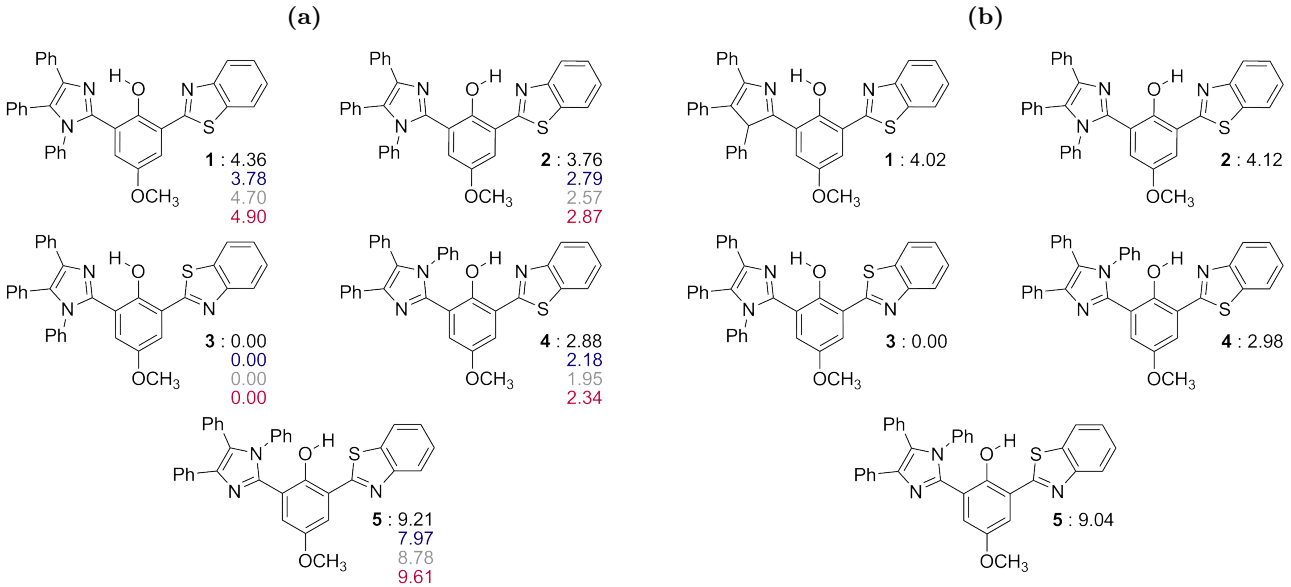

Figure 6.2: Conformers of **BTImP** resulting from the rotation of the substituents around the phenol core. Relative GS free energies (kcal/mol) in DOX (a) and THF (b). Black: $\Delta G^{\mathrm{LR}}_{\mathrm{SBS}}$; blue: $\Delta G^{\mathrm{cLR}}_{\mathrm{LBS}}$, eq. 3.43; grey: $\Delta G^{\mathrm{cLR}}_{\mathrm{MP2}}$, eq. 3.45; and red: $\Delta G^{\mathrm{cLR}}_{\mathrm{CC2}}$, eq. 3.45

can be seen in Figure 6.2, in which we list relative GS energies, the impact of the corrections brought by the LBS or the post-HF approaches is limited to ca. 1 kcal/mol for the relative energies. Therefore it does not appear necessary to include those corrections to investigate the relative stabilities. Indeed such 1 kcal/mol differences are in the range of the typical errors provided by DFT, and the fact that CC2 yields the very same trends in Figure 6.2 is reassuring.

Independently of the calculation level chosen to estimate the free energy, the most stable isomer is **3**, in agreement with the experimental X-Ray structure (with a mean absolute deviation between X-Ray and theoretical bond distances in DOX, of 0.011 Å only, see Table 6.1a and Figure 6.3a) which is a significant improvement over the previous theoretical analysis of this system.[349] Indeed, in the contribution of Yuan et al., structure **1** and another similar structure to **4** were investigated but **3** was not reported.[349] The conformers **2** and **4** are also close in energy to **3**, with a difference of 2–3 kcal/mol. As expected the least stable structure is **5**, as its intramolecular H-bond is weaker. The nature of the solvent (DOX or THF) has no influence on the general trends which designates **3** as the most stable form as reported in Figure 6.2.

To explore protonation effects, we start with the five previous conformers and protonate their Im or BT parts, then eliminating duplicates leads to structures displayed in Figure 6.4. Three forms could not converge to a separate minimum, the ones presenting no intramolecular hydrogen interactions (**4'H**, **5H**, and **5'H**), the optimisation leading back to other conformers (**1H**, **3H**, and **3'H**, respectively). Constrained optimisations have been tried without success. The enol nature of the GS is confirmed by looking at relative stabilities of the keto tautomers displayed in Figure 6.4a. In terms of relative

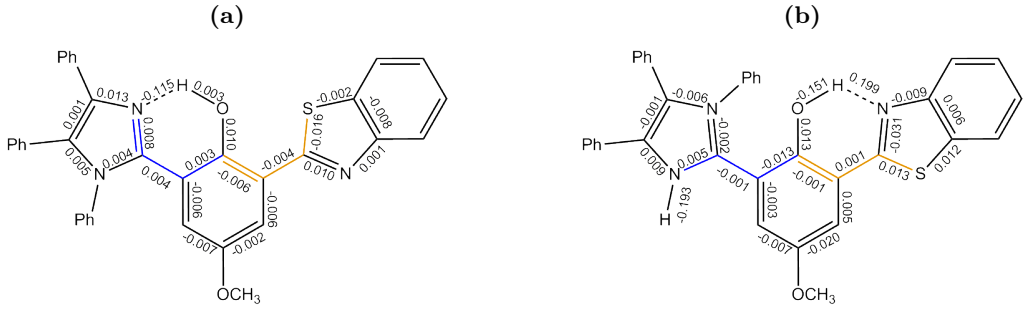

Figure 6.3: Bond lengths (Å) difference between measured structures with X-Ray (experimental values from Ref. 22) and optimised form at the PCM(DOX)/M06-2X/6-31G(d) level for **BTImP**/**3** in (a) and **BTImPH**$^+$/**4H** in (b). Theoretical and experimental bond lengths details are reported in Table A-6 in Appendix 7.2. The two dihedral angles considered in Table 6.1b are displayed in colour as well.

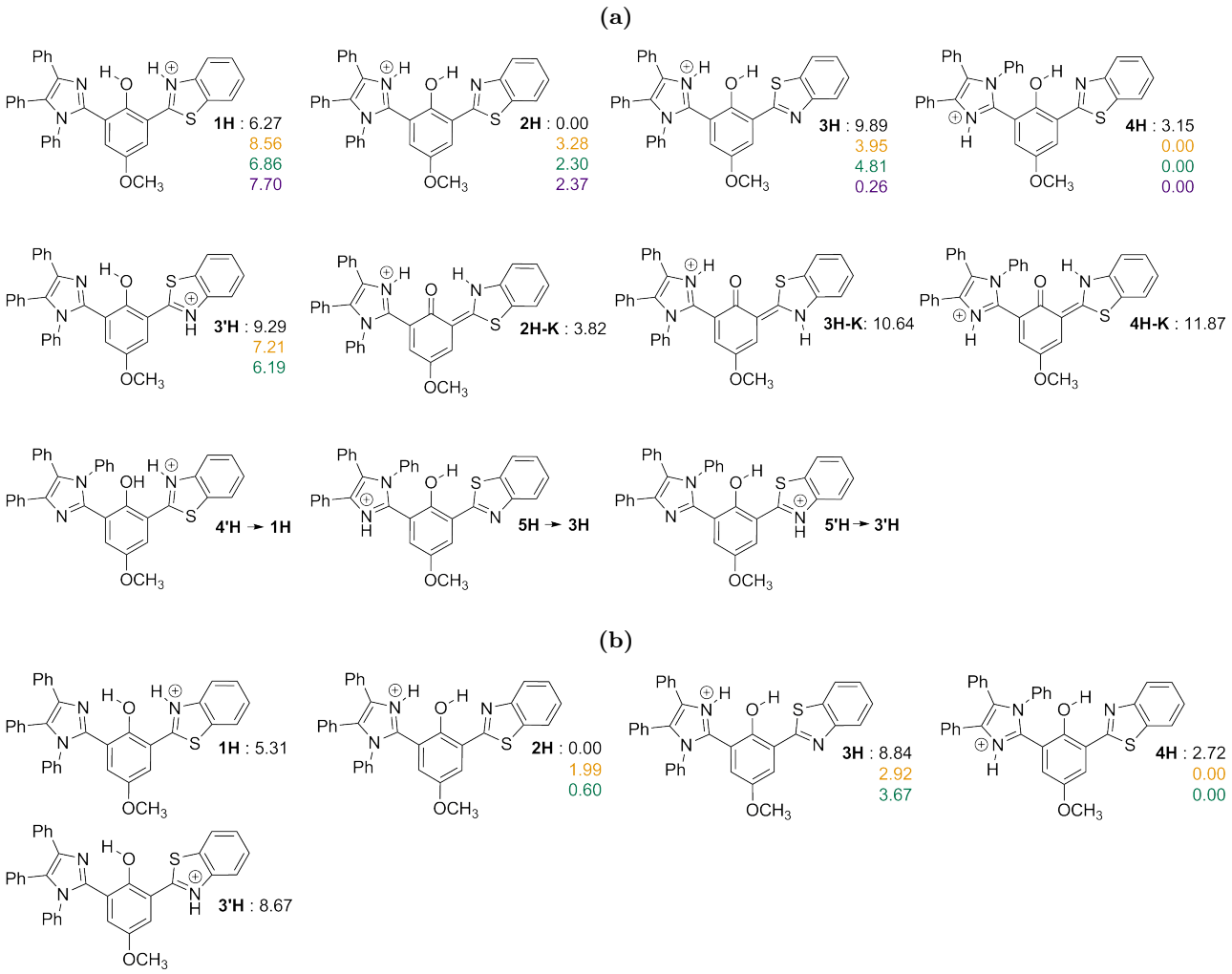

Figure 6.4: Protonated **BTImP** conformers. The relative free energy $\Delta G^{\mathrm{LR}}_{\mathrm{SBS}}$ in DOX (a) and THF (b) is indicated in kcal/mol. Black: without anion, orange: BF_4^- , green: ClO_4^-, and purple: Cl^-. The structures with their counter-ion are displayed in the Figures A-3 and A-3 in Appendix 7.2.

Table 6.1: (a) Mean absolute deviation (MAD), mean signed deviation (MSD), and maximum positive and negative deviations ($MaxD^+$ and $MaxD^-$) in Å between theoretical and experimental bond lengths for **3**. (b) Dihedral angles (degree) in **BTImP**/**3** and $\mathbf{BTImPH^+}$/**4H** optimised at the PCM(DOX)/M06-2X/6-31G(d) level and measured with X-Ray (experimental values from Ref. 22). D.1 is the dihedral angle between the Im and phenol parts and D.2 the dihedral angle between the BT and phenol, respectively represented in blue and ocher in Figure 6.3

(a)

	BTImP	$\mathbf{BTImPH^+}$
MAD	0.011	0.028
MSD	-0.005	-0.008
MaxD	0.013	0.133
MinD	-0.115	-0.156

(b)

	Theoretical	Experimental[22]
D.1 **BTImP**	-21.7	-10.0
D.2 **BTImP**	1.4	-2.0
D.1 $\mathbf{BTImPH^+}$	-132.5	-112.3
D.2 $\mathbf{BTImPH^+}$	-178.5	-177.9

ranking, **2H** and **3H** are the structures the most impacted by the protonation compared to their non-protonated forms. The protonation of the imidazole of **3H** decreases the intramolecular hydrogen bond strength, whereas for **2H**, one observes the opposite effect, the protonation inducing an extra stabilising intramolecular interaction that was absent in **2**. **1H** has also two intramolecular H-bonds but the system prefers to localise the charge on the imidazole moiety rather than on the benzothiazole group unlike its (maybe naive) Lewis' representation of Figure 6.4 (see Figure 6.5 and Table 6.2). Indeed, in the case of a protonation of the imidazole moiety (**2H**, **3H**, and **4H**), the positive charge is completely localised on this part of the system, whereas the protonation of the benzothiazole (**1H** and **3'H**) yields to a charge shared by the two sites, with ca. 0.3 and 0.7 positive charges on the benzothiazole and imidazole moieties, respectively (see Table 6.2).

The impact of counter-ion on the stability trend is explored as well. First, the complexation energies of various conformers are determined for BF_4^-, ClO_4^-, and Cl^- counter-ions. With counterpoise correction, a complexation energy of more than 70 kcal/mol is determined for all systems in gas phase, see Table 6.3. This large value can be explained by the strong Coulombic interaction between $\mathbf{BTImPH^+}$ and the anion. When considering the solvation, we use implicit solvent model and the counter-ion is constrained to remain relatively close of the dye. As expected, the counter-ion systematically interacts with one acidic proton (see Figures A-3 and A-4 in Appendix 7.2 for 3D representations), the position of the anion being typically close of the formal positive charge displayed in Figure 6.4. For the **3H'** and **4H** systems, this affirmation is verified by the investigation of an additional configuration where the counter-ion is near the hydroxy hydrogen because of the well separated localisation of the acidic and hydroxy hydrogens, see Figure 6.6. The interaction with the acidic proton, as for the other structure, is clearly favourable with a difference of more than 10 kcal/mol of difference between the both options. More importantly, with the selected level of theory, the counter-ion strongly impacts the relative stabilities of the different conformers. The most stable conformer in presence of the counter-

Table 6.2: Potential atomic charges determined for various fragments calculated with the Mertz-Kollman model at the PCM(DOX)-M062X/6-311+G(2d,p) level for the **BTImPH**$^+$ and **BTImPH**$_2^+$ conformers with and without a counter-anion (two counter-ions for **BTImPH**$_2^+$).

	1H				**2H**				**3H**			
	Ø	BF_4^-	ClO_4^-	Cl	Ø	BF_4^-	ClO_4^-	Cl	Ø	BF_4^-	ClO_4^-	Cl
Imidazole	0.8	0.7	0.8	0.5	1.1	1.2	0.8	0.9	1.0	0.0	1.0	0.8
Benzothiazole	0.3	0.3	0.2	0.3	0.0	0.0	0.1	-0.1	0.1	0.0	0.0	-0.1
phenol	-0.1	-0.1	-0.1	0.0	-0.1	-0.3	0.0	-0.1	-0.1	0.0	-0.2	-0.1
Anion	0.0	-0.9	-0.9	-0.8	0.0	-0.9	-0.9	-0.7	0.0	0.0	-0.8	-0.7
Total	1.0	0.0	0.0	0.0	1.0	0.0	0.0	0.0	1.0	0.0	0.0	0.0
	4H				**3H'**				**2HH**		**3HH**	
	Ø	BF_4^-	ClO_4^-	Cl	Ø	BF_4^-	ClO_4^-		Ø	Cl_4^-	Ø	ClO_4^-
Imidazole	1.1	0.9	0.9	0.9	0.7	0.6	0.6		1.2	0.9	1.1	1.0
Benzothiazole	0.0	0.0	0.0	0.0	0.3	0.3	0.3		0.7	0.6	0.3	0.6
phenol	-0.1	0.0	0.0	-0.1	-0.1	0.0	0.0		0.1	0.2	0.1	0.0
Anion	0.0	-0.9	-0.9	-0.8	0.0	-0.9	-0.9		0.0	-1.7	0.0	-1.6
Total	1.0	0.0	0.0	0.0	1.0	0.0	0.0		2.0	0.0	2.0	0.0

ion is **4H** irrespective of the nature of the anion, in contrast to **2H** when the counter-ion is neglected (Figure 6.4). In fact as stated above, **2H** enjoys two intramolecular hydrogen bonds but this pattern is partially destroyed by the anion. The **4H** structure is also the one found in experimental X-Ray of the red fluorescent compound. The MAD is 0.028 Å between bond lengths of the latter and our calculated 4H-Cl^--DOX structure (see Table 6.3 and Figure 6.3b). This match between the most stable conformer in presence of counter-ion and the X-Ray result highlights the importance of the inclusion of counter-ion to accurately reproduce experimental results. The conclusion drawn from this stability study performed in DOX are conserved in THF, see Figure 6.4.

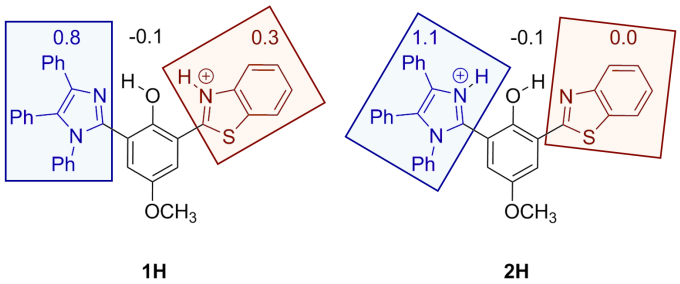

Figure 6.5: PCM(DOX)-M06-2X/6-311+G(2d,p) repartition of the Mertz-Kollman charge for **1H** and **2H**. In blue, the charge carried by the imidazole part, in black by the phenol moiety and in brown by the benzothiazole group.

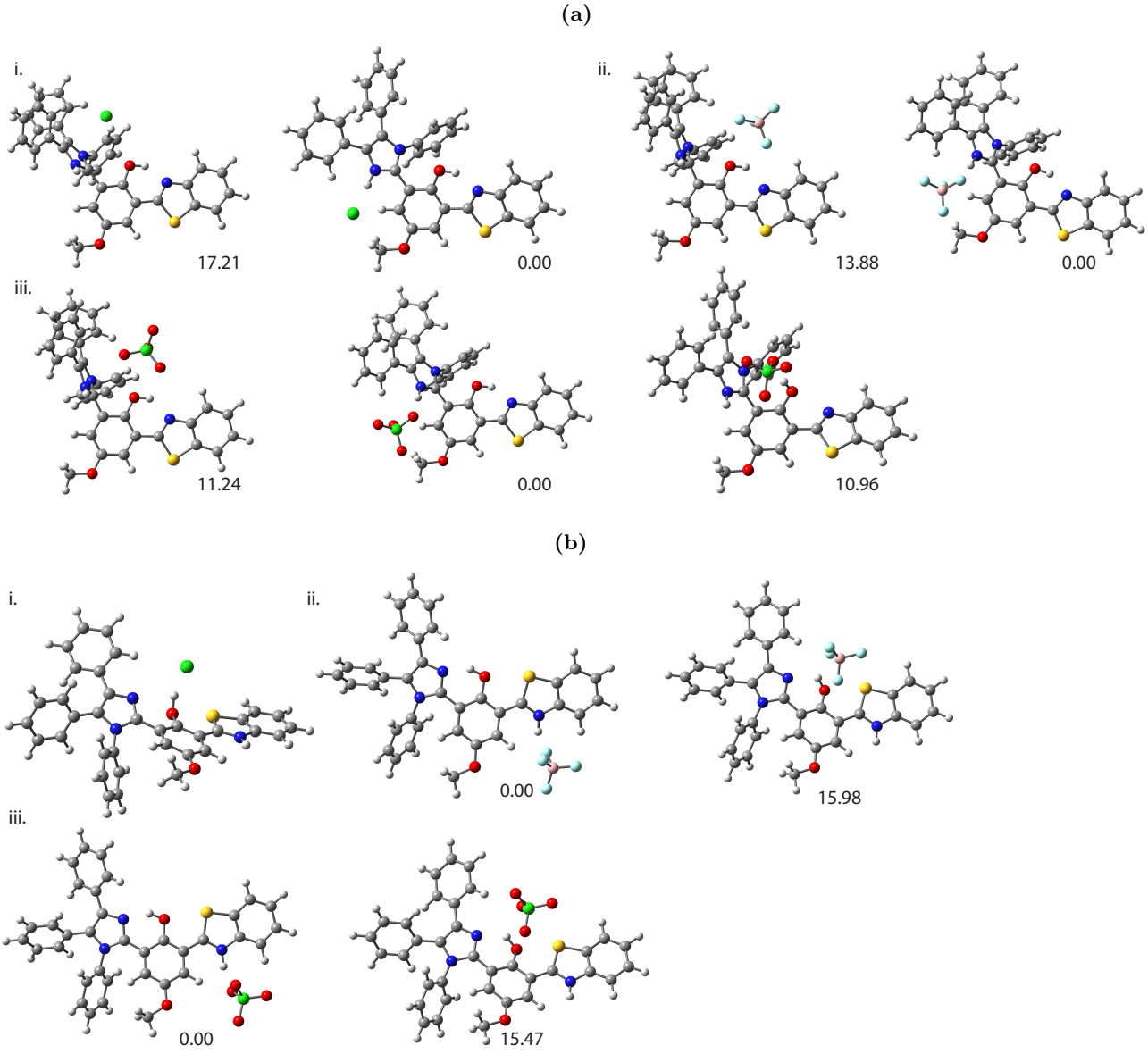

Figure 6.6: Representation of the optimised ground state of **4H** (a) and **3'H** (b) with i. Cl^-, ii. BF_4^-, and iii. ClO_4^- counter-ion. Relative stability depending of anion localisation is reported in kcal/mol. The optimisation of **3'H** with the Cl^- anion in interaction with the benzothiazole moiety did not converged.

Table 6.3: Complexation energy (kcal/mol) computed at the gas-M06-2X/6-31G(d) level on the PCM(DOX)-M06-2X/6-31G(d) structures. The counterpoise correction was applied. For **2HH** and **3HH**, two counter-ion are included in the system and the total complexation energy divided by two is reported.

	1H	**2H**	**3H**	**4H**	**3H'**	**2HH**	**3HH**
BF_4^-	-82.01	-78.18	-93.20	-88.80	-87.62	-	-
ClO_4^-	-76.00	-76.49	-89.61	-85.63	-84.28	-119.20	-118.08
Cl^-	-99.17	-93.87	-111.82	-100.52	[a]	-	-

[a] Calculation of **3'H** with the Cl− anion in interaction with the benzothiazole moiety did not converged.

The quantity of acid added experimentally to obtain a blue emission is huge (see Figure 6.1), and it is therefore interesting to have a look at the doubly protonated structures (Figure 6.7). All conformers have been investigated without counter-ion or in presence of two anions to form neutral entities. On the four tested conformers, **4HH** could not be minimised, whereas **2HH** is always the most stable form independently of the presence or not of counter-ions. As can be seen in Figure 6.7, **3HH** is really close in energy from **2HH** with $\Delta G^{\mathrm{LR}}_{\mathrm{SBS}} = 0.26$ kcal/mol in the absence of anions, but the difference becomes much larger when the two anions are accounted for.

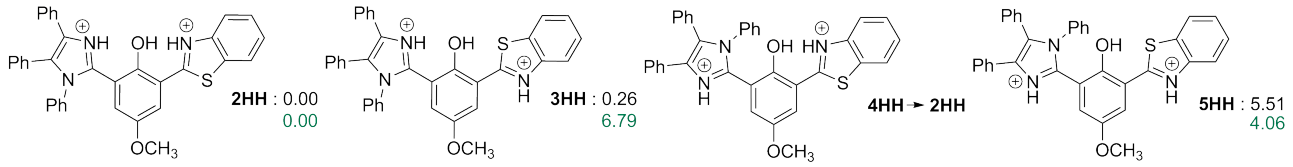

Figure 6.7: Doubly protonated **BTImP** conformers. Relative free energy, $\Delta G^{\mathrm{LR}}_{\mathrm{SBS}}$, in DOX is indicated in kcal/mol. Black: without anion, green: ClO_4^-. To consider the effect of ClO_4^-, two counter-ions are integrated as reported in Figure A-5 in Appendix 7.2.

In short, based on our calculations, **3** is the most stable conformer in DOX solution. Once $HClO_4$ or HBF_4 is added to the solution, the protonation of **3** forms **3H** and this structure is no longer the most stable. Depending on the neglect or consideration of the counter-anion in the calculation, **2H** or **4H** becomes the most stable isomer. It is noteworthy that **4H** is the structure found by X-Ray by Sakai and Tsuchiya in their X-Ray study,[22] which is consistent with our calculations in presence of counter-ion even if we do not use an explicit model for the solvent molecule. Finally in highly acidic media, **2HH** is likely to appear.

While our results are consistent with experiment, the path to reach **4H** from **3** has also to be explored. Two possibilities are considered: i) successive twists of **3** into **4** before the protonation, Figure 6.8-a, and ii) protonation of **3** into **3H** followed by rotations leading to **4H**, Figure 6.8-b and c. For the first option, the structure has to turn into less stable forms, furthermore rather high barriers have to be crossed (10 kcal/mol), which is not optimal and this path can logically be discarded. The second path seems more realistic. Without counter-ion **3H** can easily transform into **2H**, the barrier

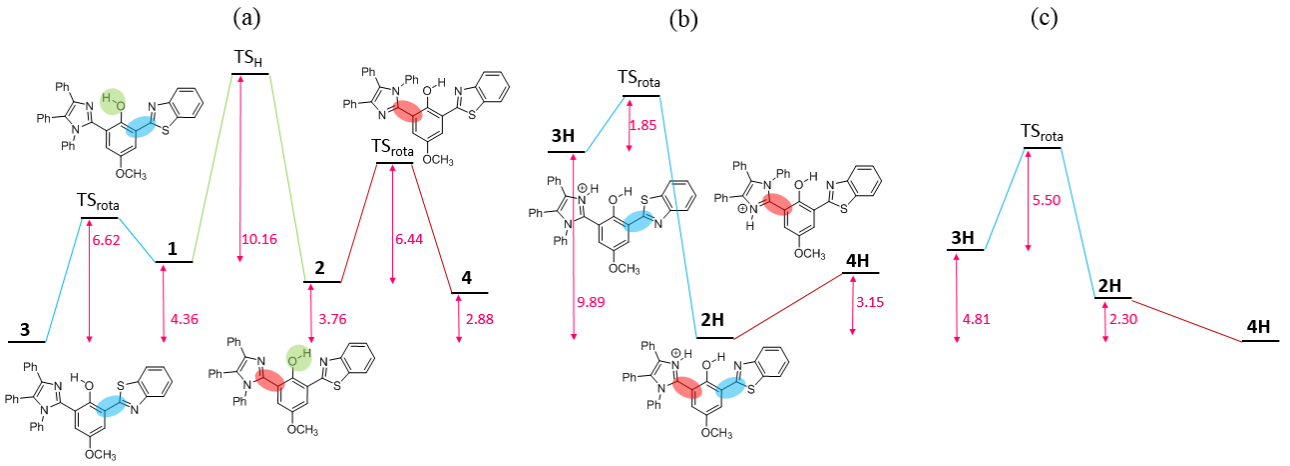

Figure 6.8: Paths to obtain **4H** from **3**. Relative electronic energies (in kcal/mol) are obtained at PCM(DOX)-M06-2X/6-31G(d) level. In a) the path i with the rotation before protonation is represented. Path ii with protonation of **3** followed by rotations is represented in b) and c) without counter-ion and with ClO_4^-, respectively. TS_{rota} and TS_H are optimised transition states (one imaginary frequency), corresponding to the twist between the phenol and the benzothiazole groups, and the change of interacting side for the hydrogen atom of the phenol, respectively. The transition from **2H** to **4H** (or vice-versa) is barrierless in both cases.

being smaller than 2 kcal/mol whereas 5.5 kcal/mol should be overcome in the presence of ClO_4^-. Between **2H** and **4H** no barrier has been detected. Barriers between **2H** and **4H**, in presence or absence of counter-ion could not be located. Relaxed scans from **2H** to **4H** in presence of counter-ion or from **4H** to **2H** in absence of counter-ion give a constant decrease of the energy. The protonation of **3H** followed by a fast rotation to **2H** before complexation with a counter-ion, and a second twist leading to **4H**, would be the most favourable option. However the strong interaction energies calculated between the compound and counter-ion hint at an immediate interaction with the counter-ion. For the formation of **2HH**, the transition state between **4HH** and **2HH** has not been investigated due to the "direct transformation" of **4HH** into **2HH** during the optimisation process (see Figure 6.7).

NMR measurements are reported in the experimental study to characterise the protonation effects on the structure.[23] The measurement are made in both DOX and THF with addition of $HClO_4$ for the ^{1}H NMR. The ^{15}N NMR was registered in THF with addition of $HClO_4$ or HBF_4. In regards of the experimental data, the NMR results in THF are discussed here. No significant change of the NMR signal has been calculated when selecting the other solvent. NMR chemical shift calculated in THF and DOX are available in Tables A-7 A-8 in the Appendix. In the stability study, the **BTImP** in its neutral form has been assigned to conformer **3**. The comparison of experimental chemical shifts (δ) to their theoretical counterparts for **3** shows a difference of less than 0.4 ppm for the ^{1}H NMR and 4 ppm for the ^{15}N NMR, see Table 6.4. As such errors are typical of DFT GIAO calculations,[350–352] these results therefore corroborate the data of the previous Section.

Tsuchhiya and co-workers[23] reported the decrease and next the disappearance of the chemical signal at 6.4 ppm (H_6) after addition of $HClO_4$ in THF. They suggested a rotation of the imidazole (induced

Table 6.4: Experimental and theoretical NMR chemical shifts, δ (ppm), of **BTImP** (**3**) and difference of NMR chemical shift (ppm) between **BTImP** (**3**) and protonated forms, $\Delta\delta$, in THF calculated at the PCM-B3LYP/cc-pVTZ level and experimentally measured. Experimental values are taken from Ref. 23. In the left, labels are reported in purple for **3**, we use the same numbering for the protonated structures.

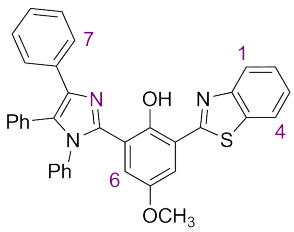

	δ		$\Delta\delta$						
	BTImP		**2H**		**3H**		**4H**		**BTImPH$^+$**
	3	EXP	$\emptyset$	ClO_4^-	$\emptyset$	ClO_4^-	$\emptyset$	ClO_4^-	EXP
H6	6.4	6.4	0.1	-0.1	0.0	-0.1	0.5	2.3	[0.8-1.2]
H7	8.5	8.1	-0.4	0.4	-0.4	0.4	-0.5	0.7	-0.3
H1	8.3	8.0	0.0	0.0	0.0	0.0	0.0	-0.1	0.1
H4	8.3	8.0	0.0	0.2	0.1	0.0	0.0	0.0	0.2
N	242	246	-81	-64	-79	-66	-77	-64	-63

by the protonation) to explain this effect on the H_6 proton. Consistently with this analysis, only **4H** with a flipped imidazole presents a deshielded signal after protonation according to our calculations (Table 6.4). The measured difference of peak position between **BTImP** and **BTImPH$^+$**, $\Delta\delta_{\mathbf{EXP}}$, is between the calculated $\Delta\delta^{\emptyset}_{\mathbf{4H}}$ and $\Delta\delta^{\mathrm{ClO4}}_{\mathbf{4H}}$, see Table 6.4. In our calculations, the structures are frozen and we can reasonably assume that the reality is in between these two models as the exact position of the counter-ion should fluctuate and therefore that **4H** is indeed the isomer formed after protonation in agreement with the computed free energies. Protonation induced changes of H_1, H_4, and H_7 signals are insignificant. As for δ_{H6}, δ_{H7} is deshielded in presence of the anion which is close to these two hydrogen atoms, see Figure 6.6a. The unsubstituted nitrogen atom on the imidazole side that undergoes protonation, has been experimentally marked and its ^{15}N NMR spectrum recorded. A shift of 63 ppm of the signal was obtained after protonation.[23] With our calculations, we corroborate this analysis: a change of ca. 65 ppm is found for the three reported forms in presence of ClO_4^-, and 80 ppm without counter-ion. With a DFT-KT3/pcS-3 approach, Semenov et. al. have studied the influence of i) protonation and ii) counter-ion, on the ^{15}N NMR signal of a N-methylimidazole.[352] They reported respective shifts of 80 ppm and 65 ppm with and without the presence of the counter-ion, values perfectly in line with ours.

6.4 Optical properties

Before discussing emission wavelengths, let us first investigate if the K* structures can be emissive. The barrier separating the K* from the conical intersection, TS2*, could not be optimised directly for the protonated structures, probably due to the limitations of TD-DFT near points of near-degeneracy. However a relaxed scan of the potential energy surface has been performed and no maximum of energy could be observed, only a constant increase of the electronic energy upon rotation from 0° to 60°. A twist of the dihedral angle between the two groups involved in the ESIPT by more than 50° induces

structures less stable by ca. 5 kcal/mol (0.2 eV) in the ES as compared to the original near planar structures for all the forms tested. Even considering the approximate nature of the method, it is reasonable to assume that this barrier is large enough to protect the system from going back to the GS through this typical non-radiative path of ESIPT compounds, which is consistent with the experimental observation of fluorescence: would the twisting mechanism be efficient, no emission would be observed.

As explained above, structure **3** fits very well experimental X-Ray and NMR data of the **BTImP** form. Based on this observation, the absorption and emission spectra of **3** are used as reference to discuss the effects of the protonation on the observed fluorescence in the next section.

6.4.1 Absorption of BTImP and protonated systems

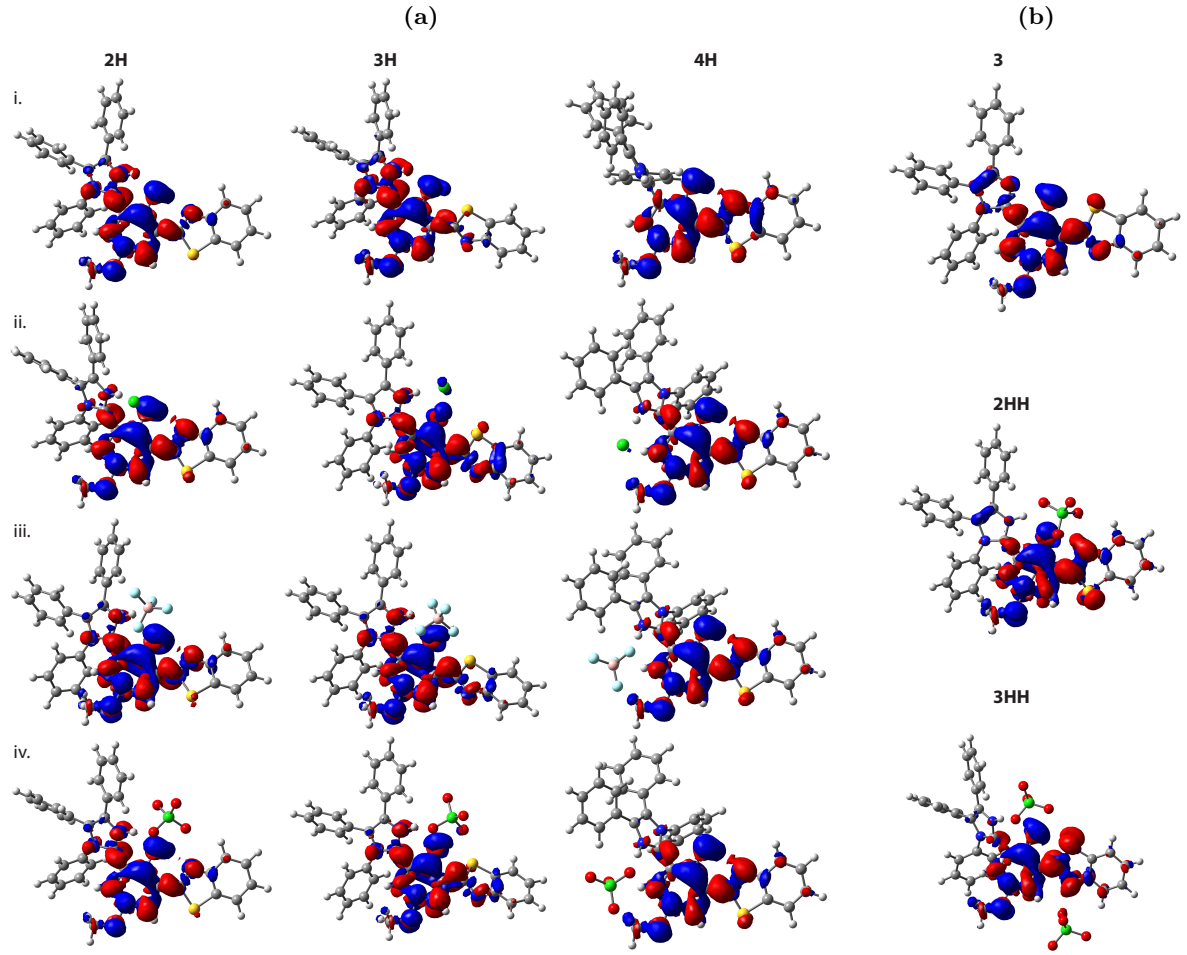

Figure 6.9: Electron density difference between ES and GS (isovalue = 0.001 a.u.) of **BTImP** and its protonated forms calculated at the PCM(DOX)-TD-M06-2X/6-311+G(2d,p) of **2H**, **3H**, and **4H** in (a) and **3**, **2HH**, and **3HH** in (b). Cl^-, BF_4^-, and ClO_4^- counter-ions are respectively included in ii, iii, and iv. For **2HH** and **3HH** two ClO_4^- are also present. For i. and **3**, no counter-ion is considered. Blue (red) regions indicate decrease (increase) of the density upon absorption of light.

The experimental maximum of absorption of **BTImP** was recorded at 3.31 eV in DOX.[23] Our

computation using ADC(2)/LR+cLR approach for **3**, reproduces this energy accurately with an error smaller than 0.1 eV whereas the equivalent TD-DFT approach yields a larger, yet acceptable, difference (Table 6.5). Although vibronic effects are neglected in these calculations, so that comparisons should be made with care, it seems that the ADC(2)/LR+cLR method is well suited for describing the absorption and is therefore used for the protonated systems (*vide infra*).

Table 6.5: Absorption (E) and emission energies (E* and K*) in eV of (non-protonated) **3** in DOX and THF using M06-2X/6-311+G(2d,p) and ADC(2)/*aug*-cc-pVDZ levels of theory, and experimental data from Ref. 23. See below for the relative energies of the tautomers in ES and the ESIPT barrier.

	DOX					THF		
	$\Delta E_{\text{cLR}}^{\text{TD-DFT}}$	$\Delta E_{\text{LR+cLR}}^{\text{TD-DFT}}$	$\Delta E_{\text{cLR}}^{\text{ADC(2)}}$	$\Delta E_{\text{LR+cLR}}^{\text{ADC(2)}}$	EXP	$\Delta E_{\text{cLR}}^{\text{TD-DFT}}$	$\Delta E_{\text{LR+cLR}}^{\text{TD-DFT}}$	EXP
E	3.72	3.67	3.39	3.34	3.31	3.70	3.66	3.28
E*	3.20	3.13	2.88	2.81	-	3.20	3.03	-
K*	2.56	2.47	2.10	2.02	2.29	2.56	2.42	2.29

A look at the electron density difference between the ES and the GS of **3** displayed in Figure 6.9b reveals a typical behaviour of an ESIPT compound:[9,14,353] the density increases on the nitrogen atom of the ESIPT centre under absorption of light, whereas, simultaneously, the density decreases on the hydroxyl oxygen atom involved in the H-bond. This combination is obviously favourable to induce proton transfer as the balance of acidity/basicity varies in a direction suggesting ESIPT.

For the protonated structure, **BTImPH**$^+$, in presence of ClO_4^-, similar absorption energies are calculated for **2H** and **4H** (Table 6.6). The same moieties are indeed involved in the excitation process in both **2H** and **4H**, as can be seen by the density difference plots in Figure 6.9a. The influence of the counter-ion on the system is again clean, especially for **4H**: if the counter-ion is neglected during the transition energy calculations, the absorption of **4H** would be overestimated by ca. 0.2 eV. Furthermore, in presence of ClO_4^-, ADC(2)/LR+cLR absorption energies of both **2H** and **4H** are similar to the ones reported by Tsuchiya for the red emitting solution obtained after addition of 4 acid equivalents, 3.33 eV. To describe the doubly protonated system, **BTImPH**$_2^+$, **2HH** is the form retained on the basis of the conformational study. In presence of two ClO_4^- anions, the computed absorption energy (3.28 eV) fits well the experimental absorption registered at 3.25 eV, after addition of a huge amount of acid. It is nevertheless obvious from the data of Table 6.6 that the difference between the absorption energies computed for **2H**, **4H**, **2HH**, and **3HH** are too small to allow discriminating them on the basis of their absorption spectra only.

6.4.2 Green fluorescent BTImP structure: 3

For the fluorescence of **3**, a look at the stabilities of the E* and K* forms, as well as at the ESIPT transition state given in Table 6.7 indicates that the emission should originate from K* only: K* is much more stable than E*, and no E* → K* barrier is detected on the free energy scale (there is a

Table 6.6: TD-DFT and ADC(2)/LR+cLR absorption energies in eV of the enol GS of singly and doubly protonated **BTImP** without and with counter-ion (ClO_4^-/BF_4^-). Experimentally registered absorption maxima appear at 3.33 eV and 3.28 eV after addition of 4 equivalent and a large excess of $HClO_4$, respectively.

	TD-DFT/LR+cLR					ADC(2)/LR+cLR				
	2H	**3H**	**4H**	**2HH**	**3HH**	**2H**	**3H**	**4H**	**2HH**	**3HH**
∅	3.55	3.85	3.84	3.56	3.49	3.19	3.49	3.50	3.23	3.17
ClO_4^-	3.59	3.90	3.62	3.67	3.58	3.23	3.57	3.24	3.28	3.19
BF_4^-	3.55	3.91	3.62	-	-	-	-	-	-	-

small maximum on the total energy profile). In addition, the theoretical E* and K* emission energies are separated of approximately 0.6 eV and it is very clear that the computed K* fluorescence is the only compatible with the measurement (see Table 6.5). Furthermore the ADC(2)/LR+cLR and TD-DFT/LR+cLR estimates bracket the experimental value. As stated above, there is also a large barrier protecting the system from going to the CI in which the imidazole fragment would be twisted by ca. 90°. Our results are therefore in line with the experimental data: a bright emission is measured. All these facts confirm the presence of the ESIPT in **BTImP** and an emission from the K* of **3** in non acidic medium.

Table 6.7: Difference of free energy (in eV) between E*, K*, and TS* for **3** obtained at the TD-DFT PCM(DOX and THF)-M06-2X/6-311+G(2d,p) and ADC(2)/*aug*-cc-pVDZ levels of theory.

	DOX				THF	
	ΔG^{cLR}_{LBS}	ΔG^{LR+cLR}_{LBS}	$\Delta G^{cLR}_{ADC(2)}$	$\Delta G^{LR+cLR}_{ADC(2)}$	ΔG^{cLR}_{LBS}	ΔG^{LR+cLR}_{LBS}
E* → K*	-0.19	-0.21	-0.19	-0.21	-0.23	-0.27
E* → TS*	-0.04	-0.04	-0.05	-0.06	-0.05	-0.05

6.4.3 Red fluorescent structure: 4H

We have previously shown that experiment and theory do agree on the form of the protonated system (**4H**) when 4 acid equivalents are experimentally added. The calculations have allowed to disclose the influence of the counter-ion on the relative energies of the conformers. Indeed, in the absence of counter-ion, **2H** would be the most stable conformer. In both cases the emission seems to result from the K* tautomer only. The E* of **4H** could not be located in any of our optimisations that always directly lead to K*, hinting that this latter is the most stable tautomer and that the ESIPT process is quantitative. Likewise, for **2H**, a difference of 0.59 eV separates the E* and K* in presence of ClO_4^- counter-ion (0.47 eV with BF_4^-) in favour of the keto form. Such energy difference should correspond to a quantitative ESIPT according to earlier calculations on a large set of compounds.[12] An unexpected result was obtained for the relative energies of the K* forms: in presence of ClO_4^-, the K* of **2H** is more stable than the one of **4H** (which is the most stable conformer at the enol GS). To estimate the

protective barrier between **4H** K* and **2H** K*, a relaxed scan of the ES potential energy surface was performed. The counter-ion could not been included in this calculation because its position would too rapidly evolve during the process. For both systems, the ESIPT, and therefore the excited-state, is localised on the BT moiety whereas the path connecting **2H** and **4H** involves a rotation between the phenol and Im moieties. As a consequence, such rotation does not yield to a conical intersection and TD-DFT can safely been applied. With this scan, the barrier separating the **2H** and **4H** K* forms can be estimated to be ca. 2.7 kcal/mol (0.12 eV), which is relatively low. Therefore, the formation of the keto form of **2H** after ESIPT in **4H** seems possible, although such rotation will obviously be in competition with the direct emission from **4H** K*.

For **2H** and **4H**, the protonation induces a shift of the K* fluorescence by -0.2/-0.4 eV compared to **3** according to TD-DFT/ADC(2) approaches (Table 6.8). The TD-DFT shift is comparable to the experimental separation between the green and red emissions, -0.24 eV. The ADC(2) values are less accurate than TD-DT ones, but as we already discussed in Chapters 4 and 5, it has been shown that ADC(2) tends to underestimate the transition energies for excited state below 2 eV.[348] We notice that the computed emission wavelengths are similar for both conformers, **2H** and **4H**. If we assume that the emission is faster than the rotation of the imidazole part (*vide supra*), we can associate **4H** to the red emission. The observed red fluorescence is very similar in presence of ClO_4^- and BF_4^- experimentally, in line with this finding, the nature of the counter-ion has a small impact in our calculations for both **2H** and **4H**, see Table 6.8.

Table 6.8: TD-DFT/LR+cLR and ADC(2)/LR+cLR emission energies (E* and K*) in eV of singly and doubly protonated **BTImP** in presence of ClO_4^- counter-ion and difference with the optical spectra of **3** K* emission. The experimental fluorescence are reported at 2.05 eV (red form; 4 equivalent of $HClO_4$) and 2.55 eV (blue form; 600 equivalent of $HClO_4$) by Tsuchiya et al in Ref. 23.

	ClO_4^- TD-DFT/LR+cLR					ClO_4^- ADC(2)/LR+cLR				
$\Delta E_{\mathrm{BTImPH}^+_{(2)}}$	**2H**	**3H**	**4H**	**2HH**	**3HH**	**2H**	**3H**	**4H**	**2HH**	**3HH**
E*	3.08	3.15	[a]	2.68	2.93	2.74	2.80	[a]	2.22	2.52
K*	2.24	-	2.28	-	-	1.68	-	1.63	-	-
$\Delta E_{\mathrm{BTImPH}^+_{(2)}} - \Delta E_{\mathrm{BTImP}}$										
E*	0.61	0.68	[a]	0.21	0.46	0.72	0.78	[a]	0.20	0.50
K*	-0.23	-	-0.22	-	-	-0.35	-	-0.39	-	-
	BF_4^- TD-DFT/LR+cLR					∅ TD-DFT/LR+cLR				
$\Delta E_{\mathrm{BTImPH}^+_{(2)}}$	**2H**	**3H**	**4H**	**2HH**	**3HH**	**2H**	**3H**	**4H**	**2HH**	**3HH**
E*	2.91	3.18	[a]	-	-	3.12	3.22	[a]	2.92	2.45
K*	2.20	-	2.24	-	-	2.33	-	2.28	-	-

[a] E* optimisation could not converge properly and directly produces a K* structure

6.4.4 Blue fluorescent structure: 2HH

As stated above, different positions are tested for the counter-ion in the case of the mono-protonated species, and the most stable do not show interactions between the OH group and the counter-ion. At this point, there is therefore an apparent contradiction between our theoretical result and the experimental analysis: the counter-ion location does not allow interactions with the hydrogen atom of the phenol and therefore cannot block the ESIPT process as proposed in Ref. 23 to explain the blue fluorescence by a frustration of the ESIPT and emission from an enol-like structure (see Figure 6.1). This experimentally proposed frustrated ESIPT structure **4H-f** with a ClO_4^- counter-ion (Figures 6.10 and 6.6a) has been optimised but this latter is less stable by 10.96 kcal/mol compared to **4H** in the ground-state, coherently with chemical intuition regarding the position of the anion.

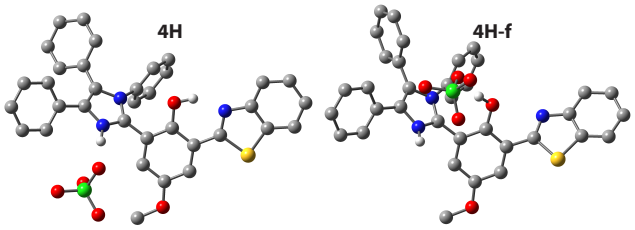

Figure 6.10: Representation of optimised GS **4H** and **4H-f** systems with a ClO_4^- counter-ion. Hydrogen atoms are omitted, except those involved in H-bonds.

Another issue with the initial hypothesis of Ref. 23 (Figure 6.1), is the emission from the enol ES of **4H**. We therefore determined the E^* for the **4H-f** system. Compared to **4H** K^*, **4H-f** E^* is less stable by 23.09 kcal/mol which again goes against the original interpretation. If the hypothesis of a frustrated ESIPT system to generate the blue light can be discarded on the basis of the stability, it has to be noted that the TD-DFT/LR+cLR absorption (3.94 eV) and emission (2.75 eV) energies computed for **4H-f** are compatible with the experimental data (3.28 eV and 2.55 eV, respectively), hinting that the ESIPT process should indeed be blocked in some way. Given the amount of acid added to the solution to obtain the blue fluorescence (600 eq.), the double protonation of **BTImP** has therefore been considered, and **2HH** has been associated to this emission with the stability investigation. We note that the computed fluorescent energy of **2HH** indeed fits experiment (Table 6.8). Indeed, the experimental shift between the green and blue emission attains 0.26 eV, a value nicely reproduced with **2HH** (0.21 eV) [but not with **3HH** (0.46 eV)].

6.5 Conclusions and Outlook

The **BTImP** system, synthesised by Sakai and Tsuchiya,[22,23] displays unusual optical properties due to it structure, composed of two excited state intramolecular proton transfer centres that can be accessed through rotations controlled by acidity of the medium. Obviously, the change of ESIPT locations induces new optical properties and gives access to a large panel of emission colours. A first

theoretical study tried to attribute a structure to the green and red fluorescent spectra.[349] However, some discrepancies appeared between this initial analysis and the deeper characterisation of the system performed by the experimental team in their second work.[23] As we demonstrate in the present Chapter, the explicit inclusion of counter-ion in the calculation is mandatory and can explain these discrepancies.

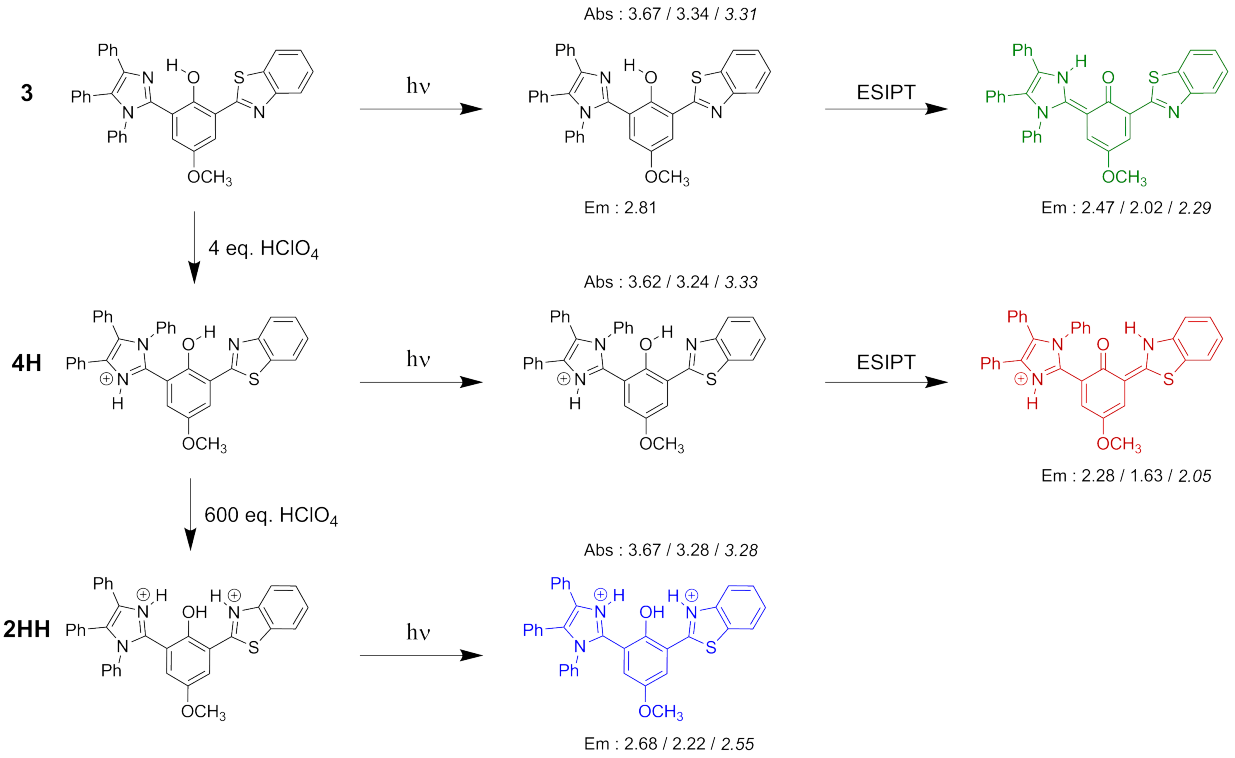

Figure 6.11: Most stable computed conformers depending on the acidic conditions and representation of the emitting structures. Theoretical TD-DFT and ADC(2) (LR+cLR in both cases) and experimental (in italic) absorption and emission energies are reported in eV. The experimental values are extracted from Ref. 23.

By exploring a large set of conformers, we are able to determine the most favoured forms of the molecule in each of its protonation states. In agreement with NMR and X-Ray experimental data, the conformers **3** and **4H** are the most stable structures in solution before and after addition of 4 equivalent of $HClO_4$, respectively. In the case of the acidic solution, our calculations highlighted that the counter-ion impacts the ranking of the conformers, and subsequently the optical properties. Indeed neglecting the counter-ion would have led to a different outcome: the **2H** conformer would be the most stable **BTImPH**$^+$ form which would not fit the X-ray structure. No significant impact of the natures of the solvent (DOX and DCM) or counter-ion (ClO_4^- and BF_4^-) could be evidenced. With the ADC2/LR+cLR approach, the absorption energies are well reproduced with an error of less than +0.1 eV however the emission is underestimated of -0.1 eV to -0.4 eV. Our calculations confirmed that the green fluorescence results from an emission of the K* of **3**, the ESIPT being quantitative between the phenol and the imidazole moieties. This green emission is estimated with an error of +-0.2 eV (TD-DFT) or -0.3 eV [ADC(2)]. The red fluorescence can be associated to a K* tautomer but the rotations

between the phenol and both imidazole and benzothiazole parts induced by protonation change the configuration of the system and the ESIPT now takes place with the BT part. The experimental shift of the emission band induced by protonation is accurately reproduced by theory as well. For the blue fluorescence, the initial hypothesis of a frustrated ESIPT and therefore an enol emission is confirmed. However, by studying the different conformers we showed that such frustration is likely originating from a double protonation of the system and not from a strong interaction between a mono-protonated form and a counter-ion, therefore proposing a new interpretation of the experimental results. Although this conclusion has been obtained with a continuum solvent model, we underline that the originally proposed form is significantly less stable (by more than 20 kcal/mol compared to **4H**). In addition, the spectral features of the doubly protonated structures matches the experimental findings obtained after addition of several hundreds of acid equivalents. A graphical representation of our actual conclusions is shown in Figure 6.11.

Chapter 7

General conclusions and perspectives

7.1 Conclusions

The exploration of dyes undergoing an excited state intramolecular proton transfer (ESIPT) with *ab initio* calculations is at the core of this thesis. The ESIPT process is a fascinating and often complex mechanism, see Figure 1.2 and Chapter 2, paving the way to a large range of applications in OLEDs, laser dyes, logic gates, photostabilisers, or probes.

Funded by the ANR (*Agence National de la recherche*), this thesis is linked to the GeDEMi project coordinated by Dr. Gilles Ulrich (*Université de Strasbourg*) in close relationship with Prof. Denis Jacquemin in Nantes. During this collaboration more than forty ESIPT dyes have been synthesised, characterised and modelled thanks to the close collaboration between the two teams. Thirty-four of these compounds are presented in Chapter 4, and of course, a part of these results has also been presented in associated publications.[7–10] These dyes have been designed to be highly emissive. The initial objective of this project was to obtain new ratiometric fluorescent probes based on HBX [2-(2'-hydroxyphenyl)benzoxazole (HBO), 2-(2'-hydroxyphenyl)benzimidazole (HBI), and 2-(2'-hydroxyphenyl)benzothiazole (HBT)] scaffold. On the thirty-four dyes reported here, and studied in benzene and toluene, only 9% emit jointly from the two tautomers excited state, 6% from the E^*, and the majority of them, 85%, present an ESIPT fluorescence resulting from the K^* form. If the optimisation of the dual emissive system in order to obtain ratiometric fluorescent probes has still to be performed, our knowledge on the keys needed for tuning the keto emission and reaching very bright fluorophores is indeed strongly improved as compared to the start of the project.

From the different dyes reported in Chapter 4, a trend emerged regarding the relationship between the emission wavelength and the substitution positions, see Figure 7.1. With the addition of ethynyl groups in *meta*, *para*, *ortho*, or *ortho-para* position of the hydroxy in the HBX scaffold, the K^* emission can be controlled. Indeed, the substitution in *ortho* position red-shifts the emission compared to the addition of an extra group in *para*. If two groups are added, one in *para* and the second in *ortho*, a similar emission profile as with the *ortho* group only is observed. The addition of moieties in *meta* gives similar fluorescence results as the *para* position. These trends have been observed with the HBO

(X=O) but also the HBI (X=NH) cores. The notable difference between these scaffolds is the blue-shift of the emission of the HBI dyes as compared to their HBO equivalents. Only bis *ortho-para* substituted structures have been tested with the HBT (X=S) core and they present a red-shifted fluorescence as to their HBO-based analogues.

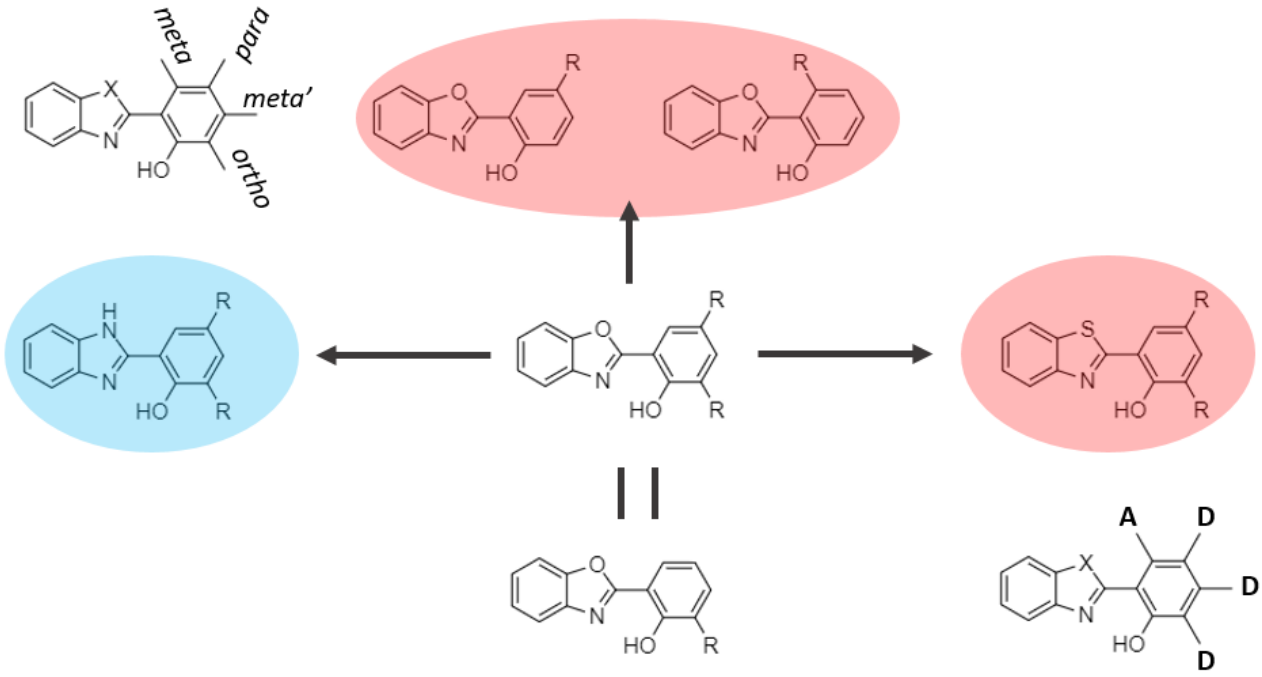

Figure 7.1: Representation of the different conclusions resulting from the work presented in Chapter 4. In red and blue are represented the fluorescence shift of the different structures compared to the *ortho-para*-HBO system. The donor (D) and acceptor(A) positions are represented as well in the right-bot structure.

An unexpected impact of the substituent has been observed thanks to electron density difference plots, a representation allowing to clearly detect donor and acceptor signatures of the various auxochromes. On the one hand, in *ortho* and *para*, the triple bonds of the substituents act as donor moieties with an impact that is (as expected) stronger in *para* than *ortho*. On the other hand, the substitution with similar groups but located in *meta* gives them an acceptor character. This difference can potentially be increased by the addition of additional strong donor/electron-withdrawing in those position. This trend is one of our most recent results, therefore this strategy has not been tested yet. The introduction of donor groups in the second *meta'* position (leading to linear systems) on HBI and HBT cores yields dual (with ethynyl methylamine) or keto (with ethynyl aniline) fluoresences. However, with the HBO core, the enol is stabilised and the emission results from this tautomer. This effect is not linked to this substitution position, it has not been reproduced with other groups such as the ethynyl tolyl moiety. The main difference between these two moieties is the terminal electron donor part present in the ethynyl aniline group.

In Chapter 5, a symmetric triply emissive dye has been investigated.[14] This dye is composed of two ESIPT sites, offering the possibility of double proton transfer. This dye indeed presents a triple

emission, clearly attributed experimentally to different tautomers: the initial enol form (EE*), the first proton transfer enol-keto tautomer (EK*), and the double proton transfer keto-keto structure (KK*).[15] The study of this system has been an opportunity to appraise different theoretical approaches combining TD-DFT and post-HF [ADC(2) and CC2] approaches but also, and maybe more importantly, a panel of continuum solvent models (LR, cLR, LR+cLR, and VEM-UD PCM) in order to obtain the best accuracy possible yet at a reasonable (computational) cost. Indeed, a refined model was obviously needed to lift the discrepancies between the previous theoretical results, all performed at TD-DFT/LR-PCM level of theory,[16–20] and the experimental findings. In ESIPT systems, the electronic transitions are typically brighter in the enol than in the keto tautomers, and their ES dipole moments strongly differ. Therefore using LR-PCM can be insufficient as this model is more adapted to describe ES showing a local and dipole-allowed character. However, if state-specific solvent models, such as cLR, are more adequate to describe the ES of the keto form, they are probably less effective for the enol isomers. For the specific dye studied in Chapter 5, the VEM-UD approach has been shown to be effective to describe the keto ES consistently with their large excited-state dipole moments. Unfortunately the self-consistency process of VEM-UD makes it computationally expensive. The combination of the LR and cLR corrections has also allowed an accurate and balanced description of both the enol and keto ES, especially when CC2 is used to describe the electronic structure. The LR+cLR/CC2 model has been retained for almost all the ESIPT systems of this thesis, in fact, even for the non-ESIPT systems of my "side" projects not detailed in this manuscript. With the LR+cLR/CC2 and VEM-UD/CC2 protocols, the systems could be properly described and all the four experimental emission peaks have been attributed to a specific tautomer, the two first peaks resulting from a strong vibronic coupling in EE*, whereas the following band are generated by the EK* and KK* tautomers as experimentally reported in the initial publication. The analysis of the relatives energies of the different ES and their associated ESIPT barriers corroborated this attribution.

Building up on this refined protocol set up during the study of the BBTP system, Chapter 5, and already applied to some of the other molecules of Chapter 4, I decided to challenge this new model with the description of the complex case,[21] reported in Chapter 6. This complex compound has the interest of presenting five different luminescent colours depending on the environment.[22,23] The dye is also presenting a very flexible structure which allows obtaining two different ESIPT through molecular rotations, that can be activated by addition of acidic solution. In the experimental publications, a structure and associated ESIPT mechanism have been proposed for each observed colours, based on available data (NMR and X-Ray), see Figure 7.2. The different conformers' i) stability, ii) NMR signal, iii) optical properties, iv) protonation states, and v) interactions with counter-ions, have been studied in order to attribute a structures to the observed green, red, and blue fluorescences. For the two first, our results are in line with the experimental conclusions. For the blue fluorescence, only one hypothesis was made in the original papers. With our calculations, a new more robust analysis of this structure could be proposed: an emission from a doubly protonated form. For this system, on a more technical point of view, I have also showed that the inclusion of the counter-ion in the calculation is required to

reach the correct trends.

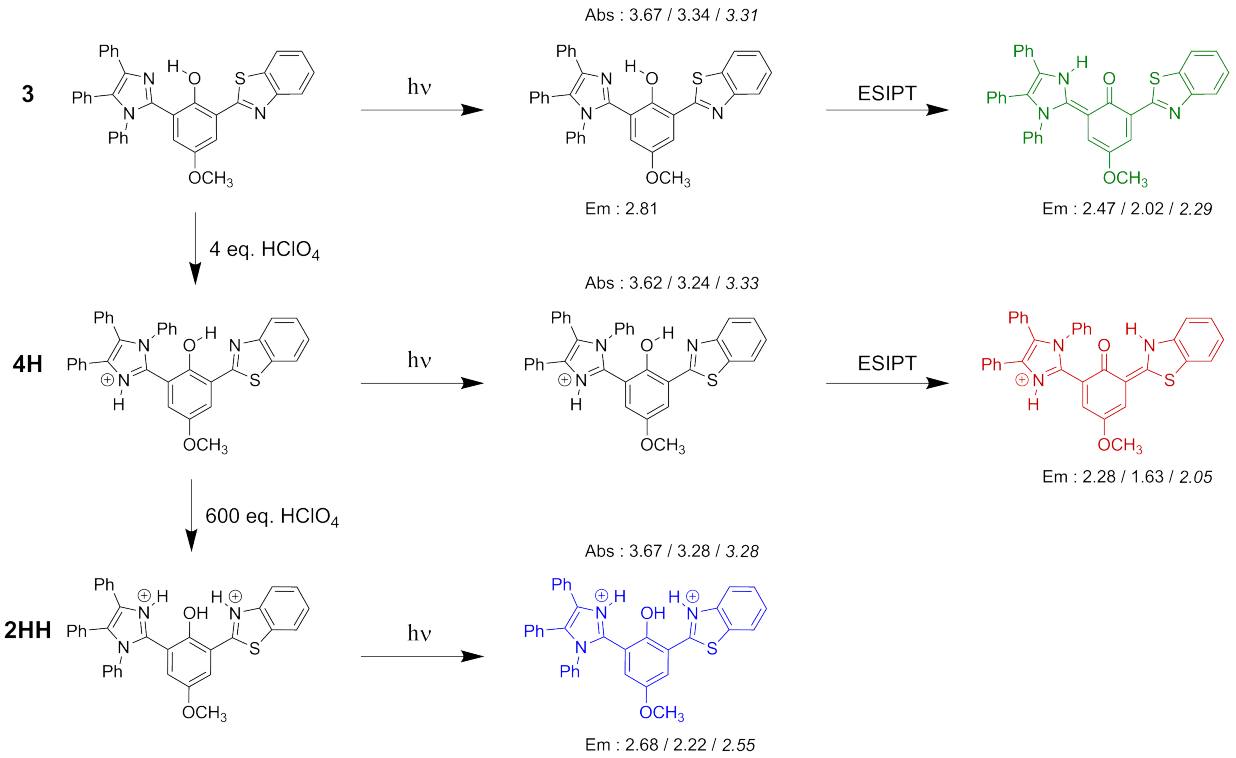

Figure 7.2: Most stable computed conformers depending on the acidic conditions and representation of the emitting structures. Theoretical TD-DFT and ADC(2) (LR+cLR in both cases) and experimental (in italic) absorption and emission energies are reported in eV. The experimental values are extracted from Ref. 23.

From a personal point of view, this thesis has been my first longterm professional experience. If it has brought me tools to accomplish research projects, it also helped me to develop personal skills. After assimilating the basics of my subject, I have learned to enjoy it. And going to work is much easier when you are interested in what you are doing. I have progressively became more autonomous to conduct my research, to define objectives for each assignment. Having a critical look on myself and my work was an important asset that I realised during the past 3 years.

Communication is key to conduct scientific research: being able to clearly explain my work, particularly to my supervisor, to obtain guidance and validate my results was not always easy but truly helped. If my first participation as a speaker in a congress was stressful, I'm glad I had this opportunity. Working on individual but also collaborative projects gave me an overview of various ways to conduct research. I had to acquire organisation and rigour to not loose myself between all these diverse tasks. I also discovered more about the nebulous systems of the research in France.

For the first time in my young life I was financially independent. I thereby gained security and also confidence to deal with small/big everyday issues; be it at home or at work. At last but not least: I started this PhD as a student, lost in face of what's in front of her; I finish it as a woman, an adult, still faced with interrogations, but way more confident in her own ability to part on new adventures. I'm now skilled to progress in my professional life and make new plans overall. As I finish writing

this thesis, I find myself happily pregnant as I decided not to have to choose between a career and building a family. If the place of women is still problematic even among scientific circles (only one female Professor in my lab for fifteen male Professor/Research directors), I won't choose, and I don't want to let my peers choose for me. I don't know yet if it is a fight that I want to fight; but I think it is important to underline that equity has not been reach yet in our academic institutions.

From a scientific point of view, I believe this work has been realised with rigour which has allowed to resolve and bring more clarity on experimental studies as described inside the results Chapters. With ESIPT systems, the inclusion of a study with *ab initio* calculations is important to determine the nature of the fluorescent excited states. Experimental characterisation techniques, such as the NMR or the X-Ray, only provide ground state structures of the compounds. Therefore to define the nature of the excited state and its associated fluorescence, the analysis is mostly based on the Stokes' shift if calculations are not performed. If this shift between absorption and emission wavelengths is strong enough, the emission is attributed to the keto form. In most of the cases, this approach will bring the correct answers. However as discussed in Chapter 4 (Section 4.4), a strong solvatochromic effect on the enol band can also enhance the Stokes' shift making attribution difficult. The systematic checking of the nature of the excited-state during our collaboration with the team of Dr. Gilles Ulrich, has allowed, I hope, to produce a more robust analysis of the results.

On a more methodological aspect, this thesis has been the opportunity to use extensively and for the first time the combination of the LR and cLR solvent corrections to describe with an increase accuracy the optical properties of different dyes. This model has emerged from an original idea of Dr. Ciro Guido, Pr. Benedetta Mennucci and my supervisor Pr. Denis Jacquemin. This method delivered accurate results for the description of ESIPT systems, especially when coupled with CC2. It would be interesting to extend the use of this model to other classes of dyes.

7.2 Perspectives

The perspectives of this work are multiple. A lot of ideas of new ESIPT compounds showing enhanced dual emission and/or brighter fluorescence have been proposed during our exchanges with the (always productive) Strasbourg's team (see Figure 7.3).

A lot of these interesting systems remains to be synthesised, characterised... and modelled. The **P1** dye of Figure 7.3 has been proposed during one of our meetings. I firstly performed some calculations to define the probability of the ESIPT to occur. As I obtained promising results in favour of a keto fluorescence, this compound has been synthesis in a second time in Strasbourg. A strong green emission at the solid state has been observed! This skeleton will continue to be studied and developed based on HBI and HBO core, and substituents will also be added so as to enhance the QY. Based on the discovery of an acceptor effect of the substituent placed in *meta* position, a new series with withdrawing electron group in this position will be explored, see structure **P2** in Figure 7.3. In the same playground of tuning the acceptor and donor groups, dyes based on the **P3** architecture have been proposed to

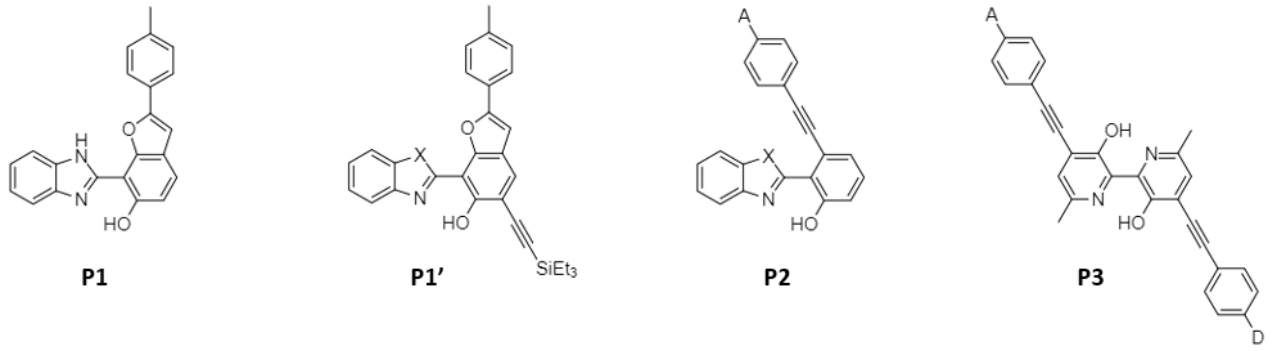

Figure 7.3: Examples of structures proposed during the collaborative study between the experimental and theoretical teams. The **P1**, **P1'** and **P2** structures are proposition directly coming from our collaboration. **P3** is a new proposal from the Strasbourg's team.

obtain a dual emission coming from the enol and keto tautomers and so eventually to obtain a double ESIPT.

During this thesis I limited my investigations to dyes in (mostly aprotic) solutions. However, ESIPT systems are remarkable for their bright luminescence not only in solution but also in solid state. The modelling of the optical properties of these dyes in polymers would clearly be interesting to get a deeper understanding of their behaviours for "real-life" applications such as OLED or logic gates. For this purpose, different tools could be potentially used. To study the mechanism of an ESIPT dye in a solid-state environment we can get inspired by the work of a team from Paris.[24,25] Assuming that the proton transfer is not occurring simultaneously in all molecules, this team proposed to construct a cluster model representing the system of interest (one molecule) surrounded by 14 other molecules in enol form. With a QM/QM' TD-DFT ONIOM approach, the central molecule is optimised with a higher level of theory than the rest of the cell. Another but quite similar strategy is to use a QM/MM ONIOM approach developped by Crespo-Otero and co-workers.[26] The chromophore is also optimised with TD-DFT whereas the rest of the surrounding crystal is fixed and evaluated using a consistent MM methods. More precislely, the AMBER forcefield using ESP charges derived from a vacuum HF/3-21G* calculation of a monomer cut from the crystal structure is used to capture the surrounding effects. With this method Crespo-Otero also investigated the possiblility of the conical intersection to occur at the QM/MM CASSCF/AMBER level, which allowed to quantify the aggregation-induced emission in molecular crystals undergoing ESIPT.

In this thesis, I used a limited numbers of theoretical approaches to characterise the ESIPT dyes. In the framework of the TD-DFT, the quantum theory of atom in molecule (QTAIM) or the electron localization function (ELF) could have been used to obtain a deeper understanding of the evolution of density of the hydrogen bonding during the process. The infrared vibrational frequencies have not been particularly used here to characterize the normal modes involved in the proton transfer either. These two analyses could have brought some valuable info. On the side of the vertical transition energies prediction, using EOM-CCSD approach could have delivered improved results but of course

with an increase of the computational cost as compared to TD-DFT or CC2. It is known that while EOM-CCSD does not necessarily provide more accurate absolute transition energies than CC2, the errors tend to be much more systematic,[354] which is clearly essential for "chemical design" purposes.

One of the frustration encountered during this work, is in Chapter 4 Section 4.7: the modelling of the impact of protic solvent such as water or, in the present case ethanol, on the relative stabilities of the enol and keto forms failed to yield convincing results. With PCM, the interaction between the solute and solvent is described with an implicit solvent model, therefore the intermolecular interactions between them are not taken into account which can lead to inaccurate predictions of the experimental outcomes. Here also, a dynamic approach, this time to model the solvent dynamic, to describe explicitly the solvent molecules and their impact on the dye could be used to lift this incertitude.[27,28]

One of the innovating approach in this work is the investigation with TD-DFT of the transition state between the keto excited state and the conical intersection to rationalise the experimental quantum yield of fluorescence. However if this approach can give a guideline within a series, no refined and accurate trends can be used to estimate the QY of emission with this approach. Two aspects could be used to cure this problem. First, using multi-reference methods such as CASPT2 would be useful to obtain not only the transition state but also a more accurate idea of the topology of the conical intersection. Second, the increasingly popular thermal vibration correlation function (TVCF) rate formalism can be used to estimate both the radiative and the nonradiative decay rates, k_{r} and k_{nr} using TD-DFT calculations of the ES Hessian.[355,356] This approach has been recently used with success to compute phosphorescent OLED efficiency for instance, but its application to more flexible systems could be an issue. Nevertheless, with this method a theoretical fluorescence QY could be obtained, which would be a huge forward step for the design of fluorescent ESIPT dyes.

Bibliography

[1] A. Weller, *Z Elektrochem*, 1956, **60**, 1144–1147.

[2] J. E. Kwon and S. Y. Park, *Adv. Mater.*, 2011, **23**, 3615–3642.

[3] J. Zhao, S. Ji, Y. Chen, H. Guo and P. Yang, *Phys. Chem. Chem. Phys.*, 2012, **14**, 8803–8817.

[4] V. S. Padalkar and S. Seki, *Chem. Soc. Rev.*, 2016, **45**, 169–202.

[5] I. Serdiuk and A. Roshal, *Dyes Pigm.*, 2017, **138**, 223–244.

[6] J. Massue, D. Jacquemin and G. Ulrich, *Chem. Lett.*, 2018, **47**, 1083–1089.

[7] J. Massue, A. Felouat, P. M. Vérité, D. Jacquemin, K. Cyprych, M. Durko, L. Sznitko, J. Mysliwiec and G. Ulrich, *Phys. Chem. Chem. Phys.*, 2018, **20**, 19958–19963.

[8] M. Munch, M. Curtil, P. M. Vérité, D. Jacquemin, J. Massue and G. Ulrich, *Eur. J. Org. Chem.*, 2019, **2019**, 1134–1144.

[9] J. Massue, A. Felouat, M. Curtil, P. M. Vérité, D. Jacquemin and G. Ulrich, *Dyes Pigm.*, 2019, **160**, 915–922.

[10] J. Massue, T. Pariat, P. M. Vérité, D. Jacquemin, M. Durko, T. Chtouki, L. Sznitko, J. Mysliwiec and G. Ulrich, *Nanomaterials*, 2019, **9**, 1093.

[11] Y. Houari, A. Charaf-Eddin, A. Laurent, J. Massue, R. Ziessel, G. Ulrich and D. , *Phys. Chem. Chem. Phys.*, 2014, **16**, 1319–1321.

[12] C. Azarias, S. Budzak, A. D. Laurent, G. Ulrich and D. Jacquemin, *Chem. Sci.*, 2016, **7**, 3763–3774.

[13] M. Raoui, J. Massue, C. Azarias, D. Jacquemin and G. Ulrich, *Chem. Commun.*, 2016, **52**, 9216–9219.

[14] P. M. Vérité, C. A. Guido and D. Jacquemin, *Phys. Chem. Chem. Phys.*, 2019, **21**, 2307–2317.

[15] Y. Hao and Y. Chen, *Dyes Pigm.*, 2016, **129**, 186–190.

[16] X. Jia, C. Li, D. Li and Y. Liu, *J. Lumin.*, 2017, **192**, 541–546.

[17] J. Huang, K. Yu, H. Ma, S. Chai and B. Dong, *Dyes Pigm.*, 2017, **141**, 441–447.

[18] J. Zhao and Y. Zheng, *Sci. Rep.*, 2017, **7**, 44897.

[19] R. Lan, Y. Yang, Y. Ma and Y. Li, *Spectro. Acta A*, 2017, **183**, 37–44.

[20] M. Lu, Y. Yang and T. Chu, *Theor. Chem. Acc.*, 2017, **136**, 62.

[21] P. M. Vérité, S. Hédé and D. Jacquemin, *Phys. Chem. Chem. Phys.*, 2019, **21**, 17400–17409.

[22] K.-i. Sakai, S. Tsuchiya, T. Kikuchi and T. Akutagawa, *J. Mater. Chem. C*, 2016, **4**, 2011–2016.

[23] S. Tsuchiya, K.-i. Sakai, K. Kawano, Y. Nakane, T. Kikuchi and T. Akutagawa, *Chem. Eu. J.*, 2018, **24**, 5868–5875.

[24] D. Presti, F. Labat, A. Pedone, M. J. Frisch, H. P. Hratchian, I. Ciofini, M. C. Menziani and C. Adamo, *J. Chem. Theory Comput.*, 2014, **10**, 5577–5585.

[25] D. Presti, F. Labat, A. Pedone, M. J. Frisch, H. P. Hratchian, I. Ciofini, M. Cristina Menziani and C. Adamo, *J. Comput. Chem.*, 2016, **37**, 861–870.

[26] M. Dommett, M. Rivera and R. Crespo-Otero, *J. Phys. Chem. Lett.*, 2017, **8**, 6148–6153.

[27] D. Loco, N. Gelfand, S. Jurinovich, S. Protti, A. Mezzetti and B. Mennucci, *J. Phys. Chem. A*, 2018, **122**, 390–397.

[28] D. Loco, S. Protti, B. Mennucci and A. Mezzetti, *J. Mol. Struct.*, 2019, **1182**, 283 – 291.

[29] B. Valeur, *Lumière et luminescence*, Belin, 2nd edn, 2017.

[30] E. Condon, *Phys. Rev.*, 1926, **28**, 1182–1201.

[31] J. Franck and E. G. Dymond, *Trans. Faraday Soc.*, 1926, **21**, 536–542.

[32] M. Kasha, *Discuss. Faraday Soc.*, 1950, **9**, 14–19.

[33] M. Kasha and S. P. McGlynn, *Ann.l Rev. Phys. Chem.*, 1956, **7**, 403–424.

[34] B. Valeur, *Molecular Fluorescence Principles and Applications*, Wiley-VCH, 2001.

[35] G. Salvato-Vallverdu, 2009 ; http://www.texample.net/tikz/examples/the-perrin-jablonski-diagram/ (last accessed February 21, 2020.).

[36] S. Park, J. E. Kwon, S. H. Kim, J. Seo, K. Chung, S.-Y. Park, D.-J. Jang, B. M. Medina, J. Gierschner and S. Y. Park, *J. Am. Chem. Soc.*, 2009, **131**, 14043–14049.

[37] J. E. Kwon and S. Y. Park, *Adv. Mater.*, 2011, **23**, 3615–3642.

[38] K. Benelhadj, W. Muzuzu, J. Massue, P. Retailleau, A. Charaf-Eddin, A. D. Laurent, D. Jacquemin, G. Ulrich and R. Ziessel, *Chem. Eur. J.*, 2014, **20**, 12843–12857.

[39] L. Yan, R. Li, W. Shen and Z. Qi, *J. Lumin.*, 2018, **194**, 151–155.

[40] L. G. T. A. Duarte, J. C. Germino, J. k. Berbigier, C. A. Barboza, M. M. Faleiros, D. de Alencar Simoni, M. T. Galante, M. S. de Holanda, F. S. Rodembusch and T. D. Z. Atvars, *Phys. Chem. Chem. Phys.*, 2019, **21**, 1172–1182.

[41] K. ichi Sakai, T. Tsuzuki, Y. Itoh, M. Ichikawa and Y. Taniguchi, *Appl. Phys. Lett.*, 2005, **86**, 081103.

[42] S. Park, O.-H. Kwon, S. Kim, S. Park, M.-G. Choi, M. Cha, S. Y. Park and D.-J. Jang, *J. Am. Chem. Soc.*, 2005, **127**, 10070–10074.

[43] J. Zhao, H. Yao, J. Liu and M. R. Hoffmann, *J. Phys. Chem. A*, 2015, **119**, 681–688.

[44] X. Cheng, K. Wang, S. Huang, H. Zhang, H. Zhang and Y. Wang, *Angew. Chem. Int. Ed.*, 2015, **54**, 8369–8373.

[45] V. Luxami and S. Kumar, *New J. Chem.*, 2008, **32**, 2074–2079.

[46] V. Luxami and S. Kumar, *RSC Adv.*, 2012, **2**, 8734–8740.

[47] M. J. Paterson, M. A. Robb, L. Blancafort and A. D. DeBellis, *J. Phys. Chem. A*, 2005, **109**, 7527–7537.

[48] L. Feng, Z.-M. Liu, J. Hou, X. Lv, J. Ning, G.-B. Ge, J.-N. Cui and L. Yang, *Biosens. Bioelectron.*, 2015, **65**, 9–15.

[49] S. Goswami, S. Das, K. Aich, B. Pakhira, S. Panja, S. K. Mukherjee and S. Sarkar, *Org. Lett.*, 2013, **15**, 5412–5415.

[50] N. Jiang, C. Yang, X. Dong, X. Sun, D. Zhang and C. Liu, *Org. Biomol. Chem.*, 2014, **12**, 5250–5259.

[51] B. J. Lampkin, C. Monteiro, E. T. Powers, P. M. Bouc, J. W. Kelly and B. VanVeller, *Org. Biomol. Chem.*, 2019, **17**, 1076–1080.

[52] A. Gangopadhyay, S. S. Ali, U. N. Guria, S. K. Samanta, R. Sarkar, P. Datta and A. K. Mahapatra, *New J. Chem.*, 2018, **42**, 15990–15996.

[53] G. Kumar, K. Paul and V. Luxami, *Sens. Actuators B-Chem.*, 2018, **263**, 585 – 593.

[54] Z. Luo, B. Liu, T. Qin, K. Zhu, C. Zhao, C. Pan and L. Wang, *Sens. Actuators B-Chem.*, 2018, **263**, 229 – 236.

[55] I. E. Serdiuk, A. D. Roshal and J. Błażejowski, *J. Phys. Chem. A*, 2016, **120**, 4325–4337.

[56] E. Heyer, J. Massue and G. Ulrich, *Dyes Pigm.*, 2017, **143**, 18–24.

[57] V. S. Padalkar, Y. Tsutsui, T. Sakurai, D. Sakamaki, N. Tohnai, K. Kato, M. Takata, T. Akutagawa, K.-i. Sakai and S. Seki, *J. Phys. Chem. B*, 2017, **121**, 10407–10416.

[58] Q. J. Meisner, A. H. Younes, Z. Yuan, K. Sreenath, J. J. M. Hurley and L. Zhu, *J. Phys. Chem. A*, 2018, **122**, 9209–9223.

[59] C. A. Barboza and A. L. Sobolewski, *Phys. Chem. Chem. Phys.*, 2018, **20**, 25164–25168.

[60] I. E. Serdiuk, *J. Phys. Chem. C*, 2017, **121**, 5277–5286.

[61] X. Liu, H. Tian, L. Yang, Y. Su, M. Guo and X. Song, *Sens. Actuators B-Chem.*, 2018, **255**, 1160 – 1165.

[62] S. Yamazaki, A. L. Sobolewski and W. Domcke, *Phys. Chem. Chem. Phys.*, 2011, **13**, 1618–1628.

[63] A. S. Klymchenko, *Acc. Chem. Res.*, 2017, **50**, 366–375.

[64] A. Mordziński, A. Grabowska, W. Kühnle and A. Kröwczyński", *Chem. Phys. Lett.*, 1983, **101**, 291–296.

[65] R. S. Becker, C. Lenoble and A. Zein, *J. Phys. Chem.*, 1987, **91**, 3517–3524.

[66] R. S. Becker, C. Lenoble and A. Zein, *J. Phys. Chem.*, 1987, **91**, 3509–3517.

[67] C. Lenoble and R. S. Becker, *Photochem. Photobiol.*, 1990, **52**, 1063–1069.

[68] J. K. Dey and S. K. Dogra, *Bull. Chem. Soc. Jpn.*, 1991, **64**, 3142–3152.

[69] R. Wortmann, K. Elich, S. Lebus, W. Liptay, P. Borowicz and A. Grabowska, *J. Phys. Chem.*, 1992, **96**, 9724–9730.

[70] P. Borowicz, A. Grabowska, R. Wortmann and W. Liptay, *J. Lumin.*, 1992, **52**, 265 – 273.

[71] N. P. Ernsting, T. Arthen-Engeland, M. A. Rodriguez and W. Thiel, *J. Chem. Phys.*, 1992, **97**, 3914–3919.

[72] L. Lavtchieva, V. Enchev and Z. Smedarchina, *J. Phys. Chem.*, 1993, **97**, 306–310.

[73] K. Das, N. Sarkar, D. Majumdar and K. Bhattacharyya, *Chem. Phys. Letters*, 1992, **198**, 443 – 448.

[74] M. S. Gudipati, *J. Phys. Chem.*, 1993, **97**, 8602–8607.

[75] K. Das, N. Sarkar, A. K. Ghosh, D. Majumdar, D. N. Nath and K. Bhattacharyya, *J. Phys. Chem.*, 1994, **98**, 9126–9132.

[76] A. Peluso, C. Garzillo and G. D. Re, *Chem. Phys.*, 1996, **204**, 347 – 351.

[77] S. H. Alarcón, A. C. Olivieri, R. M. Cravero, G. Labadie and M. González-Sierra, *J. Phys. Org. Chem.*, 1995, **8**, 713–720.

[78] F. Vollmer and W. Rettig, *J. Photochem. Photobiol. A Chem.*, 1996, **95**, 143 – 155.

[79] J. Catalán, J. C. D. Valle, R. M. Claramunt, D. Sanz and J. Dotor, *J. Lumin.*, 1996, **68**, 165 – 170.

[80] M. Knyazhansky, A. Metelitsa, A. Bushkov and S. Aldoshin, *J. Photochem. Photobiol. A Chem.*, 1996, **97**, 121 – 126.

[81] M. Kletskii, A. Millov, A. Metelitsa and M. Knyazhansky, *J. Photochem. Photobiol. A Chem.*, 1997, **110**, 267 – 270.

[82] L. Peteanu and S. Locknar, *Chem. Phys. Letters*, 1997, **274**, 79 – 84.

[83] G. N. Ledesma, G. A. Ibanez, G. M. Escandar and A. C. Olivieri, *J. Mol. Struct.*, 1997, **415**, 115 – 121.

[84] K. B. Andersen and J. Spanget-Larsen, *Spectro. Acta Part A*, 1997, **53**, 2615 – 2625.

[85] D. LeGourriérec, V. Kharlanov, R. G. Brown and W. Rettig, *J. Photochem. Photobiol. A Chem.*, 1998, **117**, 209 – 216.

[86] L. Premvardhan and L. Peteanu, *Chem. Phys. Letters*, 1998, **296**, 521 – 529.

[87] J. Catalán, J. Palomar and J. L. G. de Paz, *J. Phys. Chem. A*, 1997, **101**, 7914–7921.

[88] A. B. Tathe, V. D. Gupta, M. R. Shreykar, P. Ramasami and N. Sekar, *J. Lumin.*, 2014, **154**, 267–273.

[89] N. Manojai, R. Daengngern, K. Kerdpol, C. Ngaojampa and N. Kungwan, *J. Lumin.*, 2017, **188**, 275–282.

[90] B. K. Paul and N. Guchhait, *J. Lumin.*, 2011, **131**, 1918 – 1926.

[91] M. Zhang, D. Yang, B. Ren and D. Wang, *J. Fluores.*, 2013, **23**, 761–766.

[92] Y.-Q. Lei, J.-Y. Xi, H. Guo and R. Jia, *J. Saudi Chem. Soc.*, 2018, **22**, 777 – 785.

[93] C.-C. Hsieh, P.-T. Chou, C.-W. Shih, W.-T. Chuang, M.-W. Chung, J. Lee and T. Joo, *J. Am. Chem. Soc.*, 2011, **133**, 2932–2943.

[94] J. Hao and Y. Yang, *Chem. Phys.*, 2018, **501**, 53 – 59.

[95] A. Dreuw, J. Plötner, L. Lorenz, J. Wachtveitl, J. E. Djanhan, J. Brüning, T. Metz, M. Bolte and M. U. Schmidt, *Angew. Chem. Int. Ed.*, 2005, **44**, 7783–7786.

[96] J. Plötner, D. J. Tozer and A. Dreuw, *J. Chem. Theory Comput.*, 2010, **6**, 2315–2324.

[97] S.-H. Xia, B.-B. Xie, Q. Fang, G. Cui and W. Thiel, *Phys. Chem. Chem. Phys.*, 2015, **17**, 9687–9697.

[98] J. Zhang, Y. Li and X. Guo, *Theor. Chem. Acc.*, 2016, **135**, 72.

[99] M. Forés and L. Adamowicz, *J. Comput. Chem.*, 1999, **20**, 1422–1431.

[100] M. Forés, M. Duran, M. Solà and L. Adamowicz, *J. Comput. Chem.*, 2000, **21**, 257–269.

[101] M. J. Paterson, M. A. Robb, L. Blancafort and A. D. DeBellis, *J. Am. Chem. Soc.*, 2004, **126**, 2912–2922.

[102] J. D. Coe and T. J. Martínez, *J. Phys. Chem. A*, 2006, **110**, 618–630.

[103] A. Cembran and J. Gao, *Mol. Phys.*, 2006, **104**, 943–955.

[104] W. Zhu, W. Yang, W. Zhou, H. Liu, S. Wei and J. Fan, *J. Mol. Struct.*, 2011, **1004**, 74 – 81.

[105] W. Yang, W. Zhu, W. Zhou, H. Liu, Y. Xu and J. Fan, *RSC Adv.*, 2012, **2**, 8998–9004.

[106] W. Yang, W. Zhu, W. Zhou, H. Liu, Y. Xu and J. Fan, *J. Fluores.*, 2012, **22**, 1383–1393.

[107] Y. Shigemitsu, T. Mutai, H. Houjou and K. Araki, *J. Phys. Chem. A*, 2012, **116**, 12041–12048.

[108] F. Qiu, D. LiNa and F. WeiHai, *Sci. China Chem.*, 2012, **55**, 2089–2094.

[109] X. Chen, Q. Zhang, Y. Xu, W. Fang and D. L. Phillips, *J. Org. Chem.*, 2013, **78**, 5677–5684.

[110] X.-P. Chang, Q. Fang and G. Cui, *J. Chem. Phys.*, 2014, **141**, 154311.

[111] L. Spörkel, G. Cui, A. Koslowski and W. Thiel, *J. Phys. Chem. A*, 2014, **118**, 152–157.

[112] N. Singla and P. Chowdhury, *Chem. Phys. Letters*, 2014, **612**, 25 – 32.

[113] J. Dai, J. Han, X. Chen, W. Fang, J. Ma and D. L. Phillips, *Phys. Chem. Chem. Phys.*, 2015, **17**, 27001–27010.

[114] Y. Li, L. Wang, X. Guo and J. Zhang, *J. Comput. Chem.*, 2015, **36**, 2374–2380.

[115] P.-J. Guan, G. Cui and Q. Fang, *ChemPhysChem*, 2015, **16**, 805–811.

[116] W.-W. Guo, X.-Y. Liu, W.-K. Chen and G. Cui, *RSC Adv.*, 2016, **6**, 85574–85581.

[117] B.-b. Xie, C.-x. Li, G.-l. Cui and Q. Fang, *Chinese J. Chem. Phys.*, 2016, **29**, 38–46.

[118] D. Wu, W.-W. Guo, X.-Y. Liu and G. Cui, *ChemPhysChem*, 2016, **17**, 2340–2347.

[119] C.-X. Li, W.-W. Guo, B.-B. Xie and G. Cui, *J. Chem. Phys.*, 2016, **145**, 074308.

[120] L. Zhao, J. Liu and P. Zhou, *J. Phys. Chem. A*, 2016, **120**, 7419–7426.

[121] W.-w. Guo, Y.-g. Fang, Q. Fang and G.-l. Cui, *Chinese J. Chem. Phys.*, 2017, **30**, 696–704.

[122] M.-D. Li, N.-K. Wong, J. Xiao, R. Zhu, L. Wu, S.-Y. Dai, F. Chen, G. Huang, L. Xu, X. Bai, M. R. Geraskina, A. H. Winter, X. Chen, Y. Liu, W. Fang, D. Yang and D. L. Phillips, *J. Am. Chem. Soc.*, 2018, **140**, 15957–15968.

[123] C. Li, P. Xiao, W.-H. Fang and G. Cui, *J. Photochem. Photobiol. A Chem.*, 2018, **355**, 256 – 266.

[124] H. Yuan, X. Guo and J. Zhang, *Mater. Chem. Front.*, 2019, **3**, 1225–1230.

[125] L. Ma, W.-H. Fang, L. Shen and X. Chen, *ACS Catalysis*, 2019, **9**, 3672–3684.

[126] H. Wang, Q. Gong, G. Wang, J. Dang and F. Liu, *J. Chem. Theory Comput.*, 2019, **15**, 5440–5447.

[127] A. J. A. Aquino, H. Lischka and C. Hättig, *J. Phys. Chem. A*, 2005, **109**, 3201–3208.

[128] S. Jang, S. Il Jin and C. R. Park, *Bull. Korean. Chem. Soc.*, 2007, **28**, 2343–2353.

[129] A. J. A. Aquino, F. Plasser, M. Barbatti and H. Lischka, *Croat. Chemm. Acta*, 2009, **82**, 105–114.

[130] X. Lan, D. Yang, X. Sui and D. Wang, *Spectro. Acta Part A*, 2013, **102**, 281 – 285.

[131] H. Yin, H. Li, G. Xia, C. Ruan, Y. Shi, H. Wang, M. Jin and D. Ding, *Scientific reports*, 2016, **6**, 19774.

[132] A. Georgiev, P. Todorov and D. Dimov, *J. Photochem. Photobiol. A Chem.*, 2020, **386**, 112143.

[133] C. Ning, C. Xiao, R. Lu and P. Zhou, *J. Lumin.*, 2020, **217**, 116825.

[134] M. Ziolek, J. Kubicki, A. Maciejewski, R. Naskrecki and A. Grabowska, *Phys. Chem. Chem. Phys.*, 2004, **6**, 4682–4689.

[135] K. Kownacki, A. Mordzinski, R. Wilbrandt and A. Grabowska, *Chem. Phys. Lett.*, 1994, **227**, 270 – 276.

[136] S. Mitra and N. Tamai, *Chem. Phys.*, 1999, **246**, 463 – 475.

[137] A. Mandal, A. Koll, A. Filarowski, D. Majumder and S. Mukherjee, *Spectro. Acta Part A*, 1999, **55**, 2861 – 2868.

[138] M. Knyazhansky, A. Metelitsa, M. Kletskii, A. Millov and S. Besugliy, *J. Mol. Struct.*, 2000, **526**, 65 – 79.

[139] M. Z. Zgierski and A. Grabowska, *J. Chem. Phys.*, 2000, **112**, 6329–6337.

[140] A. Koll, A. Filarowski, D. Fitzmaurice, E. Waghorne, A. Mandal and S. Mukherjee, *Spectro. Acta Part A*, 2002, **58**, 197 – 207.

[141] A. Mandal, D. Fitzmaurice, E. Waghorne, A. Koll, A. Filarowski, D. Guha and S. Mukherjee, *J. Photochem. Photobiol. A Chem.*, 2002, **153**, 67 – 76.

[142] M. Mukhopadhyay, D. Banerjee, A. Koll, A. Filarowski, D. Guha and S. Mukherjee, *Indian J. Chem. A*, 2006, **45**, 1796–1803.

[143] M. Z. Zgierski and A. Grabowska, *J. Chem. Phys.*, 2000, **113**, 7845–7852.

[144] N. Otsubo, C. Okabe, H. Mori, K. Sakota, K. Amimoto, T. Kawato and H. Sekiya, *J. Photochem. Photobiol. A Chem.*, 2002, **154**, 33 – 39.

[145] J. M. Ortiz-Sánchez, R. Gelabert, M. Moreno and J. M. Lluch, *J. Phys. Chem. A*, 2006, **110**, 4649–4656.

[146] M. Sliwa, N. Mouton, C. Ruckebusch, L. Poisson, A. Idrissi, S. Aloïse, L. Potier, J. Dubois, O. Poizat and G. Buntinx, *Photochem. Photobiol. Sci.*, 2010, **9**, 661–669.

[147] B. Chowdhury, R. De, P. Sett and J. Chowdhury, *J. Chem. Sci.*, 2010, **122**, 857–865.

[148] F. Gao, X. Wang, H. Li and X. Ye, *Tetrahedron*, 2013, **69**, 5355 – 5366.

[149] T.-C. Fang, H.-Y. Tsai, M.-H. Luo, C.-W. Chang and K.-Y. Chen, *Chinese Chem. Lett.*, 2013, **24**, 145 – 148.

[150] T. Sekikawa, O. Schalk, G. Wu, A. E. Boguslavskiy and A. Stolow, *J. Phys. Chem. A*, 2013, **117**, 2971–2979.

[151] K.-Y. Chen and H.-Y. Tsai, *Int. J. Mol. Sci.*, 2014, **15**, 18706–18724.

[152] W.-C. Lin, S.-K. Fang, J.-W. Hu, H.-Y. Tsai and K.-Y. Chen, *Anal. Chem.*, 2014, **86**, 4648–4652.

[153] K.-Y. Chen and J.-W. Hu, *J. Lumin.*, 2015, **159**, 171 – 177.

[154] L. Gutiérrez-Arzaluz, F. Cortés-Guzmán, T. Rocha-Rinza and J. Peón, *Phys. Chem. Chem. Phys.*, 2015, **17**, 31608–31612.

[155] P. Mukherjee, A. Das, M. S. H. Faizi and P. Sen, *ChemistrySelect*, 2018, **3**, 3787–3796.

[156] O. Louant, B. Champagne and V. Liégeois, *J. Phys. Chem. A*, 2018, **122**, 972–984.

[157] W. A. Muriel, R. Morales-Cueto and W. Rodríguez-Córdoba, *Phys. Chem. Chem. Phys.*, 2019, **21**, 915–928.

[158] B. Maulén, A. Echeverri, T. Gómez, P. Fuentealba and C. Cárdenas, *J. Chem. Theory Comput.*, 2019, **15**, 5532–5542.

[159] S. Pijeau, D. Foster and E. G. Hohenstein, *J. Phys. Chem. A*, 2018, **122**, 5555–5562.

[160] B. Das, A. Chakraborty and S. Chakraborty, *Spectro. Acta Part A*, 2020, **225**, 117443.

[161] M. H. Luo, H. Y. Tsai, H. Y. Lin, S. K. Fang and K. Y. Chen, *Chinese Chem. Lett.*, 2012, **23**, 1279 – 1282.

[162] M. Savarese, r. Brémond, L. Antonov, I. Ciofini and C. Adamo, *ChemPhysChem*, 2015, **16**, 3966–3973.

[163] J. C. Germino, C. A. Barboza, F. J. Quites, P. A. M. Vazquez and T. D. Z. Atvars, *J. Phys. Chem. C*, 2015, **119**, 27666–27675.

[164] J.-W. Hu, H.-Y. Tsai, S.-K. Fang, C.-W. Chang, L.-C. Wang and K.-Y. Chen, *Dyes Pigm.*, 2017, **145**, 493 – 504.

[165] W. A. Muriel, J. F. Botero-Cadavid, C. Cárdenas and W. Rodríguez-Córdoba, *Phys. Chem. Chem. Phys.*, 2018, **20**, 29399–29411.

[166] A. Gao, J. Li, D. Wang, X. Ma and M. Wang, *Spectro. Acta Part A*, 2018, **191**, 315 – 324.

[167] P. Zhou and K. Han, *Acc. Chem. Res.*, 2018, **51**, 1681–1690.

[168] M. Budri, G. Naik, S. Patil, P. Kadolkar, K. Gudasi and S. Inamdar, *Spectro. Acta Part A*, 2020, **224**, 117462.

[169] S. Mitra and N. Tamai, *Phys. Chem. Chem. Phys.*, 2003, **5**, 4647–4652.

[170] J. Zhao, J. Chen, J. Liu and M. R. Hoffmann, *Phys. Chem. Chem. Phys.*, 2015, **17**, 11990–11999.

[171] E. Heyer, K. Benelhadj, S. Budzák, D. Jacquemin, J. Massue and G. Ulrich, *Chem. Eur. J.*, 2017, **23**, 7324–7336.

[172] J. S. Reis, A. B. Fernandes, B. C. Freitas-Dörr, E. L. Bastos and H. A. Stefani, *Tetrahedron*, 2018, **74**, 6866 – 6872.

[173] D. Yang, G. Yang, M. Jia, X. Song, Q. Zhang, T. Zhang and H. Gao, *RSC Adv.*, 2018, **8**, 29662–29669.

[174] Y. Yang, Y. Ding, W. Shi, F. Ma and Y. Li, *J. Lumin.*, 2020, **218**, 116836.

[175] Y. Houari, S. Chibani, D. Jacquemin and A. D. Laurent, *J. Phys. Chem. B*, 2015, **119**, 2180–2192.

[176] S. K. Behera, A. Karak and G. Krishnamoorthy, *J. Phys. Chem. B*, 2015, **119**, 2330–2344.

[177] Y. Li, Q. Zhu, B. An, H. Yuan, X. Guo and J. Zhang, *Mol. Phys.*, 2016, **114**, 2983–2992.

[178] H. Lin, X. Chang, D. Yan, W.-H. Fang and G. Cui, *Chem. Sci.* , 2017, **8**, 2086–2090.

[179] K. Takagi, Y. Yamada, R. Fukuda, M. Ehara and D. Takeuchi, *New J. Chem.*, 2018, **42**, 5923–5928.

[180] S. Kothavale, S. Bhalekar and N. Sekar, *Dyes Pigm.*, 2018, **159**, 209 – 221.

[181] Z. Tang, M. Lu, K. Liu, Y. Zhao, Y. Qi, Y. Wang, P. Zhang and P. Zhou, *J. Photochem. Photobiol. A Chem.*, 2018, **367**, 261 – 269.

[182] N. Zhao, Y. Li, Y. Jia and P. Li, *J. Phys. Chem. C*, 2018, **122**, 26576–26583.

[183] D. Jacquemin, M. Khelladi, A. D. Nicola and G. Ulrich, *Dyes Pigm.*, 2019, **163**, 475 – 482.

[184] L. Xie, Y. Chen, W. Wu, H. Guo, J. Zhao and X. Yu, *Dyes Pigm.*, 2012, **92**, 1361 – 1369.

[185] J. Cheng, D. Liu, L. Bao, K. Xu, Y. Yang and K. Han, *Chem. Asian J.*, 2014, **9**, 3215–3220.

[186] J. Cheng, D. Liu, W. Li, L. Bao and K. Han, *J. Phys. Chem. C*, 2015, **119**, 4242–4251.

[187] L. Wilbraham, M. Savarese, N. Rega, C. Adamo and I. Ciofini, *J. Phys. Chem. B*, 2015, **119**, 2459–2466.

[188] D. Presti, A. Pedone, I. Ciofini, F. Labat, M. C. Menziani and C. Adamo, *Theor. Chem. Acc.*, 2016, **135**, 86.

[189] S. Maity, S. S. Ray, A. Chatterjee, N. Chakraborty and J. Ganguly, *ChemistrySelect*, 2018, **3**, 6575–6580.

[190] H. Dong, J. Zhao, H. Yang and Y. Zheng, *Org. Chem. Front.*, 2018, **5**, 1241–1247.

[191] K. Liang, Q. Shao, G. Xia, Y. Wang, L. Jiang, L. Hong and H. Wang, *Dyes Pigm.*, 2020, **173**, 107926.

[192] R. de Vivie-Riedle, V. De Waele, L. Kurtz and E. Riedle, *J. Phys. Chem. A*, 2003, **107**, 10591–10599.

[193] H.-H. G. Tsai, H.-L. S. Sun and C.-J. Tan, *J. Phys. Chem. A*, 2010, **114**, 4065–4079.

[194] S. Luber, K. Adamczyk, E. T. J. Nibbering and V. S. Batista, *J. Phys. Chem. A*, 2013, **117**, 5269–5279.

[195] H. Roohi, N. Mohtamedifar and F. Hejazi, *Chem. Phys.*, 2014, **444**, 66 – 76.

[196] C. Prommin, N. Kanlayakan, W. Chansen, R. Salaeh, K. Kerdpol, R. Daengngern and N. Kungwan, *J. Phys. Chem. A*, 2017, **121**, 5773–5784.

[197] L. G. T. A. Duarte, F. S. Rodembusch, T. D. Z. Atvars and R. G. Weiss, *J. Phys. Chem . A*, 2020, **124**, 288–299.

[198] C. Schriever, M. Barbatti, K. Stock, A. J. Aquino, D. Tunega, S. Lochbrunner, E. Riedle, R. de Vivie-Riedle and H. Lischka, *Chem. Phys.*, 2008, **347**, 446 – 461.

[199] M. Higashi and S. Saito, *J. Phys. Chem. Lett.*, 2011, **2**, 2366–2371.

[200] Y. Yang, Y. Liu, H. Zhai, X. Jia, Y. He, Q. Ma, R. Zhang, Y. Liu and K. Jiang, *J. Lumin.*, 2020, **223**, 117224.

[201] I. Deperasińska, D. T. Gryko, E. Karpiuk, B. Kozankiewicz, A. Makarewicz and J. Piechowska, *J. Phys. Chem. A*, 2012, **116**, 12049–12055.

[202] I. Deperasińska, D. T. Gryko, E. Karpiuk, B. Kozankiewicz, A. Makarewicz and J. Piechowska, *J. Phys. Chem. A*, 2012, **116**, 2109–2116.

[203] A. J. Stasyuk, M. K. Cyrański, D. T. Gryko and M. Solà, *J. Chem. Theor. Comput.*, 2015, **11**, 1046–1054.

[204] H. Marciniak, S. Hristova, V. Deneva, F. S. Kamounah, P. E. Hansen, S. Lochbrunner and L. Antonov, *Phys. Chem. Chem. Phys.*, 2017, **19**, 26621–26629.

[205] H.-Y. Tsai, Y. Chang, J.-W. Hu and K.-Y. Chen, *Crystals*, 2017, **7**, 60.

[206] B. An, S. Feng, K. Wen, W. Wu, H. Yuan, Q. Zhu, X. Guo and J. Zhang, *Org. Electronics*, 2017, **45**, 1 – 8.

[207] X.-f. Yu, B. Xiao, J. Cheng, Z.-b. Liu, X. Yang and Q. Li, *ACS Omega*, 2019, **4**, 10516–10523.

[208] X. fang Yu, X. ye Sun, B. Xiao, Z. bo Liu, J. Cheng, X. Yang, W.-Z. Li and Q.-Z. Li, *J. Photochem. Photobiol. A Chem.*, 2019, **383**, 111989.

[209] H. Roohi, R. Nokhostin and M. Mohamadnia, *Dyes Pigm.*, 2016, **134**, 106 – 117.

[210] H. Roohi, H. R. Sherkhani and H. Mahbob, *J. Lumin.*, 2018, **204**, 230 – 243.

[211] K.-C. Tang, M.-J. Chang, T.-Y. Lin, H.-A. Pan, T.-C. Fang, K.-Y. Chen, W.-Y. Hung, Y.-H. Hsu and P.-T. Chou, *J. Am. Chem. Soc.*, 2011, **133**, 17738–17745.

[212] H. Roohi and P. Alizadeh, *Spectro. Acta Part A*, 2018, **196**, 83 – 102.

[213] Z. Tang, Y. Yang, Y. Yang, Y. Wang, J. Tian and X. Fei, *J. Lumin.*, 2018, **194**, 785 – 790.

[214] J. Hao and Y. Yang, *Org. Chem. Front.*, 2018, **5**, 1330–1341.

[215] M. Ni, S. Su and H. Fang, *Theor. Chem. Acc.* , 2019, **138**, year.

[216] J. Hao and Y. Yang, *J. Phys. Chem. A*, 2019, **123**, 3937–3948.

[217] D. Hessz, M. Bojtár, D. Mester, Z. Szakács, I. Bitter, M. K. llay and M. Kubinyi, *Spectro. Acta Part A*, 2018, **203**, 96 – 105.

[218] X. Lopez, M. A. L. Marques, A. Castro and A. Rubio, *J. Am. Chem. Soc.*, 2005, **127**, 12329–12337.

[219] G. Cui, Z. Lan and W. Thiel, *J. Am. Chem. Soc.*, 2012, **134**, 1662–1672.

[220] Y.-J. Ai, R.-Z. Liao, W.-H. Fang and Y. Luo, *Phys. Chem. Chem. Phys.*, 2012, **14**, 13409–13414.

[221] P. O. Hubin, A. D. Laurent, D. P. Vercauteren and D. Jacquemin, *Phys. Chem. Chem. Phys.*, 2014, **16**, 25288–25295.

[222] X.-Y. Liu, X.-P. Chang, S.-H. Xia, G. Cui and W. Thiel, *J. Chem. Theory Comput.*, 2016, **12**, 753–764.

[223] H. Roohi and R. Nokhostin, *J. Lumin.*, 2018, **196**, 406 – 424.

[224] Y.-H. Chen, R. Sung and K. Sung, *J. Phys. Chem. A*, 2018, **122**, 5931–5944.

[225] H. Yuan, S. Feng, K. Wen, X. Guo and J. Zhang, *Spectro. Acta Part A*, 2018, **191**, 421 – 426.

[226] H. Roohi and P. Alizadeh, *Spectro. Acta Part A*, 2019, **214**, 407 – 428.

[227] Y. Qi, Z. Tang, H. Zhan, Y. Wang, Y. Zhao, X. Fei, J. Tian, L. Yu and J. Liu, *Spectro. Acta Part A*, 2020, **224**, 117359.

[228] Y. Yang, Z. Tang, P. Zhou, Y. Qi, Y. Wang and H. Wang, *J. Mol. Liq.*, 2018, **260**, 447 – 457.

[229] A. L. Sobolewski, *Phys. Chem. Chem. Phys.*, 2008, **10**, 1243–1247.

[230] V. Barone and C. Adamo, *Chem. Phys. Letters*, 1995, **241**, 1–6.

[231] A. L. Sobolewski and L. Adamowicz, *Chem. Phys. Letters*, 1996, **252**, 33 – 41.

[232] V. Barone, A. Palma and N. Sanna, *Chem. Phys. Letters*, 2003, **381**, 451 – 457.

[233] R. Gelabert, M. Moreno and J. M. Lluch, *ChemPhysChem*, 2004, **5**, 1372–1378.

[234] J. M. Ortiz-Sánchez, R. Gelabert, M. Moreno and J. M. Lluch, *ChemPhysChem*, 2007, **8**, 1199–1206.

[235] J. M. Ortiz-Sánchez, R. Gelabert, M. Moreno and J. M. Lluch, *ChemPhysChem*, 2008, **9**, 2068–2076.

[236] F. Plasser, M. Barbatti, A. J. A. Aquino and H. Lischka, *J. Phys. Chem. A*, 2009, **113**, 8490–8499.

[237] M. A. Rios and M. C. Rios, *J. Phys. Chem.*, 1995, **99**, 12456–12460.

[238] R. Wortmann, S. Lebus, H. Reis, A. Grabowska, K. Kownacki and S. Jarosz, *Chem. Phys.*, 1999, **243**, 295 – 304.

[239] J. Weiß, V. May, N. Ernsting, V. Farztdinov and A. Mühlpfordt, *Chem. Phys. Lett.*, 2001, **346**, 503–511.

[240] M. Z. Zgierski, A. Fernández-Ramos and A. Grabowska, *J. Chem. Phys.*, 2002, **116**, 7486–7494.

[241] E. Luzina, J. Sepioł, Y. N. Svartsov and A. Grabowska, *J. Chem. Phys.*, 2007, **126**, 194308.

[242] J. Sepioł, A. Grabowska, P. Borowicz, M. Kijak, M. Broquier, C. Jouvet, C. Dedonder-Lardeux and A. Zehnacker-Rentien, *J. Chem. Phys.*, 2011, **135**, 034307.

[243] Y. Syetov, *J. Fluoresc.*, 2013, **23**, 689–696.

[244] P. Wnuk, G. Burdzinski, M. Sliwa, M. Kijak, A. Grabowska, J. Sepiol and J. Kubicki, *Phys. Chem. Chem. Phys.*, 2014, **16**, 2542–2552.

[245] S. Peukert, M. Gil, M. Kijak and J. Sepioł, *Chem. Phys. Lett.*, 2015, **641**, 153–157.

[246] M. M. Jadhav, L. Rhyman, P. Ramasami and N. Sekar, *J. Fluo.*, 2016, **26**, 1295–1307.

[247] M. M. Jadhav, I. A. Alswaidan, L. Rhyman, P. Ramasami and N. Sekar, *J. Sol. Chem.*, 2017, **46**, 1005–1023.

[248] D. Bao, M. Wang, C. Yang, Y. Yang and X. Ma, *J. Phys. Chem. A*, 2017, **121**, 8217–8226.

[249] R. Daengngern, R. Salaeh, T. Saelee, K. Kerdpol and N. Kungwan, *J. Mol. Liq.*, 2019, **286**, 110889.

[250] A. Grabowska, A. Mordzinski, N. Tamai and K. Yoshihara, *Chem. Phys. Letters*, 1990, **169**, 450 – 456.

[251] Y. Su and S. Chai, *J. Photochem. Photobiol. A Chem.*, 2014, **290**, 109 – 115.

[252] C. Ma, Y. Yang, C. Li and Y. Liu, *J. Phys. Chem. A*, 2015, **119**, 12686–12692.

[253] D. Yang, G. Yang, J. Zhao, R. Zheng and Y. Wang, *RSC Adv.*, 2017, **7**, 1299–1304.

[254] J. Lv and D. Yang, *J. Theor. Comput. Chem.*, 2017, **16**, 1750073.

[255] K. Hunger and W. Herbst, in *Ullmann's Encyclopedia of Industrial Chemistry*, American Cancer Society, vol. 3rd edition, ch. Pigments, Organic.

[256] J. Plötner and A. Dreuw, *Phys. Chem. Chem. Phys.*, 2006, **8**, 1197–1204.

[257] L. Lorenz, J. Plötner, V. V. Matylitsky, A. Dreuw and J. Wachtveitl, *J. Phys. Chem. A*, 2007, **111**, 10891–10898.

[258] J. Plötner and A. Dreuw, *Chem. Phys.*, 2008, **347**, 472 – 482.

[259] K. Fletcher, A. Dreuw and S. Faraji, *Comput. Theor. Chem.*, 2014, **1040-1041**, 177 – 185.

[260] M. A. Satam, R. D. Telore and N. Sekar, *Dyes Pigm.*, 2015, **123**, 274 – 284.

[261] J. J. Du, L. Váradi, J. Tan, Y. Zhao, P. W. Groundwater, J. A. Platts and D. E. Hibbs, *Phys. Chem. Chem. Phys.*, 2015, **17**, 4677–4686.

[262] M. Zhang, Q. Zhou, C. Du, Y. Ding and P. Song, *RSC Adv.*, 2016, **6**, 59389–59394.

[263] M. R. Shreykar and N. Sekar, *Dyes Pigm.*, 2017, **142**, 121 – 125.

[264] S. Shen, X. Liu, J. Sun, M. Wang, Z. Jiang, G. Xia and H. Wang, *Spectro. Acta Part A*, 2019, **217**, 93 – 100.

[265] B. Xiao, J. Cheng and X.-f. Yu, *Theor. Chem. Acc.*, 2015, **134**, 111.

[266] B. Xiao, X. fang Yu, Q. Li and J. Cheng, *J. Photochem. Photobiol. A Chem.*, 2018, **353**, 185 – 190.

[267] E. Falkovskaia, V. G. Pivovarenko and J. C. del Valle, *Chem. Phys. Lett.*, 2002, **352**, 415 – 420.

[268] E. Falkovskaia, V. G. Pivovarenko and J. Carlos del Valle, *J. Phys. Chem. A*, 2003, **107**, 3316–3325.

[269] A. D. Roshal, V. I. Moroz, V. G. Pivovarenko, A. Wróblewska and J. Błażejowski, *J. Org. Chem.*, 2003, **68**, 5860–5869.

[270] V. V. Moroz, A. G. Chalyi, I. E. Serdiuk, A. D. Roshal, B. Zadykowicz, V. G. Pivovarenko, A. Wróblewska and J. Błażejowski, *J. Phys. Chem. A*, 2013, **117**, 9156–9167.

[271] J. Zhao, H. Dong, H. Yang and Y. Zheng, *Org. Chem. Front.*, 2018, **5**, 2710–2718.

[272] Z. Tang, Y. Wang, D. Bao, M. Lv, Y. Yang, J. Tian and L. Dong, *J. Phys. Chem. A*, 2017, **121**, 8807–8814.

[273] Q. Meng, S. Yang, G. Ren and T. Chu, *J. Lumin.*, 2018, **200**, 14 – 18.

[274] S. Sartyoungkul, M. Ehara and H. Sakurai, *J. Phys. Chem. A*, 0, **0**, null.

[275] A. D. Laurent and D. Jacquemin, *Sci. China Chem.*, 2014, **57**, 1363–1368.

[276] A. D. Laurent, Y. Houari, P. H. P. R. Carvalho, B. A. D. Neto and D. Jacquemin, *RSC Adv.*, 2014, **4**, 14189–14192.

[277] S. Budzák and D. Jacquemin, *J. Phys. Chem. B*, 2016, **120**, 6730–6738.

[278] S. Budzák and D. Jacquemin, *Phys. Chem. Chem. Phys.*, 2018, **20**, 25031–25038.

[279] A. Chrayteh, C. Ewels and D. Jacquemin, *Phys. Chem. Chem. Phys.*, 2020, **22**, 854–863.

[280] J. B. Foresman and A. Frisch, *Exploring Chemistry with Electronic Structure methods*, Gaussian, Inc, 2nd edn, 1996.

[281] A. Szabo and N. S. Ostlund, *Modern Quantum Chemistry: Introduction to Advanced Electronic Structure Theory*, Dover Publications, Inc., 1st edn, 1996.

[282] C. Leforestier, *Introduction à la Chimie Quantique*, Dunod, 2005.

[283] C. J. Cramer, *Essentials of Computational Chemistry: Theories and Models*, John Wiley & Sons, 2013.

[284] M. A. Marques, N. T. Maitra, F. M. Nogueira, E. K. Gross and A. Rubio, *Fundamentals of time-dependent density functional theory*, Springer Science & Business Media, 2012, vol. 837.

[285] F. Jensen, *Introduction to Computational Chemistry*, John Wiley & Sons, 2nd edn, 2017.

[286] A. Dreuw and M. Head-Gordon, *Chem. Rev.*, 2005, **105**, 4009–4037.

[287] M. Casida and M. Huix-Rotllant, *Annu. Rev. Phys. Chem.*, 2012, **63**, 287–323.

[288] D. Jacquemin, Quantum chemistry lectures of Master 1 at Nantes University, 2015.

[289] D. Jacquemin, Quantum chemistry lectures of Master 2 at Nantes University, 2016.

[290] E. Schrödinger, *Phys. Rev.*, 1926, **28**, 1049–1070.

[291] B. M and O. R, *Annalen der Physik*, 1927, **389**, 457–484.

[292] J. C. Slater, *Phys. Rev.*, 1929, **34**, 1293–1322.

[293] R. Ditchfield, W. J. Hehre and J. A. Pople, *J. Chem. Phys.*, 1971, **54**, 724–728.

[294] T. H. Dunning, *J. chem. Phys.*, 1970, **53**, 2823–2833.

[295] P.-O. Löwdin, *Rev. Mod. Phys.*, 1962, **34**, 80–87.

[296] C. Møller and M. S. Plesset, *Phys. Rev.*, 1934, **46**, 618–622.

[297] M. Head-Gordon, J. A. Pople and M. J. Frisch, *Chem. Phys. Lett.*, 1988, **153**, 503 – 506.

[298] O. Christiansen, H. Koch and P. Jørgensen, *Chem. Phys. Lett.*, 1995, **243**, 409 – 418.

[299] P. Hohenberg and W. Kohn, *Phys. Rev.*, 1964, **136**, B864–B871.

[300] W. Kohn and L. J. Sham, *Phys. Rev.*, 1965, **140**, A1133–A1138.

[301] D. Jacquemin, V. Wathelet, E. A. Perpète and C. Adamo, *J. Chem. Theory Comput.*, 2009, **5**, 2420–2435.

[302] A. D. Becke, *Phys. Rev. A*, 1988, **38**, 3098–3100.

[303] J. P. Perdew, K. Burke and M. Ernzerhof, *Phys. Rev. Lett.*, 1996, **77**, 3865–3868.

[304] A. D. Becke, *J. Chem. Phys.*, 1993, **98**, 1372–1377.

[305] D. Jacquemin, A. Planchat, C. Adamo and B. Mennucci, *J. Chem. Theory Comput.*, 2012, **8**, 2359–2372.

[306] Y. Zhao and D. G. Truhlar, *Theor. Chem. Acc.*, 2008, **120**, 215–241.

[307] A. D. Becke, *J. Chem. Phys.*, 1993, **98**, 5648–5652.

[308] J.-D. Chai and M. Head-Gordon, *Phys. Chem. Chem. Phys.*, 2008, **10**, 6615–6620.

[309] A. Dreuw and M. Wormit, *WIREs Comput. Mol. Sci.*, 2015, **5**, 82–95.

[310] J. Schirmer, *Phys. Rev. A*, 1982, **26**, 2395–2416.

[311] P.-F. Loos and D. Jacquemin, *J. Phys. Chem. Lett.*, 2020, **11**, 974–980.

[312] P.-F. Loos, F. Lipparini, M. Boggio-Pasqua, A. Scemama and D. Jacquemin, *J. Chem. Theory Comput.*, 2020, **16**, 1711–1741.

[313] C. Hättig, *J. Chem. Phys.*, 2003, **118**, 7751–7761.

[314] E. Runge and E. K. U. Gross, *Phys. Rev. Lett.*, 1984, **52**, 997–1000.

[315] A. D. Laurent and D. Jacquemin, *Int. J. Quantum Chem.*, 2013, **113**, 2019–2039.

[316] K.-i. Sakai, T. Ishikawa and T. Akutagawa, *J. Mater. Chem. C*, 2013, **1**, 7866–7871.

[317] D. Dziuba, I. A. Karpenko, N. P. F. Barthes, B. Y. Michel, A. S. Klymchenko, R. Benhida, A. P. Demchenko, Y. Mély and A. Burger, *Chem. Eur. J.*, 2014, **20**, 1998–2009.

[318] J. Tomasi, B. Mennucci and R. Cammi, *Chem. rev.*, 2005, **105**, 2999–3094.

[319] B. Mennucci, S. Caprasecca and C. Guido, *C. Guido*, Academic Press, 2016, vol. 50, pp. 203–241.

[320] R. Cammi and B. Mennucci, *J. Chem. Phys.*, 1999, **110**, 9877–9886.

[321] M. Caricato, B. Mennucci, J. Tomasi, F. Ingrosso, R. Cammi, S. Corni and G. Scalmani, *J. Chem. Phys.*, 2006, **124**, 124520.

[322] A. V. Marenich, C. J. Cramer, D. G. Truhlar, C. A. Guido, B. Mennucci, G. Scalmani and M. J. Frisch, *Chem. Sci.*, 2011, **2**, 2143–2161.

[323] C. A. Guido, G. Scalmani, B. Mennucci and D. Jacquemin, *J. Chem. Phys.*, 2017, **146**, 204106.

[324] B. G. Levine, C. Ko, J. Quenneville and T. J. MartÍnez, *Mol. Phys.*, 2006, **104**, 1039–1051.

[325] D. R. Yarkony, *Rev. Mod. Phys.*, 1996, **68**, 985–1013.

[326] D. R. Yarkony, *J. Phys. Chem. A*, 2001, **105**, 6277–6293.

[327] C. Hättig and F. Weigend, *J. Chem. Phys.*, 2000, **113**, 5154–5161.

[328] M. J. Frisch, G. W. Trucks, H. B. Schlegel, G. E. Scuseria, M. A. Robb, J. R. Cheeseman, G. Scalmani, V. Barone, G. A. Petersson, H. Nakatsuji, X. Li, M. Caricato, A. V. Marenich, J. Bloino, B. G. Janesko, R. Gomperts, B. Mennucci, H. P. Hratchian, J. V. Ortiz, A. F. Izmaylov, J. L. Sonnenberg, D. Williams-Young, F. Ding, F. Lipparini, F. Egidi, J. Goings, B. Peng, A. Petrone, T. Henderson, D. Ranasinghe, V. G. Zakrzewski, J. Gao, N. Rega, G. Zheng, W. Liang, M. Hada, M. Ehara, K. Toyota, R. Fukuda, J. Hasegawa, M. Ishida, T. Nakajima, Y. Honda, O. Kitao, H. Nakai, T. Vreven, K. Throssell, J. A. Montgomery, Jr., J. E. Peralta, F. Ogliaro, M. J. Bearpark, J. J. Heyd, E. N. Brothers, K. N. Kudin, V. N. Staroverov, T. A. Keith, R. Kobayashi, J. Normand, K. Raghavachari, A. P. Rendell, J. C. Burant, S. S. Iyengar, J. Tomasi, M. Cossi, J. M. Millam, M. Klene, C. Adamo, R. Cammi, J. W. Ochterski, R. L. Martin, K. Morokuma, O. Farkas, J. B. Foresman and D. J. Fox, *Gaussian 16 Revision A.03*, 2016, Gaussian Inc. Wallingford CT.

[329] *TURBOMOLE V6.6 2014, a development of University of Karlsruhe and Forschungszentrum Karlsruhe GmbH, 1989-2007, TURBOMOLE GmbH, since 2007; available from* `http://www.turbomole.com`.

[330] S. Boys and F. Bernardi, *Mol. Phys.*, 1970, **19**, 553–566.

[331] C. Adamo and D. Jacquemin, *Chem. Soc. Rev.*, 2013, **42**, 845–856.

[332] D. Jacquemin and C. Adamo, in *Computational Molecular Electronic Spectroscopy with TD-DFT*, ed. N. Ferré, M. Filatov and M. Huix-Rotllant, Springer International Publishing, 2016, pp. 347–375.

[333] M. J. Paterson, M. A. Robb, L. Blancafort and A. D. DeBellis, *J. Am. Chem. Soc.*, 2004, **126**, 2912–2922.

[334] R. Cammi, B. Mennucci and J. Tomasi, *J. Phys. Chem. A*, 2000, **104**, 5631–5637.

[335] C. Hättig, *Phys. Chem. Chem. Phys.*, 2005, **7**, 59–66.

[336] C. A. Guido and S. Caprasecca, *Int. J. Quantum Chem.*, 2019, **119**, e25711.

[337] C. A. Guido, D. Jacquemin, C. Adamo and B. Mennucci, *J. Chem. Theory Comput.*, 2015, **11**, 5782–5790.

[338] C. A. Guido, B. Mennucci, G. Scalmani and D. Jacquemin, *J. Chem. Theory Comput.*, 2018, **14**, 1544–1553.

[339] F. Santoro, *FCclasses, A Fortran 77 Code*, 2011, See: http://village.pi.iccom.cnr.it [last accessed 06.15.17].

[340] F. Santoro, R. Improta, A. Lami, J. Bloino and V. Barone, *J. Chem. Phys.*, 2007, **126**, 084509.

[341] F. Santoro, A. Lami, R. Improta and V. Barone, *J. Chem. Phys.*, 2007, **126**, 184102.

[342] F. Santoro and D. Jacquemin, *WIREs Comput. Mol. Sci.*, 2016, **6**, 460–486.

[343] D. Jacquemin, E. A. Perpète, I. Ciofini and C. Adamo, *Theor. Chem. Acc.*, 2011, **128**, 127–136.

[344] M. Dierksen and S. Grimme, 2004, **108**, 10225–10237.

[345] F. Muniz-Miranda, A. Pedone, G. Battistelli, M. Montalti, J. Bloino and V. Barone, *J. Chem. Theory Comput.*, 2015, **11**, 5371–5384.

[346] L. Goerigk, J. Moellmann and S. Grimme, *Phys. Chem. Chem. Phys.*, 2009, **11**, 4611–4620.

[347] N. O. C. Winter, N. K. Graf, S. Leutwyler and C. Hattig, *Phys. Chem. Chem. Phys.*, 2013, **15**, 6623–6630.

[348] D. Jacquemin, I. Duchemin and X. Blase, *J. Chem. Theory Comput.*, 2015, **11**, 5340–5359.

[349] H. Yuan, S. Feng, K. Wen, Q. Zhu, B. An, X. Guo and J. Zhang, *Spectro. Acta Part A*, 2017, **183**, 123 – 130.

[350] D. O. Samultsev, V. A. Semenov and L. B. Krivdin, *Magn. Reson. Chem.*, 2014, **52**, 222–230.

[351] D. Flaig, M. Maurer, M. Hanni, K. Braunger, L. Kick, M. Thubauville and C. Ochsenfeld, *J. Chem. Theory Comput.*, 2014, **10**, 572–578.

[352] V. A. Semenov, D. O. Samultsev and L. B. Krivdin, *Magn. Reson. Chem.*, 2015, **53**, 433–441.

[353] D. Jacquemin, M. Khelladi, A. D. Nicola and G. Ulrich, *Dyes Pigm.*, 2019, **163**, 475–482.

[354] P.-F. Loos, F. Lipparini, M. Boggio-Pasqua, A. Scemama and D. Jacquemin, *J. Chem. Theor. Comput.*, 2020, **16**, 1711–1741.

[355] X. Zhang, D. Jacquemin, Q. Peng, Z. Shuai and D. Escudero, *J. Phys. Chem. C*, 2018, **122**, 6340–6347.

[356] S. Lin, Q. Peng, Q. Ou and Z. Shuai, *Inorg. Chem.*, 2019, **58**, 14403–14409.

Appendix to Chapter 5

Table A-1: Bond lengths of the GS and ES of EE optimised with (TD-)DFT (B3LYP, M06-2X, and ωB97X-D) and CC2. All the optimisations are performed in gas phase and use the cc-pVTZ basis set. The C_{2v} symmetry is used in all cases except B3LYP/TD-DFT that leads a C_s structure. See Figure A-1 for labels.

		GS				ES			
		B3LYP	M06-2X	ωB97X-D	CC2	B3LYP	M06-2X	ωB97X-D	CC2
1	C-C	1.424	1.427	1.427	1.410	1.392	1.384	1.383	1.380
2	C-C	1.385	1.374	1.375	1.390	1.422	1.422	1.423	1.428
3	C-S	1.743	1.730	1.730	1.727	1.766	1.753	1.754	1.753
4	C-O	1.334	1.331	1.327	1.334	1.337	1.332	1.328	1.333
5	O-H	0.984	0.977	0.978	0.991	0.984	0.979	0.980	0.996
6	H-N	1.898	1.942	1.898	1.822	1.891	1.915	1.876	1.785
7	C-C	1.423	1.430	1.429	1.410	1.388	1.387	1.387	1.371
8	C-N	1.307	1.298	1.298	1.317	1.337	1.331	1.331	1.354
9	N-C	1.389	1.391	1.389	1.383	1.363	1.361	1.361	1.355
10	C-C	1.397	1.392	1.389	1.396	1.414	1.409	1.405	1.414
11	C-O	1.376	1.369	1.368	1.374	1.368	1.360	1.367	1.365
12	O-C	1.366	1.355	1.351	1.368	1.381	1.371	1.367	1.386

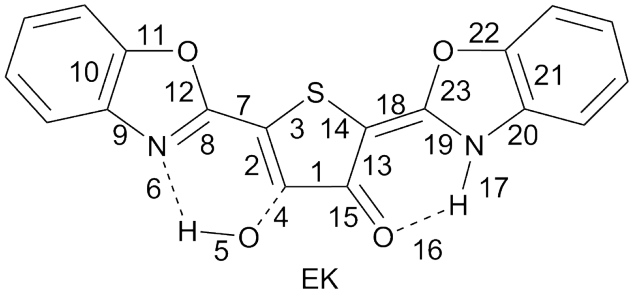

Figure A-1: Bond labels of the Enol-Keto **BBTP** form. Labels are identical for EE and KK.

Table A-2: Bond lengths of EK* and KK* optimised with TD-DFT (B3LYP, M06-2X, and ωB97X-D) and CC2. All the optimisations are in gas phase and use the cc-pVTZ atomic basis set. See Figure A-1 for labels.

		EK*				KK*			
		B3LYP	M06-2X	ωB97X-D	CC2	B3LYP	M06-2X	ωB97X-D	CC2
1	C-C	1.452	1.447	1.447	1.415	1.485	1.477	1.474	1.458
2	C-C	1.394	1.394	1.399	1.401	1.458	1.464	1.464	1.462
3	C-S	1.757	1.740	1.734	1.768	1.738	1.719	1.719	1.714
4	C-O	1.327	1.321	1.315	1.343	1.244	1.236	1.238	1.266
5	O-H	0.994	0.987	0.990	0.996	1.972	1.978	1.959	1.780
6	H-N	1.843	1.876	1.830	1.812	1.021	1.020	1.019	1.039
7	C-C	1.400	1.402	1.401	1.381	1.371	1.364	1.364	1.369
8	C-N	1.329	1.317	1.317	1.337	1.361	1.358	1.357	1.357
9	N-C	1.375	1.381	1.381	1.374	1.380	1.380	1.378	1.371
10	C-C	1.405	1.398	1.394	1.403	1.397	1.394	1.391	1.397
11	C-O	1.378	1.372	1.371	1.374	1.386	1.378	1.377	1.383
12	O-C	1.379	1.365	1.361	1.385	1.365	1.357	1.354	1.366
13	C-C	1.467	1.472	1.466	1.485	1.458	1.464	1.464	1.462
14	C-S	1.720	1.701	1.705	1.696	1.738	1.719	1.719	1.714
15	C-O	1.242	1.236	1.238	1.269	1.244	1.236	1.238	1.266
16	O-H	2.002	2.006	1.998	1.776	1.972	1.978	1.959	1.780
17	H-N	1.019	1.019	1.017	1.040	1.021	1.020	1.019	1.039
18	C-C	1.377	1.373	1.372	1.378	1.371	1.364	1.364	1.369
19	C-N	1.359	1.357	1.357	1.355	1.361	1.358	1.357	1.357
20	N-C	1.380	1.379	1.377	1.367	1.380	1.380	1.378	1.371
21	C-C	1.397	1.394	1.391	1.398	1.397	1.394	1.391	1.397
22	C-O	1.385	1.377	1.376	1.379	1.386	1.378	1.377	1.383
23	O-C	1.360	1.335	1.352	1.362	1.365	1.357	1.354	1.366

Table A-3: Bond length of EE* optimised with TD-DFT/6-31G(d) in gas and solution (LR and VEM-UD), considering both M06-2X and ωB97X-D XCFs. See Figure A-1 for labels.

		M06-2X			ωB97X-D		
		gas	LR	VEM-UD	gas	LR	VEM-UD
1	C-C	1.391	1.385	1.395	1.390	1.385	1.389
2	C-C	1.425	1.428	1.410	1.427	1.430	1.427
3	C-S	1.761	1.760	1.758	1.763	1.762	1.762
4	C-O	1.333	1.337	1.349	1.334	1.335	1.335
5	O-H	0.986	0.986	0.984	0.986	0.986	0.987
6	H-N	1.911	1.910	1.923	1.881	1.879	1.875
7	C-C	1.391	1.386	1.403	1.391	1.387	1.389
8	C-N	1.335	1.338	1.327	1.336	1.339	1.337
9	N-C	1.364	1.361	1.376	1.365	1.363	1.365
10	C-C	1.414	1.416	1.407	1.410	1.412	1.411
11	C-O	1.362	1.362	1.368	1.363	1.363	1.364
12	O-C	1.372	1.372	1.371	1.370	1.370	1.369
13	C-C	1.425	1.428	1.436	1.427	1.430	1.427
14	C-S	1.761	1.760	1.765	1.763	1.762	1.762
15	C-O	1.333	1.337	1.325	1.334	1.335	1.335
16	O-H	0.986	0.986	0.989	0.986	0.986	0.987
17	H-N	1.911	1.910	1.881	1.881	1.879	1.875
18	C-C	1.391	1.386	1.372	1.391	1.387	1.389
19	C-N	1.335	1.338	1.356	1.336	1.339	1.337
20	N-C	1.364	1.361	1.349	1.365	1.363	1.365
21	C-C	1.414	1.416	1.428	1.410	1.412	1.411
22	C-O	1.362	1.362	1.365	1.363	1.363	1.364
23	O-C	1.372	1.372	1.369	1.370	1.370	1.369

Table A-4: Bond lengths of EK* optimised with TD-DFT/6-31G(d) in gas and solution (LR and VEM-UD) considering both M06-2X and ωB97X-D XCFs. See Figure A-1 for labels.

		M06-2X			ωB97X-D		
		gas	LR	VEM-UD	gas	LR	VEM-UD
1	C-C	1.448	1.439	1.445	1.450	1.440	1.443
2	C-C	1.395	1.390	1.383	1.401	1.395	1.388
3	C-S	1.759	1.774	1.801	1.751	1.770	1.797
4	C-O	1.328	1.339	1.346	1.323	1.335	1.341
5	O-H	0.991	0.987	0.988	0.994	0.989	0.989
6	H-N	1.895	1.929	1.928	1.848	1.886	1.887
7	C-C	1.404	1.402	1.396	1.403	1.401	1.393
8	C-N	1.321	1.321	1.337	1.322	1.322	1.336
9	N-C	1.382	1.384	1.374	1.384	1.386	1.379
10	C-C	1.403	1.403	1.409	1.400	1.400	1.404
11	C-O	1.374	1.373	1.371	1.375	1.374	1.373
12	O-C	1.368	1.369	1.379	1.365	1.366	1.375
13	C-C	1.483	1.488	1.500	1.477	1.485	1.495
14	C-S	1.708	1.707	1.716	1.712	1.706	1.712
15	C-O	1.241	1.245	1.231	1.244	1.247	1.235
16	O-H	1.977	2.031	2.069	1.977	2.022	2.049
17	H-N	1.024	1.022	1.020	1.023	1.021	1.019
18	C-C	1.377	1.384	1.374	1.377	1.385	1.379
19	C-N	1.360	1.357	1.354	1.361	1.356	1.352
20	N-C	1.380	1.377	1.381	1.381	1.378	1.383
21	C-C	1.400	1.402	1.399	1.397	1.399	1.395
22	C-O	1.377	1.374	1.375	1.379	1.376	1.379
23	O-C	1.356	1.353	1.349	1.355	1.351	1.346

Table A-5: Bond length of KK* optimised with TD-DFT/6-31G(d) in gas and solution (LR and VEM-UD) considering both M06-2X and ωB97X-D XCFs. See Figure A-1 for labels.

		M06-2X			ωB97X-D		
		gas	LR	VEM-UD	gas	LR	VEM-UD
1	C-C	1.479	1.476	1.484	1.476	1.474	1.479
2	C-C	1.471	1.465	1.493	1.472	1.466	1.469
3	C-S	1.728	1.727	1.710	1.730	1.728	1.738
4	C-O	1.242	1.248	1.229	1.244	1.250	1.244
5	O-H	1.975	2.046	2.066	1.964	2.036	2.084
6	H-N	1.023	1.020	1.019	1.022	1.019	1.016
7	C-C	1.367	1.371	1.372	1.366	1.371	1.363
8	C-N	1.363	1.360	1.355	1.363	1.360	1.364
9	N-C	1.382	1.383	1.386	1.382	1.383	1.384
10	C-C	1.399	1.398	1.396	1.396	1.396	1.395
11	C-O	1.379	1.380	1.380	1.380	1.381	1.382
12	O-C	1.360	1.358	1.351	1.358	1.356	1.359
13	C-C	1.471	1.465	1.442	1.472	1.466	1.469
14	C-S	1.728	1.727	1.768	1.730	1.728	1.738
15	C-O	1.242	1.248	1.255	1.244	1.250	1.244
16	O-H	2.046	2.046	2.099	2.046	2.036	2.084
17	H-N	1.023	1.020	1.017	1.022	1.019	1.016
18	C-C	1.367	1.371	1.363	1.366	1.371	1.363
19	C-N	1.363	1.360	1.374	1.363	1.360	1.364
20	N-C	1.382	1.383	1.381	1.382	1.383	1.384
21	C-C	1.399	1.398	1.401	1.396	1.396	1.395
22	C-O	1.379	1.380	1.380	1.380	1.381	1.382
23	O-C	1.360	1.358	1.370	1.358	1.356	1.359

Appendix to Chapter 6

Table A-6: Bond lengths (Å) and dihedral angles (degree) of **3** and **4H** optimised at the PCM(DOX)/M06-2X/6-31G(d) level and measured with X-Ray (experimental values from Ref. 22). The Cl^- counter-ion is included in the optimisation of **4H**. See Figure A-2 for labels.

Bond length	**3** (theo.)	**BTImP**[22] (exp.)	**4H** (theo.)	**BTImPH**$^+$[22] (exp.)
1	1.740	1.625	1.868	1.749
2	0.993	0.996	0.840	0.991
3	1.345	1.355	1.354	1.341
4	1.409	1.403	1.414	1.415
5	1.394	1.388	1.401	1.396
6	1.392	1.390	1.372	1.392
7	1.390	1.383	1.387	1.394
8	1.402	1.396	1.394	1.397
9	1.411	1.414	1.390	1.403
10	1.470	1.474	1.465	1.466
11	1.371	1.375	1.354	1.349
12	1.391	1.396	1.403	1.394
13	1.379	1.380	1.372	1.373
14	1.371	1.384	1.375	1.381
15	1.321	1.329	1.329	1.331
16	1.475	1.471	1.465	1.464
17	1.298	1.308	1.314	1.301
18	1.379	1.380	1.395	1.383
19	1.407	1.399	1.413	1.407
20	1.738	1.736	1.733	1.742
21	1.770	1.754	1.730	1.761
22			0.880	1.073

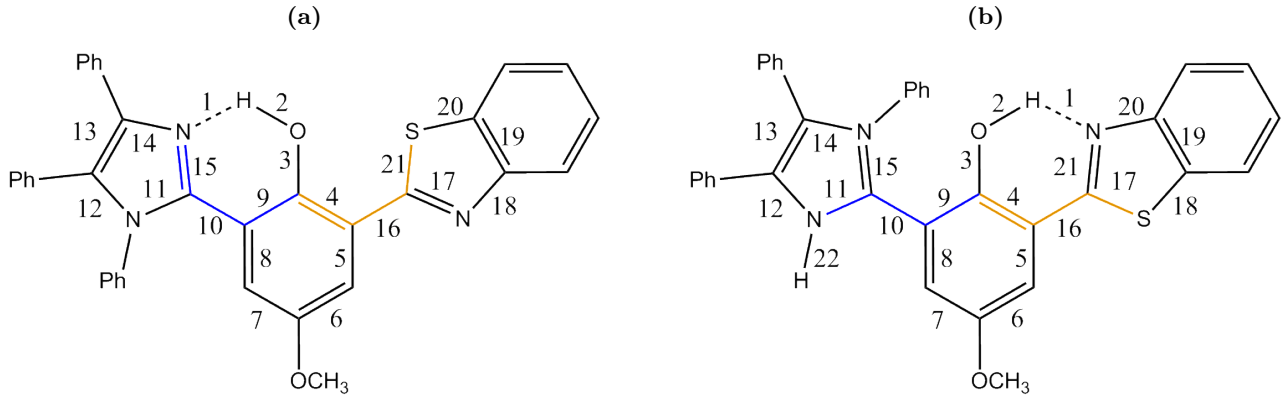

Figure A-2: Bond labels of **3**(a) and **4H** (b)

Table A-7: NMR chemical shift (ppm) calculated with B3LYP/cc-pVTZ in THF for **BTImP** and **BTImPH**$^+$ in presence and absence of counter-ion.

	3	**2H**			**3H**			**4H**		
	∅	∅	BF_4^-	ClO_4^-	∅	BF_4^-	ClO_4^-	∅	BF_4^-	ClO_4^-
H6	6.3	6.4	6.2	6.1	6.4	6.1	6.1	6.8	9.1	9.0
H7	8.6	8.0	9.7	9.3	8.1	8.9	9.1	7.9	9.6	9.4
H1	8.2	8.3	8.2	8.1	8.3	8.3	8.2	8.3	8.2	8.2
H4	8.3	8.3	8.3	8.6	8.5	8.2	8.3	8.3	8.2	8.2
N	249	166	182	181	168	178	179	170	180	181

Table A-8: NMR chemical shift (ppm) calculated with B3LYP/cc-pVTZ in THF for **BTImPH**$^+$ in presence and absence of counter-ion.

	2H			**3H**			**4H**		
	∅	BF_4^-	ClO_4^-	∅	BF_4^-	ClO_4^-	∅	BF_4^-	ClO_4^-
H6	6.5	6.3	6.3	6.4	6.3	6.3	6.9	8.8	8.7
H7	8.1	9.4	8.9	8.1	8.7	8.9	8.0	9.3	9.2
H1	8.3	8.3	8.3	8.3	8.3	8.3	8.3	8.2	8.2
H4	8.3	8.3	8.5	8.4	8.4	8.4	8.3	8.2	8.3
N	161	178	178	163	175	176	165	171	178

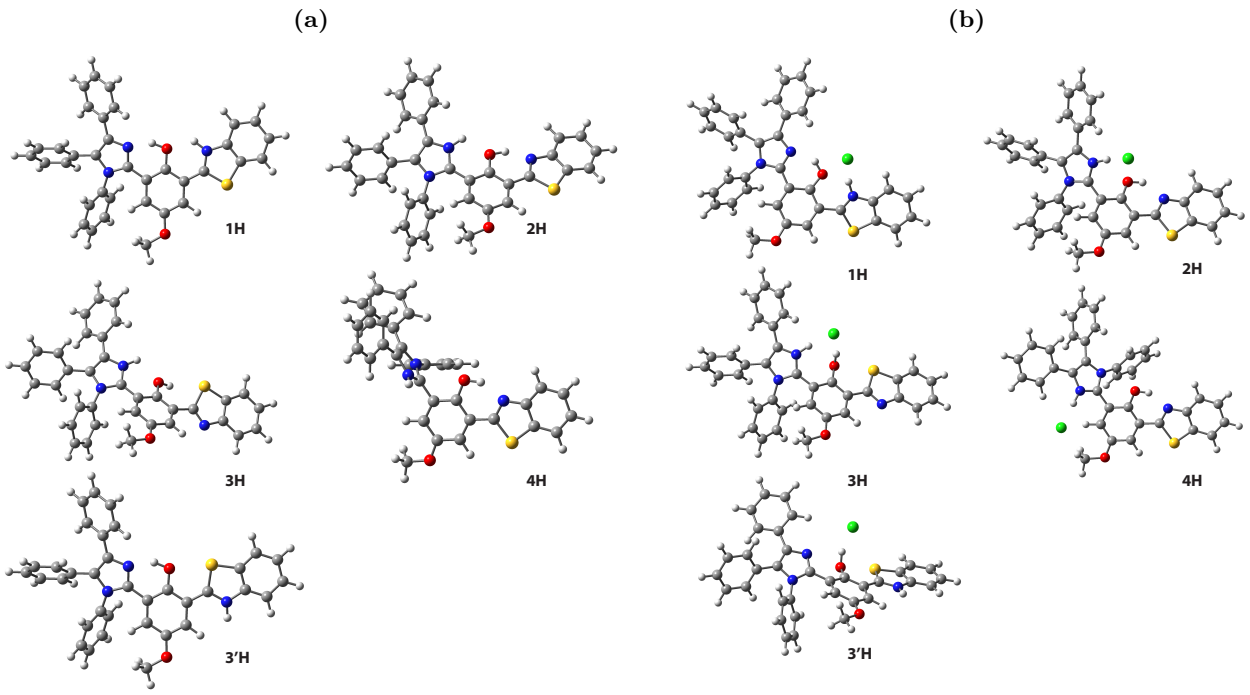

Figure A-3: Representation of the optimised ground state of **BTImPH**$^+$ conformers in absence (a) or presence (b) of Cl^- counter-ion.

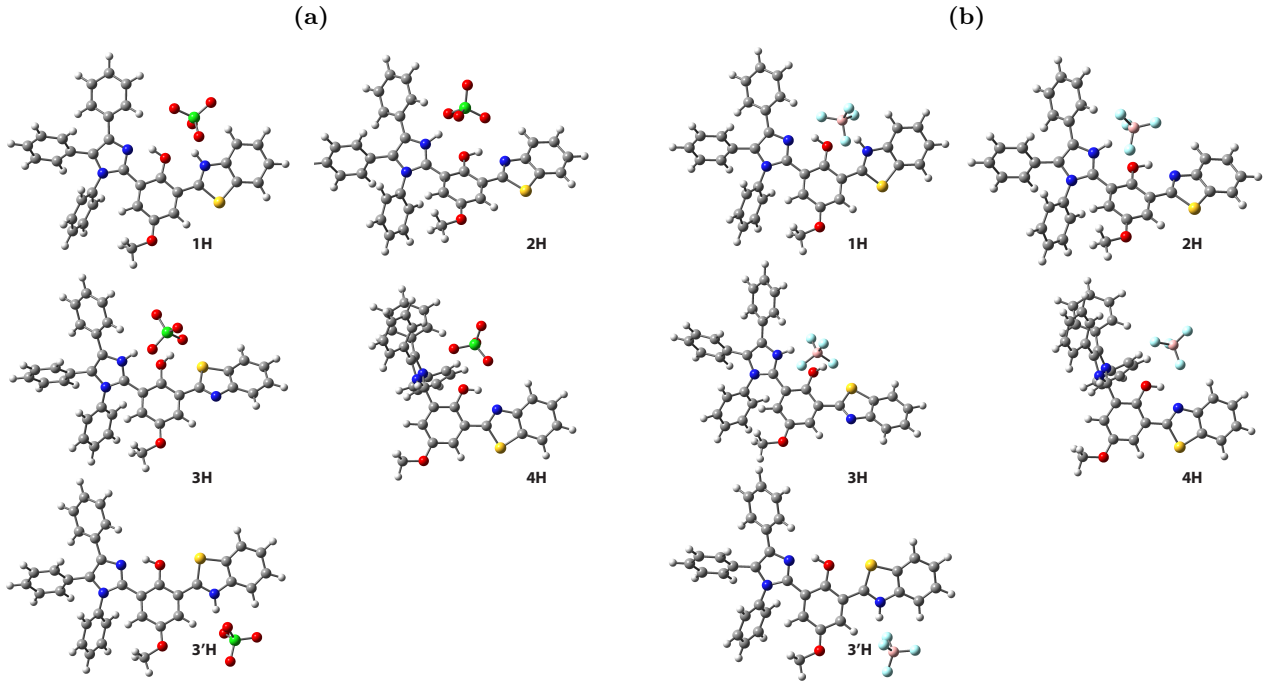

Figure A-4: Representation of the optimised ground state of **BTImPH**$^+$ conformers in presence of ClO_4^- (a) and BF_4^- (b) counter-ion.

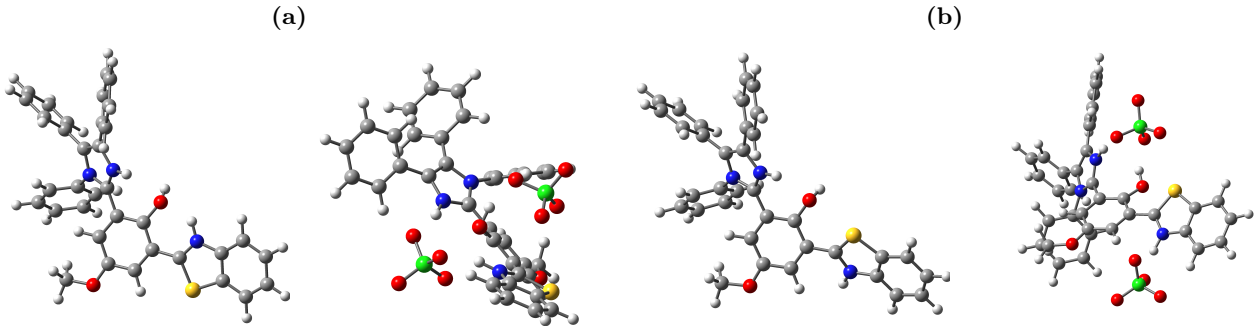

Figure A-5: Representation of the optimised ground state of (a) **2HH** and (b) **3HH** in absence (left) or presence (right) of two ClO_4^- counter-ions.

UNIVERSITE MATIERE BRETAGNE MOLECULES LOIRE ET MATERIAUX

UNIVERSITÉ DE NANTES

Titre : **Modélisation de transferts de protons à l'état excité**

Mots clés : Calcul *ab initio* (Chimie quantique), Colorants ESIPT, TD-DFT, CC2, Fluorescence, Dérivés hydroxyphenylbenzoxazole

Résumé : Cette thèse est dédiée à l'exploration des surfaces d'énergie potentielle des états électroniques excités de colorants "ESIPT" (*Excited-State Intramolecular Proton Transfer*) à l'aide d'approches de chimie quantique. Le phénomène ESIPT s'observe typiquement dans des molécules présentant une liaison hydrogène intramoléculaire forte. Le changement de géométrie provoqué par ce transfert permet d'obtenir une grande différence entre l'absorption et l'émission (grand déplacement de Stokes), ouvrant la voie à de multiples applications. Le but de cette thèse est d'identifier les substituants les plus adéquats pour obtenir des signatures d'émission spécifiques, en étroite collaboration avec le groupe expérimental de G. Ulrich à Strasbourg. Pour ce faire, la théorie fonctionnelle de la densité dépendante du temps (TD-DFT) ainsi que des approches post-Hartree-Fock [ADC(2) et CC2] ont été utilisées pour modéliser les propriétés de nombreux colorants. Une attention particulière a été portée aux effets de l'environnement avec l'utilisation d'approches de continuum sous leurs formes de réponse linéaire (LR) et de réponse linéaire corrigée (cLR). Les travaux réalisés lors cette thèse ont permis : i) d'évaluer l'impact des auxochromes (accepteurs et donneurs d'électrons) sur la stabilité des tautomères à l'état excité ; ii) de quantifier les états de transition entre deux ou trois formes tautomériques ; iii) de déterminer les propriétés spectrales des isomères ; et iv) d'identifier les espèces émissives dans le cas d'un système acidochrome complexe.

Title : **Modelling of excited state proton transfer in fluorescent dyes**

Keywords : *Ab initio* calculations (Quantum chemistry), ESIPT dye, TD-DFT, CC2, Fluorescence, Hydroxyphenylbenzoxazole derivatives

Abstract : This thesis is dedicated to the exploration of potential energy surfaces of excited electronic states of "ESIPT" (Excited-State Intramolecular Proton Transfer) dyes, using quantum chemistry approaches. The ESIPT phenomenon is typically found in molecules possessing a strong intramolecular hydrogen bond. The change in geometry induced by the ESIPT yields a large difference between the absorption and emission wavelengths (large Stokes' shift), paving the way to multiple applications. The aim of this thesis is to identify the most suitable auxochromes to obtain specific emissive signatures, in close collaboration with the experimental group of G. Ulrich (Strasbourg). To this end, Time-Dependent Density Functional Theory (TD-DFT) as well as post-Hartree-Fock approaches [ADC(2) and CC2] have been used to model the properties of many dyes. A specific attention was paid to accurately model the environmental effects by using continuum approaches in their linear response (LR) and corrected linear response (cLR) forms. The work carried out during this thesis allowed: i) to evaluate the impact of auxochromes (acceptors and electron donors) on the stability of the tautomers in the excited state; ii) to quantify the transition states between two or three tautomeric forms; iii) to determine the spectral properties of all relevant isomers; and iv) to identify the emissive species in a complex acidochromic system.